

Current and Evolved Physical Layer Concepts: Potentials and Limitations of Mobile Broadband Wireless Access

Von der Fakultät für Elektrotechnik und Informationstechnik
der Rheinisch-Westfälischen Technischen Hochschule Aachen
zur Erlangung des akademischen Grades eines
Doktors der Ingenieurwissenschaften genehmigte Dissertation

vorgelegt von

Diplom-Ingenieur
Helge Erik Lüders

aus Bernau bei Berlin

Berichter: Universitätsprofessor Dr.-Ing. Peter Vary
 Universitätsprofessor Dr. rer. nat. Rudolf Mathar

Tag der mündlichen Prüfung:
27. Juli 2010

Diese Dissertation ist auf den Internetseiten der Hochschulbibliothek online verfügbar.

AACHENER BEITRÄGE ZU DIGITALEN NACHRICHTENSYSTEMEN

Herausgeber:

Prof. Dr.-Ing. Peter Vary
Institut für Nachrichtengeräte und Datenverarbeitung
Rheinisch-Westfälische Technische Hochschule Aachen
Muffeter Weg 3a
52074 Aachen
Tel.: 0241-80 26 956
Fax.: 0241-80 22 186

Bibliografische Information der Deutschen Bibliothek

Die Deutsche Bibliothek verzeichnet diese Publikation in der Deutschen Nationalbibliografie; detaillierte bibliografische Daten sind im Internet über <http://dnb.ddb.de> abrufbar

1. Auflage Aachen:

Wissenschaftsverlag Mainz in Aachen
(Aachener Beiträge zu digitalen Nachrichtensystemen, Band 26)
ISSN 1437-6768
ISBN 3-86130-652-2

© 2010 Helge Erik Lüders

Wissenschaftsverlag Mainz
Süsterfeldstr. 83, 52072 Aachen
Tel.: 02 41 / 2 39 48 oder 02 41 / 87 34 34
Fax: 02 41 / 87 55 77
www.Verlag-Mainz.de

Herstellung: Druckerei Mainz GmbH,
Süsterfeldstr. 83, 52072 Aachen
Tel.: 02 41 / 87 34 34; Fax: 02 41 / 87 55 77
www.Druckservice-Aachen.de

Gedruckt auf chlorfrei gebleichtem Papier

"D 82 (Diss. RWTH Aachen University, 2010)"

Danksagung

Die vorliegende Arbeit entstand im Rahmen meiner Tätigkeit als wissenschaftlicher Mitarbeiter des Instituts für Nachrichtengeräte und Datenverarbeitung (IND) der Rheinisch-Westfälischen Technischen Hochschule Aachen und wurde unterstützt durch meine Mitarbeit im Exzellenzcluster Ultra High Speed Mobile Information and Communication (UMIC).

Mein besonders herzlicher Dank gilt Herrn Prof. Dr.-Ing. Peter Vary für die Betreuung dieser Arbeit und die Schaffung eines abwechslungs- und facettenreichen Tätigkeitsfeldes, welches die vielen Aspekte dieser Dissertation prägte.

Herrn Prof. Dr. rer. nat. Rudolf Mathar danke ich für sein Interesse an meiner Arbeit und die Übernahme des Koreferats.

Durch die vermutlich einzigartige Zusammenarbeit und Kollegialität sowie den daraus entstandenen Freundschaften wird mir die Arbeit am IND für immer in Erinnerung bleiben. Dafür möchte ich mich bei allen aktiven und ehemaligen Kollegen am Institut und im UMIC-Cluster herzlich bedanken! Vielen Dank Andreas, Annika, Aulis, Bastian, Bernte, Birgit, Carsten, Christiane, Christoph, Florian, Frank, Hauke, Heiner, Laurent, Magnus, Marc A., Marc W., Marco, Martin, Matthias P., Matthias R., Sanne, Sylvia, Thomas E., Thomas S., Thorsten und Tobias!

Wichtige Teile dieser Arbeit stützen sich auf die Studien- und Diplomarbeiten der von mir betreuten Studenten und Studentinnen, bei denen ich mich an dieser Stelle herzlich bedanken möchte, insbesondere bei meinen späteren Kollegen Benedikt, Andreas und Katrin.

Schließlich danke ich meinen Eltern, die mir das Studium der Elektrotechnik ermöglicht und mich stets nach Kräften unterstützt haben. Dir, liebe Jutta, danke ich für Deine Geduld, Dein Verständnis und Deine Nähe!

Köln, im Juli 2010

Helge Lüders



Abstract

Two important factors fuel the fast evolution of mobile broadband access technologies: The ever-increasing demand for high data rates due to the availability and acceptance of mobile devices and applications and the demand for affordable broadband access in under served areas where radio technologies are regarded as a substitute to fixed line technologies.

This thesis highlights potentials and limitations of current and future mobile radio systems for area-wide mobile broadband access. It describes and thoroughly analyzes the physical layer of the current Release 8 of the UMTS LTE mobile radio standard implemented as single-antenna system. Different novel modifications and alternative concepts are introduced and analyzed which aim at either increasing the physical layer performance or at decreasing the computational complexity. In addition, upper bounds on the performance concerning the obtainable bits per channel use are regarded for single- and multiple-antenna systems. It is observed that single-antenna LTE operates at approximately 65 % of the Shannon limit.

On top of the physical layer simulation results, system-level simulations of the downlink in a cellular environment are performed to evaluate the potentials and limitations of UMTS LTE and the introduced physical layer modifications concerning the coverage, quality and capacity of a radio cell within a mobile radio network. Two carrier frequencies are considered: 0.8 GHz and 2.0 GHz representing the frequencies from the digital dividend and of current UMTS deployments, respectively. The employed frequency bandwidths of 5 MHz and 20 MHz represent the frequency bandwidth of current UMTS and the largest frequency bandwidth supported by UMTS LTE Release 8, respectively. Additionally, different propagation scenarios representing typical mobile radio environments are considered.

System-level simulation results reveal an imbalance concerning the individual user goodputs (error-free throughput) within a radio cell: near the cell edges these individual user goodputs might drop to only one tenth of the user goodputs that are achieved near the base station. The average cell goodput is derived and given for all combinations of the considered system-level parameters. It is shown that the achieved goodputs scale linearly with the available frequency bandwidth. The influence of the carrier frequency is observed to significantly influence the coverage and capacity of a radio cell only if it is interference limited.

In the future, major gains can be expected from more sophisticated coding and signal processing. The most promising options are multiple-antenna systems and intelligent interference management algorithms. With the derived bounds it is shown that in theory, a capacity achieving 4×4 multiple-antenna system using 20 MHz frequency bandwidth and ideal interference cancellation could achieve an average cell goodput > 1 Gbit/s.



Contents

Abbreviations	xi
1 Introduction	1
2 Mobile Broadband Access	3
2.1 What Is Broadband?	3
2.2 What Is Mobile Access?	4
2.3 Current Situation in Germany	5
3 Fundamentals	9
3.1 Network Architecture Aspects	9
3.2 Spectral Efficiency, Throughput, and Coverage	11
4 Physical Layer Concepts	15
4.1 General Transmission System Model	15
4.1.1 Source Coding	16
4.1.2 Channel Coding	16
4.1.3 Complex Mapping	17
4.1.4 Baseband Modulation	17
4.1.5 Channel Model and Equalization	18
4.1.6 Performance Measures	21
4.1.7 EXIT Analysis	22
4.2 System Concepts and Their Evolution	23
4.2.1 Second Generation Mobile Radio: FDM(A)/TDM(A)	24
4.2.2 Third Generation Mobile Radio: CDM(A)	26
4.2.3 Fourth Generation Mobile Radio: OFDM(A)	28
4.3 LTE Performance Analysis	34
4.3.1 EXIT Analysis	34
4.3.2 Bits Per Channel Use and Spectral Efficiency	35
5 Beyond UMTS LTE	41
5.1 Improving UMTS LTE 64QAM Performance	41
5.1.1 UEP and Bit Reordering	41
5.1.2 Simulation Results	43
5.2 BICM-ID with Repetition Coding	47

5.2.1	System Model	48
5.2.2	Simulation Parameters and Results	49
5.2.3	EXIT Analysis	51
5.2.4	Algorithmic Complexity	52
5.3	EXIT optimized BICM-ID	53
5.3.1	SDM EXIT Characteristics	54
5.3.2	Simulation Results	56
5.4	OFDM Turbo DeCodulation	61
5.4.1	OFDM TDeC with Convolutional Coding	62
5.4.2	EXIT optimization of the BICM-ID stage	63
5.4.3	Simulation examples	63
5.4.4	Block Coded OFDM TDeC	66
5.5	OFDM Turbo DeCodulation vs. UMTS LTE	67
5.6	MIMO Approximation	69
5.7	Concepts for Interference Management	72
6	From Bit-Level to System-Level	73
6.1	Abstraction and System Model	73
6.1.1	Network Geometry, Carrier Frequencies, and Frequency Bandwidth	73
6.1.2	Signal-to-Interference-and-Noise Ratio	76
6.1.3	Service Scenarios	82
6.1.4	Summary of System-Level Simulation Parameters	83
6.2	Prediction of Average Cell Goodput $\bar{\mathcal{G}}$	84
6.2.1	HSDPA vs. LTE	85
6.2.2	Influence of the Propagation Scenario	85
6.2.3	PHY Simulation vs. Approximation	86
6.2.4	Influence of the PHY Channel Model	86
6.2.5	Influence of Interference Cancellation	88
6.2.6	Bounds on $\bar{\mathcal{G}}$	89
7	Coverage, Quality, and Capacity	91
7.1	Coverage and Capacity of UMTS LTE	91
7.1.1	Adaptive Modulation and Coding	91
7.1.2	User Data Rates	94
7.1.3	Capacity with Fixed Services	99
7.2	Beyond UMTS LTE	104
7.2.1	Interference Cancellation	104
7.2.2	Bounds for MIMO Systems	107
7.2.3	Reordered bit mapping for 64QAM	110
7.2.4	BICM-ID with Repetition Coding	112
7.2.5	OFDM Turbo DeCodulation	114
8	Summary	117

A	Typical Urban Channel Model	119
B	System-Level Simulation Parameters	121
B.1	Urban Micro-Cell Propagation Scenario (UMi)	121
B.2	Urban Macro-Cell Propagation Scenario (UMa)	122
B.3	Rural Macro-Cell Propagation Scenario (RMa)	124
C	System-Level Performance	125
C.1	UMTS LTE with AWGN Channel	125
C.2	UMTS LTE Approximation	126
C.3	UMTS LTE with TU Channel	127
C.4	UMTS LTE with Rayleigh Channel	128
C.5	Shannon	129
C.6	2×2 MIMO	130
C.7	4×4 MIMO	131
D	Deutschsprachige Kurzfassung	133
	Bibliography	143

Abbreviations

2G	second generation
3G	third generation
3GPP	Third Generation Partnership Project
ACM	adaptive coding and modulation
AMR	adaptive multi-rate
AWGN	additive white Gaussian noise
BC-TDeC	block coded Turbo DeCodulation
BCS	block check sequence
BER	bit error rate
BICM-ID	bit-interleaved coded modulation with iterative decoding
BMWi	German Federal Ministry of Economics and Technology (Bundesministerium für Wirtschaft und Technologie)
BNetzA	Federal Network Agency for Electricity, Gas, Telecommunications, Postal Service and Railways (Bundesnetzagentur für Elektrizität, Gas, Telekommunikation, Post und Eisenbahnen)
bit/s	bit per second
BS	base station
CC-TDeC	convolutional coded Turbo DeCodulation
CCI	co-channel interference
CD	channel decoder
CDF	cumulative distribution function
CDM	code division multiplex

Abbreviations

CDMA	code division multiple access
CIR	channel impulse response
CoMP	cooperative multipoint
COST	European Co-operation in the Field of Scientific and Technical Research
CP	cyclic prefix
CRC	cyclic redundancy check
CS	circuit-switched
CSD	circuit-switched data
CSFB	circuit-switched fallback
CSI	channel state information
CTF	channel transfer function
DAB	digital audio broadcast
DFT	Discrete Fourier Transform
DM	demapper
DSL	digital subscriber line
DTAG	Deutsche Telekom AG
DVB	digital video broadcast
DVB-C	digital video broadcast - cable
DVB-H	digital video broadcast - handhelds
DVB-S	digital video broadcast - satellite
DVB-T	digital video broadcast - terrestrial
EDGE	Enhanced Data Rates for GSM Evolution
EFF	error-free feedback
EFR	enhanced full-rate
ETSI	European Telecommunications Standards Institute
EXIT	extrinsic information transfer

FDD	frequency division duplex
FDM	frequency division multiplex
FDMA	frequency division multiple access
FER	frame error rate
FFT	Fast Fourier Transform
FH	frequency hopping
FIR	finite impulse response
FTTB	fiber to the building
FTTC	fiber to the curb
FTTH	fiber to the home
FTTx	fiber to the x
Gbit/s	gigabit per second
GPRS	General Packet Radio Service
GMSK	Gaussian minimum shift keying
GSM	Global System for Mobile Communication
HARQ	hybrid automatic repeat request
HSCSD	high-speed circuit-switched data
HSDPA	high-speed downlink packet access
HSPA	high-speed packet access
HSUPA	high-speed uplink packet access
IC	interference cancellation
ICI	inter-carrier interference
IDFT	Inverse Discrete Fourier Transform
IEEE	Institute of Electrical and Electronics Engineers, Inc.
IFFT	Inverse Fast Fourier Transform
IP	internet protocol

Abbreviations

IMS	IP multimedia subsystem
ISI	inter-symbol interference
ISCD	iterative source channel decoding
ISDN	integrated services digital network
ISI	inter-symbol interference
ISO	International Organization for Standardization
ITU	International Telecommunication Union
kbit/s	kilobit per second
LLR	log-likelihood ratio
LOS	line-of-sight
LTE	Long Term Evolution
MAC	medium access
MAP	maximum a posteriori
Mbit/s	megabit per second
Mchip/s	megachip per second
MCS	modulation and coding scheme
MIMO	multiple-input multiple-output
MMSE	minimum mean-square error
MRC	maximum ratio combining
NGMN	Next Generation Mobile Network
NLOS	non-line-of-sight
OECD	Organization for Economic Co-Operation and Development
OFDM	orthogonal frequency division multiplex
OFDMA	orthogonal frequency division multiple access
OPTA	optimum performance theoretically attainable
OSI	open systems interconnection

OVSF	orthogonal variable spreading factor
PAN	personal area network
PCCC	parallel concatenated convolutional code
PCS	Personal Communication System
PHY	physical layer
POTS	plain old telephone system
PS	packet-switched
PSK	phase shift keying
PSNR	parameter SNR
PSTN	public switched telephone network
QAM	quadrature amplitude modulation
QPSK	quadrature phase shift keying
RB	resource block
RE	resource element
RF	radio frequency
RIA	redundant index assignment
RMa	rural macro-cell
RV	redundancy version
SC	subcarrier
SCS	signal constellation set
SDM	soft demapper
SDSD	soft decision source decoder
SF	spreading factor
SINR	signal-to-interference-and-noise ratio
SISO	soft-input-soft-output
SNR	signal-to-noise ratio

Abbreviations

SP	set partitioning
SQ	scalar quantizer
SSP	semi-set partitioning
TDD	time division duplex
TDeC	Turbo DeCodulation
TDM	time division multiplex
TDMA	time division multiple access
TR	technical report
TU	typical urban
UE	user equipment
UEP	unequal error protection
UMa	urban macro-cell
UMi	urban micro-cell
UMTS	Universal Mobile Telecommunication System
VoIP	Voice over IP
VoLGA	Voice over LTE Generic Access
WAN	wide area network
Wi-Fi	Wireless Fidelity
WiMAX	Worldwide Interoperability for Microwave Access
WLAN	wireless local area networks
WMAN	wireless metropolitan area network
ZF	zero-forcing

Introduction

It is commonly accepted that hardly any technological development in the last decades has influenced everyday life so significantly and enduring as the evolution of information technology. The internet has become a key infrastructure not only supporting the internationally intertwined economy but influencing the whole way of life of millions of people. The development of high performing hand-held devices for mobile data access in combination with widely spread easy-to-use mobile applications are key drivers for the fast growing demand for data access in mobile radio networks. As a matter of fact, Håkan Eriksson, Senior Vice President and Chief Technical Officer of hardware vendor Ericsson, reported in June 2009 that the average mobile data traffic measured in Ericsson's third generation mobile networks has been growing from 2.5 gigabit per second (Gbit/s) in September 2007 to more than 15.3 Gbit/s in March 2009, while in the same period voice traffic has been growing only moderately from approximately 2.0 Gbit/s to 3.0 Gbit/s. This development is believed to continue during the next decade. Hardware vendor Nokia Siemens Networks projects the demand for mobile data traffic to exceed 6000 Gbit/s ($2.0 \cdot 10^{18}$ byte per month) in 2015. A survey conducted by the Münchener Kreis in 2009 [70] suggests that a majority of international experts expects that between 2015 and 2019 more people in Germany will access the internet using mobile devices rather than using fixed line computers, while less than 10% of the interviewed experts expect that to never take place. At the same time, mobile network operators observe that with the dominance of data traffic over voice traffic, the growth of revenues does not follow the progression of the traffic growth but is expected to stagnate, leaving smaller revenues per transmitted bit. Furthermore, mobile data access at high data rates is currently possible only in densely populated areas with good communication infrastructure, leaving people in several sparsely populated rural areas under served.

These facts motivate the current research and development in the field of mobile radio communication striving to evolve mobile data access technologies to support higher data rates while keeping the complexity of network architecture and algorithms as low as possible to limit investment and operational costs. This thesis sketches the evolution of digital physical layer technologies from those of second generation mobile radio systems to those of the current fourth generation represented by the Long Term Evolution (LTE) of the Universal Mobile Telecommunication System (UMTS). The physical layer performance of UMTS LTE is analyzed by means of computer simulation for the single antenna case and the simulation results are used in system-level simulations to illustrate the potentials concerning

coverage, capacity, and quality of the downlink of UMTS LTE under different conditions. In a second step, modifications of and alternative concepts to the UMTS LTE physical layer aiming either at improving performance or reducing computational complexity are introduced and analyzed. This includes performance bounds assuming multi-antenna techniques and concepts for interference cancellation. The impact of these modifications and alternative concepts on coverage, capacity, and quality of mobile radio networks is illustrated by system-level simulations.

This thesis is structured as follows: Chapters 2 and 3 introduce and define the basic terms and measures used throughout this work. A general model of the utilized transmission system is given in Chapter 4 which also sketches the evolution of selected digital mobile radio systems and analyzes the physical layer performance of the fourth generation UMTS LTE. Modifications of the UMTS LTE physical layer and alternative concepts are introduced and analyzed in Chapter 5. The abstractions and assumptions used for system-level simulations are summarized in Chapter 6 along with a capacity analysis of UMTS LTE radio cells. Chapter 7 discusses the system-level simulation results for UMTS LTE as well as for the modifications and alternative concepts. Finally, this work is summarized and concluded in Chapter 8.

Mobile Broadband Access

Analyzing potentials and limitations of mobile broadband access, this thesis is concerned with one of the major topics in the field of communication engineering and research as well as in the fields of business and administration. This chapter explains the two fundamental terms *broadband* and *mobile* which play a key role in the classification and description of communication systems. Since both terms are commonly used in every day language, their meaning is usually quite broad and rather imprecise. The clarification of these terms for the use in this thesis is wrapped up by a summary of the current state of mobile broadband access in Germany.

2.1 What Is Broadband?

The term *broadband* has its root in the definition of *bandwidth*, with the latter term also having different definitions which are often mixed up. The authors of the *Internet Report 2006* [58] published by the *International Telecommunication Union (ITU)* distinguish between *analog* and *digital bandwidth*, describing the first term as an amount of radio frequency measured in Hertz (Hz). In this thesis, the analog bandwidth is denoted as *frequency bandwidth* to assure a clear distinction from the bandwidth of speech and audio signals also measured in Hz which are referred to as *audio bandwidth*. The digital bandwidth on the other hand describes an amount of data transmitted in a given time interval and is measured in bit per second (bit/s). To avoid any confusion this digital bandwidth is referred to as *data rate* in this work.

The term *broadband* in the context of digital data transmission describes a certain data rate. However, the exact amount is subject to a steady change varying in place, time, and context. The aforementioned ITU report [58] defines broadband access by a data rate greater than or equal to 256 kilobit per second (kbit/s). A similar definition holds for the *Communications Outlook 2007* [72] issued by the *Organization for Economic Co-Operation and Development (OECD)* defining broadband as a minimum data rate of 256 kbit/s in the downstream – i.e., the direction from the provider to the user, also referred to as forward link or downlink – and 128 kbit/s in the upstream (direction from user to provider, also referred to as reverse link or uplink). The German Federal Ministry of Economics and Technology (Bundesministerium für Wirtschaft und Technologie) (BMWi) annually reports on the development of internet access in Germany in its *Breitbandatlas* [22] where the term broadband

defined data rates greater than or equal to 128 kbit/s in the downstream. However, for the 2009 edition this key figure has been increased to one megabit per second (Mbit/s). A wider definition, also given by the ITU, dates back to 1988 and is based on the bundling of integrated services digital network (ISDN) channels for achieving a so-called primary rate. According to [55], the term broadband qualifies a service or system requiring transmission channels capable of supporting rates greater than the primary rate. Here, primary rate means either 1544 kbit/s or 2048 kbit/s, depending on the number of bundled ISDN channels [54]. Further definitions of broadband are summarized, e.g., in [43].

Considering the user experience, an independent user-centric and application related definition of broadband is used by different groups and organizations. It states that broadband data connections have to enable the access to broadband services, contents, and applications. Thereby, the definition of the term broadband grows with the data rate demand of applications and is therefore not numerically evaluable. However, it is a well formulated guideline for authorities and industry which have to cope with the steadily increasing demand for higher data rates for emerging services and applications on the internet.

2.2 What Is Mobile Access?

Generally, three different classes of mobility are distinguished in the context of communication and data access: *fixed*, *nomadic*, and *mobile* access.

Fixed access describes a stationary terminal of a communication link. However, this does not imply that the communication link has to be realized by fixed lines as in, e.g., *digital subscriber line (DSL)*, fiber or cable access. There exist different radio communication standards like IEEE 802.16-2004 [1] (cf. section 4.2) issued by the Institute of Electrical and Electronics Engineers, Inc. (IEEE) that rely on fixed, e.g., roof-mounted, antennas to provide a certain transmission quality.

Nomadic access allows for wireless connectivity within a certain range around an *access point* which itself is usually stationary. Within this transmission range, commonly referred to as *hot spot*, users may roam freely, usually at pedestrian speeds. A seamless transition, also referred to as *handover* or *handoff*, between hot spots is mostly not possible. The connection to the first serving access point has to be terminated and a different connection to the new serving access point has to be set up. The most popular nomadic access networks are *wireless local area networks (WLAN)* defined in the IEEE 802.11 standards family [2].

Mobile access refers to any kind of connection that allows the user seamless communication over great areas at medium and high speeds. This is generally fulfilled by voice and data services of mobile radio networks like the *Global System for Mobile Communication (GSM)* or *UMTS*. These networks consist of centrally controlled base stations each forming one radio cell. Therefore, one also speaks of *cellular networks*. Seamless handovers can be performed when moving from one cell to an adjacent cell. Furthermore, technical precautions are taken to combat distorting effects due to movement for a given range of velocities.

2.3 Current Situation in Germany

Broadband internet access in Germany is mainly realized by DSL, i.e., through wireline connections. Cable modems, another major technology, are just beginning to gain some market shares. The reason for that is the historical development of the deregulation of the communication market. The cable networks and phone lines had both been operated by the state-run Deutsche Bundespost. After liberalization and deregulation, cable networks and phone lines were operated by Deutsche Telekom AG (DTAG) who focused on DSL technology for broadband access. However, not all areas could be economically covered with DSL technology, especially rural areas with low population density or areas with fiber infrastructure which is not designed to support DSL. To close this gap and to cover these so-called white spots, the BMWi conducted a study in 2005 evaluating different wireless technologies for their potential to provide broadband wireless access to these areas [30].

While in the densely populated areas different economically profitable technologies have been set up by incumbent operators, the development has been much slower in the sparsely populated areas that do not provide business cases for profit-oriented private companies. Depending on the definition of broadband (see above) the current *Breitbandatlas 2009_01* [22] states that for 98.99 % of the German population broadband access (data rate > 256 kbit/s) is available. With the stricter definition of broadband (data rate > 1 Mbit/s), broadband access is still available for 93.43 % of the German population. These figures reflect a theoretical availability based on the availability of different broadband access technologies including DSL, cable modem, fiber, fixed or mobile broadband access.

The availability of mobile broadband access is of special interest as it reflects the current state of second generation (2G) and third generation (3G) networks, i.e., GSM and UMTS with its extension high-speed packet access (HSPA), respectively. Figure 2.1 taken from [88] shows the coverage of Germany by GSM and UMTS as provided by the two biggest mobile telecommunication providers. It can be seen that, while only small regions are not covered by GSM, a larger part of the area is not covered by UMTS. Although Fig. 2.1 represents the coverage in November 2007, more recent coverage maps show hardly any increase of the area covered with UMTS. At the end of 2005 more than 50 % of the German population had UMTS access by all providers, which was a condition for obtaining UMTS radio frequency spectra in the 2001 auction conducted by the Federal Network Agency for Electricity, Gas, Telecommunications, Postal Service and Railways (Bundesnetzagentur für Elektrizität, Gas, Telekommunikation, Post und Eisenbahnen) (BNetzA). The figure reflects the high urbanization in Germany. To give an example: mobile radio access can be provided to 80 % of the German population by covering only 20 % of the area.

Mobile broadband access with data rates greater than 256 kbit/s is only possible in UMTS covered areas, while mobile access with data rates greater than 1 Mbit/s can only be provided by HSPA. The availability of HSPA, although steadily rolled out, is currently limited to the bigger cities and therefore to those areas, that usually already provide different technologies for broadband access. It is stated in [22] that the roll out of HSPA could improve the availability of broadband connections by only 1.17 %. An alternative approach based on 2G networks is *Enhanced Data Rates for GSM Evolution (EDGE)* generally providing data rates

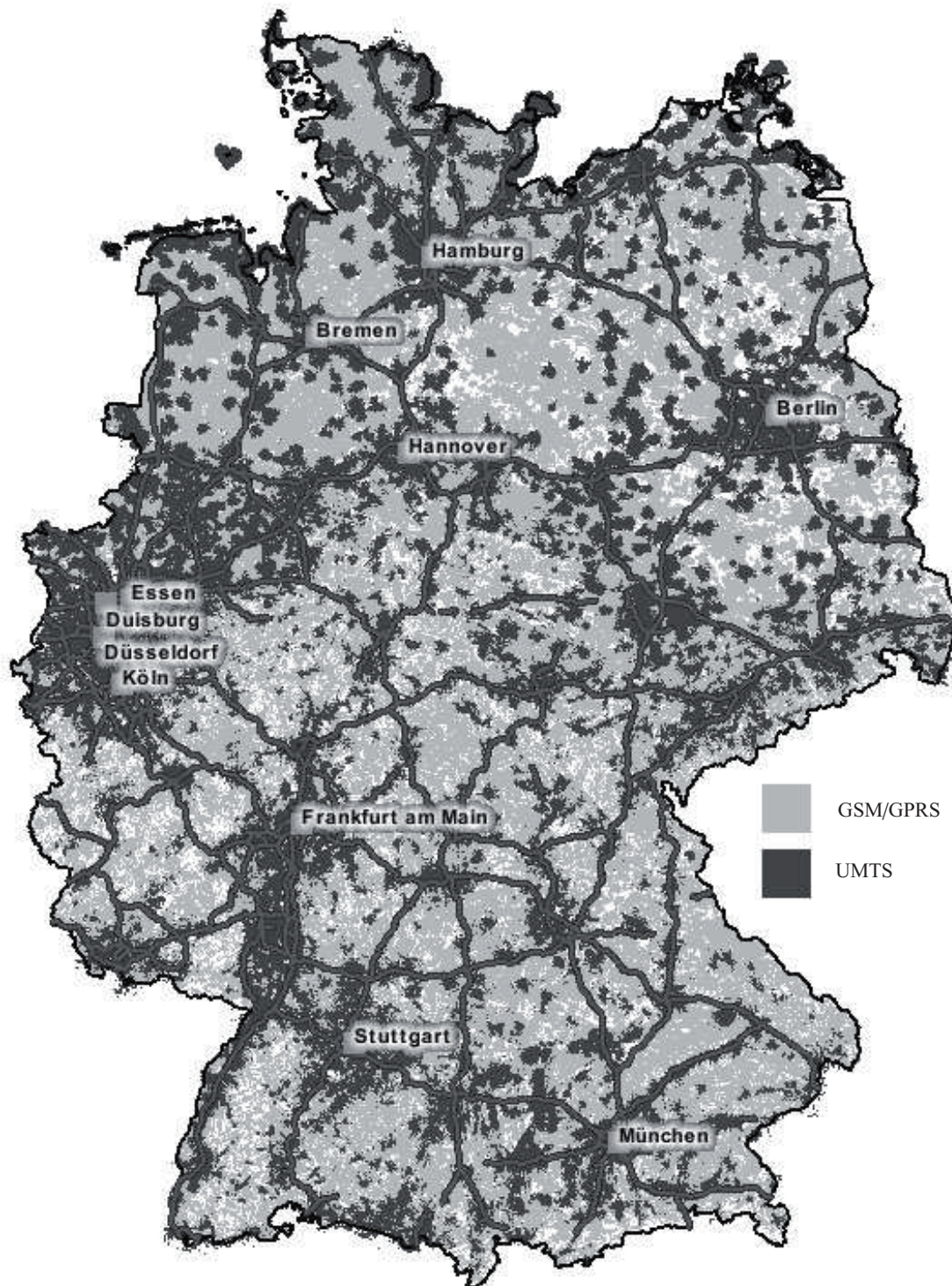


Figure 2.1: 2G and 3G coverage in Germany (November 2007).

between 100 kbit/s and 200 kbit/s. While all four mobile radio network operators in Germany are claiming to extend their EDGE networks steadily, no reliable numbers are available on the population or area coverage. It can be expected that due to the ongoing replacement of old base station hardware in GSM networks, EDGE will sooner or later be available in most GSM covered areas.

One issue common to EDGE and UMTS/HSPA is the fact that all radio resources contributing to a sum data rate have to be shared among all users. Therefore, in densely populated areas many radio cells with small coverage areas (small cell sizes) have to be set up to guarantee wireless access to a large number of users at a tolerable rate of rejections due to depletion of radio resources.

Furthermore, with transmission systems like EDGE or HSPA the data rate achieved with certain radio resources assigned to a specific user decreases with decreasing channel quality which generally relates to the distance between user and transmitting base station. Especially in rural areas with a low density of base station this leads to low data rates at cell edges, cf. Chapter 7.

Obviously, an area-wide coverage with mobile broadband access based on current technology is hardly economic for a single profit-oriented mobile network operator. That is why *infrastructure sharing* is lately getting back into the focus of the regulatory authorities [88] as an option for UMTS *Long Term Evolution (LTE)*, the current enhancement of UMTS specified in Release 8 of 3GPP's UMTS standards. By sharing some resources between operators, the economical effort may be reduced such that mobile broadband access can be provided to the remaining white spots. These shared resources might include in compliance with regulatory aspects back bone infrastructure, antenna sites, base station hardware or even radio frequencies.

Another aspect regarding the problem of mobile broadband coverage in sparsely populated rural areas of Germany is the so-called *digital dividend*. By switching from analogue broadcasting of TV programs to digital video broadcast - terrestrial (DVB-T), frequency bandwidth becomes available at carrier frequencies lower than those used in current mobile radio networks. It will be shown later (cf. Section 3.2) that lower frequencies generally yield better propagation characteristics. Therefore, larger areas can be covered by a single base station.

It can be seen that the challenges for providing area-wide mobile broadband access are manifold and include physical, technological, regulatory and economical aspects which influence each other. The following chapters will focus on the physical and technological aspects, their interaction and their influence on the coverage and capacity of mobile radio networks.

Fundamentals

This chapter provides some fundamental prerequisites for the performance evaluation of radio access networks. It will first review architectural aspects necessary for a classification of radio networks before introducing *spectral efficiency*, the main performance measure of radio systems, and its main influencing factors.

3.1 Network Architecture Aspects

An important classification of radio networks relates to their range. Here, the distinction between nomadic and mobile radio networks is important. Generally, nomadic access networks consist of one or many independent cells that do not support handovers from one cell to an adjacent one. The cell sizes of such networks differ. Depending on their purpose, nomadic access networks can be classified into personal area network (PAN), wireless local area networks (WLAN), and wireless metropolitan area network (WMAN). Typical ranges and examples for each of these types are given in Tab. 3.1.

Type	Range	Example
PAN	several decimeters to a few meters	Bluetooth™(IEEE 802.15.1-2005)
WLAN	several tens of meters	Wi-Fi™(IEEE 802.11-2007)
WMAN	several kilometers	WiMAX™(IEEE 802.16-2004)

Table 3.1: Typical ranges for different nomadic radio access networks.

A more general classification of cell sizes applicable to both nomadic and mobile radio access networks distinguishes between *macro-*, *micro-*, *pico-*, and *femto-cells*. Generally, different cell sizes are supported in one mobile radio network to improve coverage or capacity depending on the local volume of data traffic. The definitions of these sizes are not unique in literature. The definitions of cell types, their sizes, and their deployment scenario used in this theses are summarized in Tab. 3.2 following the definitions in [44].

Two parallel developments influenced the evolution of radio access. Data access networks were introduced to allow for the interconnection of different data processing entities, like main frame computers, terminals, data servers, or printers. By their nature these net-

Type	Range	Deployment
Macro-cell	several tens of kilometers	rural areas, umbrella cells
Micro-cell	approx. 100 m – approx. 2 km	cities, densely populated areas
Pico-cell	approx. 100 m	public places, single buildings
Femto-cell	below 50 m	single rooms, apartments, offices

Table 3.2: Typical cell sizes of mobile radio networks.

works are fixed or, in case of radio access, nomadic. The purpose of these networks is the fast distribution of data packages generally without knowledge of the data itself and is subject to different constraints such as delay, packet loss rate or variable packet sizes. These networks are referred to as *packet-switched (PS)* networks. The high flexibility of these networks and their protocols comes at the cost of high overheads of headers from different protocols working on different layers.

Any mobile radio network on the other hand is basically an extension of a public switched telephone network (PSTN). For the fixed-line analogue transmission of speech signals, an electrical circuit has to be established between the users of the network. This principle also holds for digital networks like ISDN and was also adopted to the first analog and digital mobile radio networks such as Global System for Mobile Communication (GSM). Hence, these networks are referred to as *circuit-switched (CS)* networks. While demanding only limited flexibility, delay is a crucial issue for these networks. According to an ITU recommendation, the delay from one user to another (one-way delay) must not exceed 400 ms for real-time services [57]. Protocols for these networks have to enable the establishment of a connection and have to support its continuity, which is a demanding task especially in mobile radio networks.

Despite the convergence of data access and mobile radio networks, the distinction between CS and PS networks still holds. A packet-switched domain has been added to GSM known as General Packet Radio Service (GPRS) which was evolved into Enhanced Data Rates for GSM Evolution (EDGE). UMTS was designed from the beginning to support both circuit-switched and packet-switched traffic. To increase data rates and decrease delay in the packet-switched domain of UMTS, high-speed downlink packet access (HSDPA) has been introduced in Release 5, followed by high-speed uplink packet access (HSUPA) in Release 6 of the standard. With the introduction of Voice over IP (VoIP) and IP multimedia subsystem (IMS) [27], speech communication over packet-switched networks has become possible. This is why the circuit-switched domain is steadily losing importance. It is widely agreed that PS networks will be dominating in future mobile radio systems as they will provide the flexibility to support different demands concerning delay, data rates, and security. Figure 3.1 illustrates the transition from CS to PS systems.

Release 8 of the UMTS standard introduced the current extension UMTS LTE. Data transmission will solely be IP-based using packet-switched technology [87]. Different options for circuit-switched services such as voice calls or video telephony are currently under

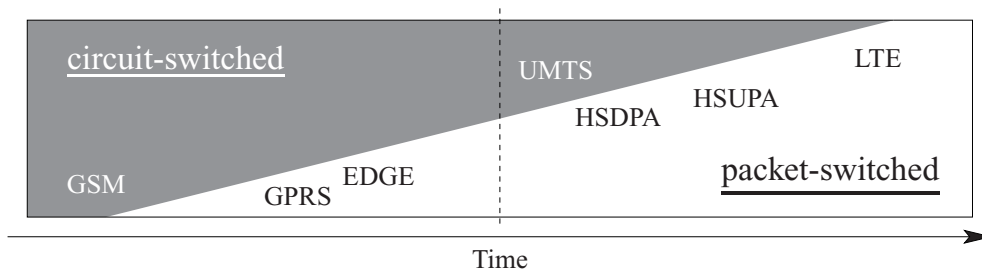


Figure 3.1: Evolution from circuit-switched to packet-switched systems.

discussion. The solution favored by most of the mobile network operators is the aforementioned IMS providing VoIP as standardized in [19]. As this solution is technically demanding, an interim solution is represented by *circuit-switched fallback (CSFB)* which is standardized in [18] and provides CS services by rerouting these connections through GSM or UMTS networks. This of course requires multi-standard devices. Finally, a third option is standardized by the Voice over LTE Generic Access (VoLGA) Forum which was initiated to specify and promote an approach for extending traditional GSM and UMTS circuit-switched services over LTE access networks [89]. The Next Generation Mobile Network (NGMN) Alliance – an international consortium of representatives of hardware manufacturers, mobile network operators, and academia – announced in a press release in February 2010 that it confirmed its commitment to an IMS based target solution for Voice over LTE while recommending the implementation of CSFB in all devices that support GSM or UMTS and that provide a voice service, thus providing a migratory non-IMS voice solution that guarantees voice roaming with LTE handsets whilst allowing the use of LTE data roaming in the same device.

With this transition from circuit-switched to packet-switched traffic another paradigm change related to the system architecture is at hand: While in CS networks resources are exclusively assigned to a single user, in PS networks resources are taken from a shared medium. This is due to the different purposes of these systems. While a typical CS service like voice communication has to guaranty one exclusive communication link for each direction at all times during the conversation, data services like web browsing or sending and receiving e-mails produce highly asymmetric data traffic in time and direction (up-/downlink). Periods with high demands for data rate alternate with periods of low demand, leaving the opportunity for other users to use the same resource. The transition from dedicated resources to shared resources is also reflected by the evolution of technologies. While in GSM dedicated data services like circuit-switched data (CSD) and high-speed circuit-switched data (HSCSD) exist, more recent data services with higher data rates and low delay like UMTS HSDPA, HSUPA and LTE rely on shared media.

3.2 Spectral Efficiency, Throughput, and Coverage

A common optimization goal in research and development of mobile radio systems is to transmit as many *information* or *data bits* as necessary using as few radio resources as possi-

ble. One of the most valuable resources for mobile radio operators is the used radio spectrum or *frequency bandwidth* allocated around a central *carrier frequency* f_0 .

It is well known that any sinusoidal function representing phase and amplitude of a radio wave at the transmitter is represented in frequency domain by a pair of complex Dirac pulses at the positive and negative carrier frequency without any spectral spread. This signal will not be able to carry any information as it is unlimited in time and therefore does not change. However, in radio communications information is transmitted, e.g., by switching amplitude, phase, carrier frequency, etc., of the carrier wave at certain intervals T . In case of discrete amplitude and phase modulation, the bandwidth of the modulated carrier is determined by the transmit filter $h(t)$, which in the simplest case is a rectangular window with a length T . In frequency domain this leads to a spectral spread of the signal which demands a certain amount of bandwidth B . The product of frequency bandwidth B and duration T is known as *time bandwidth product* and is lower bounded. With the general definition of duration T and bandwidth B from [61]

$$T = \sqrt{\int_{-\infty}^{\infty} t^2 \cdot h^2(t) dt} \quad (3.1)$$

$$B = \sqrt{\frac{1}{2\pi} \int_{-\infty}^{\infty} \omega^2 \cdot |H(j\omega)|^2 d\omega} \quad (3.2)$$

with $H(\omega)$ being the Fourier transform of $h(t)$ and $\omega = 2\pi f$, it follows

$$T \cdot B \geq \frac{1}{2}. \quad (3.3)$$

It can be seen that any time domain signal carrying information requires a certain frequency bandwidth B which increases with a decreasing symbol duration. Following Heisenberg's uncertainty principle from quantum mechanics, equation (3.3) is called the *uncertainty relation of communications engineering* [61].

T and B are general symbols representing time continuous pass band signals. When discussing physical layer signal processing in this thesis, the equivalent time discrete baseband model is regarded with sample duration T_S . While different definitions of frequency bandwidth exist in literature, in this thesis the frequency bandwidth Δf denotes the part of the frequency spectrum which is occupied by an information carrying signal such that a second signal is not disturbed, if it uses adjacent non-overlapping spectrum.

For single carrier modulation, the sample duration T_S also denotes the *symbol duration*. Depending on the underlying technique, each symbol of duration T_S can carry an arbitrary and not necessarily integer number of *information* bits $\mathcal{N}^{[\text{info}]}$ (non-integer e.g., due to coding) resulting in a *throughput* (data bit rate) R in bit/s:

$$R = \frac{\mathcal{N}^{[\text{info}]}}{T_S}. \quad (3.4)$$

At this point it is important to point out that this definition of throughput takes into account only the transmitted information bits. These information bits, however, can be corrupted during transmission leading to an integer number of bit errors $\epsilon^{[\text{info}]} \leq \mathcal{N}^{[\text{info}]}$ per symbol leading to the *net bit error rate (BER)*

$$\text{net BER} = \frac{\mathcal{E}\{\epsilon^{[\text{info}]}\}}{\mathcal{N}^{[\text{info}]}} \quad (3.5)$$

where $\mathcal{E}\{\cdot\}$ denotes expectation. Different measures (c.f. Chapter 4) are employed to reduce the net BER, also called *residual BER*. The resulting error-free throughput is called *goodput* \mathcal{G} . From both measures, R and \mathcal{G} , the *spectral efficiency* η of the system can be derived. However, as many systems might not assess the residual BER or consider it negligible, i.e., $\mathcal{G} \approx R$, the spectral efficiency given in bit/s/Hz is widely defined using throughput rather than goodput:

$$\eta = \frac{R}{\Delta f} = \frac{\mathcal{N}^{[\text{info}]}}{T_S \Delta f} \quad (3.6)$$

This definition of η does not take into account range or transmission power of the signal. However, in state-of-the-art mobile radio systems like HSPA, LTE, or WiMAX™, the available data rate R is highly dependent on the received signal power and therefore on the transmit power and the attenuation of the signal. A major part of attenuation is due to path loss L resulting from the propagation of the radio signal over a certain distance d between transmitter and receiver. It is defined as the ratio of received power P_{Rx} and transmit power P_{Tx} :

$$L = \frac{P_{\text{Rx}}}{P_{\text{Tx}}} \quad (3.7)$$

$$\begin{aligned} L^{[\text{dB}]} &= 10 \log_{10} P_{\text{Rx}} - 10 \log_{10} P_{\text{Tx}} \\ &= P_{\text{Rx}}^{[\text{dB}]} - P_{\text{Tx}}^{[\text{dB}]} \end{aligned} \quad (3.8)$$

A broad variety of models exist to describe L with different degrees of abstraction. Most of these have in common that L depends on the carrier frequency f_0 . The path loss models used throughout this thesis are introduced in Sec. 6.1.2 and described in detail in Appendix B. Generally, a higher carrier frequency f_0 leads to a higher path loss, i.e., less coverage. To give an example, Fig. 3.2 compares the path loss for the two practical carrier frequencies $f_0 = 0.8$ GHz and $f_0 = 2.0$ GHz as given by the path loss model for an urban macro-cell environment (see Sec. 6.1.2) at different distances d from the base station.

It can be seen that the path loss for $f_0 = 2.0$ GHz is approximately 12 dB higher compared to $f_0 = 0.8$ GHz in the macro cell (cf. Section 6.1.2). That means that due to the frequency dependency of the propagation characteristics of radio waves, for $f_0 = 2.0$ GHz approximately 6.3 % of the power is received compared to $f_0 = 0.8$ GHz. Considering coverage, Fig. 3.2 indicates that for a given minimum received power (maximum tolerable path loss) the cell size severely decreases with increasing carrier frequency.

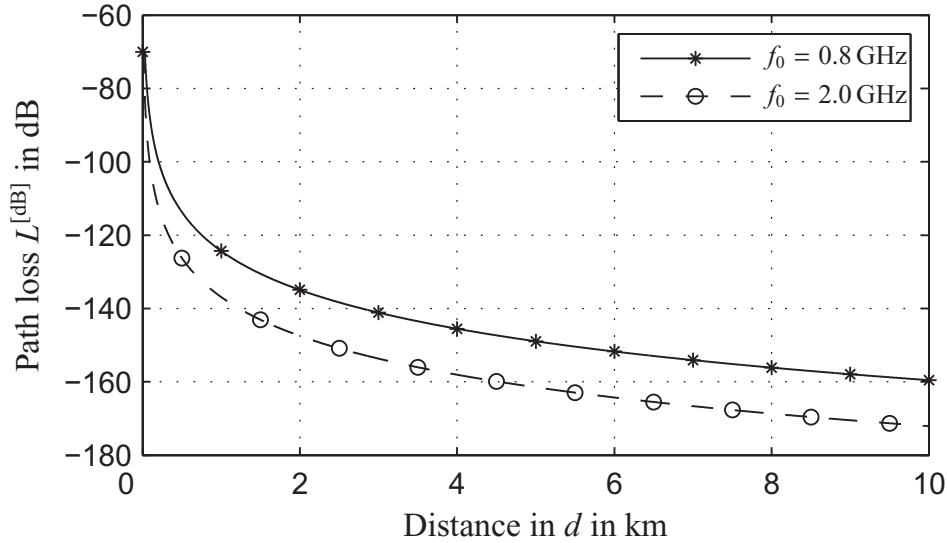


Figure 3.2: Exemplary path loss in urban macro-cell propagation scenario.

Given the system immanent dependence between distance from base station and throughput, the indistinctness of the spectral efficiency η becomes obvious and is illustrated by the following example: A UMTS LTE system with a system bandwidth of $\Delta f = 5$ MHz theoretically allows the transmission of a maximum of $\mathcal{N}^{[\text{info}]} = 12600$ bit during a period of 0.5 ms resulting in a theoretical throughput of $R = 25.2$ Mbit/s (for details see Section 4.2). This assumption does not take into account transmission errors which occur due to a lack of channel coding in combination with noisy reception. Therefore, a rather high figure of $\eta = 5.04$ bit/s/Hz is reached. Given a fully loaded cell with users at different distances from the base station, the average cell goodput $\overline{\mathcal{G}}$, i.e., the sum of all individual user goodputs \mathcal{G} averaged over the cell area, might drop to $\overline{\mathcal{G}} \approx 8.5$ Mbit/s due to adaptive coding and modulation (c.f. Section 4.2) leading to $\eta = 1.7$ bit/s/Hz for the LTE system. In conclusion it has to be stated that spectral efficiency has to be used carefully as a performance measure for any data transmission system and must not be taken out of its context. To deliver a fair judgment on system performance, it has to be complemented by additional figures and assumptions such as number of users, goodput or throughput, etc.

Physical Layer Concepts

The purpose of this chapter is the description of different concepts of physical layer (PHY) implementations based on a general transceiver model. After the introduction of the model and the description of its signals and components, examples of mobile radio systems which are currently in use are given. The most currently developed UMTS LTE technology is described in detail and its performance is analyzed by computer simulation.

4.1 General Transmission System Model

This section introduces the general system model considered throughout this thesis, discusses its relevant components, and describes the notation of the different signals. As the title of this chapter indicates, the focus is on the *physical layer* of transmission systems as it is defined by the International Organization for Standardization (ISO) in the open systems interconnection (OSI) reference model [59] which is applicable to all standardized communication systems. Therein the physical layer is also denoted *layer 1*. As parts of this work are also concerned with applications (OSI layer 7) while considering the layers between application and PHY as transparent, a different approach is taken distinguishing between an *application related* and a *link related* part of the transceiver.

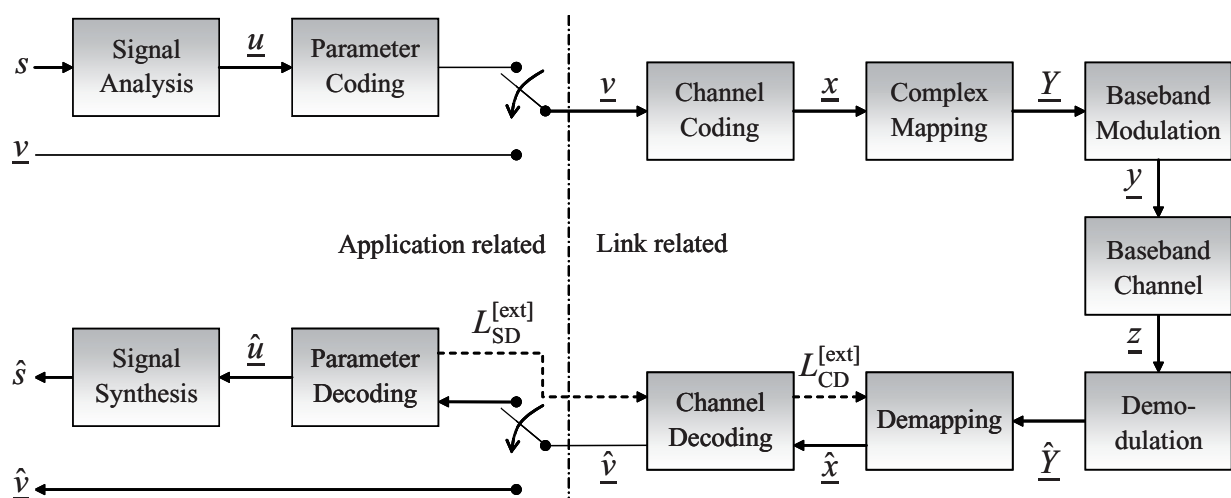


Figure 4.1: General baseband system model.

The general model of the considered transceiver (= transmitter + receiver) is sketched in Fig. 4.1. All given signals are discrete time baseband signals which are processed frame-wise. A signal frame is denoted by an underlined symbol. Generally, the signal processing for one input frame at a certain time instance is performed individually and independent of the preceding or following frames. Therefore, time indices are omitted where possible. The upper blocks of the diagram depict the transmitter, while the lower blocks describe the receiver.

4.1.1 Source Coding

Depending on the purpose of a specific system, the input to the transceiver can either consist of a multimedia signal s or data bit frames \underline{v} . Using model based source coding, the multimedia signal is transformed into a parameter frames \underline{u} containing a set of real valued discrete time parameters by employing a parametric speech, audio or video codec. This parameter frame \underline{u} is then encoded into a data bit frame \underline{v} according to a coding rule that depends on the specific system. The elements $v^{(i)}$ with $i \in \{0, \dots, l_v - 1\}$ of the data bit frame $\underline{v} = [v^{(0)}, v^{(1)}, \dots, v^{(l_v-1)}]$ of length l_v are given in binary representation, i.e., $v^{(i)} \in \{0, 1\}$. One simple example for parameter encoding is simple quantization with binary representation of the quantizer reproduction levels.

The received and reconstructed data frame is denoted by $\hat{\underline{v}}$ and consists, depending on the specific system, either of bits $\hat{v}^{(i)} \in \{0, 1\}, i \in \{0, \dots, l_v - 1\}$ or log-likelihood-ratios (LLRs, L-values) $\hat{v}^{(i)} \in \mathbb{R}, i \in \{0, \dots, l_v - 1\}$ reflecting the probabilities of the transmitted bit $v^{(i)}$ being either 1 or 0 [51]. If the transmitter used an application related source coder, an application related source decoder reconstructs the parameter frame $\hat{\underline{u}}$ either from the hard decided bits or the L-values of the received data frame $\hat{\underline{v}}$. From that an estimate \hat{s} of the originally transmitted signal s can be reconstructed by signal synthesis. For iterative decoding the source decoder may generate extrinsic information $L_{SD}^{[ext]}$ on the data bits $\hat{\underline{v}}$ in form of L-values.

4.1.2 Channel Coding

On the link related side of the transmitter the data frames \underline{v} are protected against transmission errors by means of system specific channel coding, i.e., the data bits are segmented into frames \underline{v} of length l'_v . Generally, the length l'_v fed to the channel coder may differ from the length l_v of the source coded parameter frame. Each frame \underline{v} is mapped onto a binary code frame \underline{x} of length l_x , where generally $l_x \geq l'_v$. The resulting code rate cr is defined as:

$$cr = \frac{l'_v}{l_x} \quad (4.1)$$

In the receiver, a channel decoder reconstructs the data frame $\hat{\underline{v}}$ from the received frame $\hat{\underline{x}}$, where $\hat{\underline{x}}$ can consist of hard decided bits or L-values. In case of $\hat{\underline{x}}$ and $\hat{\underline{v}}$ both consisting of L-values, the channel decoder is called *soft-input-soft-output (SISO) decoder*. The channel decoder might additionally be able to process extrinsic information $L_{SD}^{[ext]}$ fed back

by the source decoder to iteratively improve its estimates on $\hat{\underline{y}}$, a process called *iterative source channel decoding (ISCD)* [21, 49]. Basis for ISCD is appropriate interleaving and deinterleaving of the frames exchanged between SDS and SISO decoder. Interleaving and deinterleaving are assumed to be either part of the source or channel coding/decoding and therefore are not explicitly depicted in Fig. 4.1. For iterative processing, a SISO decoder might also be capable of calculating extrinsic information $L_{\text{CD}}^{[\text{ext}]}$ on the encoded bits $\hat{\underline{x}}$.

4.1.3 Complex Mapping

The code frame \underline{x} is mapped to a frame of complex modulation symbols \underline{Y} . Therefore, the bits of \underline{x} are grouped into sets of I bits, where $I \in \mathbb{N}$ can vary within one code frame. The sets are mapped to complex elements Y from a signal constellation set (SCS) \mathcal{Y} according to a mapping rule μ :

$$\mu\left(\left[x^{(i)} \dots x^{(i+I-1)}\right]\right) = Y \in \mathcal{Y} \subset \mathbb{C}. \quad (4.2)$$

Demapping is performed in the receiver by applying the inverse mapping rule μ^{-1} on the frame of received complex symbols $\hat{\underline{Y}}$. The demapper either calculates hard decided bits or L-values as output $\hat{\underline{x}}$. A so-called *soft demapper (SDM)* returns $\hat{\underline{x}}$ consisting of L-values. This soft demapper might additionally be able to process extrinsic information $\mathcal{I}_{\text{CD}}^{[\text{ext}]}$ fed back by the channel decoder to iteratively improve its estimates on $\hat{\underline{x}}$. This process is called *bit-interleaved coded modulation with iterative decoding (BICM-ID)* [63, 77, 38]. Like ISCD, bit-interleaved coded modulation with iterative decoding also demands appropriate interleaving and deinterleaving of the frames exchanged between SISO decoder and SDM. Again these processes are assumed to be part either of the SDM or of the SISO decoder and are not explicitly depicted in Fig. 4.1.

4.1.4 Baseband Modulation

In this work *baseband modulation* refers to a transformation or mapping of the complex valued frame \underline{Y} with elements $Y \in \mathcal{Y}$ to the complex valued frame \underline{y} with elements $y \in \mathbb{C}$. This transformation or mapping accounts for different measures taken in baseband signal processing like, e.g., system specific filtering, spreading, or multi-carrier transformation, before passing the signal on to the radio frequency (RF) domain. The most simple case is the identity $\underline{Y} = \underline{y}$. The phases and amplitudes of the symbols $y \in \mathbb{C}$ describe the phase and amplitude of the transmitted radio wave at carrier frequency f_0 which changes with the rate of the symbols \underline{y} . Hence, the duration of each symbol y defines the symbol duration T_s and therefore directly influences the used frequency bandwidth Δf (cf. Sec. 3.2). The average energy of the symbols y is normalized to unity:

$$\mathcal{E}\{|y|^2\} = E_s = 1$$

where E_S denotes symbol energy. As the lengths of frames \underline{Y} and \underline{y} are not necessarily equal, e.g., due to *spreading*, the *spreading factor (SF)* is defined as

$$\text{SF} = \frac{l_Y}{l_y}$$

with l_y and l_Y denoting the lengths of the frames \underline{y} and \underline{Y} , respectively.

The demodulator in the receiver performs the inverse operation of the system specific modulator. From the received channel observation \underline{z} the complex valued frame $\hat{\underline{Y}}$ is calculated.

4.1.5 Channel Model and Equalization

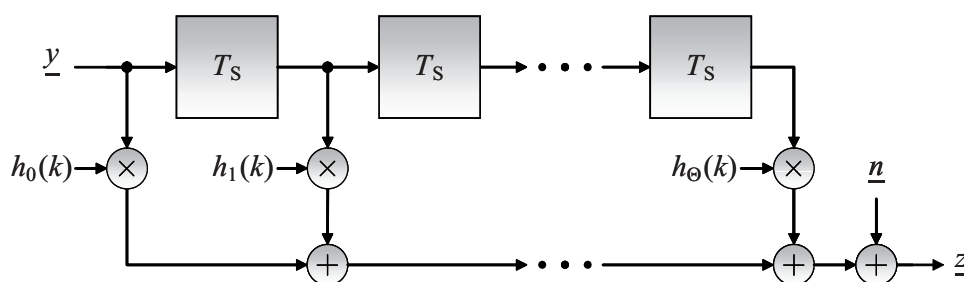


Figure 4.2: General baseband channel model.

Figure 4.2 depicts a generalized baseband channel model used in this thesis. It consists of two basic parts each modeling an important aspect of radio channels. The first part is an finite impulse response (FIR) structure modeling multi-path propagation resulting from reflections with delays of up to several symbol durations T_S . Being a band limited process, the effect of transmitting through a multi-path environment can be modeled in baseband by a so-called *tapped delay line* using T_S as sample time. With this assumption, each tap has a constant delay of iT_S and a complex fading factor $h_i(k) \in \mathbb{C}$ with $i \in 0, \dots, \Theta$ which may vary over discrete time instances k . The number of taps is determined by the considered scenario and reflects the delay spread and determines the frequency selectivity of the radio channel. If only one tap exists, i.e., if $h_j(k) \neq 0$ and $h_i(k) = 0 \forall i \neq j$, the channel will exhibit no frequency selectivity (flat fading channel). The more non-zero entries the *channel impulse response (CIR)* $\underline{h}(k) = [h_0(k), h_1(k), \dots, h_\Theta(k)]$ exhibits, the greater the *frequency dynamic* of the channel becomes, i.e., the correlation of the channel in the frequency domain at a fixed time instance k . The maximum delay ΘT_S is determined by the considered propagation scenario. With tap delays in the order of magnitude of the symbol length T_S *inter-symbol interference (ISI)* is introduced. That is why such a channel is also known as *ISI channel*.

Each element $h_i(k)$ can be regarded as product of two independent factors

$$h_i(k) = h_i^{\text{[att]}} \cdot h_i^{\text{[fad]}}(k).$$

The term $h_i^{\text{[att]}}$ comprises the effects of path specific propagation loss due to path length or shadowing effects. Although the path length and shadowing may vary during transmission,

it is modeled to vary slowly enough to be considered constant. The term $h_i^{\text{fad}}(k)$ relates to the superposition of local reflections of the propagation path with deviations in the range of the wave length of the carrier wave with frequency f_0 . This leads to the well known Rayleigh fading in non-line-of-sight (NLOS) conditions and to Rice fading in line-of-sight (LOS) conditions. The fading coefficient $h_i^{\text{fad}}(k)$ changes over time (fast fading, time selective) if the receiver or the transmitter moves. The dynamic of this fading process, i.e., the correlation of two consecutive fading coefficients $h_i^{\text{fad}}(k)$ and $h_i^{\text{fad}}(k+1)$ is determined by the velocity of transmitter and receiver. The different directions of the local reflections in combination with a transmitter or receiver moving at a certain velocity causes a direction dependent offset in the carrier frequency of each local reflection (Doppler effect) which in the frequency domain leads to a spreading of the received signal power spectral density, the so-called Doppler spread. Different models describe this spreading, a well-known model is the U-shaped Jakes spectrum. The time-domain dynamics and the amount of Doppler spread increase with increasing velocity. More details on the baseband model of the time and frequency selective (doubly selective) channel are given, e.g., in [74].

The employed FIR baseband channel model does not change the long-term average energy of the sum signal. The CIR \underline{h} is therefore chosen in such way, that

$$\mathcal{E} \left\{ \sum_{i=0}^{\Theta} |h_i(k)|^2 \right\} \stackrel{!}{=} 1$$

holds. In most channel models it is assumed that real and imaginary parts of h^{fad} are zero-mean. Therefore it suffices to ensure that

$$\sum_{i=0}^{\Theta} |h_i^{\text{att}}|^2 \stackrel{!}{=} 1. \quad (4.3)$$

The second part of the generalized channel model consists of additive white Gaussian noise (AWGN) denoted by the vector \underline{n} which consists of uncorrelated random elements $n \in \mathbb{C}$. The real and the imaginary parts $\Re\{n\}$ and $\Im\{n\}$ are independently Gaussian distributed with zero mean and variance

$$\mathcal{E} \{ |\Re\{n\}|^2 \} = \mathcal{E} \{ |\Im\{n\}|^2 \} \stackrel{!}{=} \frac{\sigma_n^2}{2}. \quad (4.4)$$

Assuming unity average energy of the transmitted symbols y and coherent reception, the channel signal-to-noise ratio (SNR) is defined as

$$\text{SNR} = \frac{\mathcal{E} \{ |y|^2 \}}{\mathcal{E} \{ |\Re\{n\}|^2 \} + \mathcal{E} \{ |\Im\{n\}|^2 \}} = \frac{1}{\sigma_n^2} = \frac{E_s}{N_0} \quad (4.5)$$

with $N_0 = \sigma_n^2$ being the noise power spectral density of the complex baseband noise. In real world transmissions the noise power spectral density is assumed constant for a given temperature (thermal noise) making the noise power a system specific figure depending on the

system frequency bandwidth Δf . The received signal power is varying due to propagation loss (see Chapter 6) and shadowing (slow fading) resulting in a varying SNR. For PHY layer simulations, these variations are simulated the other way round: The received signal power is fixed (see above) while the noise power is varied.

In this thesis three specific channel models are employed which are described in the following:

AWGN The simplest but fundamental model is the frequency flat AWGN channel with time invariant CIR $\underline{h}(k) = [1] \forall k$ and zero mean complex AWGN with noise power spectral density N_0 .

Rayleigh The frequency flat Rayleigh fading channel consists of a single time varying tap in combination with complex AWGN with noise power spectral density N_0 . The CIR is given by $\underline{h}(k) = [h^{\text{fad}}(k)]$ with $h^{\text{fad}}(k) \in \mathbb{C}$ exhibiting a uniformly distributed phase and Rayleigh distributed absolute value with

$$\mathcal{E} \left\{ |h^{\text{fad}}(k)|^2 \right\} = 1. \quad (4.6)$$

However, with the assumption of sufficiently large interleaving, the temporal correlation of the complex fading factor $h^{\text{fad}}(k)$ does not influence the simulation. For this reason $h^{\text{fad}}(k)$ is implemented as a temporally uncorrelated fading process.

TU The *doubly selective*, i.e., time and frequency selective, typical urban (TU) channel model is based on 3GPP's TU model recommended in [8]. It consists of a variable number of taps that depends on the system bandwidth Δf . The taps are characterized by fixed attenuation $\underline{h}^{\text{att}}$ and independent uncorrelated Rayleigh fading processes $\underline{h}^{\text{fad}}(k)$ with elements $h^{\text{fad}}(k)$ fulfilling (4.6). Details on the derivation of the model and a complete parametrization is given in Section A. The distorted output is subject to AWGN with noise power spectral density N_0 .

Being a deterministic process, the effects of the distortion due to fading can be inverted in the absence of noise, if the CIR $\underline{h}(k)$ is known. This process is known as *linear equalization*. Equalization strategies are not only system specific but even vendor specific as equalization algorithms are often not standardized. An approach to fully compensate for the frequency-selectivity is *zero-forcing (ZF)* [74] equalization which uses a time domain FIR filter that completely inverts the estimated CIR. However, this might lead to a highly increased noise level. A trade-off is given by the *minimum mean-square error (MMSE)* [74] equalizer aiming at minimizing the error between equalizer output and transmitted signal. For all equalization strategies, the CIR has to be estimated. To enable this CIR estimation, different measures are standardized for all state-of-the-art transmission systems, e.g., the insertion of so-called training sequences or pilot symbols at predefined positions of the signal. Different receiver algorithms may additionally demand knowledge of the current SNR which can also be estimated. These estimates of CIR and SNR are referred to as *channel state information (CSI)* in the following. As equalization and SNR estimation are beyond the scope of this thesis, only the basic concepts for the estimation of $\underline{h}(k)$ will be sketched for the systems in Sec. 4.2. Generally, all received symbols z are considered to be synchronized to time and frequency.

4.1.6 Performance Measures

With the given general transceiver model it is now possible to elaborate further into the performance measures introduced in Section 3.2. Given a transmission of K data frames \underline{v}_k at time instances $k \in \{0, \dots, K-1\}$ a number of transmitted information bits of $\mathcal{N}^{[\text{info}]} = Kl_v$ is obtained. With (3.5) the net BER is consequently calculated as

$$\text{net BER} = \frac{1}{Kl_v} \sum_{k=0}^{K-1} \epsilon_k^{[\text{info}]} \quad (4.7)$$

with $\epsilon_k^{[\text{info}]}$ being the number of errors in the received data frame $\hat{\underline{v}}_k$ at time instance k . In a similar manner the *frame error rate (FER)* can be determined as

$$\text{FER} = \frac{1}{K} \sum_{k=0}^{K-1} \epsilon_k \quad (4.8)$$

with

$$\epsilon_k = \begin{cases} 1 & \text{for } \epsilon_k^{[\text{info}]} > 0 \\ 0 & \text{for } \epsilon_k^{[\text{info}]} = 0 \end{cases} .$$

Assuming that any receiver discards erroneous frames, the goodput \mathcal{G} given in bit/s can be defined based on the frame error rate, the code rate cr , the number of bits per complex modulation symbol I , and the spreading factor SF:

$$\mathcal{G} = \frac{(1 - \text{FER}) cr I}{\text{SF} \cdot T_s} . \quad (4.9)$$

A normalized performance measure of a system not taking into account the time bandwidth product of the underlying modulation technique but only channel coding and mapping is given by the *bit per channel use* \mathcal{B} in bit, i.e., the number of information bits $\mathcal{N}^{[\text{info}]}$ transmitted per complex mapping symbol Y independent of the underlying modulation technique:

$$\mathcal{B} = (1 - \text{FER}) cr I. \quad (4.10)$$

However, BER and FER might not be appropriate measures for audio-visual applications. To judge the quality of the received parameters the relative error between \hat{u} and u is calculated as *parameter SNR (PSNR)*:

$$\text{PSNR} = \mathcal{E} \left\{ \frac{u^2}{(u - \hat{u})^2} \right\} \quad (4.11)$$

$$\text{PSNR}^{[\text{dB}]} = 10 \log_{10} (\text{PSNR}) \quad (4.12)$$

which is upper bounded by the *optimum performance theoretically attainable (OPTA)* PSNR_{max} [39].

4.1.7 EXIT Analysis

With the discovery of Turbo codes [26], channel coding close to the Shannon limit has become possible with moderate computational complexity and delay. This principle has successfully been adopted to many other components of the receiver chain, e.g., the aforementioned ISCD or BICM-ID systems. *Extrinsic information transfer (EXIT) charts* [83] are a powerful tool to analyze and optimize the convergence behavior of such iterative systems utilizing the Turbo principle, i.e., systems exchanging and refining extrinsic information. EXIT charts are based on the mutual information \mathcal{I} measure [40], where $\mathcal{I}(x; L)$ specifies the amount of information one variable L contains in average on the other variable x . With the L-value L of the binary variable x , the mutual information $\mathcal{I}(x; L)$ is generally given by the probability density function $p_L(\lambda|x)$ [83]

$$\mathcal{I}(x; L) = \frac{1}{2} \sum_{b=0}^1 \int_{-\infty}^{\infty} p_L(\lambda|x=b) \log_2 \frac{2 \cdot p_L(\lambda|x=b)}{p_L(\lambda|x=0) + p_L(\lambda|x=1)} d\lambda, \quad 0 \leq \mathcal{I} \leq 1. \quad (4.13)$$

The convergence behavior of the iterative process can be predicted by analyzing the *characteristics* \mathcal{T} of the components which describe the amount of extrinsic information $\mathcal{I}^{[ext]}$ that can be generated from a given amount of a priori information $\mathcal{I}^{[apri]}$:

$$\mathcal{I}^{[ext]} = \mathcal{T}(\mathcal{I}^{[apri]}).$$

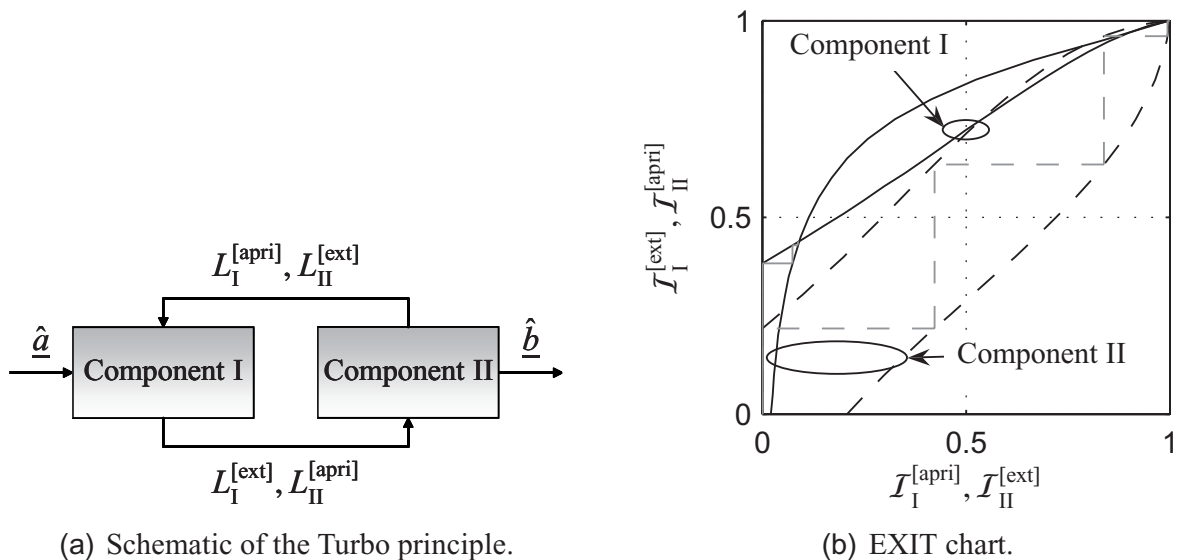


Figure 4.3: Example of a Turbo system using two serially concatenated components and its analysis using an EXIT chart.

An example of a Turbo system is given in Fig. 4.3(a) with its according EXIT chart depicted in Fig. 4.3(b). Goal is the reliable estimation of \hat{b} given the observation \hat{a} . Assuming

two serially concatenated components I and II exchanging extrinsic information in form of LLRs, the extrinsic information $\mathcal{I}_I^{[\text{ext}]}$ carried by the LLRs $L_I^{[\text{ext}]}$ of component I serves as the a priori information $\mathcal{I}_{II}^{[\text{apri}]}$ to component II and vice versa. Plotting both characteristics in one figure allows for a graphical representation of the iterative process. In Fig. 4.3(b) two possible realizations for both components are given as solid (—) and dashed (- -) line, respectively. The iterative process of refining the extrinsic information is depicted by the stair step-like *trajectory* plotted in gray between the characteristics of component I and component II. In the first iteration no a priori information is available for component I, the extrinsic information $\mathcal{I}_I^{[\text{ext}]}$ has to be generated from the observation \hat{a} . In case of the system represented by the solid lines, the system converges after two iterations (two stair steps) without yielding a reliable estimate on \hat{b} as $\mathcal{I}_{II}^{[\text{ext}]} < \mathcal{I}_I^{[\text{ext}]} \ll 1$ bit. A different convergence can be expected from the system represented by the dashed lines. A tunnel between both characteristics exists and iterative gains can therefore be achieved. The further the tunnel reaches to the right, the higher the amount of extrinsic information $\mathcal{I}_{II}^{[\text{ext}]}$ that can be generated in the final iteration by component II. In the optimum case error-free feedback (EFF) is achieved, i.e., $\mathcal{I}_{II}^{[\text{ext}]} = 1$ bit.

4.2 System Concepts and Their Evolution

All parts of the transmission chain described in the previous section have evolved more or less independently over the past. Each generation of mobile radio systems reflects the state-of-the-art technology available at the time of its standardization. In the following this evolution is sketched by describing examples of the second, third, and fourth generation of mobile radio systems. The labeling of radio systems as *2G*, *3G*, and *4G* is widely used although it does not give a precise technical specification. In this work these labels are used to distinguish the different *multiplex* and *multiple access* schemes employed in the different systems.

Multiplex refers to the transmission of data from one central entity to different users employing the same resources. In radio transmission this is usually the case in downlink transmission when one base station (BS) has to transmit data to all user equipments (UEs) in its cell in a specific manner. Multiple access refers to the opposite case when many users have to utilize, hence to access, the same resources to transmit their data to one central entity in a coordinated manner. In mobile radio communication that is the case for the uplink when independent UEs in one radio cell have to transmit their data to their central BS.

The separation of uplink and downlink transmission is called *duplex scheme*. Two basic duplex schemes exist. In *time division duplex (TDD)* systems up- and downlink are realized on the same frequency channel by assigning alternating but not necessarily equal time slots to both directions. In *frequency division duplex (FDD)* systems up- and downlink are separated by utilizing different frequency channels to each direction. Unless stated otherwise, this work restricts to FDD operation and focuses on the downlink. However, most of the physical layer features described in the following are common to both directions.

4.2.1 Second Generation Mobile Radio: FDM(A)/TDM(A)

As mentioned in Section 3.1, the purpose of the Global System for Mobile Communication (GSM) was to enable area-wide connectivity for mobile voice services. The data services General Packet Radio Service (GPRS) and Enhanced Data Rates for GSM Evolution (EDGE) were consecutively added to fulfill the increasing demand of mobile data access. The multiplex and multiple access schemes for these systems are a combination of frequency division multiplex (FDM) and time division multiplex (TDM) in the downlink and a combination of frequency division multiple access (FDMA) and time division multiple access (TDMA) in the uplink. To enable TDM(A) the time domain is divided into slots of 0.577 ms, 8 slots form one TDMA frame (4.615 ms). FDM(A) is realized by defining different frequency channels each with a bandwidth of $\Delta f_{[\text{GSM}]} = 200 \text{ kHz}$ including guard bands to avoid overlapping of adjacent channels, the so-called inter-carrier interference (ICI). The number of frequency channels and their carrier frequency depends on the specific GSM system. A single GSM radio cell will operate on a certain number of frequency channels, typically 1 to 6, depending on the cell size and its expected traffic. Adjacent radio cells are assigned frequency channels with different carrier frequencies to avoid co-channel interference (CCI), i.e., interference induced by a secondary transmitter using the same carrier frequency f_0 as the primary transmitter. Therefore, the so-called *frequency reuse factor* in GSM is typically > 1 . By employing *frequency hopping (FH)*, one voice or data connection uses different frequency channels for consecutive time frames in a predefined pattern which leads to transmit diversity to combat the doubly selective fading of the mobile radio channel. There are two commercially important implementations. On the one hand, GSM 900 operating in the 0.9 GHz band and GSM 1800 operating in the 1.8 GHz band are mainly deployed in Europe, Africa, and Asia. On the other hand, GSM 850 operating in the 0.85 GHz band and PCS 1900 (Personal Communication System) operating in the 1.9 GHz band are mainly deployed in Northern America [6].

Source Coding In the current release of the GSM standard, the adaptive multi-rate (AMR) codec [17] is used as the latest option for speech coding which adaptively chooses one out of eight codec modes with different data rates, allowing for rate adaptive channel coding for different channel conditions. The most robust codec mode represents a 20 ms speech frame by 95 bit, while the codec mode with the highest data rate and accordingly with the best quality of the reconstructed speech signal, the enhanced full-rate (EFR) mode, uses 244 bit. These bits are separated into three different streams according to their importance for the reconstruction of the encoded speech signal and undergo unequal error protection (UEP) by the channel coder [5]. As mentioned before, speech services in GSM are circuit-switched services. However, the main focus of this thesis is on packet-switched data transmission.

Channel Coding For packet-switched data transmission General Packet Radio Service (GPRS) and later Enhanced Data Rates for GSM Evolution (EDGE) have been added to GSM. Both are using a combination of block check sequence (BCS) and convolutional coding for protection against transmission errors. The code rate cr can be adapted by using

different puncturing schemes after convolutional coding with fixed mother codes of rates $cr_{[GPRS]} = 1/2$ and $cr_{[EDGE]} = 1/3$ for GPRS and EDGE, respectively [5]. For both system the code rates can be chosen between $cr = 1/2$ and $cr \approx 1$ (uncoded). GPRS defines four different coding schemes [79], while EDGE defines combinations of different coding schemes and different complex mappings, as described in the following paragraph. The concept of using different coding and complex mapping schemes according to a user's current channel quality is referred to as *adaptive coding and modulation (ACM)*.

Complex Mapping and TDMA Modulation GSM uses *Gaussian minimum shift keying (GMSK)* for modulation to achieve the effective frequency bandwidth $\Delta f_{[GSM]} = 200$ kHz by artificially spreading the modulation symbol in time. Each encoded bit evokes an approximation of a Gaussian pulse shape of duration $5T_s$ which intentionally introduces inter-symbol interference (ISI) of consecutive symbols. This pulse shaping keeps approximately 99% of the spectral power within the bandwidth of $\Delta f_{[GSM]} = 200$ kHz. With bipolar mapping ($Y \in \{-1, +1\}$) this corresponds to $I = 1$ bit per modulation symbol. For EDGE, 8PSK mapping (PSK = phase shift keying) has additionally been introduced allowing for the transmission of $I = 3$ bit per modulation symbol. Nine different combinations of code rate cr and mapping scheme μ are possible for EDGE transmissions which are defined as *modulation and coding schemes (MCSs)* [4, 78].

An equivalent of 156.25 modulation symbols are transmitted per time slot in a so-called *normal burst* consisting of 2×3 tail symbols, 2×57 data symbols, 2×1 flag symbols (stealing flag), 26 predefined symbols (training sequence), and a guard band with an equivalent length of 8.25 symbols. This leads to a symbol duration of $T_s \approx 3.69 \mu s$. GPRS and EDGE are transmitted together with other GSM traffic such as voice calls by allocating a defined number of time slots to the data services. The number of slots for GPRS or EDGE transmission in a GSM radio cell is chosen by the operator according to the available frequency channels and the expected data traffic in that cell. Multislot classes group different mobiles according to their ability to transmit and receive on a certain number of GPRS/EDGE slots per TDMA frame [7, 78, 79].

Equalization Equalizing is based on the known training symbols transmitted in each slot (burst) and realized, e.g., by a Viterbi equalizer [50]. This process does not only combat the influence of the doubly selective ISI channel but also the aforementioned ISI introduced due to GMSK modulation.

Throughput Estimation Examples With a mobile supporting the reception and processing of 8 GPRS slots (multislot classes 24 – 29) and coding scheme CS-4 with $r \approx 1$ a maximum data rate of $R \approx 8 \times 21.4 = 171.2$ kbit/s could be achieved [79] including approximately 11.2 kbit/s in-band control information. Assuming the same theoretical maximum of 8 slots allocated for EDGE and coding rate $r \approx 1$ in combination with 8PSK modulation (MCS-9) a maximum data rate of $R \approx 8 \times 59.4 = 475.2$ kbit/s (including low-rate in-band signaling) could be achieved.

However, these figures are hardly realistic. A more practical setting is the allocation of 4 slots for GPRS downlink and a code rate of $cr \approx 3/4$ (coding scheme CS-3) leading to a data rate of $R = 57.6$ kbit/s. This results in a spectral efficiency of $\eta = 0.288$ bit/s/Hz neglecting the spreading effect from frequency hopping. A state-of-the-art high-quality EDGE terminal of multislot class 32 can process 5 downlink slots allocated to EDGE. With a code rate of $cr \approx 3/4$ and 8PSK modulation (MCS-7) a data rate of $R = 225$ kbit/s can be achieved in very good channel conditions (cf. Section 2.3), leading to a spectral efficiency of $\eta = 1.125$ bit/s/Hz again neglecting the effects of frequency hopping and in-band signaling. Note that these data rates represent sum rates of one radio cell that have to be shared among all packet-switched data users. Time slots are dynamically allocated to support GPRS and EDGE services as long as they are available. To maintain the parallel support of circuit-switched voice or data traffic which usually has a higher priority, network operators will generally relocate time slots carrying PS GPRS or EDGE traffic to CS voice or data if demanded by a user in the same radio cell.

4.2.2 Third Generation Mobile Radio: CDM(A)

With the introduction of the Universal Mobile Telecommunication System (UMTS) by the Third Generation Partnership Project (3GPP) a more flexible approach to allocate resources for speech or data traffic has been implemented. This system is based on *code division multiplex (CDM)* and *code division multiple access (CDMA)* for downlink and uplink respectively. However, *CDMA* is commonly used to describe the complete modulation scheme and is therefore used accordingly in the following. Before becoming the basis of UMTS, CDMA had already successfully been employed in the cellular mobile radio standard IS-95 and is basis of the standard CDMA 2000 in northern America [47]. Furthermore it is used in the wireless local area networks (WLAN) standard IEEE 802.11b for providing fixed and nomadic broadband wireless access [2].

Source Coding For circuit-switched speech in UMTS the same AMR codec [17] as in GSM has been standardized. Currently, only the highest (EFR) mode is used in most of the networks. In contrast to GSM where the different codec modes offered by AMR are used to adapt to channel conditions, in UMTS the different rates could also be used to improve the capacity, i.e., the number of parallel voice connections in one radio cell [91]. However, so far this option has not been used.

High-rate packet-switched data transmission in UMTS is realized with high-speed packet access (HSPA), an amendment to the UMTS standard which has been published as high-speed downlink packet access (HSDPA) in release 5 of the standard for the downlink and as high-speed uplink packet access (HSUPA) in release 6 for the uplink, respectively. The physical layer procedures for HSDPA resemble those for the downlink of UMTS Long Term Evolution (LTE) very closely, cf. Section 4.2.3. Therefore, the procedures are only sketched for HSDPA and given in more detail later together with a throughput estimation.

Channel Coding Coding for HSDPA is defined in [12]. Each data frame from the medium access (MAC) layer is protected by means of a cyclic redundancy check (CRC) and bit scrambling is performed. After segmentation into code frames of maximum size 5114, a rate-1/3 systematic parallel concatenated convolutional code (PCCC) is used for channel coding. The code rate r is adapted using flexible puncturing of the output of the PCCC, thus enabling adaptive coding and modulation (ACM). Hybrid automatic repeat request (HARQ) allows for up to three retransmissions of a frame if corruption was detected by the CRC after decoding [41].

Complex Mapping and CDMA Modulation HSPA modulation is defined in [13]. A choice of quadrature phase shift keying (QPSK), 16QAM (quadrature amplitude modulation), and π -BPSK with so called HSPA+ – 64QAM all with Gray mapping as mapping rule μ allows for adaptive mapping with $I \in \{2, 4, 6\}$ bit per complex symbol. In the following HSDPA is considered to include 64QAM (HSPA+).

One of the major evolutions of UMTS compared to the 2G mobile radio systems using TDMA/FDMA is the use of CDMA modulation. In CDMA systems complex symbols are spread by *orthogonal sequences* of variable lengths operating at a common chip rate R_{chip} which in case of UMTS is defined as $R_{\text{chip}} = 3.84 \text{ Mchip/s}$ (megachip per second). The number of chips used for one spreading sequence is called SF , which also determines the maximum number of orthogonal codes of the same rate (the same SF). Each spreading code thereby generates one *code channel* which can be further subdivided by doubling the SF . Different code channels can be assigned to the same user at the same time to realize different logical connections or increase the data rate of one service. A comprehensive description of this orthogonal variable spreading factor (OVSF) technique originally proposed in [52] is given in [20].

UMTS is generally deployed as a cellular radio network with frequency reuse one, i.e., each radio cell transmits on the same carrier frequency f_0 with the same frequency bandwidth Δf . To distinguish different base stations in downlink, pseudo-random scrambling sequences with chip rate $R_{\text{chip}} = 3.84 \text{ Mchip/s}$ are used. These pseudo-random codes are designed to exhibit good correlation properties, i.e., high autocorrelation and low cross correlation. In the uplink these codes are used to distinguish different users. Pulse shape filtering, e.g., with root-raised cosine filters, is utilized to satisfy the spectral mask defined in [14] leading to the commonly known frequency bandwidth of $\Delta f_{[\text{UMTS}]} = 5 \text{ MHz}$ of the UMTS system. Matched filter reception is performed at the receiver using the known scrambling and spreading sequence of the transmitter.

HSDPA is using a fixed SF of 16, allowing a maximum of 15 HSDPA code channels per UMTS radio cell (one code channel is reserved for signaling and basic UMTS services). Like the different multi-slot classes defined for GPRS or EDGE, user equipment (UE) categories defined in [16] describe the capability of mobile devices to simultaneously decode different combinations of HSDPA channel codes and different signal constellation sets. These capabilities range between simultaneous decoding of 5 HSDPA channels using QPSK and 16QAM only, i.e., $I \in \{2, 4\}$ bit per complex symbol (category 1), and simultaneous de-

coding of 15 HSDPA channels with QPSK, 16QAM, and 64QAM, i.e., $I \in \{2, 4, 6\}$ bit per complex symbol (category 24).

Equalization With its frequency bandwidth of $\Delta f_{[\text{UMTS}]} = 5$ MHz the UMTS systems is particularly sensitive to frequency selective channels. To combat these effects different methods exist for CDMA. Historically often used is the *Rake* receiver structure which is meant to provide *channel matched filtering* by using a FIR filter structure adapted to the estimated channel impulse response. However, this does not always compensate the full frequency-selectivity of the channel [41]. Therefore, the aforementioned zero-forcing equalization or minimum mean-square error equalizer are additionally employed. In current devices the Rake receiver is used for CS voice services, while ZF or MMS equalizers are used for HSPA services. Estimation of the channel impulse response is based on pilot symbols.

4.2.3 Fourth Generation Mobile Radio: OFDM(A)

Defining different generations of mobile radio systems by their underlying multiplexing and access technology, the fourth generation is consequently characterized by the multicarrier modulation schemes orthogonal frequency division multiplex (OFDM) and orthogonal frequency division multiple access (OFDMA), respectively. The OFDM principle has been first published as early as 1966 by Chang [32], its realization using Inverse Discrete Fourier Transform (IDFT) and Discrete Fourier Transform (DFT) has been introduced by Weinstein and Ebert [90] in 1971 [84]. With the advances in microelectronics and the introduction of the Fast Fourier Transform (FFT) and Inverse Fast Fourier Transform (IFFT) algorithms, first applications of OFDM in different fields occurred. Today this technique is widely used for data transmission, e.g. in digital audio broadcast (DAB) [45], digital video broadcast (DVB) [46], and also in the WLAN standard IEEE 802.11-2007 (known as IEEE 802.11a/g) for fixed wireless or nomadic broadband access [2].

Its improved spectral efficiency compared to earlier technologies and advantageous properties in doubly selective channels makes OFDM a well suited candidate for future mobile radio systems. Two major players are pursuing their tracks to employ OFDM for mobile radio communication and broadband access.

On the one hand the Institute of Electrical and Electronics Engineers, Inc. introduced a fixed wireless standard with IEEE 802.16-2004 [1] called WiMAX (Worldwide Interoperability for Microwave Access). The term *WiMAX* relates to the WiMAX forum, an industry-led corporation promoting and certifying the compatibility of IEEE 802.16-2004 technology. The extended version IEEE 802.16-2009 [3] additionally features mobility aspects, making it a full mobile radio standard. With its strong focus on data transmission capability, the IEEE 802.16 standard family provides specifications only for the lower ISO layers.

3GPP, on the other hand, introduced UMTS Long Term Evolution (LTE) with the 2008 release 8 of its UMTS standard. LTE is considered the first step toward the goals set by the Next Generation Mobile Networks Alliance (NGMN). With this backing of mobile network operators and hardware manufacturers, LTE is expected to play a major roll in future mobile

communication. The following analysis of the LTE physical layer shall provide the basis for highlighting its potentials for providing area-wide mobile broadband access.

It has to be stated that the basic concepts of the physical layers of LTE resemble those of IEEE 802.16 and therefore similar performances have been reported for both technologies [25].

Channel Coding and HARQ The channel coding procedures for LTE are given in [10]. Data frames \underline{v} from the MAC layer are protected with a CRC code adding 24 bits to each frame. These data frames are of variable length, however, if a MAC frame including CRC bits exceeds a length of 6144 bits, i.e., $l_v > 6120$, the frame is segmented into smaller frames to fulfill that constraint. To ease notation, in the following \underline{v} denotes the data frame including the 24 CRC bits unless stated otherwise. As depicted in Fig. 4.4 this data frame is encoded by a systematic rate- $\frac{1}{3}$ turbo coder consisting of two parallel concatenated convolutional codes (PCCC) with octal generator polynomial $G = \{1, 15/13\}_8$ and an interleaver π which in LTE is implemented as *quadratic permutation polynomials* interleaver [10] allowing an easy implementation for different frame sizes l_v . Each component convolutional coder generates one parity bit per data bit which leads to three separate streams: The first contains the systematic, i.e., the uncoded data bits \underline{v} , whereas the second and third contain the parity bits of the two constituent coders \underline{p}_I and \underline{p}_{II} , respectively.

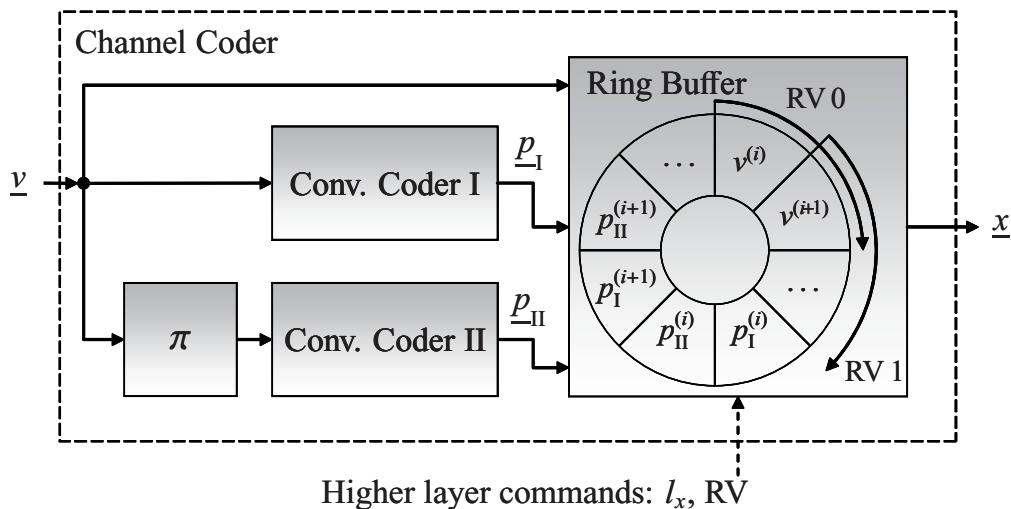


Figure 4.4: Turbo coding and rate matching in UMTS LTE.

For an efficient and easy to implement rate matching the three streams are individually interleaved and written to a ring buffer [33]. For the sake of clarity, these subinterleavers are not shown in Fig. 4.4. A frame of l_x encoded bits is selected for transmission from the ring buffer resulting in an effective code rate $cr = l_v/l_x$, cf. (4.1). The size l_x of the block of encoded bits is determined by a scheduler (dashed arrow in Fig. 4.4) according to the user's instantaneous channel quality, the user's requested throughput, maximum delay, targeted BER/FER and the current load of the radio cell. Thereby the scheduler implicitly determines the code rate of the user. A block size $l_x < 3 \cdot l_v$ results in a code rate $cr > \frac{1}{3}$. The

code rate can also take values $cr < \frac{1}{3}$ by repetition of systematic and parity bits.

In addition to turbo coding, the LTE hybrid automatic repeat request scheme allows for up to four transmissions of different combinations of systematic and parity bits, the so-called *redundancy versions (RV)*. For the initial transmission (RV 0), first, systematic bits are selected and then the remaining space of the code frame \underline{x} is filled up with parity bits. Note, that due to possible systematic puncturing, the first bit in RV 0 is not necessarily the first systematic bit, i.e., generally $x^{(0)} \neq v^{(0)}$ (cf. Fig. 4.4, [10]). Each following retransmission (RV 1 – RV 3) which may be requested by the receiver starts at a different position within the ring buffer, i.e., each redundancy version consists of a different combination of systematic and parity bits or even solely of parity bits. The decision of requesting a retransmission is based on the CRC of the decoded frame \hat{y} and signaled over a feed-back channel to the MAC layer of the transmitter, which in turn orders the retransmission with the corresponding RV (dashed arrow in Fig. 4.4). Obviously, each retransmission of a code block implicitly results in a decrease of the effective code rate and directly leads to losses in throughput and latency.

As mentioned before, the receiver is not covered by standardization, only minimum performance requirements are given. For this work a parallel turbo decoding structure is considered, consisting of two soft-input-soft-output (SISO) channel decoders (CD) using the LogMAP algorithm [75] for soft channel decoding. For the initial decoding step L-values \hat{x} are fed into CD I without using any a priori information. The obtained extrinsic information is properly interleaved and fed into CD II as a priori information. From this a priori information CD II generates extrinsic information for the next decoding iteration in CD I. After a fixed number of decoding iterations the frame of hard data bits \hat{y} is estimated from the resulting L-values.

Complex Mapping The bits selected for transmission are grouped to vectors of I bits with $I \in \{2, 4, 6\}$ which then are assigned to complex modulation symbols $Y \in \mathcal{Y}_I$ out of a of a signal constellation set \mathcal{Y}_I , i.e., QPSK, 16QAM, or 64QAM. Gray mapping is used as mapping rule μ for all signal constellation sets to form the frame of complex modulation symbols \underline{Y} [11]. If the size of the frame of encoded bits l_x is not an integer multiple of I , padding bits are used to form the final symbol $Y^{(l_y-1)}$. Assuming that $l_x \gg I$, the effect of these padding bits is negligible for throughput analysis.

OFDM Modulation As indicated by its name, *orthogonal frequency division multiplex* is a special form of frequency division multiplex aiming at spacing different frequency channels, also called subcarriers (SCs), as close as possible while avoiding inter-carrier interference. This is achieved by a fixed relation between the number of subcarriers n_{SC} , sample rate T_S^{-1} and frequency offset δf_{SC} between adjacent subcarriers. The number of complex baseband samples output by the OFDM modulator equals the number of subcarriers n_{SC} . The frequency offset between adjacent subcarriers in LTE is fixed to $\delta f_{SC} = 15$ kHz. The sampling frequency of the of the modulator output \underline{y}' is then given by $T_S^{-1} = n_{SC} \cdot \delta f_{SC}$ leading to a

fixed OFDM symbol duration of \underline{y}' :

$$T_{\text{OFDM}} = n_{\text{SC}} T_s = \frac{1}{\delta f_{\text{SC}}} = \frac{2}{3} 10^{-4} \text{ s.} \quad (4.14)$$

The complex mapped symbols \underline{Y} are segmented into frames $\underline{Y}' = [Y'^{(0)}, \dots, Y'^{(n_{\text{SC}}-1)}]$ of size n_{SC} . Then the time discrete complex OFDM symbol $\underline{y}' = [y'^{(0)}, \dots, y'^{(n_{\text{SC}}-1)}]$ is given by the sum of n_{SC} subcarriers where each subcarrier i carries one symbol $Y'^{(i)}$. Each subcarrier is modulated with frequency $i\delta f_{\text{SC}}$ and sampled at n_{SC} discrete time instances $\tilde{k} = [0, T_s, \dots, (n_{\text{SC}} - 1)T_s]$:

$$y'^{(\tilde{k}/T_s)} = \sum_{i=0}^{n_{\text{SC}}-1} Y'^{(i)} \exp(j2\pi i\delta f_{\text{SC}} \tilde{k}) \quad \text{for } 0 \leq \tilde{k} \leq (n_{\text{SC}} - 1)T_s \quad (4.15)$$

Substituting the time instances \tilde{k} by $k = \frac{\tilde{k}}{T_s} = \tilde{k} n_{\text{SC}} \delta f_{\text{SC}}$ in (4.15) leads to

$$y'^{(k)} = \sum_{i=0}^{n_{\text{SC}}-1} Y'^{(i)} \exp\left(j2\pi \frac{ik}{n_{\text{SC}}}\right) \quad \text{for } 0 \leq k \leq n_{\text{SC}} - 1 \quad (4.16)$$

which can be expressed by using the Inverse Discrete Fourier Transform (IDFT) of size n_{SC} :

$$\underline{y}' = n_{\text{SC}} \text{IDFT}_{n_{\text{SC}}} \{ \underline{Y}' \}. \quad (4.17)$$

Consequently, demodulation is performed by the Discrete Fourier Transform (DFT) of size n_{SC} :

$$\underline{\hat{Y}}' = \frac{1}{n_{\text{SC}}} \text{DFT}_{n_{\text{SC}}} \{ \underline{\hat{y}}' \}. \quad (4.18)$$

As mentioned before, this modulation scheme became feasible with the introduction of the Fast Fourier Transform (FFT) and Inverse Fast Fourier Transform (IFFT) algorithms, performing the DFT and IDFT with reasonable low computational complexity and low memory demand. Assuming a power-of-two number of subcarriers n_{SC} (Radix-2 FFT) and a subcarrier spacing $\delta f_{\text{SC}} = 15 \text{ kHz}$, the sample rate $1/T_s = n_{\text{SC}} \cdot \delta f_{\text{SC}}$ is a multiple or sub-multiple of the CDMA chip rate $R_{\text{chip}} = 3.84 \text{ Mchip/s}$ of the standard UMTS and HSDPA system [41], allowing for an easy implementation of multi-mode terminals and base stations.

With OFDM modulation a complex information carrying symbol $Y'^{(i)}$ is mapped to a narrow subcarrier over the complete duration of frame \underline{y}' making the transmission robust against time selective fast fading channels. To also increase the robustness in frequency selective ISI channels a *cyclic prefix (CP)* of a predefined length l_{CP} is additionally added at the modulator completing the frame of modulation symbols \underline{y} of size $l_y = n_{\text{SC}} + l_{\text{CP}}$. Although the CP extends the duration of the OFDM symbol \underline{y} and thereby reduces the spectral efficiency of the system, it still allows for an elegant and easy to implement equalization of the frequency selective radio channel (see below). An example clarifying the relation between different

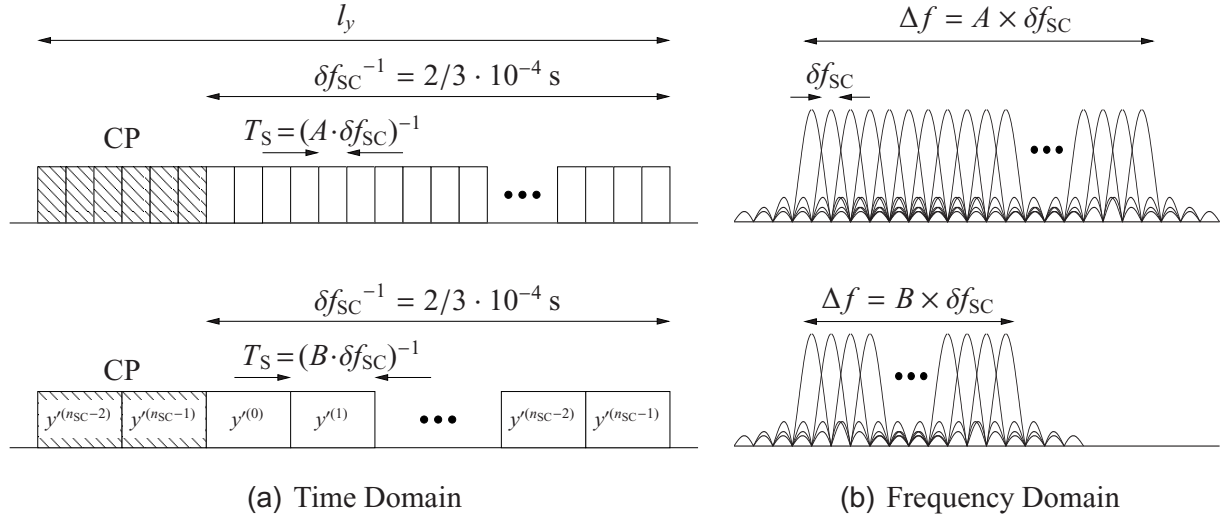


Figure 4.5: Time and frequency domain dependencies for different numbers of subcarriers $n_{SC} = A$ (upper) and $n_{SC} = B$ (lower) with $A > B$

parameters in time and frequency domain is sketched in Fig. 4.5 for different frame sizes n_{SC} .

One LTE time slot of $T_{\text{slot}} = 0.5$ ms duration is divided into six or seven OFDM symbols depending on the CP length. Two CP lengths are defined for LTE, an extended and a normal cyclic prefix. This work considers the scheme using the normal cyclic prefix, i.e., seven OFDM symbols per time slot. According to [11] the CP of the first OFDM symbol in a time slot has a duration of $5.2 \mu\text{s}$, while the CPs of the other six symbols have a duration of $4.7 \mu\text{s}$, leading to the aforementioned standardized LTE slot duration of

$$T_{\text{slot}} = 7 \times \frac{2}{30} \text{ ms} + 0.0052 \text{ ms} + 6 \times 0.0047 \text{ ms} \approx 0.5 \text{ ms}.$$

12 adjacent subcarriers in 7 consecutive OFDM symbols in each time slot make up one *resource block (RB)* consisting of $7 \times 12 = 84$ *resource elements (REs)*, each carrying one complex symbol $Y^{(i)}$. One RB is the smallest unit of transmission resources a user can be assigned. The number of available resource blocks per time slot n_{RB} and thereby the number of resource elements per time slot n_{RE} depends on the frequency bandwidth Δf of the transmission system and is given in Tab. 4.1 along with the number of used subcarriers, the number of theoretically available subcarriers n_{SC} (DFT size) and CP lengths l_{CP} (first symbol/other symbols) for different system bandwidths Δf as recommended in [9].

Using 100 RBs in the 20 MHz system leads to 1200 out of 2048 subcarriers used for transmission (cf. Tab. 4.1). The reason for not using all subcarriers are the spectral restrictions given in [9, 14]. Using 2048 subcarriers of $\delta f_{SC} = 15$ kHz frequency bandwidth leads to a system bandwidth of $\Delta f > 20$ MHz. Therefore, only the innermost 1200 subcarriers are used resulting in a bandwidth of $\Delta f = 18$ MHz, leaving 2×1 MHz as guard band. Additionally, pulse shape filtering can be employed to further reduce the out-of-band emissions of the LTE modulator.

Δf	5 MHz	10 MHz	15 MHz	20 MHz
number RBs n_{RB} per time slot	25	50	75	100
number REs n_{RE} per time slot	2100	4200	6300	8400
used subcarriers	300	600	900	1200
DFT size n_{SC}	512	1024	1024	2048
CP length l_{CP}	40/36	80/72	120/108	160/144

Table 4.1: LTE physical layer parameters.

Equalization Figure 4.5(b) illustrates the orthogonality of OFDM subcarriers in frequency domain. This orthogonality is lost, if inter-symbol interference is introduced during the transmission or if a timing or frequency offset occurs. While synchronization issues, i.e., correction of timing and frequency offsets, are out of scope of this work, zero-forcing (ZF) equalization to combat ISI is derived in the following.

Assuming a *block fading* channel, the channel impulse response $\underline{h}(k)$ is time-invariant for the duration of one OFDM symbol. The time index k is therefore omitted in the following. Given an OFDM symbol \underline{y} which is transmitted over an frequency selective ISI channel with fixed CIR \underline{h} , the received signal is then the linear convolution (denoted by $*$) of the OFDM symbol \underline{y} with the CIR \underline{h} plus additive noise \underline{n} :

$$\underline{z} = \underline{y} * \underline{h} + \underline{n} \quad (4.19)$$

With addition of a cyclic prefix of size $l_{\text{CP}} > l_h$, i.e., with larger duration than the channel impulse response, the transmitted signal appears periodic to the channel. With that, the linear convolution becomes circular, denoted by \circledast . Transforming (4.19) into frequency domain, the circular convolution becomes an element-wise multiplication:

$$\underline{z} = \underline{y} \circledast \underline{h} + \underline{n} \quad (4.20)$$

$$\begin{aligned} & \Downarrow \\ \Rightarrow \underline{Z} &= \underline{Y} \cdot \underline{H} + \underline{N} \end{aligned} \quad (4.21)$$

with \Downarrow denoting the Discrete Fourier Transform, \underline{Z} the DFT of \underline{z} , \underline{N} the DFT of the noise samples \underline{n} and \underline{H} the DFT of the zero-padded CIR \underline{h} , i.e., the channel transfer function. The DFTs are of size $l_y = l_z$ which is the reason behind the zero-padding of \underline{h} . With \underline{Z} being the output of the DFT of the OFDM demodulator, zero-forcing equalization can be performed to obtain the estimate $\hat{\underline{Y}}$:

$$\hat{\underline{Y}} = \frac{\underline{Z}}{\underline{H}} = \underline{Y} + \frac{\underline{N}}{\underline{H}} \quad (4.22)$$

Due to the normalization of the DFT in the OFDM demodulator, the average noise power of the samples \underline{N} is equal to that of \underline{n} . However, (4.22) indicates that the noise on subcarriers with small values of \underline{H} is amplified, a so-called noise-rise occurs. Estimation of \underline{h} respectively \underline{H} is based on a reference signal, i.e., predefined complex symbols Y that are inserted at

predefined positions in time and frequency. For the single-antenna case, 4 resource elements are used per resource block for the reference signal [11].

4.3 LTE Performance Analysis

The LTE physical layer is analyzed by computer simulation. A sufficiently large number of data frames \underline{v} containing random and uncorrelated bits is generated. Unless stated otherwise, the data frame size is fixed to $l_v = 6120$ which after adding 24 CRC bits leads to the maximum frame size of 6144 bits which are processed by the standard conform PCCC and fed to the rate matching buffer. OFDM modulation is performed with $n_{SC} = 512$ subcarriers and $n_{SC} = 2048$ subcarriers for LTE system bandwidths of $\Delta f = 5$ MHz and $\Delta f = 20$ MHz, respectively. Accordingly, the cyclic prefixes are set to $l_{CP} = 36$ and $l_{CP} = 144$. The longer CP of the first OFDM symbol of each LTE time slot does not influence the simulation results for the given channel models and is therefore omitted. The employed channel models are AWGN, Rayleigh and TU as described in Section 4.1.

The OFDM demodulator performs zero-forcing equalization as described by (4.22). A soft demapper calculates log-likelihood ratios \hat{x} according to [31] which are, in case of retransmission, combined with earlier redundancy versions and demultiplexed into systematic and parity streams. These three streams are fed to a SISO Turbo decoder utilizing the LogMAP algorithm [75] for a fixed number of 10 iterations. From the hard decided output \hat{y} of the channel decoder the CRC bits are evaluated and, in case of failure, a retransmission is initiated. Finally, BER and FER are determined by comparing \underline{v} and \hat{y} and recorded for statistical analysis.

4.3.1 EXIT Analysis

An example illustrates the influence of the LTE HARQ on the SISO Turbo decoder. Figure 4.6 shows the EXIT charts of the Turbo decoder consisting of the two component decoders CDI and CDII for different channel qualities and different redundancy versions (RVs). The fixed coding rate is $cr = 1/3$ and 16QAM with Gray mapping is employed. RV 0 denotes the initial transmission and RV 1, RV 2, and RV 3 denote the first, second, and third retransmission, respectively. The channel model is AWGN, therefore the OFDM stage, though implemented and simulated, does not influence the depicted results.

For channel qualities $SNR < -3$ dB no decoding is possible for the chosen configuration with RV 3 as indicated by Fig. 4.6(a) where the characteristics of the component decoders intersect early for $SNR = -3$ dB (solid black lines). For $SNR = 3.5$ dB (dashed black lines) a decoding tunnel opens and the decoding trajectory (dashed gray line) reaches the error-free feedback case.

In Fig. 4.6(b) the same configuration ($cr = 1/3$, 16QAM) is analyzed for higher channel qualities and RV 0 and RV 1. For $SNR = 2.5$ dB decoding is possible with one retransmission (dashed gray lines), both characteristics of the component decoders form a wide tunnel. However, decoding is impossible with the initial transmission RV 0 at the same channel quality as the decoder characteristics intersect for that case (solid gray lines). For $SNR = 3$ dB

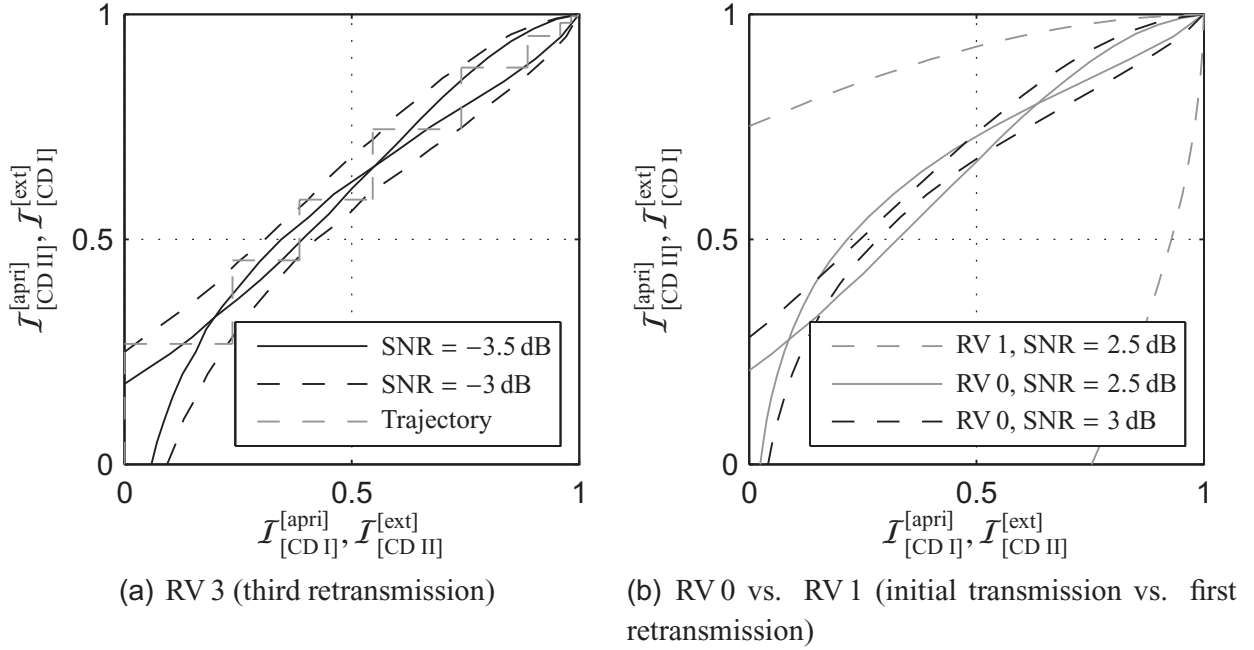


Figure 4.6: EXIT analysis of the LTE HARQ scheme and Turbo decoder with 16QAM and $cr = 1/3$.

a tunnel exists between the characteristics for RV 0 (dashed black lines) and thus decoding becomes possible with the initial transmission.

4.3.2 Bits Per Channel Use and Spectral Efficiency

The physical layer performance of UMTS LTE is first analyzed in terms of the amount of error-free transmitted information bits $\mathcal{N}^{[info]}$ per resource element (RE), from where the spectral efficiency is derived in a second step. The measure $\mathcal{N}^{[info]}$ per RE corresponds to bits per channel use \mathcal{B} as given in (4.9). Taking into account the number of necessary transmissions $n_{Tr} \in \{1, 2, 3, 4\}$ leads to

$$\mathcal{B} = \frac{(1 - FER) cr I}{n_{Tr}}. \quad (4.23)$$

Figure 4.7 shows the achieved bits per channel use \mathcal{B} for the three signal constellation sets QPSK, 16QAM and 64QAM and code rate $cr = 1/3$ in an AWGN environment.

The findings from Section 4.3.1 are reflected in Fig. 4.7 by the progression of the achieved bits per channel use \mathcal{B} with 16QAM (\square) and up to 3 retransmissions. As predicted by the EXIT chart in Fig. 4.6(a), the first successful decoding of RV 3 ($n_{Tr} = 4$) takes places at $SNR = -3$ dB indicated by a small plateau between -3 dB $<$ $SNR <$ -2.5 dB. At this range of channel qualities, error-free decoding is possible for $n_{Tr} = 4$ but not for $n_{Tr} = 3$. Each of the four plateaus in the curves of Fig. 4.7 reflects the error-free decoding for a certain number of transmissions $n_{Tr} \in \{1, 2, 3, 4\}$. Error-free decoding of RV 0 with $n_{Tr} = 1$ in the

16QAM case is achieved for $\text{SNR} > 3$ dB, cf. Fig. 4.6(b). Note that the results are independent of the system frequency bandwidth Δf as the OFDM modulation/demodulation stage is transparent for the non-frequency selective AWGN channel model.

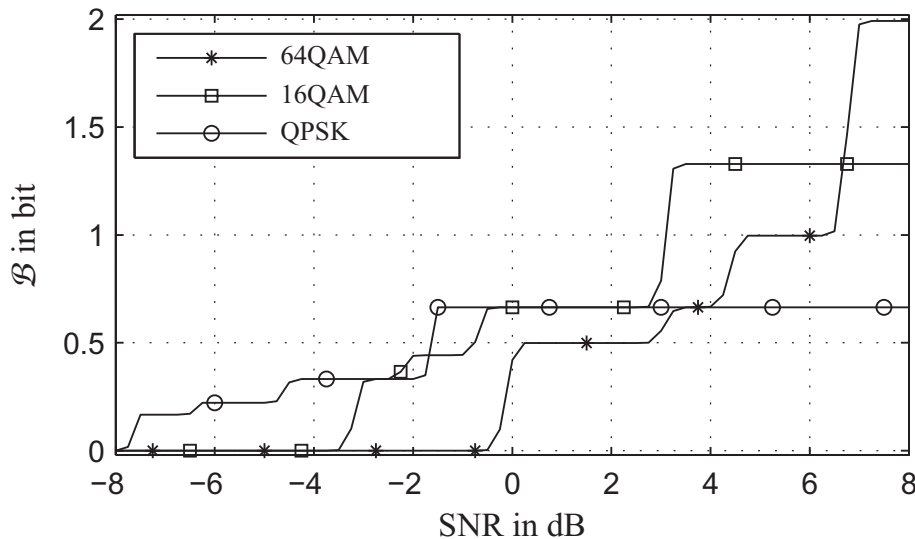


Figure 4.7: Bit per channel use \mathcal{B} of LTE in AWGN with code rate $\text{cr} = 1/3$.

Conducting simulations for code rates $\text{cr} \in \{\frac{1}{3}, \frac{1}{2}, \frac{2}{3}, \frac{3}{4}, \frac{4}{5}\}$ and the three SCSs QPSK, 16QAM and 64QAM with $I \in 2, 4, 6$ leads to 15 individual performance curves. The envelope of these individual curves indicates the performance of the physical layer if adaptive coding and modulation (ACM) is applied and is depicted in Fig. 4.8 for the three considered channel models AWGN (solid), Rayleigh (dashed), and TU (dash-dotted). As expected, the simulations yield the best results for the AWGN environment. The depicted performance curve for the AWGN case coincides very well with the curve recommended by 3GPP for throughput analysis with ACM as given in [15]. The performance in the typical urban (TU) environment is slightly better for $\Delta f = 5$ MHz than for $\Delta f = 20$ MHz. One explanation for that are the higher channel dynamics in the 20 MHz channel compared to the 5 MHz channel.

Also given in [15] is an approximation of the achievable bits per channel use in an AWGN environment which is based on the Shannon capacity

$$\mathcal{G}_{\max} = \Delta f \log_2(1 + \text{SNR}) \quad (4.24)$$

where \mathcal{G}_{\max} describes the maximum achievable goodput for a given system frequency bandwidth Δf at a given channel quality. (4.24) can also be interpreted as the maximum bits per channel use assuming a unity time bandwidth product, i.e., $\Delta f T_s = 1$. With that assumption 3GPP recommends the following approximation for the achievable bits per channel use $\tilde{\mathcal{B}}$ in LTE with ACM [15]:

$$\tilde{\mathcal{B}} = \begin{cases} 0 & \text{for } \text{SNR} < \text{SNR}_{\min} \\ 0.75 \log_2(1 + \text{SNR}) & \text{for } \text{SNR}_{\min} \leq \text{SNR} \leq \text{SNR}_{\max} \\ \mathcal{B}_{\max} & \text{for } \text{SNR} > \text{SNR}_{\max} \end{cases} \quad (4.25)$$

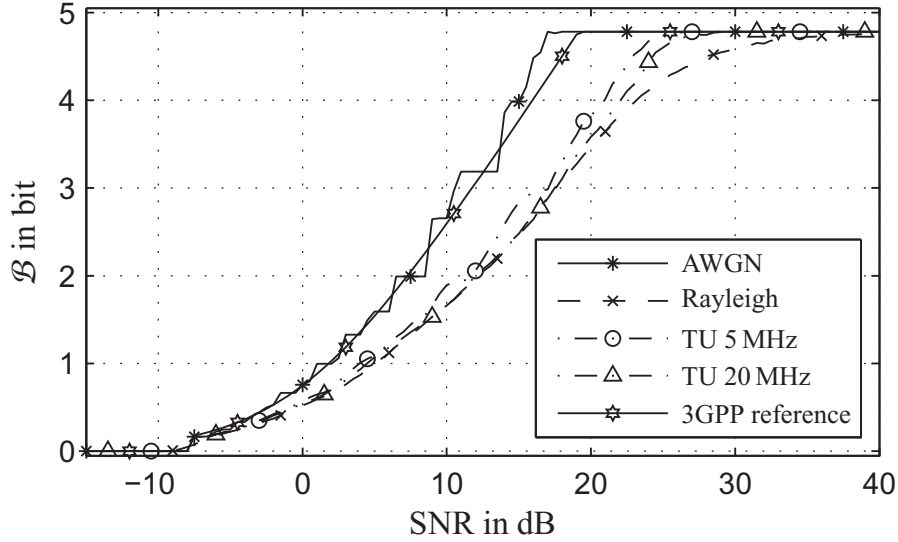


Figure 4.8: Bit per channel use \mathcal{B} of LTE with ACM for different channel models and 3GPP reference from [15].

where $\text{SNR}_{\min} = -7.5$ dB denotes the minimum SNR where data is successfully decoded, $\mathcal{B}_{\max} = 4.8$ bit the maximum bits per channel use that can be achieved by ACM, and $\text{SNR}_{\max} = 19$ dB the SNR at which \mathcal{B}_{\max} is reached. The according curve defined by (4.25) is given in Fig. 4.8 confirming its applicability.

Figure 4.8 implies that the LTE PHY layer operates at 75 % of the Shannon capacity (see also [15], Appendix A.2). This is not the case! As explained above, the approximation in (4.25) assumes an underlying transmission system with unity time bandwidth product which is not the case for LTE. An optimistic assumption is based on the time bandwidth product of one resource block containing 7 OFDM symbols per time slot of 0.5 ms duration and using 12 subcarriers with $\delta f_{\text{SC}} = 15$ kHz. With that assumption the SNR dependent spectral efficiency $\eta_{\text{RB}}^{[\text{LTE}]}(\text{SNR})$ based on the resource blocks of the LTE system in bit/s/Hz is given by

$$\eta_{\text{RB}}^{[\text{LTE}]}(\text{SNR}) = \frac{7 \cdot 12}{12 \cdot 15 \text{ kHz} \cdot 0.5 \text{ ms}} \mathcal{B}(\text{SNR}) \approx 0.933 \cdot \mathcal{B}(\text{SNR}). \quad (4.26)$$

Furthermore, the number of utilized subcarriers does not occupy the complete bandwidth Δf allotted to the system (see Table 4.1). For $\Delta f = 20$ MHz and 100 RBs (4.26) can be further refined taking into account the nominal occupied bandwidth Δf :

$$\eta_{\Delta f}^{[\text{LTE}]}(\text{SNR}) = \frac{7 \cdot 12 \cdot 100}{20 \text{ MHz} \cdot 0.5 \text{ ms}} \mathcal{B}(\text{SNR}) = 0.84 \cdot \mathcal{B}(\text{SNR}). \quad (4.27)$$

The corresponding spectral efficiencies from (4.26) and (4.27) are depicted in Fig. 4.9 as solid lines and compared to the Shannon capacity (4.24) normalized by Δf which results in a Shannon limit for the spectral efficiency (dash-dotted line). It can be seen that with the given assumptions the LTE PHY reaches approximately 65 % of the Shannon limit. Taking furthermore the reference symbols (4 per RB) and PHY and MAC layer signaling (1 – 3

OFDM symbols per 2 time slots) into account, the LTE spectral efficiency achieves 55 % of the Shannon limit (not shown). Note that (4.27) holds for all system bandwidths and number of RBs given in Tab. 4.1.

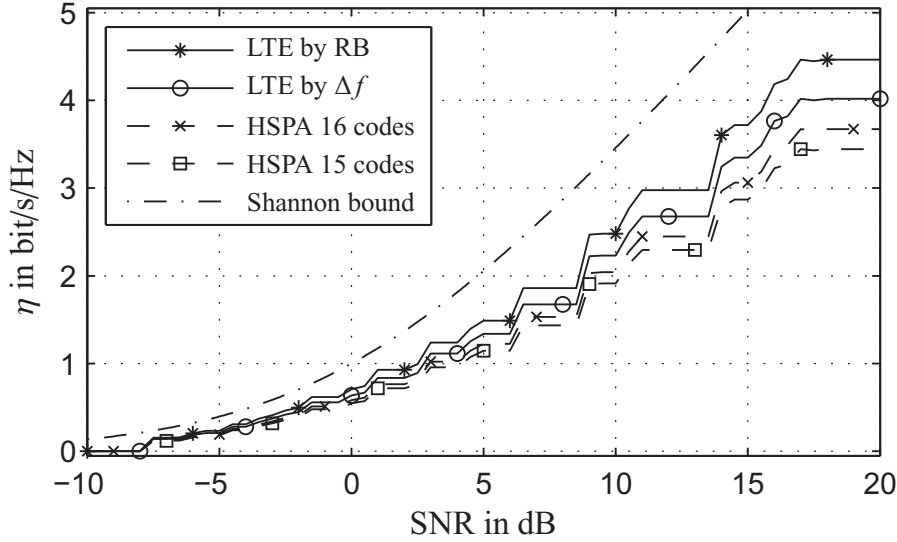


Figure 4.9: Spectral efficiency.

Figure 4.9 reveals another important fact: The spectral efficiency depends on the channel quality, i.e., $\eta = \eta(\text{SNR})$, and therefore on the position of a user within a radio cell. It is high at positions with good channel conditions, i.e., close to the base station, but decreases for decreasing channel qualities, e.g., at the edge of a radio cell. This behavior is a major reason for the vagueness of the spectral efficiency η as a performance measure foreshadowed in Section 3.2.

Many of the basic features of the LTE physical layer can be considered as refinements of the HSPA amendment to UMTS, see Section 4.2.2. Therefore, the performance of the HSPA PHY can be considered to be upper bounded by the LTE PHY. Regarding the spectral efficiency of HSDPA the CDMA modulation scheme has to be accounted for. For the AWGN case the spreading and correlation reception is considered transparent, an equivalent HSPA resource element is then represented by a single spreading chip of rate $T_s^{-1} = 3.84 \text{ Mchip/s}$. The allotted system frequency bandwidth is $\Delta f = 5 \text{ MHz}$. With these optimistic assumptions considering all resources (16 code channels each with SF = 16) to be dedicated to HSDPA data transmission, the HSDPA spectral efficiency in bit/s/Hz is given by

$$\eta_{16}^{[\text{HSDPA}]}(\text{SNR}) = \frac{3.84 \text{ Mchip/s}}{5 \text{ MHz}} \mathcal{B}(\text{SNR}) = 0.768 \cdot \mathcal{B}(\text{SNR}). \quad (4.28)$$

Taking into account signaling and dedicated traffic, a maximum of 15 code channels (SF = 16) is assigned to HSDPA resulting in

$$\eta_{15}^{[\text{HSDPA}]}(\text{SNR}) = \frac{15}{16} \eta_{16}^{[\text{HSDPA}]}(\text{SNR}) = 0.72 \cdot \mathcal{B}(\text{SNR}). \quad (4.29)$$

Both spectral efficiencies are depicted in 4.9 as dashed curves. It should be noted that for the two HSDPA examples no in-band control information is taken into account. The comparison of the spectral efficiencies of the LTE and the HSDPA system clearly illustrates the gain achieved by OFDM over CDMA. Assuming a dedication of all radio resources (REs in LTE and code channels in HSDPA) to data transmission, the ratio of

$$\frac{\eta_{\Delta f}^{[\text{LTE}]}(\text{SNR})}{\eta_{16}^{[\text{HSDPA}]}(\text{SNR})} = \frac{0.84}{0.768} = 1.094 \quad (4.30)$$

implies a gain of 9.4% due to the better time bandwidth product of OFDM in UMTS LTE compared to CDMA in UMTS HSDPA.

Beyond UMTS LTE

The UMTS LTE physical layer (PHY) as described in Section 4.2.3 and analyzed in Section 4.3 can be considered a state-of-the-art transmission technique. It has been shown that for the single antenna case UMTS LTE reaches approximately 65 % of the Shannon bound. This chapter introduces two novel modifications of the single antenna LTE PHY and analyzes their performance and complexity. Additionally, a novel optimization scheme based on EXIT charts is introduced. The modifications of the LTE PHY lead to an alternative transceiver concept: the novel combination of the Turbo DeCodulation (TDeC) approach [34] with OFDM. TDeC aims at the joint optimization of source decoding, channel decoding, and demapping. Two different TDeC schemes in combination with OFDM are analyzed and optimized. The performance of these two novel OFDM TDeC schemes are then compared to UMTS LTE. Finally, theoretical bounds on the achievable bits per channel use \mathcal{B} are derived for multiple-input multiple-output (MIMO) transmission enabling the estimation of a performance bound for future PHY concepts. A brief sketch of future interference management techniques concludes this chapter.

5.1 Improving UMTS LTE 64QAM Performance

This section shows a novel scheme resulting in significant gains in terms of residual BER and achievable bits per channel use \mathcal{B} . The basic idea is a sophisticated reordering of the encoded bits of the LTE turbo coder taking into account the unequal error protection (UEP) property of Gray mapped 64QAM [66, 65].

5.1.1 UEP and Bit Reordering

Considering a high order modulation scheme like 64QAM with Gray mapping as given in [11] for UMTS LTE, it can be observed that each bit position or bit level in the 6 bit symbol $Y \in \mathcal{Y}_6$ exhibits a different BER and therefore a different level of protection. This is illustrated by Fig. 5.1 where the mutual information $\mathcal{I} \hat{=} \mathcal{I}(x; \hat{x})$ between transmitted code bit x and L-value \hat{x} is plotted versus the SNR for each bit position of the 64QAM mapping in an AWGN environment. The L-values \hat{x} are obtained from the soft demapper (SDM), while the distributions $p_{\hat{x}}$ used for the calculation of \mathcal{I} according to (4.13) are determined in PHY simulations. The mutual information \mathcal{I} serves as a measure of robustness of each bit level.

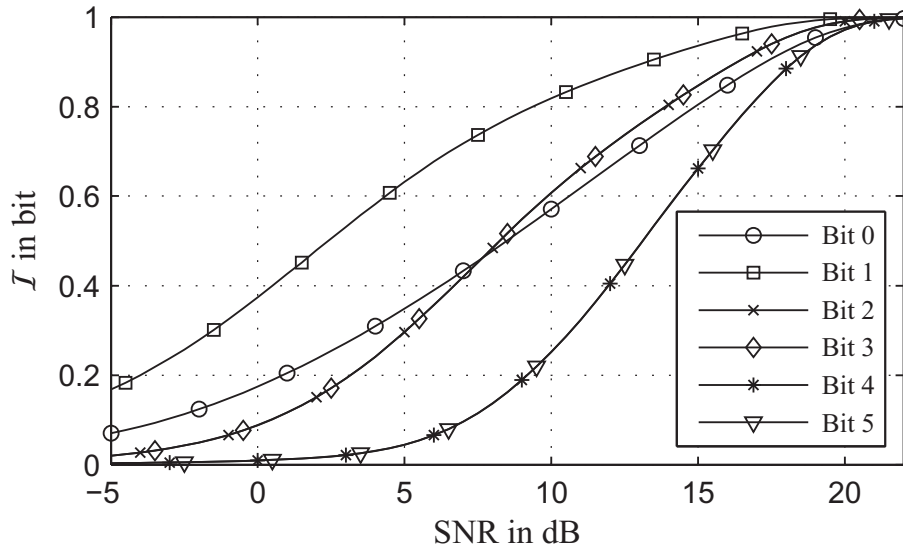


Figure 5.1: Mutual information \mathcal{I} between transmitted bits and received LLRs versus channel quality for the different bit levels of 64QAM with Gray mapping.

It is observed that for the six bits (Bit 0, ..., 5) of each Gray mapped 64QAM symbol there exist four different levels of protection, i.e., two groups consisting of two bits (first group: Bits 2 and 3, second group: Bits 4 and 5, cf. Fig. 5.1) exhibit the same error protection properties while the best protection against bit errors at low channel qualities (SNR < 7 dB) is provided by Bits 0 and 1. This behavior can be interpreted as an unequal error protection property inherent in 64QAM with Gray mapping.

There are various ways of making use of unequal error protection in communication systems, e.g., unequal protection of different codec parameters of encoded speech (cf. Section 4.2.1), or unequal energy distribution of complex mapping symbols Y [29]. The scheme described here exploits UEP by unequally protecting systematic and parity bits. The employment of UEP for systematic and parity bits of a turbo coded system has been shown, e.g., in [48] where a faster convergence of a joint turbo decoding and channel estimation process is observed if systematic bits get stronger protection against channel impairments than parity bits. This directly leads to gains in the BER performance in case of a fixed number of turbo decoding and channel estimation iterations. In LTE, the unequal error protection property present in the complex signal constellations is not taken into account, cf. Section 4.2.3. This motivates the following approach to exploit this UEP property: By a simple reordering of the encoded bits, systematic bits are placed in the well protected positions of the complex signal constellation symbol while the parity bits are asymmetrically placed in the less protected positions.

The scheme is depicted in Fig. 5.2: With rate-1/3 coding data bits are encoded to become systematic bits \underline{v} with their corresponding parity bits \underline{p}_I and \underline{p}_{II} (cf. Fig. 4.4). In the standard LTE system these bits are sequentially read out of the ring buffer and mapped to the 6 bit positions of the 64QAM symbol resulting in complex modulation symbols that either consist

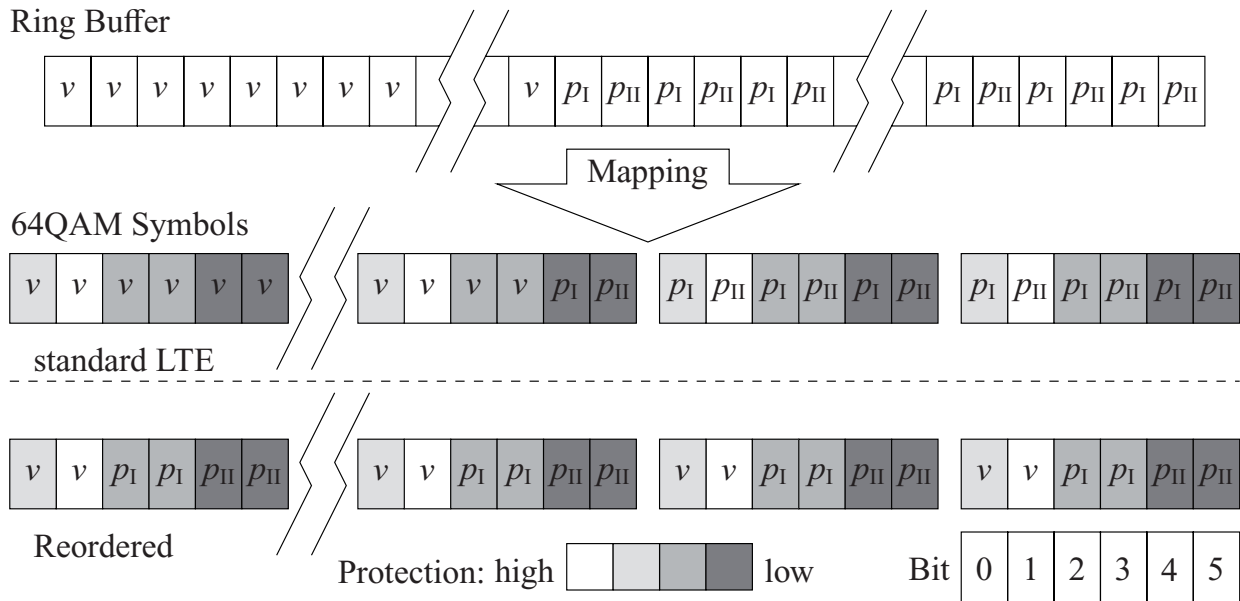


Figure 5.2: Standard LTE and reordered mapping of encoded bits to complex 64QAM symbols.

of 6 systematic bits v or of 6 parity bits p_I and p_{II} (with the possible exception of one symbol consisting of both types of bits). By reordering, the bits are mapped according to the levels of protection illustrated by Fig. 5.1: The systematic bits v are mapped to Bits 0 and 1 of the constellation symbol, the parity bits p_I of the first constituent encoder of the PCCC are mapped to Bits 2 and 3, respectively, leaving Bits 4 and 5 for the parity bits p_{II} of the second constituent encoder. In that way the systematic bits obtain the highest level of protection while the parity bits p_{II} are most error-prone.

5.1.2 Simulation Results

The impact of the modified mapping scheme for 64QAM is illustrated in Fig. 5.3 in terms of the average mutual information \mathcal{I} obtained by the systematic and parity bits of both constituent encoders. This is compared to the average mutual information of all coded bits as obtained for the standard LTE system.

Obviously, the weighted average of the mutual information obtained by the systematic and parity bits of the proposed scheme equals the average mutual information obtained by all bits in standard LTE. Furthermore, the average mutual information of p_I corresponds to the curves for Bit 2 and 3 of the 64QAM symbol while the average mutual information of p_{II} corresponds to the curves for Bit 4 and 5 (cf. Fig. 5.1). The quintessence in Fig. 5.3, however, is the significance of the unequal error protection of systematic bits v and parity bits p_I and p_{II} in this mapping scheme.

This fact is also illustrated by the EXIT characteristics of the two component channel decoders using a overall code rate of $cr = 1/3$ and 64QAM. Only the initial transmission (RV 0, cf. Sec. 4.2.3) is considered without retransmissions. The upper plots of Fig. 5.4 compare the characteristics of CD I and CD II obtained from simulations of the proposed system to

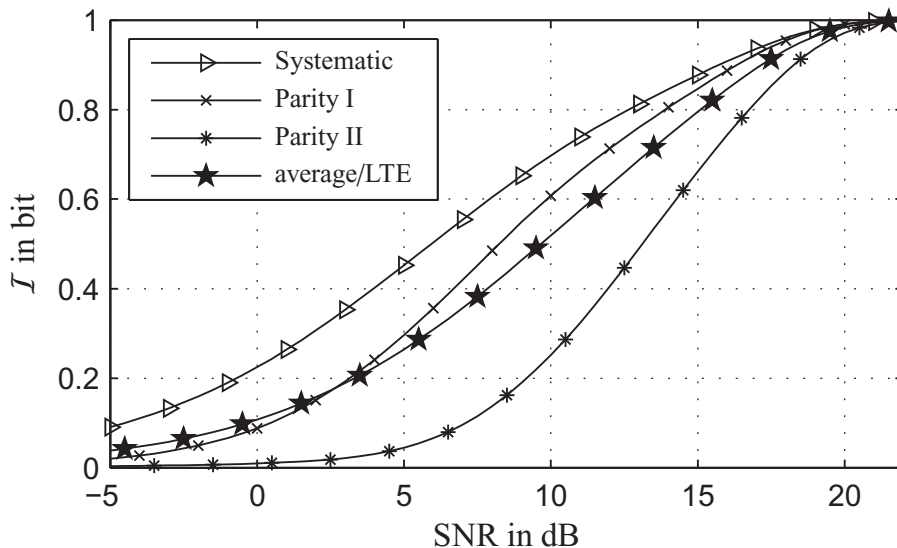
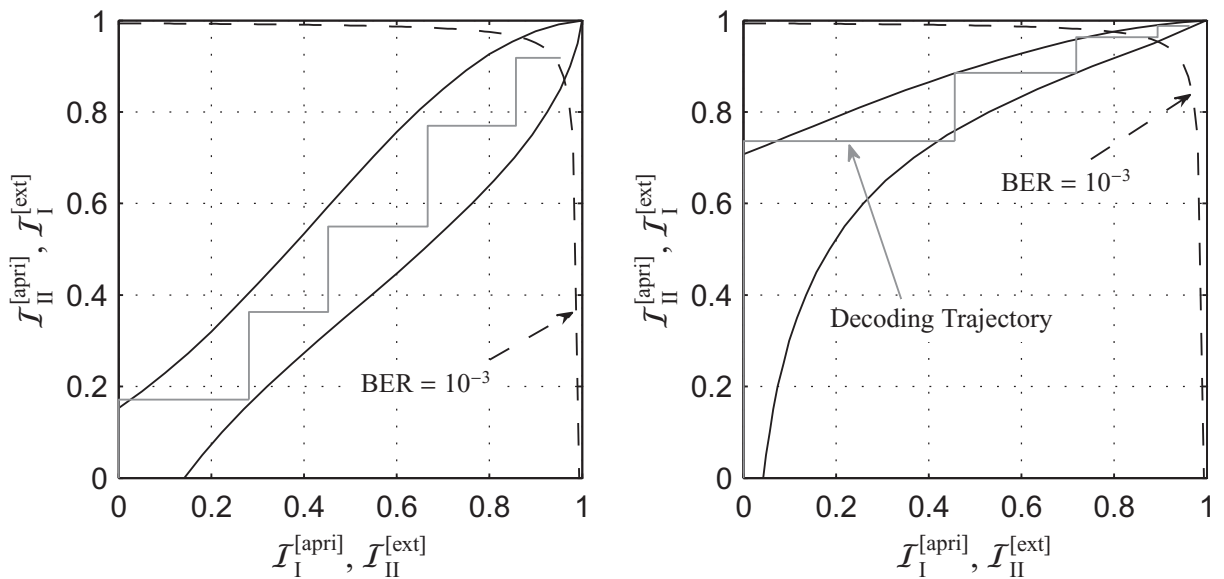
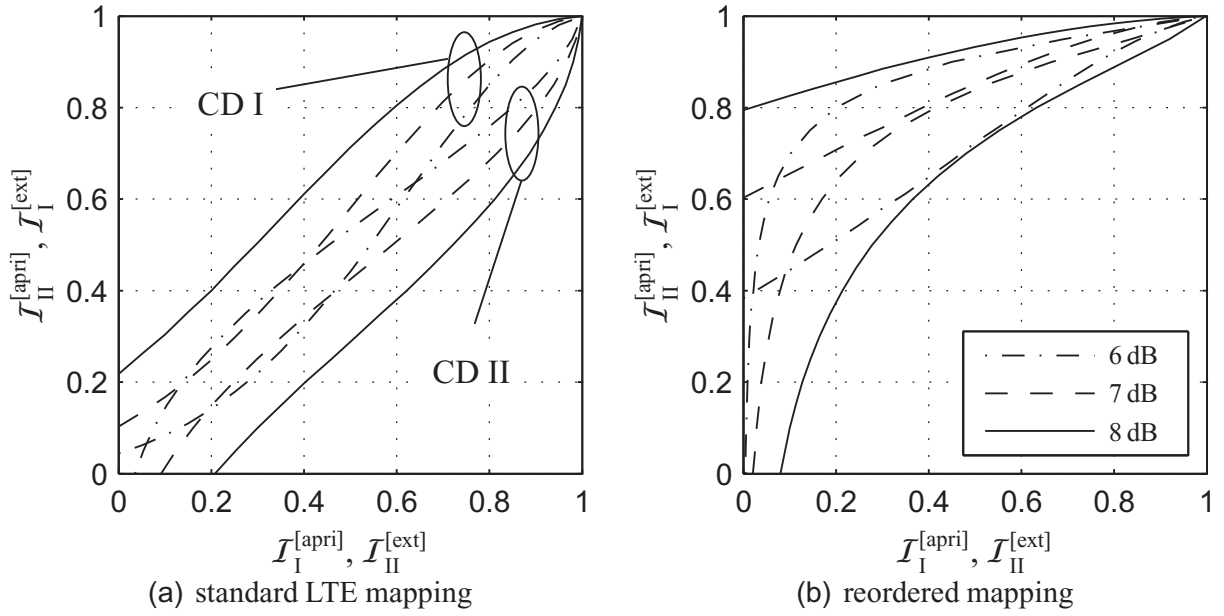


Figure 5.3: Average mutual information \mathcal{I} for systematic and parity bits with re-ordered mapping compared to the average mutual information for all transmitted bits in standard LTE versus channel quality.

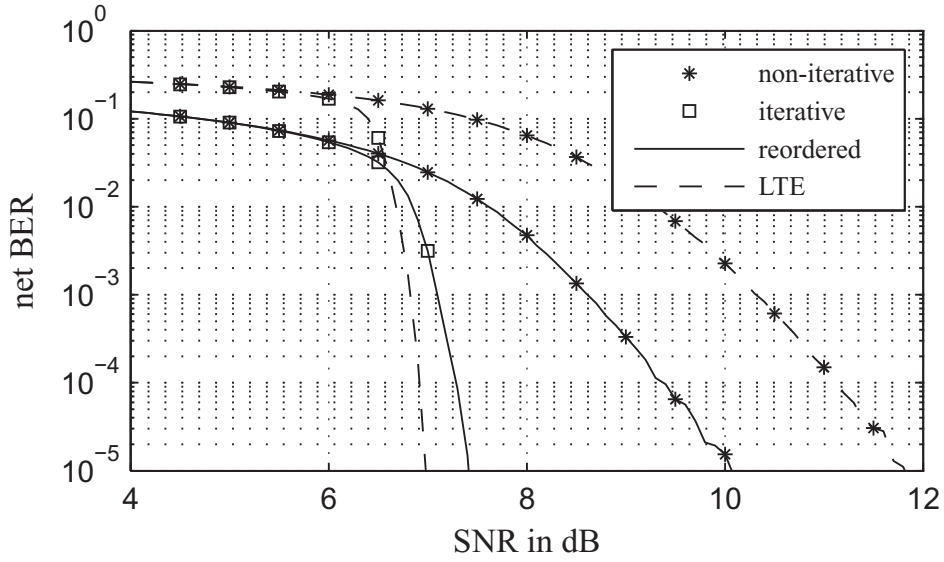
those obtained from simulations of standard LTE under different channel conditions. The difference is evident: While in the standard LTE case in Fig. 5.4(a) the EXIT characteristics of both SISO CDs show the expected symmetric behavior, the proposed reordering of bits leads to highly asymmetric characteristics, i.e., CD I and CD II yield different transfer functions leading to a different convergence behavior (cf. Fig. 5.4(b)). The higher protection of its parity bits \underline{p}_I enables CD I to produce a high amount of extrinsic information $\mathcal{I}_I^{[\text{ext}]}$ in the initial decoding step, i.e., for $\mathcal{I}_I^{[\text{apri}]} = 0$. Contrary, CD II suffers from its less protected parity bits \underline{p}_{II} which results in a poor performance, i.e., $\mathcal{I}_{II}^{[\text{ext}]}(\mathcal{I}_{II}^{[\text{apri}]} = 0)$ is rather low for the initial decoding step. However, this initial decoding step without a priori information is never executed by the second decoder in a parallel turbo decoding structure: CD II will always perform its first decoding step with a priori knowledge obtained from the initial decoding of CD I.

Recording and averaging the mutual information during simulations of both systems for $\text{SNR} = 7.5$ dB leads to the staircase-like decoding trajectories depicted by solid gray lines in the lower plots of Fig. 5.4. These trajectories confirm the above statements for the depicted case: As the trajectory of the system with reordered bit mapping in Fig. 5.4(d) reaches further to the right after the first complete turbo decoding iteration, i.e., the first stair step, compared to the standard LTE system in Fig. 5.4(c), a better BER performance for the non-iterative case can be predicted. Furthermore, while in case of standard LTE approximately 5 turbo decoding iterations are necessary to reach a residual bit error rate of 10^{-3} depicted by the dashed line in both plots, only 3 such iterations suffice in the modified system. This behavior points at a faster convergence speed of the system with reordered mapping. Note that no a superiority in terms of residual BER is claimed for either one of the systems after convergence.

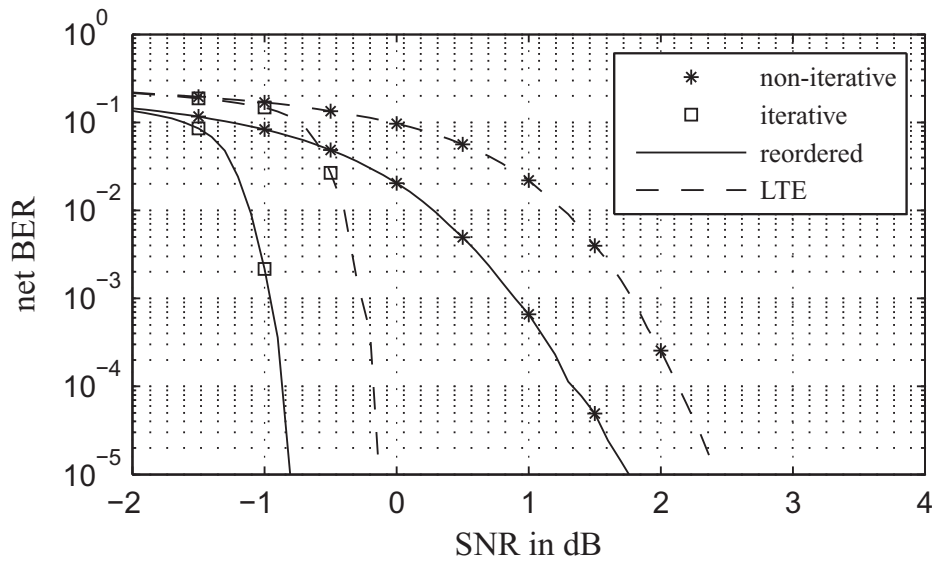


(c) standard LTE mapping, SNR = 7.5 dB: 5 iterations necessary (d) reordered mapping, SNR = 7.5 dB: only 3 iterations necessary

Figure 5.4: EXIT characteristics of the SISO component decoders for different channel qualities.



(a) RV 0



(b) RV 3

Figure 5.5: BER performance for standard LTE mapping and the proposed re-ordered mapping with non-iterative and iterative decoding, $l_v = 6144$ data bits.

Figure 5.5 compares the residual BER performance of the proposed reordered mapping scheme (dashed lines) to an standard LTE system (solid lines) for the initial transmission (RV 0, Fig. 5.5(a)) and for up to 3 retransmissions (RV 3, Fig. 5.5(b)). Furthermore, both plots illustrate the performance for the non-iterative case (one decoding step in each component decoder) and the iterative case with 10 Turbo iterations which has been found to lead to convergence in both considered systems. In the non-iterative case (*), the proposed mapping yields an SNR gain of approximately 2 dB over the standard LTE system for RV 0 and approximately 0.5 dB for RV 3. For iterative decoding (\square), the standard LTE system slightly outperforms the proposed scheme by 0.5 dB for the initial transmission RV 0. However, in case of retransmissions (RV 3) the proposed reordering provides a residual BER performance gain of approximately 0.7 dB.

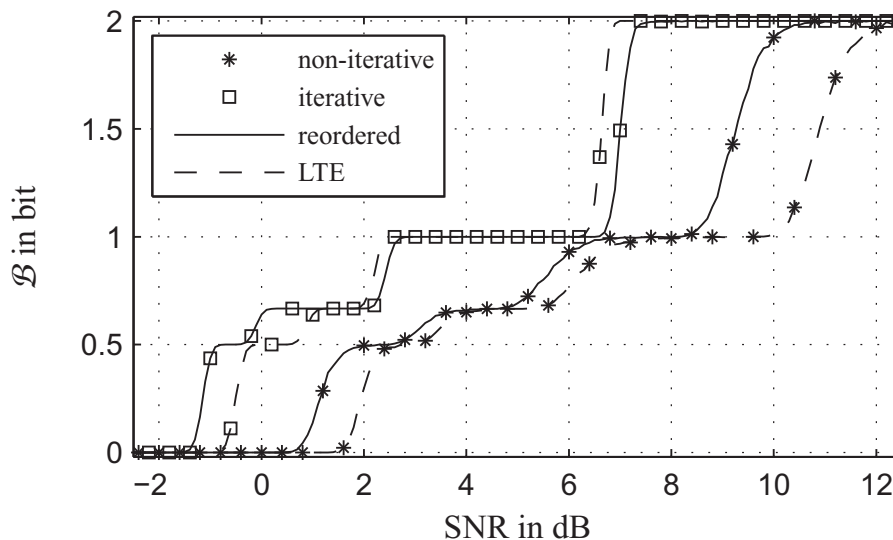


Figure 5.6: Achievable bits per channel use \mathcal{B} for standard LTE mapping and the proposed reordered mapping with non-iterative and iterative decoding.

Finally, Fig. 5.6 illustrates the achievable bits per channel use \mathcal{B} of the two systems considering 64QAM with rate-1/3 coding. It is observed that the proposed scheme outperforms standard LTE for all redundancy versions in case of the non-iterative decoding (*). In accordance with the findings of Fig. 5.5(a), standard LTE slightly outperforms the proposed reordering for the initial transmission and the first retransmission (RV 0 and RV 1) for iterative decoding (\square). For the second and third retransmission (RV 2 and RV 3), however, a SNR gain is achieved, leading to an increased performance for users with bad channel conditions.

5.2 BICM-ID with Repetition Coding

A different objective is the saving of computational complexity for channel encoding and decoding. A novel bit-interleaved coded modulation with iterative decoding (BICM-ID) scheme [62] based on simple repetition coding and complex symbol mapping with so-called *bit doping* [73, 76] is introduced and its performance is compared to UMTS LTE. It turns out

that for higher order modulation schemes (16QAM, 64QAM) a comparable performance is achieved while the algorithmic complexity is significantly lower [67].

5.2.1 System Model

To provide a fair comparison to the physical layer of UMTS LTE, the considered BICM-ID system features a similar transceiver structure sketched in Fig. 5.7. The binary input bit stream \underline{v} is segmented into data frames which are then protected by a 24 bit cyclic redundancy check. Instead of transmitting combinations of systematic and parity bits from a rate-1/3 turbo coder as in UMTS LTE (cf. Section 4.2.3), in this approach data bits are simply repeated at the same rate for channel coding. After repetition coding the coded frames \underline{x} of size l_x are interleaved by an S-random interleaver π and fed to the bit doping stage [73, 76]. This is a simple rate-1 memory-1 recursive convolutional code which periodically replaces single bits of the interleaved frame with coded bits at a period length P , the so-called *doping period*. The significant influence of this bit doping will be discussed in Sec. 5.2.3.

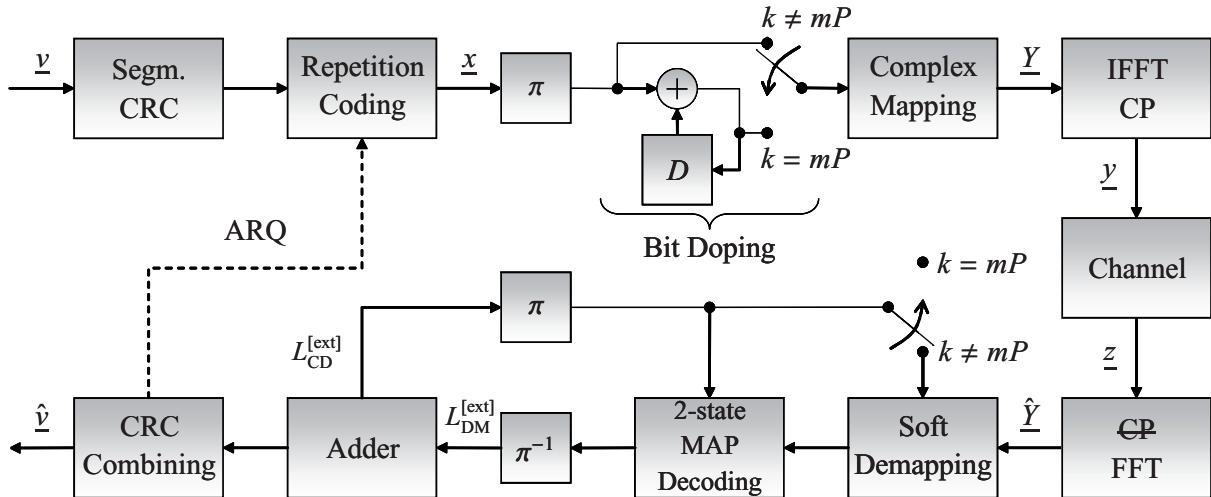


Figure 5.7: Baseband physical layer of the BICM-ID approach with bit doping.

As opposed to the Gray mapped signal constellation sets of UMTS LTE, constellations with mappings that are optimized for BICM-ID, i.e. QPSK and 64QAM with Anti-Gray mapping [92] and 16QAM with *Maximum Squared Euclidean Weight* (MSEW) mapping [80] are employed. The complex symbols \underline{Y} are then mapped to the resource elements of an OFDM modulator with a cyclic prefix equal to UMTS LTE forming a complex base band signal with averaged unit energy E_s per symbol.

After transmission over the channel and OFDM demodulation the complex symbols $\hat{\underline{Y}}$ are soft demapped resulting in L-values which are fed to a 2-state MAP decoder to revert the bit doping process. Deinterleaving is performed and the resulting L-values $L_{DM}^{[ext]}$ are fed to an adder that generates extrinsic information $L_{CD}^{[ext]}$ [42]. This extrinsic information is then interleaved and fed back to the 2-state MAP decoder and to the soft demapper. As no extrinsic information on the doped bits is available from the adder, $L_{CD}^{[ext]}$ is set to zero for those bits at time instances $k = m \cdot P$ with doping period P and $m \in \mathbb{N}$. After a fixed number

of iterations $n_{it}^{[REP]}$ an estimate of the data frame is passed to the CRC where in case of failure up to 3 retransmissions can be requested. Finally, the received data frames are combined to the output data frame \hat{v} .

5.2.2 Simulation Parameters and Results

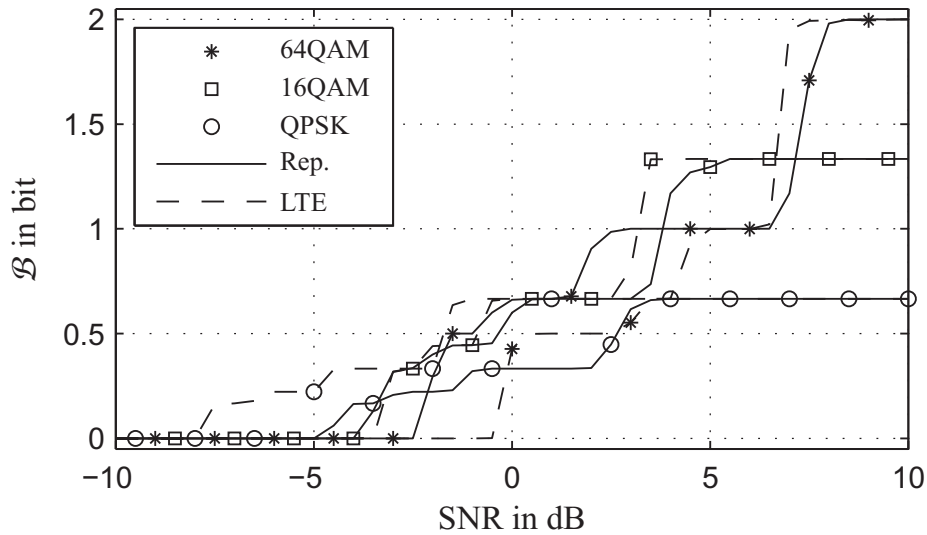


Figure 5.8: Bits per channel use \mathcal{B} for code rate $cr = 1/3$ and AWGN, $n_{it}^{[REP]} = 20$.

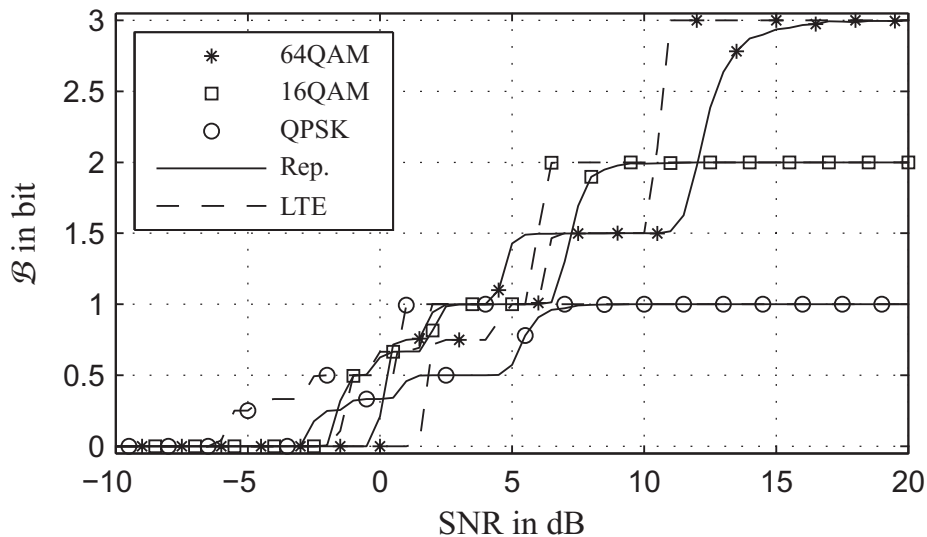


Figure 5.9: Bits per channel use \mathcal{B} for code rate $cr = 1/2$ and AWGN, $n_{it}^{[REP]} = 20$.

The same simulation parameters have been chosen for UMTS LTE and the BICM-ID approach to obtain a fair comparison. Since the data frame size is known to have a significant effect on the performance of iterative decoding, the maximum data frame size of $l_v = 6120$ is

chosen. Two effective code rates are selected: For $cr = 1/3$ the complete buffer is transmitted in the LTE case, while for BICM-ID the data frame is repeated twice resulting in the same code frame size. Accordingly, for $cr = 1/2$ the buffer of the LTE transmitter is punctured in compliance with the LTE standard, while the data is repeated only once for BICM-ID. A maximum number of $n_{Tr} = 4$ transmissions (3 retransmissions) per code frame is allowed, each retransmission reducing the effective code rate to $cr_{eff} = cr/n_{Tr}$ with $n_{Tr} \in \{1, 2, 3, 4\}$. The AWGN channel model and the Rayleigh channel model with block fading are used for performance evaluation. The LTE decoder executes $n_{it}^{[LTE]} = 10$ Turbo decoding iterations, while the BICM-ID system uses $n_{it}^{[REP]} = 20$ demodulation and decoding iterations. Both numbers have been observed to lead to convergence. Performance is measured in bits per channel use \mathcal{B} .

Figures 5.8 and 5.9 depict the performance of both systems achieved in an AWGN environment with initial code rates $cr = 1/3$ and $cr = 1/2$, respectively. It can be seen that for QPSK the proposed BICM-ID scheme is outperformed by standard LTE by up to 3 dB. For 16QAM, however, the performance loss is less than 1 dB and for 64QAM using $n_{Tr} > 1$ transmissions the proposed scheme even partially outperforms standard LTE despite its lower receiver complexity which is discussed in detail in Sec. 5.2.4.

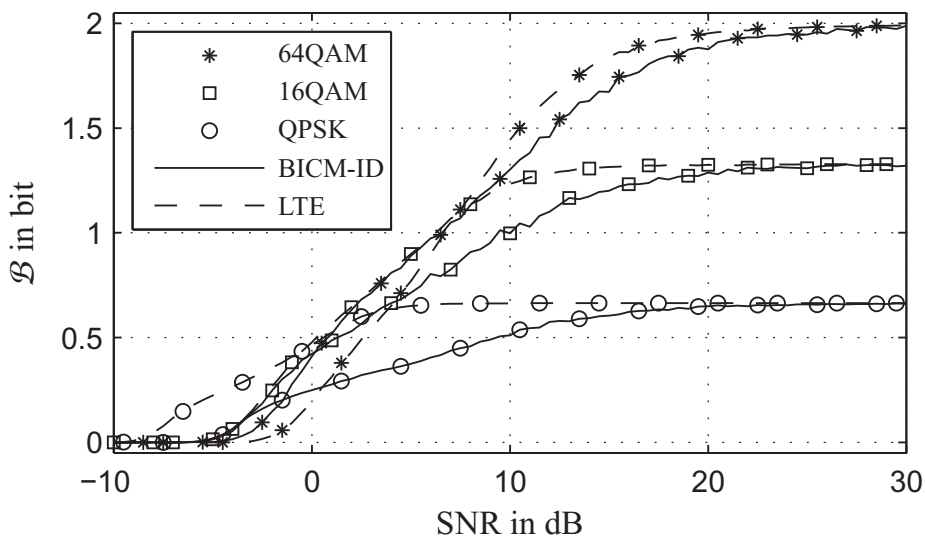


Figure 5.10: Bits per channel use \mathcal{B} for code rate $r = 1/3$ and Rayleigh channel, $n_{it}^{[REP]} = 20$.

Figures 5.10 and 5.11 depict the achieved \mathcal{B} in case of the Rayleigh fading channel for both employed code rates $cr = 1/3$ and $cr = 1/2$, respectively. Surprisingly, the performance of the BICM-ID approach with 64QAM outperforms the other SCSs and performs fairly close to the LTE system for 64QAM and 16QAM without the need of adapting coding or mapping scheme.

The performance depicted in Fig. 5.12 provides a notion of the influence of the number of demapping and decoding iterations $n_{it}^{[REP]}$ executed in the proposed BICM-ID receiver. It can be seen that decreasing the number of iterations in the BICM-ID system to

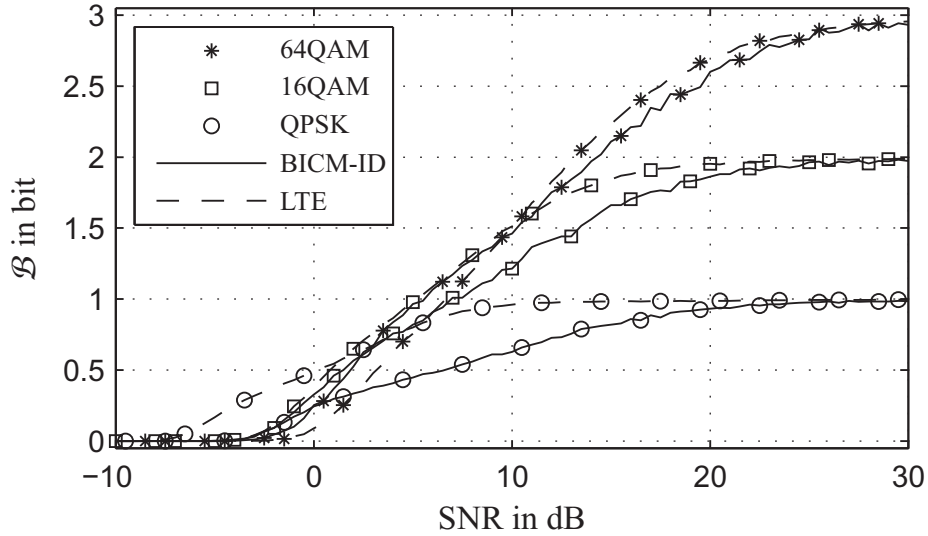


Figure 5.11: Bits per channel use \mathcal{B} for code rate $r = 1/2$ and Rayleigh channel, $n_{it}^{[REP]} = 20$.

$n_{it}^{[REP]} = n_{it}^{[LTE]} = 10$ leads to a performance degradation of 0.5 to 1.0 dB.

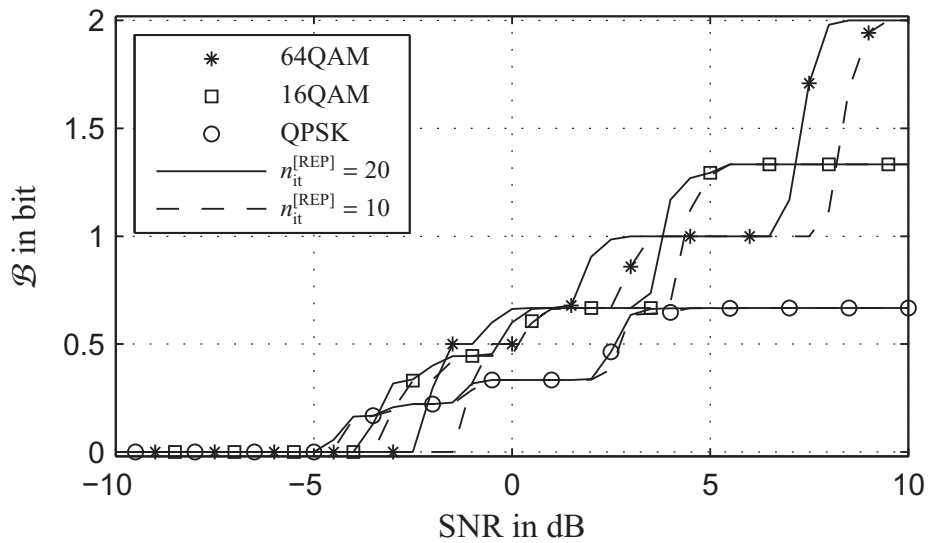


Figure 5.12: Performance comparison for different $n_{it}^{[REP]}$ of the proposed BICM-ID system for code rate $r = \frac{1}{2}$ and AWGN.

5.2.3 EXIT Analysis

Figure 5.13 depicts an EXIT chart for the BICM-ID system with rate-1/3 coding and AWGN for 16QAM. The dashed black lines correspond to the EXIT characteristic of the repetition decoder, i.e., the adder (cf. Fig. 5.7), for n_{Tr} transmissions with $n_{Tr} \in \{1, 2, 3, 4\}$, while the

solid curves represent the SDM characteristics for different channel qualities including bit doping.

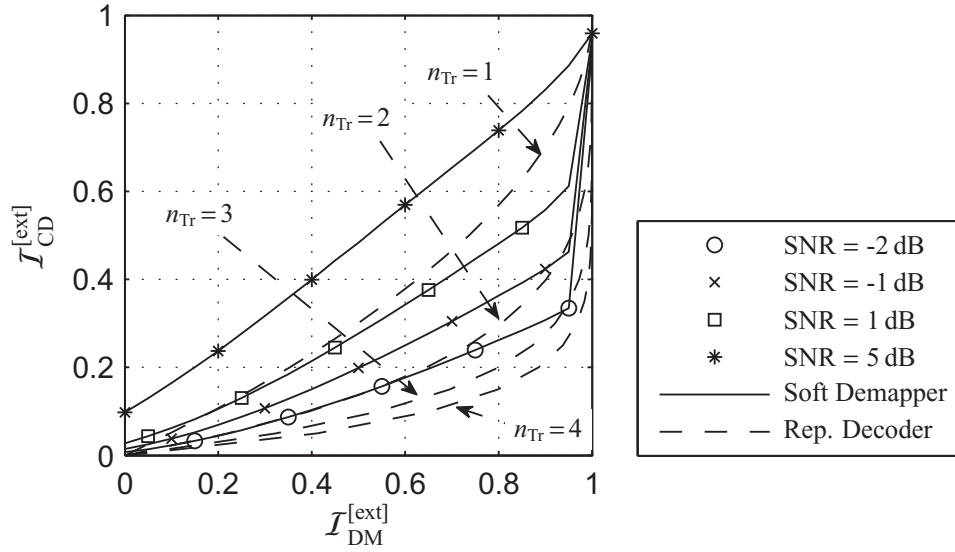


Figure 5.13: EXIT chart of proposed BICM-ID system for code rate $r = 1/3$ and 16QAM.

The effect of bit doping is clearly visible: While the slope of the SDM characteristics is quite moderate for low and medium amounts of a priori information, it is increased for high amounts of fed back a priori information, thus heavily bending the SDM characteristic toward high amounts of extrinsic information. Figure 5.13 reflects the performance of the BICM-ID system depicted in Fig. 5.8: The first plateau for 16QAM (medium gray line in Fig. 5.8) is reached at SNR ≈ -2 dB, when a tunnel opens in Fig. 5.13 between the decoder characteristic for the 4th transmission and the SDM characteristic at -2 dB (\circ) the same holds for the other plateaus starting at channel qualities of -1 dB (\times), 1 dB (\square), and 5 dB ($*$), respectively. For all these channel qualities a decoding tunnel exists in the EXIT chart in Fig. 5.13 between the decoder characteristics of the 3rd, 2nd, and 1st transmission and the SDM characteristic of the corresponding channel quality.

5.2.4 Algorithmic Complexity

The complexity is evaluated for the receiver which provides the major part of the complexity reduction. For evaluating the MaxlogMAP algorithm complexity [75] the number of additions (ADD) and so-called max*-operations executed per data bit and iteration is evaluated. max*-operations are used to add probabilities in the logarithmic domain and consist of three operations: a max-operation, a table look-up and an addition. Both numbers depend on the code rate $r^{[cc]}$ of the constituent code and on the number of trellis states S . The number of ADD operations n_{ADD} and max*-operations n_{max^*} are given as:

$$n_{\text{ADD}} = 8S + \frac{1}{r^{[cc]}} 2^{\frac{1}{r^{[cc]}}}, \quad n_{\text{max}^*} = 4S. \quad (5.1)$$

In the LTE receiver two MaxlogMAP algorithms with $S^{[\text{LTE}]} = 8$ states and $r^{[\text{cc,LTE}]} = 1/2$ are executed, while the BICM-ID system with repetition coding uses code rate $r^{[\text{cc,REP}]} = 1$ for convolutional coding and a trellis with $S^{[\text{REP}]} = 2$ states. However, while LTE executes the MaxlogMAP algorithm on the data frame of length l_v , the MaxlogMAP decoder of BICM-ID receiver uses the coded bit frames \hat{x} as input. Their length is determined by the code rate of the complete system $l_x = l_v/\text{cr}$. Additionally, LTE and BICM-ID receiver run different numbers of Turbo iterations $n_{\text{it}}^{[\text{LTE}]}$ and $n_{\text{it}}^{[\text{REP}]}$, respectively. Therefore, considering the same data frame size l_v for both systems, the ratios of the two performance measures from (5.1) of the two considered systems are given by:

$$\frac{n_{\text{ADD}}^{[\text{REP}]}}{n_{\text{ADD}}^{[\text{LTE}]}} = \frac{n_{\text{max}^*}^{[\text{REP}]}}{n_{\text{max}^*}^{[\text{LTE}]}} = \frac{n_{\text{it}}^{[\text{REP}]}}{8\text{cr}n_{\text{it}}^{[\text{LTE}]}}. \quad (5.2)$$

For the exemplary scenario depicted in Figs. 5.9 and 5.11 with $\text{cr} = 1/2$, $n_{\text{it}}^{[\text{REP}]} = 20$, and $n_{\text{it}}^{[\text{LTE}]} = 10$ the number of additions and max*-operations in the MaxlogMAP decoder can accordingly be reduced by 50 %.

Additionally, the BICM-ID receiver uses an adder for decoding, executing $(1/\text{cr} - 1)$ additions per bit and iteration for the repetition rate, i.e., coding rate cr . The soft demapper has to calculate extrinsic information for each coded bit in each iteration, which would lead to an additional number of $2^I - 2$ additions with $I \in \{2, 4, 6\}$ representing the corresponding SCS size. However, the complexity of the SDM can be reduced vastly by reducing the number of transition probabilities considering only the nearest neighbors in a given signal constellation. This modification only marginally decreases the performance of the SDM. A further complexity reduction for both systems is obviously obtained when a proper stopping criterion for the iterative processes is used, e.g., based on the CRC, instead of a fixed number of iterations.

5.3 EXIT optimized BICM-ID

As the energy consumption of iterative schemes increases linearly with the number of iterations, iterative processing of soft information is always more complex and thereby more energy consuming than non-iterative hard decided demodulation, channel decoding and source decoding. As already pointed out, analysis of the EXIT characteristics is an easy way of estimating the number of necessary decoding/demodulation iterations using knowledge of components of the transmission system and of the channel. In [82] it has been shown that the EXIT characteristic of the soft demodulator (SDM) depends on the channel characteristics. In case of a flat fading AWGN channel, the characteristics depend on the channel signal-to-noise ratio (SNR) – a fact, which has already been illustrated by the above EXIT analysis of the BICM-ID scheme (Fig. 5.13). The assumption of a flat fading AWGN channel is not valid when analyzing broadband mobile communication systems with doubly selective channels. These variations of the channel result in steady variations of the SDM characteristics which can hardly be predicted. This section suggests a simple novel approach to approximate

EXIT characteristics of an SDM used in an OFDM BICM-ID system with doubly selective fading by channel dependent weighted summation of SDM characteristics drawn from a limited set of SDM characteristics recorded from AWGN simulations. If such a limited set of AWGN SDM characteristics is present at the receiver together with the channel state information (CSI) (cf. Sec. 4.1), the convergence behavior of the BICM-ID process can be predicted and the number of necessary iterations can be estimated. Furthermore, if the CSI is slowly varying (block fading) and fed back to the transmitter, EXIT-optimized resource allocation becomes possible by assigning signal constellation sets (contingently *non-regular signal constellation sets* [37, 34]), symbol mappings μ , and transmit powers individually per subcarrier [68].

To illustrate the concept of system optimization by weighted summation of SDM characteristics, a simplified BICM-ID transceiver is considered which is depicted in Fig. 5.14. The main difference compared to the structure considered in Sec. 5.2 is the use of a convolutional code instead of a repetition code. Furthermore the bit doping stage is omitted as it is not necessary for the utilized channel coder. The goal of the optimization is to minimize the residual BER according to (3.5), therefore no repeat request structure is implemented.

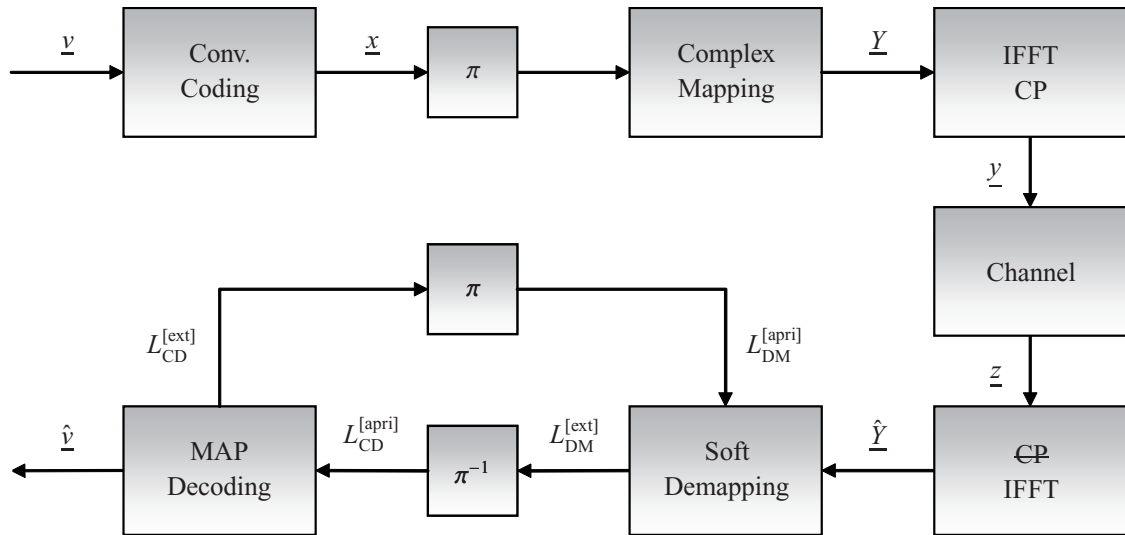


Figure 5.14: Simple OFDM BICM-ID transmission system.

5.3.1 SDM EXIT Characteristics

The generation of the characteristics of extrinsic information transfer by simulation is described in [82]. For the given OFDM BICM-ID system the convergence behavior of the iterative demapping and decoding process depends on the characteristics of the soft demapper (SDM) and of the channel decoder (CD). While the CD characteristic $\mathcal{I}_{CD}^{[ext]} = \mathcal{T}_{CD}(\mathcal{I}_{CD}^{[apri]})$ is fixed, the soft demapper (SDM) characteristic $\mathcal{I}_{DM}^{[ext]} = \mathcal{T}_{DM}(\mathcal{I}_{DM}^{[apri]})$ depends on the current channel state. In case of AWGN it depends on the noise power σ_n^2 of the noise process \underline{n} , i.e.,

$$\mathcal{I}_{DM}^{[ext]} = \mathcal{T}_{DM}(\mathcal{I}_{DM}^{[apri]}, \sigma_n^2) := \mathcal{T}_{DM,n}. \quad (5.3)$$

For an AWGN channel the SDM characteristic in (5.3) can be obtained from simulations for different values of σ_n^2 . In the same way it is also possible to obtain the transfer characteristic $\mathcal{I}_{\text{DM}}^{\text{[ext]}} = \mathcal{T}_{\text{DM}}(\mathcal{I}_{\text{DM}}^{\text{[apri]}})$ of SDMs for different kinds of channels like Rayleigh fading channels. The only prerequisite is that the distribution of the a priori information $\mathcal{I}_{\text{DM}}^{\text{[apri]}}$ has to be Gaussian. If that is not the case, the simulated values $\mathcal{I}_{\text{DM}}^{\text{[apri]}}$ have to be adapted according to the given distribution (see, e.g., [71]).

As seen in Sec. 4.1 the complex channel impulse response $\underline{h}(k)$ is time variant due to Doppler induced fast fading effects. Recording EXIT characteristics of the soft demodulator would consequently result in a different characteristic for each realization and channel noise power which results in high computational effort as the number of possible channel realizations may be extremely large, depending on the number of taps and distributions of the complex fading coefficients h . Moreover, regarding a mobile receiver that tries to estimate the number of necessary demodulation and decoding iterations, the characteristics need to be known in advance and thus have to be stored in the memory of the receiver which is hardly implementable nor reasonable.

A first approximation is picking the characteristic $\mathcal{T}_{\text{DM},n}$ for each transmitted data frame \underline{y} with the corresponding noise power σ_n^2 from a set of stored EXIT characteristics recorded beforehand from AWGN simulations. This, of course, ignores the impact of the frequency selective channel which results in an overestimation of the capability of the SDM.

Due to the ability of OFDM to split up the bandwidth of a broadband frequency selective transmission channel into narrow band flat fading channels, the received symbols $\hat{Y}^{(i)}$ with $i \in 0 \dots n_{\text{SC}} - 1$ after zero-forcing equalization can be regarded as outputs of n_{SC} independent AWGN channels with different (though correlated) noise powers $\sigma_{n,i}^2$. Via the theoretical maximum capacity of each subcarrier and the resulting overall capacity from (4.24) it is easy to show that an equivalent noise power $\bar{\sigma}_n^2$ can be calculated with the help of the individual noise powers of each subcarrier $\sigma_{n,i}^2$, assuming unity signal powers $E_s = 1$ on all subcarriers:

$$\begin{aligned} \log_2 \left(1 + \frac{1}{\bar{\sigma}_n^2} \right) &= \frac{1}{n_{\text{SC}}} \sum_{i=0}^{n_{\text{SC}}-1} \log_2 \left(1 + \frac{1}{\sigma_{n,i}^2} \right) \\ \Rightarrow \bar{\sigma}_n^2 &= \left[\prod_{i=0}^{n_{\text{SC}}-1} \left(1 + \frac{1}{\sigma_{n,i}^2} \right)^{1/n_{\text{SC}}} - 1 \right]^{-1}. \end{aligned} \quad (5.4)$$

Using (4.22) the individual noise powers $\sigma_{n,i}^2$ are obtained by

$$\text{E} \left\{ \left(\frac{N^{(i)}}{H^{(i)}} \right)^2 \right\} = \sigma_{n,i}^2 = \frac{\sigma_n^2}{|H^{(i)}|^2}. \quad (5.5)$$

Using (5.4) and (5.5) SDM characteristics $\mathcal{T}_{\text{DM},\bar{n}}$ obtained from AWGN simulations can approximate the ISI SDM characteristic of an OFDM BICM-ID system. However, this approximated SDM characteristic $\mathcal{T}_{\text{DM},\bar{n}}$ is still not congruent with the SDM characteristic directly recorded for a certain realization \underline{h} of the ISI channel at time instant k .

Therefore a method is utilized which is similar to the generation of EXIT characteristics of decoders for irregular codes by weighted superposition as employed, e.g., in [86, 23]. Using the assumption of flat fading AWGN channels for each subcarrier i and a block fading channel with time-invariant channel impulse response \underline{h} for the duration of one OFDM symbol (block fading channel), it is possible to calculate the noise powers $\sigma_{n,i}^2$ as described above. For each subcarrier i there exists an SDM characteristic $\mathcal{T}_{\text{DM},n,i} := \mathcal{T}(\mathcal{I}_{\text{DM}}^{[\text{apri}]}, \sigma_{n,i}^2)$ which can be easily recorded in AWGN simulations. A very good approximation of the SDM characteristic of the multi-carrier system is now obtained by weighted summation of the AWGN SDM characteristics $\mathcal{T}_{\text{DM},n,i}$ according to their occurrence for the arbitrary but known CIR \underline{h} :

$$\mathcal{T}(\mathcal{I}_{\text{DM}}^{[\text{apri}]}, \underline{h}) = \frac{1}{n_{\text{SC}}} \sum_{i=0}^{n_{\text{SC}}-1} \mathcal{T}_{\text{DM},n,i},$$

which using (5.5) can be written as

$$\mathcal{T}(\mathcal{I}_{\text{DM}}^{[\text{apri}]}, \underline{h}) = \frac{1}{n_{\text{SC}}} \sum_{i=0}^{n_{\text{SC}}-1} \mathcal{T}\left(\mathcal{I}_{\text{DM}}^{[\text{apri}]}, \frac{\sigma_n^2}{|H^{(i)}|^2}\right). \quad (5.6)$$

So far one fixed signal constellation set (SCS) with a certain mapping μ has been considered. For single carrier modulation it is known [82] that different mapping rules μ and non-uniform SCSs \mathcal{Y} [37, 34] can improve the performance of BICM-ID systems. In the case of OFDM, carrier-wise allocation of different types of mappings and/or transmit powers is used to optimize the goodput. The extension of the described method to systems using different mappings, SCSs and transmit powers per subcarrier is straight forward: Instead of using one set of AWGN SDM trajectories $\mathcal{T}_{\text{DM},n}$ for different noise powers and a constant complex mapping, for each kind of mapping a different set of SDM characteristics has to be recorded under AWGN conditions. The weighted summation has then to take into account the possibly different numbers of bits I per subcarrier.

If the CIR is changing slowly enough in time and therefore can be fed back to the transmitter sufficiently accurate, it is also possible to predict the convergence behavior of the transmission of one data block for a certain allocation of different modulation types and transmit powers to single subcarriers. In this case, optimization of the allocation with respect to the ISI channel becomes possible.

5.3.2 Simulation Results

In order to evaluate the performance of the employed system and to show the applicability of the suggested method of weighted summation of AWGN SDM characteristics, computer simulations have been executed with the following parameters: The frame size of \underline{v} is set to 10000, and a rate 1/2 feed-forward convolutional encoder with zero termination, constraint length 4, and octal generator polynomials $G_0 = \{17\}_8$ and $G_1 = \{15\}_8$ is chosen for channel coding. The utilized SCS is 8PSK with $I = 3$ bits and Gray mapping, set partitioning (SP),

or semi-set partitioning (SSP) [62] as mapping rule μ . The number of subcarriers is set to $n_{\text{SC}} = 256$. For better reproducibility of the results, the ISI channel in all simulations is exemplarily chosen as time invariant real FIR with fixed CIR

$$\underline{h} \sim [1.0, 0.0, 0.5, 0.2, 0.1]. \quad (5.7)$$

Consequently the length of the cyclic prefix is set to $l_{\text{CP}} = 4$.

SDM Characteristics for ISI Channels Figure 5.15 depicts the convergence analysis for the BICM-ID OFDM system using SSP mapping at $\text{SNR} = 6$ dB with ISI channel CIR according to (5.7). The dashed line illustrates the characteristic of the channel decoder, the solid gray line is the decoding trajectory of the iterative demapping and decoding process, which approaches the point $\mathcal{I}_{\text{DM}}^{[\text{apri}]} = 1$ very closely. Regarding the BER performance, that means an error-floor is reached as $\mathcal{I}_{\text{DM}}^{[\text{ext}]} = \mathcal{T}(\mathcal{I}_{\text{DM}}^{[\text{apri}]} \approx 1) < 1$, so no error-free decoding will be possible.

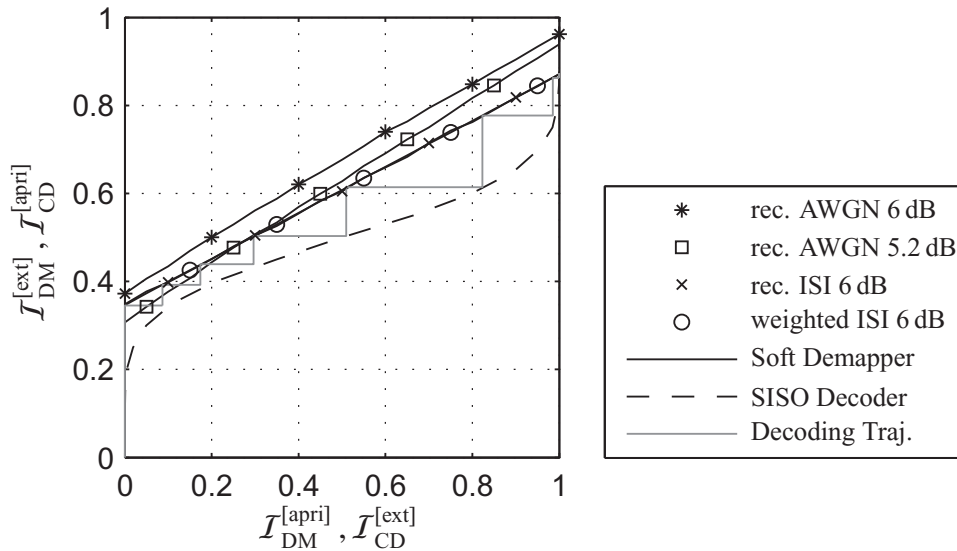


Figure 5.15: Comparison of different SDM characteristics using 8PSK with SSP for exemplary CIR \underline{h} according to (5.7).

The marked lines in Fig. 5.15 represent different approximations ($*$, \square , \circ) and the actual recording (\times) of the SDM characteristic $\mathcal{T}_{\text{DM},n}$ for the corresponding channel noise power. As predicted, neglecting of the influence of the ISI channel ($*$) results in an overestimation of the capability of the SDM: the decoding trajectory falls short of the approximated SDM characteristic recorded with 6 dB AWGN. The second approximation which is the SDM characteristic recorded under AWGN conditions with $\overline{\sigma}_n^2 \hat{=} -5.2$ dB (\square), first underestimates the capability by suggesting a narrow tunnel for $\mathcal{I}_{\text{DM}}^{[\text{apri}]} < 0.3$: The decoding trajectory overshoots the characteristic in this region. For $\mathcal{I}_{\text{DM}}^{[\text{apri}]} > 0.3$, however, the approximated SDM characteristic overestimates the capability of the SDM suggesting a lower error-floor than the one reached in the simulation.

The most exact approximation of the SDM characteristic in Fig. 5.15 is delivered by the suggested weighted summation of AWGN SDM characteristics (\circ) which is congruent with the characteristic recorded in an ISI simulation (\times). The decoding trajectory is exactly upper bounded by this characteristic. It becomes possible to predict the convergence of the system after seven demodulation and decoding iterations by counting the number of stair steps of the decoding trajectory.

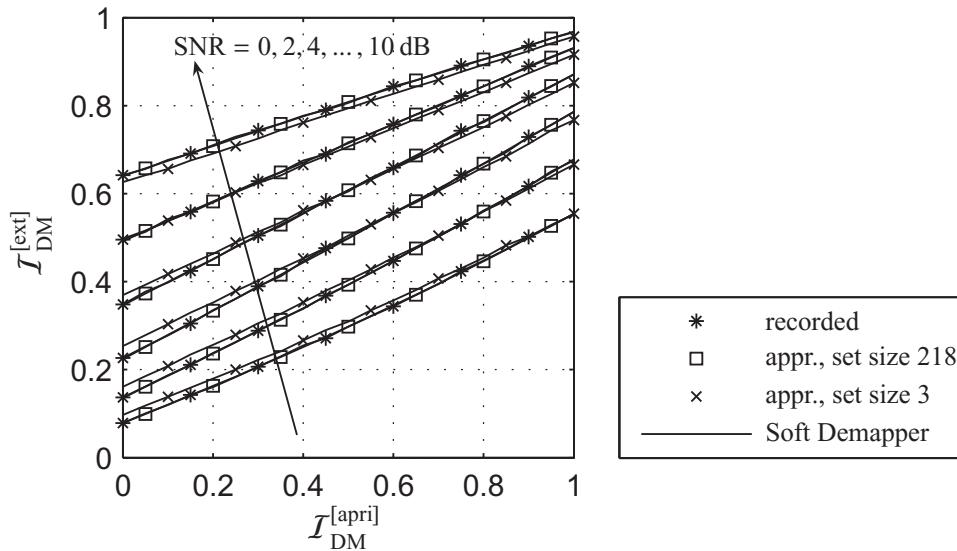


Figure 5.16: Comparison of weighted and measured SDM characteristics: 8PSK SSP, exemplary CIR \underline{h} according to (5.7).

Figure 5.16 depicts SDM characteristics using 8PSK SSP mappings for different noise powers recorded directly from simulations under ISI conditions ($*$) with \underline{h} according to (5.7). These measured SDMs are compared to SDMs approximated by weighted summation (\square , \times). Two different sizes of AWGN SDM characteristic sets were used. For the exemplary CIR \underline{h} the difference between AWGN noise power σ_n^2 and resulting noise power on the subcarriers $\sigma_{n,i}^2$ is between -7.7 dB and 4 dB. These figures in combination with the considered SNR values in the range of 0 dB to 10 dB demand for AWGN SDM characteristics recorded in simulations with noise powers between -7.7 dB and 14 dB. For the first approximation (solid lines in Fig. 5.16) the resolution for the AWGN simulations was set to $\Delta\sigma_n^2 = 0.1$ dB leading to a set of $(14 + 7.7) \cdot 10 + 1 = 218$ AWGN SDM characteristics each with 21 positions ($J_{DM}^{[apri]} = 0, 0.05, 0.1, \dots, 1$). This set size leads to a high degree of congruence of the recorded and approximated SDM characteristics. The mean deviation between the recorded and the approximated SDM characteristics averaged over all points of the characteristics for all channel qualities is observed to be around 0.0015 bit which is expected to be in the range of the statistical error of directly recording an SDM characteristic.

The dashed lines in Fig. 5.16 show the approximated SDM characteristics using a set of only three AWGN SDM characteristics per SNR value resulting in a set size of $3 \cdot 6 = 18$ for the six given channel qualities. For each channel quality the set contains the AWGN SDM characteristics for the corresponding minimum subcarrier SNR σ_{\min}^2 , maximum subcarrier

SNR σ_{\max}^2 , and their mean. Comparing these SDM characteristics to the recorded ones reveals higher deviations. The average deviation of the SDM characteristic is slightly above 0.01 Bit for the considered case.

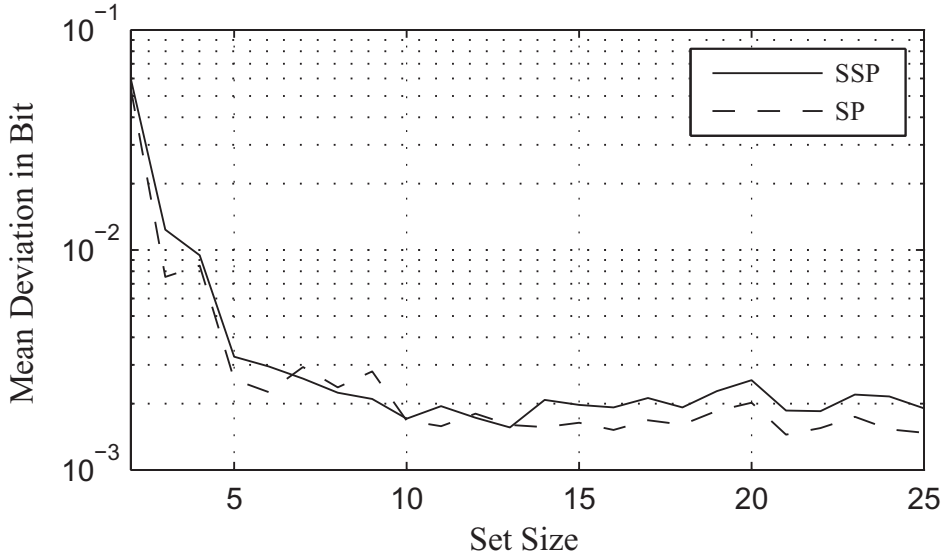


Figure 5.17: Mean deviation between weighted and measured SDM characteristics: 8PSK, SP and SSP, exemplary CIR \underline{h} according to (5.7).

Figure 5.17 shows the mean deviations observed for different set sizes optimized for SNR = 4 dB and the given CIR \underline{h} , i.e., sets containing AWGN SDM characteristics for the corresponding σ_{\min}^2 , σ_{\max}^2 and uniformly distributed values in-between. The deviations for other channel qualities yield similar figures and progressions. For this example, a set of only five AWGN SDM characteristics per expected SNR seems to be sufficient for a very accurate approximation of the ISI SDM characteristics for the chosen CIR. It can be seen that the mean deviation using a set of five AWGN SDM characteristics is approximately the same as for the earlier mentioned set of 218 AWGN SDM characteristics with $\Delta\sigma_n^2 = 0.1$ dB. These findings can also be interpreted as a relaxation of the previously demanded prerequisite of perfect CSI: Also a coarsely quantized estimate of the expected noise power $\sigma_{n,i}^2$ per sub-carrier seems to be sufficient for a satisfactorily accurate estimate of the corresponding ISI SDM characteristic.

Fig. 5.18 shows a possible application in the transmitter. In this example the SDM characteristic for 8PSK with SSP (\square) and with Gray mapping ($*$) for a channel quality of SNR = 5 dB is considered. The difference between the mappings is obvious and well known: While for Gray mapping the information gain for $\mathcal{I}_{\text{DM}}^{\text{[apri]}} = 0$ is relatively high as compared to SSP the possible information gain for good a priori knowledge ($\mathcal{I}_{\text{DM}}^{\text{[apri]}} \approx 1$) for Gray falls far behind the possibilities of SSP. Consequently, the SDM characteristic using SSP intersects very early with the SISO characteristic (dashed line) preventing BER gains after more than 3 iterations. With Gray mapping on the other hand the SDM will not be able to generate extrinsic information $\mathcal{I}_{\text{DM}}^{\text{[apri]}} > 0.7$ bit resulting in a high error-floor.

With CIR and SNR known at the transmitter, it is possible to design an SDM characteris-

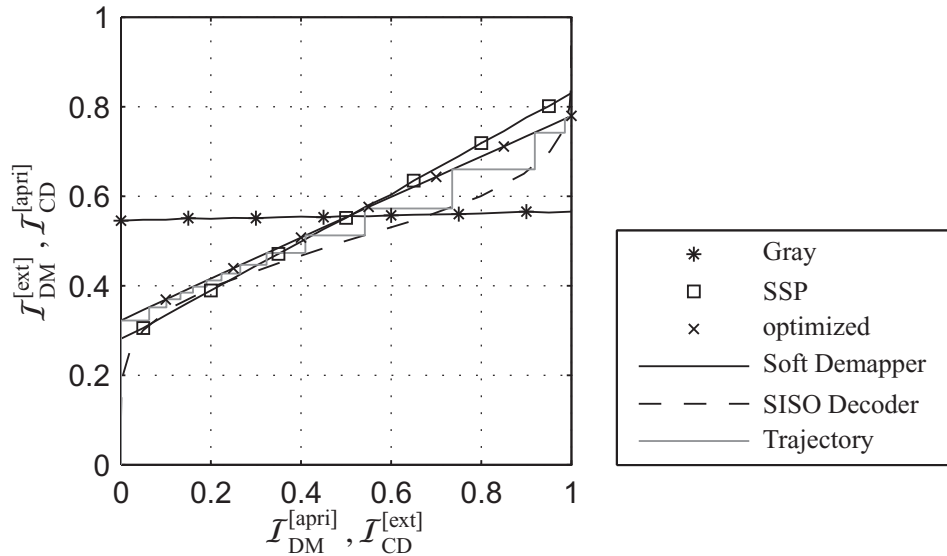


Figure 5.18: EXIT optimized construction of SDM characteristic using Gray and SSP mappings, \underline{h} according to (5.7).

tic which yields a decoding tunnel and enables the SDM to generate a maximum amount of extrinsic information that allows for a good BER performance (low error-floor) after SISO decoding. Such an SDM characteristic can easily be constructed by weighted superposition of AWGN SDM characteristics of both kinds of mapping. In the depicted example this is achieved by choosing an threshold σ_{thresh}^2 and assigning Gray mapped 8PSK to subcarriers with $\sigma_{n,i}^2 \leq \sigma_{\text{thresh}}^2$ while assigning 8PSK with SSP mapping to subcarriers with $\sigma_{n,i}^2 > \sigma_{\text{thresh}}^2$. The resulting SDM characteristic (\times) obtained for $1/\sigma_{\text{thresh}}^2 \hat{=} 0$ dB predicts a narrow decoding tunnel and the possibility to generate a large amount of extrinsic information which enables the SISO decoder to decode at a BER with low error-floor after a limited number of demodulation and decoding iterations.

BER Performance of OFDM BICM-ID The bit error rate performance of the system with the above described ISI channel with known CIR \underline{h} is depicted in Fig. 5.19 for SP and SSP as mapping rules μ . As expected for SP the BER waterfall region (or Turbo cliff) starts at low channel qualities SNR > 4 dB ending in a high error-floor. The waterfall region for SSP on the other hand starts at higher channel qualities SNR > 5.5 dB but leads to a lower error-floor, indicating the known superior convergence behavior of SSP in better channel conditions [62]. The subcarrier-wise mapping of mapping rules SSP and Gray optimized for SNR = 5 dB exhibits the expected behavior: The waterfall region starts at SNR = 5 dB and ends in an error-floor between those of SSP and SP, indicating the necessary trade-off between iterative gain at low SNRs (early waterfall) and error-floor after convergence (net BER at high SNRs).

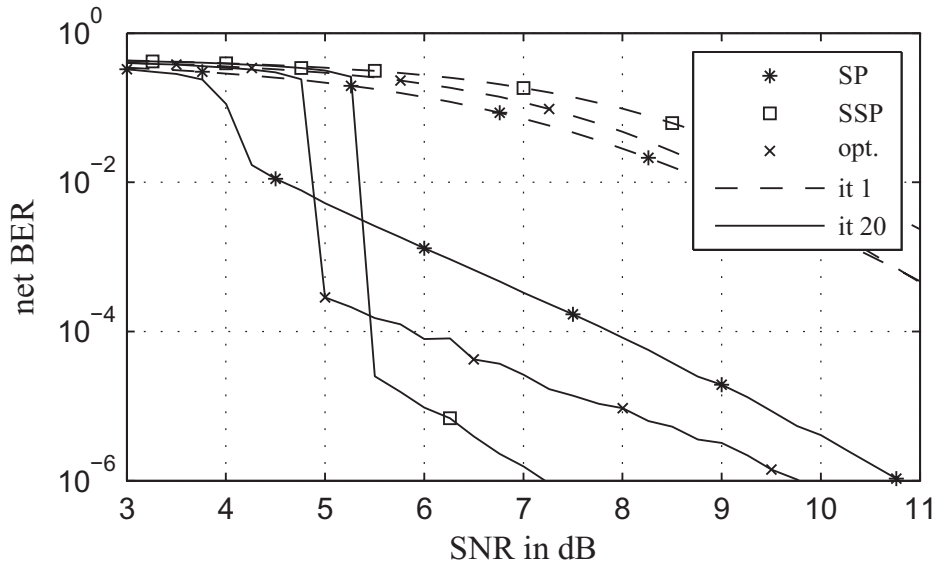


Figure 5.19: BER performance of OFDM BICM-ID transmission over an ISI channel using 8PSK with SP and SSP, exemplary CIR \underline{h} according to (5.7).

5.4 OFDM Turbo DeCodulation

The iterative combination of demapper, channel decoder, and source decoder with two iterative loops called Turbo DeCodulation (TDeC) [36] provides performances near the optimum performance theoretically attainable (OPTA) [39] in AWGN and flat Rayleigh fading environments. In order to employ TDeC in doubly selective fading environments with intersymbol interference (ISI), an OFDM stage with zero-forcing equalization is added resulting in an alternative novel transceiver concept called *OFDM TDeC*. This bi-directionally linking of application and link related components enables cross-layer optimization which is required by the next generation of mobile communication and can be applied wherever these components are physically co-located, e.g., in mobile devices [64].

In addition to the possibility of transmitting source coded data over frequency selective multi-path channels with reasonable complexity, another benefit of the combination of OFDM and TDeC is the option to exploit the ability of OFDM systems to transform these ISI channels into parallel flat fading channels. With the new method described in Sec. 5.3 a strategy for individually assigning signal constellation sets and bit mapping rules μ to different subcarriers is introduced, which optimizes the convergence behavior of the inner iterative loop with respect to the residual bit error rate. This method dynamically adapts the transmitter and receiver to the current channel condition. The performance of the OFDM TDeC system and its adapted version is analyzed and illustrated by means of EXIT charts, residual bit error rate (net BER), and parameter signal-to-noise ratio (PSNR).

By addition of a comparable application related source coder and soft decision decoder to the LTE physical layer as described in Sec. 4.2.3, a direct comparison between the two transceivers based on PSNR and goodput \mathcal{B} becomes possible.

5.4.1 OFDM TDeC with Convolutional Coding

Figure 5.20 depicts the baseband model of the novel OFDM Turbo DeCodulation system with convolutional coding (CC-TDeC). It generally follows the system model for TDeC with convolutional coding given in [36] but uses a simplified notation to describe only the relevant functionalities. For a detailed description of the transmission and reception process the reader is referred to [36] and the literature given there.

Source codec parameters u of a frame \underline{u} are quantized and mapped to unique bit patterns representing the quantizer reproduction levels. The concatenation of these bit patterns forms the data bit frame \underline{v} . After outer interleaving the resulting block is encoded by a convolutional encoder to obtain the code frame \underline{x} which then is interleaved by an inner interleaver. Appropriate interleaving and deinterleaving assumed to be part of encoding and decoding and therefore is not depicted in Fig. 5.20. Differing from [36], the code frame is then passed to a complex mapper where the block is first split into groups of bit patterns \underline{x}_i of predefined lengths I_i with $i \in [0, \dots, n_{SC} - 1]$ representing the n_{SC} subcarriers of the OFDM system. Therefore, one OFDM symbol carries $I_\Sigma \doteq \sum_i I_i$ coded bits. If the size of the vector of coded bits \underline{x} is not an integer multiple of I_Σ the vector is zero-padded. The patterns \underline{x}_i are subcarrier-wise mapped to complex modulation symbols Y_i according to a subcarrier-dependent mapping rule μ_i so that $Y_i = \mu_i(\underline{x}_i)$. For a fair comparison to UMTS LTE, bit patterns are restricted to size $I_i \in [2, 3, 4, 6]$ with different signal constellation sets \mathcal{Y} and mapping rules μ . In the following the expression \mathcal{Y}_μ will refer to a specific combination of SCS \mathcal{Y} and mapping rule μ . n_{SC} complex modulation symbols and a cyclic prefix of length l_{CP} form one OFDM symbol \underline{y} . A block fading channel with AWGN is considered that is described by its CIR \underline{h} which is sufficiently well estimated at the receiver.

As shown in Fig 5.20, the receiver consists of two iterative loops. The inner loop corresponds to a bit-interleaved coded modulation with iterative decoding (BICM-ID) system [63] where the soft demapper and the soft input soft output (SISO) channel decoder (CD) exchange extrinsic information on the encoded bits in form of extrinsic L-values $L_{CD}^{[apri]}$ and $L_{CD}^{[ext]}$

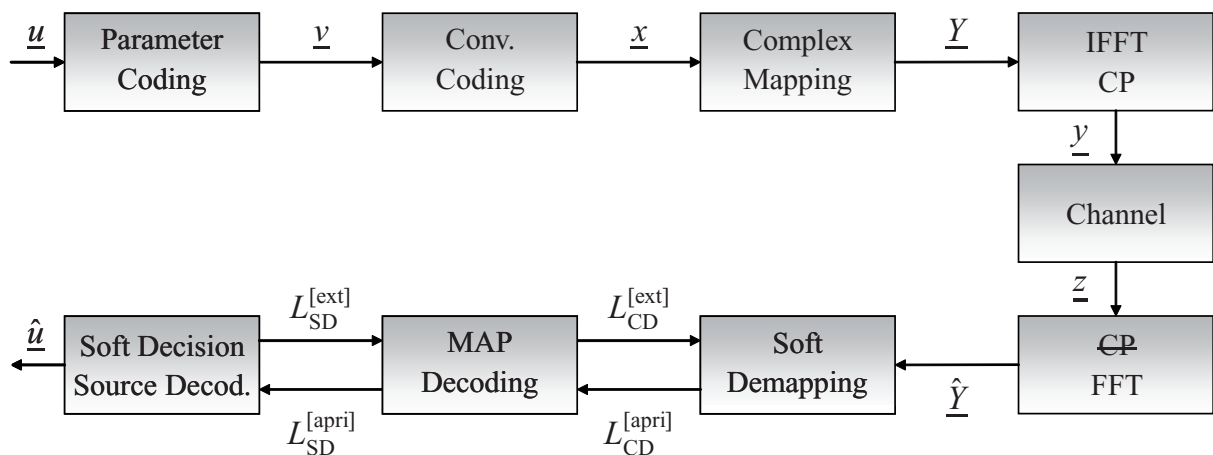


Figure 5.20: Baseband model of the OFDM Turbo DeCodulation system with convolutional coding (OFDM CC-TDeC).

respectively. The outer loop is an iterative source channel decoding (ISCD) system [21, 49] where the SISO CD and the soft decision source decoder (SDSD) exchange extrinsic information $L_{SD}^{[apri]}$ and $L_{SD}^{[ext]}$. After the final outer iteration, parameter-oriented a posteriori knowledge is determined for each quantizer reproduction level and each parameter \hat{u} is estimated by SDSD employing these reliabilities as weighting factors for a summation of all possible quantizer reproduction levels. Again, the reader is referred to [36] for a more detailed description of the employed iterative decoding stages.

5.4.2 EXIT optimization of the BICM-ID stage

The optimized single carrier TDeC system proposed in [36] employs 8PSK with mixed signal space mapping [63] in combination with an optimized quantizer bit mapping of the source encoder. However, as seen in Sec. 5.3, semi-set partitioning (SSP) is the optimum mapping rule μ for BICM-ID as it provides the lowest error-floor possible for 8PSK. Set partitioning (SP) on the other hand achieves an earlier water-fall for low channel qualities but yields a higher error-floor when compared to SSP (cf. Fig. 5.19). For OFDM systems, individual signal constellation sets on each subcarrier which depend on the current channel characteristics can maximize the goodput or minimize the BER or power consumption of the system [24]. This concept is known as bit/power loading or water-filling.

A possible optimization strategy is therefore to minimize the residual BER of the BICM-ID stage while keeping a constant overall bit rate and an average constant transmit power on all subcarriers. To take into account the iterative behavior of BICM-ID, the EXIT characteristics of the channel decoder and the SDM are considered. As already pointed out, a decoding tunnel has to exist between the EXIT characteristic of the SDM \mathcal{T}_{DM} and the inverse EXIT characteristic of the SISO channel decoder \mathcal{T}_{CD}^{-1} . The constraint is $\mathcal{T}_{DM} > \mathcal{T}_{CD}^{-1}$ for the largest possible range of $\mathcal{I}_{DM}^{[apri]}$. With the results from the preceding Sec. 5.3 a SDM characteristic can be constructed by weighted summation of the SDM characteristics of each individual subcarrier. The optimization problem is formulated as:

$$\max_{\mathcal{T}_{DM}} \left(\mathcal{I}_{max}^{[apri]} \mid \mathcal{T}_{DM}(\mathcal{I}) > \mathcal{T}_{CD}^{-1}(\mathcal{I}) + \delta\mathcal{I} \text{ and } 0 \leq \mathcal{I} \leq \mathcal{I}_{max}^{[apri]} \right) \quad (5.8)$$

with threshold $\delta\mathcal{I}$ ensuring the convergence of the BICM-ID stage for limited frame lengths and numbers of iterations.

A full search for a large number of subcarriers and combinations \mathcal{Y}_{μ} would be far too complex to be performed once per period during which the channel is considered time-invariant, e.g., one OFDM symbol. Therefore, two novel algorithms are proposed in [64] to find suitable solutions for (5.8) with reasonable computational complexity.

5.4.3 Simulation examples

The applicability of the OFDM TDeC system and the performance gains achieved with the optimization of the BICM-ID stage are demonstrated by computer simulation. An OFDM modulator with $n_{SC} = 256$ subcarriers is used and a time-invariant ISI channel is exemplarily

chosen as real FIR with the known CIR \underline{h} according to (5.7). Consequently the length of the cyclic prefix is set $l_{\text{CP}} > 4$.

BICM-ID optimization For the EXIT optimization of the BICM-ID stage the transmission of data frames \underline{v} , each containing $l_v = 200000$ bits, is considered. The data bits are encoded using a rate 1/2 feed-forward non-systematic convolutional encoder with zero termination, constraint length 4, and octal generator polynomials $G_0 = \{17\}_8$ and $G_1 = \{15\}_8$. 9 possible \mathcal{Y}_μ have been selected for the optimization of the mapper which are summarized in Tab. 5.1. These \mathcal{Y}_μ have been chosen regarding the variety of progressions of their SDM characteristics.

Bits per symbol I	SCS \mathcal{Y}	Mapping rule μ
$I = 2$	QPSK	Gray, Anti-Gray
$I = 3$	8PSK	Gray, SP, SSP
$I = 4$	16QAM	Gray, A1 [38]
	16QAMw [69]	optimized [69]
	16PSK	Ray [38]

Table 5.1: \mathcal{Y}_μ for EXIT optimization of the BICM-ID stage.

The EXIT chart resulting from the optimization is depicted in Fig. 5.21. It can be seen that for the exemplary target channel quality of SNR = 5 dB no decoding tunnel exists for 8PSK with SSP mapping. For the \mathcal{Y}_μ optimized assignment a tunnel exists enabling the system to converge already after 10 iterations. Furthermore, the SDM characteristic of the optimized system reaches an even higher value of $\mathcal{I}_{\text{DM}}^{\text{[ext]}}$ for the error-free feedback (EFF) case at $\mathcal{T}_{\text{DM}}(\mathcal{I}_{\text{DM}}^{\text{[apri]}} = 1)$. Note that the area property of the EXIT chart stating that the area beneath the SDM characteristic corresponds to the capacity of the channel for the regarded signal constellation sets is not violated: the superposition of SCSs with different numbers of bits I_i can lead to an increased capacity compared to a set up using, e.g., only SCSs with $I_i = 3$ bit for all subcarriers. These findings are confirmed by the residual bit error rates given in Fig. 5.22: For the optimized assignment the water-fall region starts at the optimization point of SNR = 5 dB, about 0.5 dB earlier compared to 8PSK with SSP mapping and converges into an error-floor which is about half a decade lower.

OFDM-TDeC performance For the OFDM-TDeC the system parameters of the ISCD stage (codec parameter correlation, quantizers, quantizer bit mappings, ISCD iterations, etc.) have been chosen according to [36]. Parameter frames \underline{u} , each containing 250 source codec parameters, are quantized and encoded using a rate 1/2 recursive systematic convolutional encoder with zero termination, constraint length 4, and octal generator polynomials $G_0 = \{10\}_8$ and $G_R = \{17\}_8$. 10 inner loop iterations are executed. After estimation of the parameters \hat{u} the parameter SNR is calculated according to (4.11) as a measure of quality which is upper bounded by $\text{PSNR}_{\text{max}} \approx 14.6$ dB due to the selected quantizers assigning 3 bit per quantizer reproduction level [39].

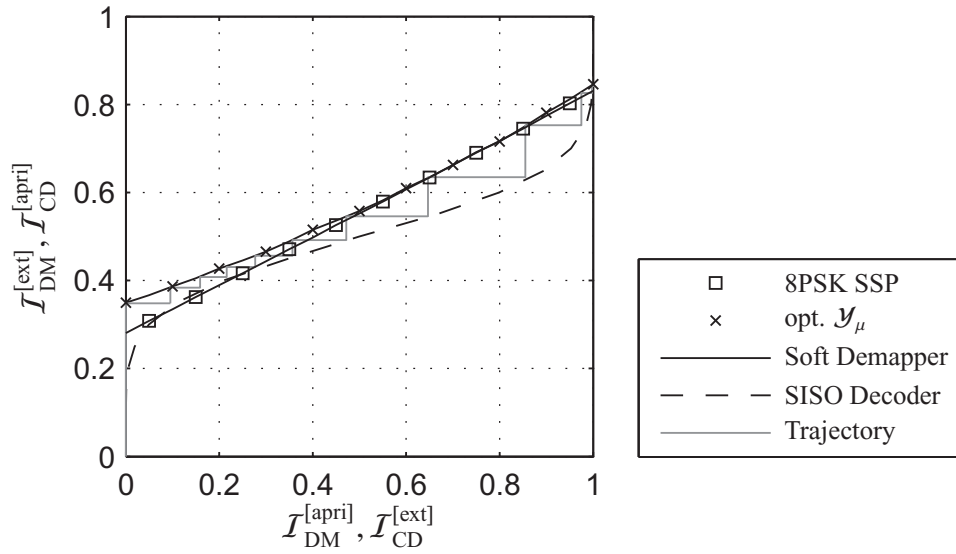


Figure 5.21: EXIT chart for BICM-ID at SNR = 5 dB in an ISI environment, exemplary CIR \underline{h} according to (5.7).

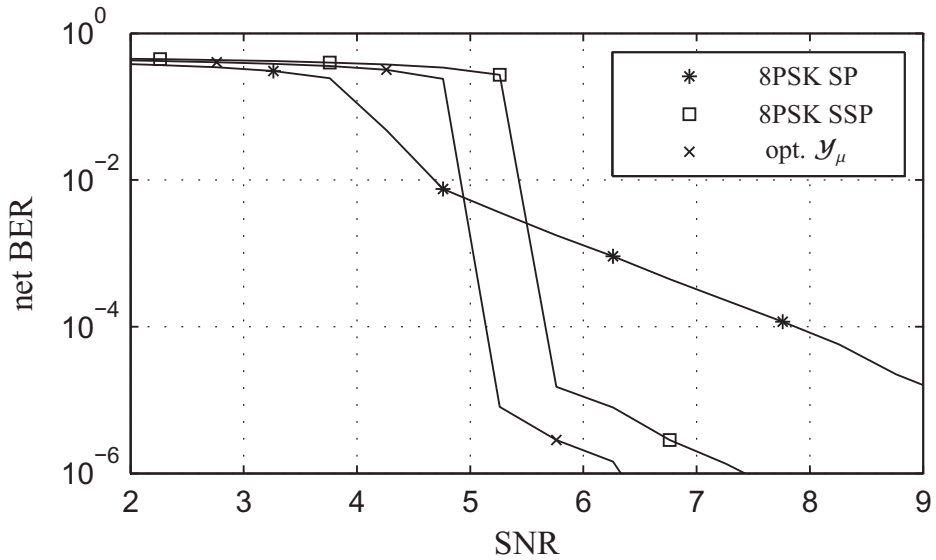


Figure 5.22: BER performance after BICM-ID stage (10 BICM-ID iterations) in an ISI environment, exemplary CIR \underline{h} according to (5.7).

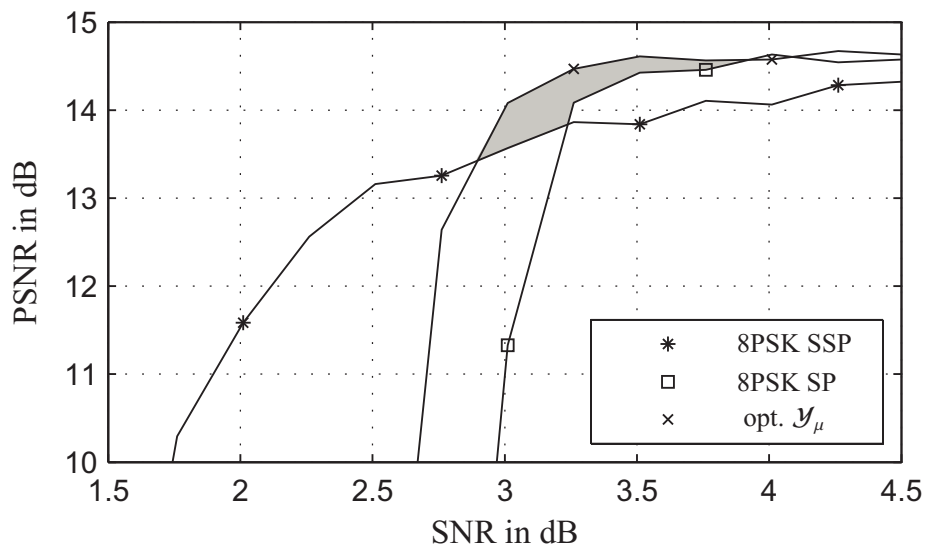


Figure 5.23: Parameter SNR versus SNR for OFDM TDeC (10 BICM-ID iterations) in an ISI environment, exemplary CIR \underline{h} according to (5.7).

Figure 5.23 illustrates the simulation results for an OFDM CC-TDeC system using 8PSK with SSP, 8PSK with SP, and a \mathcal{Y}_μ assignment optimized according to Sec. 5.4.2. It can be seen that a good performance concerning PSNR is achieved for very low channel qualities of SNR ≈ 3 dB for all depicted cases which proves the applicability of OFDM-TDeC for frequency selective ISI channels. Furthermore, the system with optimized \mathcal{Y}_μ assignment outperforms 8PSK SSP concerning PSNR. 8PSK SP on the other hand outperforms both other depicted systems for very low channel qualities with the trade-off of reaching PSNR_{max} only for very high channel qualities. The corresponding gain of the optimized system is illustrated by the marked area in Fig. 5.23.

5.4.4 Block Coded OFDM TDeC

A disadvantage of the CC-TDeC system is its high computational complexity due to its two iterative loops exchanging extrinsic information. Therefore, the concept of block coded Turbo DeCodulation (BC-TDeC) [34, 35] has been introduced. This work introduces the novel combination of BC-TDeC and OFDM, a simplified block diagram is depicted in Figure 5.24. The basic idea of BC-TDeC is to split the channel encoding stage into two parts and combine these parts with the source encoder on the application related side and with the complex mapper on the link related side of the transmitter.

On the application related side, a block code of rate ≤ 1 is added to the quantizer forming a so-called *redundant index assignment (RIA)*. That means, redundancy is added by the RIA directly to the binary representations of the quantizer reproduction levels.

On the link related side, a rate-1 non-linear block code is combined with the complex mapper leading to multi-dimensional complex mapping symbols [85]. To give an example: With a standard complex mapper using 8PSK as SCS, $I = 3$ bits are mapped to each symbol

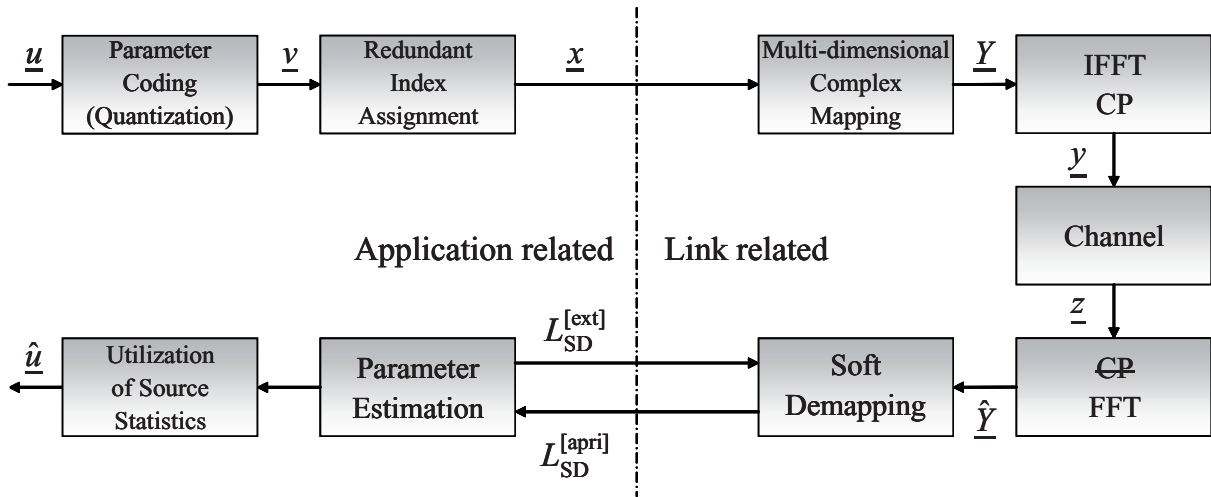


Figure 5.24: Baseband model of the OFDM Turbo DeCodulation system with block coding (OFDM BC-TDeC).

$Y \in \mathcal{Y} \subset \mathbb{C}$. For a (I^*, I^*) -block code with $I^* = 2 \cdot I$ in combination with 8PSK, two 8PSK symbols are combined to form a multi-dimensional complex mapping symbol $Y \in \mathcal{Y} \subset \mathbb{C}^2$ representing $I^* = 6$ bit.

In the receiver, the redundancy added by RIA can be used in combination with the known source statistics to calculate extrinsic information $L_{SD}^{[ext]}$ (cf. Fig. 5.24) which is fed back to the complex demapper. The reliability of the estimated parameters is therefore improved using only one iterative loop. Another advantage is the high flexibility: Different RIAs are employed which add different degrees of redundancy, i.e., the code rate of the RIA can be adapted to the current channel quality. In that way, a multi-mode system is implemented similar to adaptive coding and modulation (ACM) in UMTS LTE. A detailed description and analysis of block coded Turbo DeCodulation can be found in [34].

The physical layer performance of OFDM CC-TDeC and OFDM BC-TDeC in terms of parameter SNR (PSNR) and achievable bits per channel use \mathcal{B} are compared to the performance of UMTS LTE in the following Sec. 5.5, while the impact on system-level performance is analyzed in Sec. 7.2.5.

5.5 OFDM Turbo DeCodulation vs. UMTS LTE

The benefit of the cross-layer optimized TDeC system is the possibility to exploit extrinsic information generated on the link related side of the transceiver in the application related side and vice versa. Such a feed-back loop is not provided by current transceiver concepts like UMTS LTE. For a comparison of LTE and TDeC, the LTE transceiver structure is extended by the same parameter source and scalar quantizer (SQ) used for the TDeC evaluation. Vectors \underline{u} of $L = 2040$ correlated real valued parameters u are generated and represented by 3 bits after scalar quantization leading to a frame of $l_v = 6120$ data bits which in case of LTE are extended by 24 CRC bits.

To provide a fair comparison, code rates and SCSs for the three compared systems (CC-

TDeC, BC-TDeC, UMTS LTE) are limited in such a way that the achievable bits per channel use are limited to $\mathcal{B} < 1.5$ in case of both TDeC systems and to $\mathcal{B} < 1.6$ for UMTS LTE. Consequently, for LTE adaptive coding and modulation (ACM) is used with code rates $cr \in \{1/2, 1/3, 2/3, 3/4, 4/5\}$ and the standardized SCSs \mathcal{Y} with $I \in \{2, 4\}$ (QPSK, 16QAM) and Gray mapping. The convolutional coded OFDM TDeC uses the same rate 1/2 recursive systematic convolutional encoder as described in Sec. 5.4 and SCSs \mathcal{Y} with $I \in \{2, 3\}$ (QPSK, 8PSK). BC-TDeC uses different RIAs with a maximum code rate of 1/2, i.e. a (3,6)-block code, and multi-dimensional mappings based on 8PSK from [85].

The HARQ scheme of UMTS LTE effectively rejects erroneous data frames $\hat{\underline{v}}$. That is the reason for the observation that no significant gains can be obtained using a soft decision source decoder (SDSD): As soon as a frame $\hat{\underline{v}}$ passes the CRC, the received bits can be considered error-free. Therefore, for UMTS LTE, hard decided bits $\hat{v} \in \{0, 1\}$ are used for reconstruction of the parameters \hat{u} by the reproduction levels of the scalar quantizer.

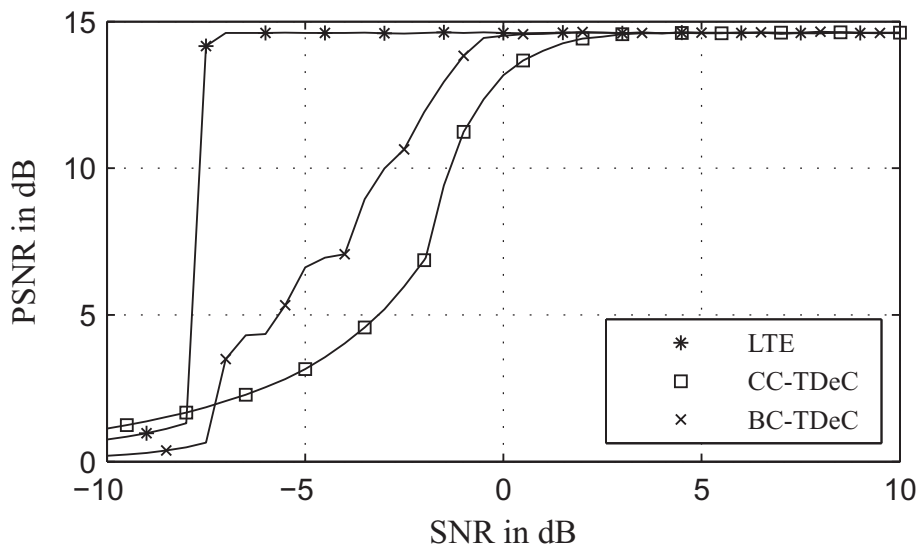


Figure 5.25: Parameter SNR versus SNR for OFDM TDeC and LTE in an AWGN environment.

Figure 5.25 compares the achieved PSNR of the three systems for different channel qualities in an AWGN environment. For all allowed combinations of coding and complex mapping schemes only the best performing combinations, i.e., the envelope of all combinations is depicted. A first conclusion that can be drawn from Fig. 5.25 is that due to the aforementioned effect of the HARQ scheme, UMTS LTE (*) reaches the upper bound of $PSNR_{\max} \approx 14.6$ dB instantly for $SNR > -7$ dB. The CC-TDeC performance (\square) shows the typical slow degradation of the PSNR for decreasing channel qualities starting at $SNR < 2.5$ dB, which complies with the findings of Fig. 5.23. With BC-TDeC \times performs gains of approximately 1.5 – 2 dB are achieved compared to CC-TDeC. UMTS LTE, however, outperforms both concepts in terms of PSNR.

Figure 5.26 compares the bits per channel use \mathcal{B} obtained by both systems. While for the LTE system this measure is drawn from the goodput \mathcal{G} based on the CRC, no predictions

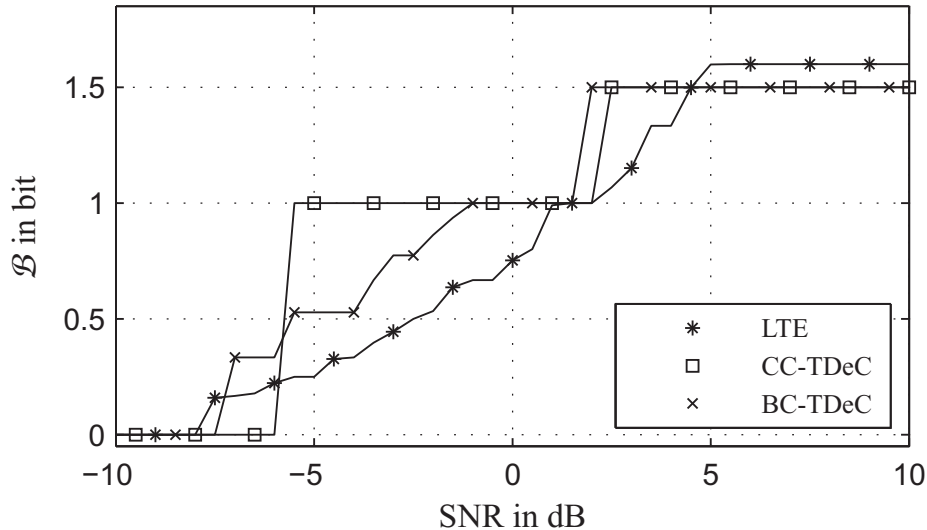


Figure 5.26: Bits per channel use \mathcal{B} versus SNR for OFDM TDeC and LTE in an AWGN environment.

are made about the correctness of the frames $\hat{\mathbf{y}} \hat{=} L_{\text{SD}}^{\text{[apri]}}$ of the TDeC systems. Therefore, the bits per channel use are based on throughput R rather than on goodput \mathcal{G} . However, \mathcal{B} is set to zero for both TDeC systems at those SNRs where the transmission quality drops below $\text{PSNR} < 2.5$ dB, cf. Fig. 5.25.

The results depicted in Fig. 5.26 relativize those depicted in Fig. 5.25. The seemingly superiority of the UMTS LTE system comes at the cost of its efficiency. In those regions of poor channel qualities where UMTS LTE outperforms the TDeC systems in terms of PSNR (-7 dB $<$ SNR $<$ 0 dB), both TDeC systems provide a larger spectral efficiency. The implications of this observation for system-level performance are discussed in Section 7.2.5.

5.6 MIMO Approximation

All modifications and alternative concepts described in the previous sections consider transceivers with one transmit and one receive antenna. The most current versions of standards for mobile broadband radio systems like UMTS LTE or IEEE 802.16-2009 are also considering multiple-input multiple-output (MIMO) techniques, i.e., systems with multiple transmit (Tx) and receive (Rx) antennas. A transceiver system with A_{Tx} transmit and A_{Rx} receive antennas is therefore dubbed $A_{\text{Tx}} \times A_{\text{Rx}}$ MIMO system. For this work the same number of Tx and Rx antennas is assumed, i.e., $A_{\text{Tx}} = A_{\text{Rx}} \hat{=} A$.

Goal of all MIMO techniques is to increase the transmission capacity without increasing system bandwidth Δf or transmit power P_{Tx} . Many publications describe the bounds on the capacity achievable with different MIMO techniques. One of the most popular papers in that field has been published by Telatar in 1999 [81]. A large research community has been striving to provide techniques and algorithms to approach these theoretical bounds producing remarkable results. As this research goes beyond the scope of this work, basic upper bounds

on the maximum achievable spectral efficiency η and bit per channel use \mathcal{B} are sketched in the following. A detailed overview of MIMO fundamentals, algorithms and transceiver design is provided, e.g., in [28].

The spectral efficiency for a single antenna system is bounded by $\eta_{1 \times 1}$ which is derived from the Shannon bound (4.24):

$$\eta_{1 \times 1} = \frac{\mathcal{G}_{\max}}{\Delta f} = \log_2(1 + \text{SNR}). \quad (5.9)$$

With that, it can be shown that for an $A \times A$ MIMO system, the spectral efficiency is upper bounded by

$$\eta_{A \times A} = A \log_2 \left(1 + \frac{\text{SNR}}{\Xi} \right) \quad \text{with } \Xi \in \{1, A\} \quad (5.10)$$

where Ξ denotes a certain MIMO implementation described in the following.

$\Xi = A$ describes *spatial multiplexing* where one individual data stream is transmitted per Tx-Rx antenna pair, thus increasing the spectral efficiency by factor A . Due to the relatively small spatial separation of transmit and receive antennas, each Rx antenna will receive a superposition of the different transmissions from the different Tx antennas. In the case of spatial multiplexing the unwanted signals from the other Tx antennas are suppressed by appropriate pre- and post-processing of the transmit and receive signals. In that way, only $\frac{1}{A}$ th of the received signal power is used at each Rx antenna. It can be seen in (5.10) that in good channel conditions, i.e., for high SNR values, this splitting of the power has a negligible influence on the bound on the spectral efficiency.

$\Xi = 1$ describes *joint combining*, i.e., a MIMO technique which aims at increasing the received power of a transmitted signal by combining the signals of all Rx antennas. The concept of combining one transmission received by different receive antennas has long been known. The optimum form to exploit this *receive diversity* is known as *maximum ratio combining (MRC)*. The challenge for MIMO is the combination of spatial multiplexing and receive diversity. Therefore, in an $A \times A$ MIMO system, it is necessary to jointly process the A spatially multiplexed signals from all A Rx antennas, increasing the SNR for each stream by factor A . In that way the transmission capacity can theoretically increased by a factor of A compared to the Shannon bound [28]. In the following, (5.10) with $\Xi = 1$ will be considered as upper bound on the spectral efficiency $\eta_{A \times A}$ of MIMO systems.

Figure 5.27 depicts the resulting bounds on the spectral efficiencies versus the channel quality. It can be seen from this figure as well as from (5.10) that the spectral efficiency increases linearly with the number of antennas A .

Assuming the LTE OFDM modulation stage with the time bandwidth product $\delta f_{\text{SC}} \cdot T_{\text{S}}$, the maximum achievable bits per channel use \mathcal{B} are bounded by

$$\mathcal{B} = \eta_{A \times A} \delta f_{\text{SC}} T_{\text{S}} = A \delta f_{\text{SC}} T_{\text{S}} \log_2(1 + \text{SNR}). \quad (5.11)$$

The resulting bounds on \mathcal{B} are depicted in Fig. 5.28. The curves illustrate the potential of MIMO transmission to drastically increase the capacity of mobile radio networks when

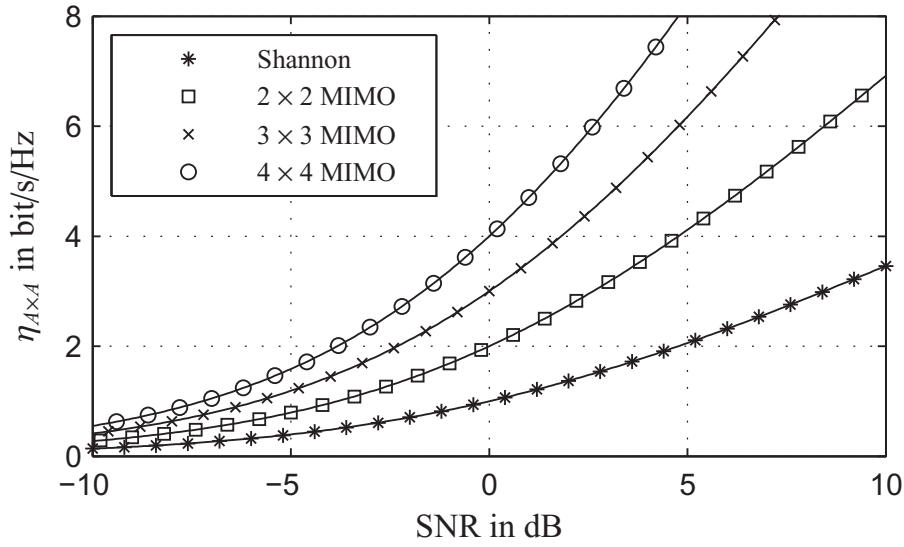


Figure 5.27: Upper bound on spectral efficiency η achievable with $A \times A$ MIMO with joint combining.

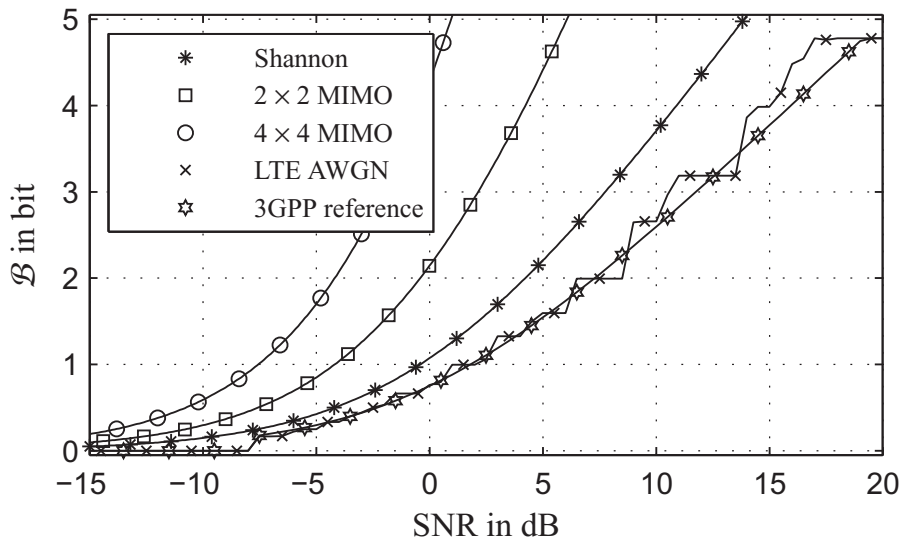


Figure 5.28: Upper bounds on the obtainable bits per channel use employing MIMO with joint combining assuming uncorrelated channels and the time bandwidth product of LTE OFDM modulation, comparison to LTE simulation results in AWGN environment and 3GPP approximation (4.25).

compared to standard UMTS LTE as simulated in an AWGN environment or approximated by 3GPP. However, these figures represent upper bounds which will hardly be achieved in practical systems due to computational complexity, physical implementation aspects and the mere physics of the radio channel.

5.7 Concepts for Interference Management

It will be shown in the following chapters that in many typical deployment scenarios the coverage of a radio cell is interference limited, i.e., inter-cell interference (interference from adjacent radio cells) dominates the channel quality perceived by user equipments (UEs) near the cell edges. To tackle that problem, different concepts are currently developed for future releases of mobile radio standards, e.g., for *LTE Advanced* (Release 10 and following of 3GPP's UMTS standard, [53]) or IEEE 802.16m. Generally, two major concepts can be identified which are briefly sketched here, while the influence of interference management on coverage and capacity of mobile radio systems is analyzed in the following chapters.

interference cancellation (IC) is an algorithmic approach assuming that the UE is not only able to decode its useful transmission but also to (partially) decode the interfering transmissions. With this knowledge, the interfering transmissions can be subtracted from the received signal and thus the perceived channel quality is improved.

cooperative multipoint (CoMP) aims at interference reduction by coordinated access of the radio resources of adjacent radio cells. If the current cell load allows, resource blocks (RBs) are assigned to a cell edge UE only, if the same RBs are not assigned by the BS of the adjacent interfering BS. An obvious extension of this concept is the reintroduction of *macro diversity*, i.e., the support of a cell edge UE by transmitting the same data on the same RBs of adjacent base stations. This multi-point transmission will appear to the UE identical to a transmission over a multi-path propagation channel and, assuming a maximum path delay difference smaller than the cyclic prefix duration, can be compensated by the equalizer while improving the instantaneous channel quality. The concept of macro-diversity has been implemented in 3G mobile radio systems like UMTS and CDMA 2000.

Both sketched concepts rely on intensive signaling between neighboring base stations, or even between complete clusters of base stations. Obviously, this imposes several problems concerning computational complexity, backhaul capacity and delay constraints. The questions of what needs to be signaled and how it is signaled efficiently concerning capacity and computational complexity remain open issues and are currently subject to exhaustive research.

From Bit-Level to System-Level

The preceding chapters described the physical layers of different transceiver concepts and evaluated their performance by means of transmitted bits per channel use \mathcal{B} or parameter quality PSNR. It has been shown that these measures vary with the channel quality which generally depends on the user position. To evaluate the impact of the different physical layer concepts on the coverage, capacity, and quality of a mobile radio cell, system-level simulations based on the physical layer (PHY) simulation results have been conducted. The purpose of this chapter is twofold: In its first part it describes the models and assumptions on which system-level simulations are based. The second part derives the system-level performance concerning the capacity of a radio cell in a semi-analytically manner. The main focus is on UMTS LTE and its upper bounds when MIMO is considered.

6.1 Abstraction and System Model

To adequately simulate the behavior of a mobile radio network, different aspects have to be taken into account and abstracted in a way that guarantees a fair trade-off between generality, accuracy, and complexity. The main aspects which are defined in the following are network geometry, path loss, services, and traffic.

6.1.1 Network Geometry, Carrier Frequencies, and Frequency Bandwidth

Radio cell and network geometry are determined by the location and configuration of base stations (BS). These positions or sites are chosen carefully by the mobile network operators taking into account landscape and topology, building, population density, expected data traffic, and costs of investment and operation. Radio cells in densely populated cities and urban areas with high traffic load will generally be smaller than radio cells in sparsely populated rural areas. That motivates the distinction between capacity driven radio cell deployment aiming at providing more capacity to areas with high demand and coverage driven radio cell deployment aiming at providing area-wide mobile access in sparsely populated areas. If different carrier frequencies f_0 are available, like, e.g., in GSM, a trade-off between capacity and frequency reuse (distance of radio cells with identical carrier frequencies) has to be

made. It can easily be seen that appropriate network planning is a crucial and non-trivial part of mobile radio network operation.

Cell edges will naturally appear between two adjacent base station sites when a moving user equipment (UE) receives the signals from both base stations at the same power level. Due to irregular building, vegetation or topology, this does not necessarily has to be the case at equidistant locations between both sites. The UE will handover to the radio cell providing the stronger signal, obeying a certain threshold to avoid steady handovers near cell edges (ping pong effect). For analytical and simulative investigations of mobile radio networks, a hexagonal network layout with base stations in the center of each hexagon is the most common abstraction, because regular hexagons will cover a given surface with the smallest number of base stations at a given distance. If isotropic radiation is assumed, hexagons define the ideal handover limits between radio cells. For this work, a simple network layout depicted in Fig. 6.1 is chosen, focusing on one hexagonal radio cell and the surrounding adjacent cells as given.

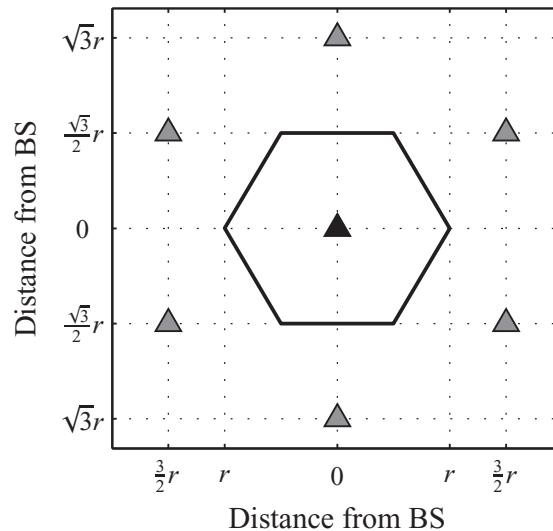


Figure 6.1: Position of serving base station (black triangle) and interfering base stations (gray triangles) as function of cell radius r .

It can be seen that the cell radius r defines the size of the cell and the distance between adjacent base stations. The serving base station is denoted by the black triangle in Fig. 6.1 while the adjacent base stations are denoted by gray triangles. The resulting cell edges representing the equidistant locations between serving base station and nearest adjacent base station are given as black lines. The cell radius r indicates the maximum distance between base station and cell edge.

To increase network capacity, practically all base stations of current mobile networks are equipped with sectorized antennas. Using antennas with high directivity, only an angular portion of the cell, usually 120° , is covered forming a *sector* which acts as a radio cell of its own concerning the procedures of the radio resource management, e.g., scheduling. Sectorization can be simulated in different but equivalent ways. Assuming three sectors of 120° , one way is dividing the hexagon into three rhombus shaped sectors leaving the base

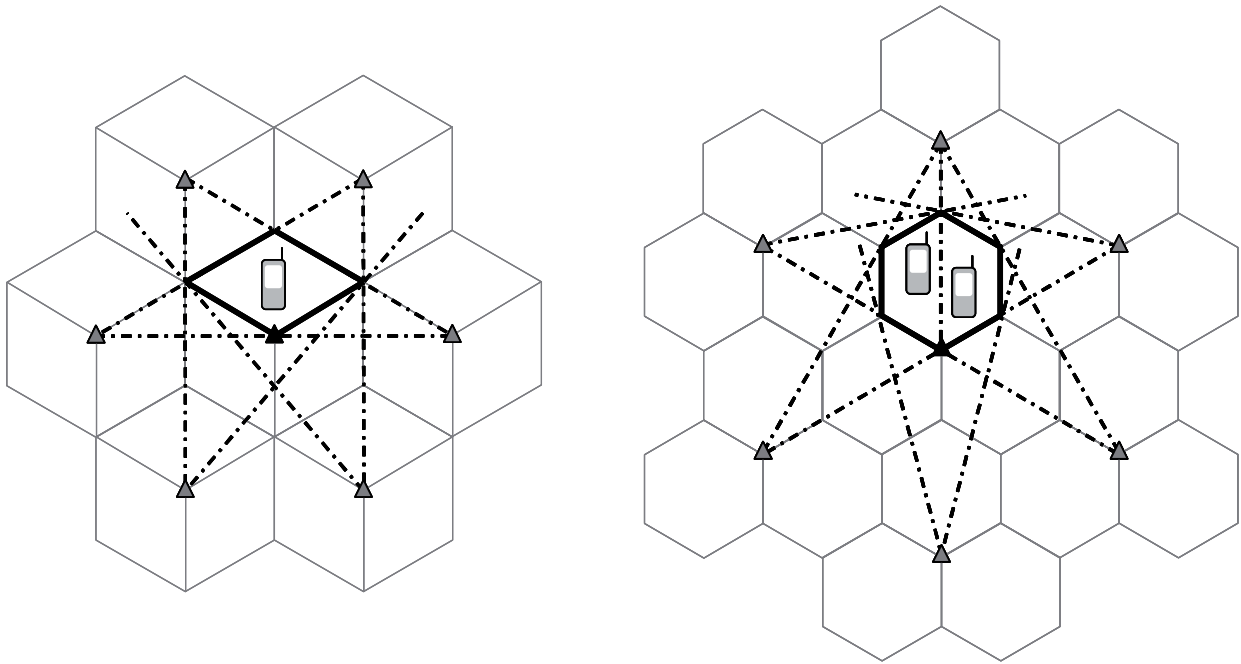


Figure 6.2: Sectorization and inter-cell interference in downlink for sectorized cells.

station in the center of the hexagon. The second way takes into account the directivity and beam form of base station antennas by placing base stations at three-corner points of the hexagonal grid, thus representing each sector by a hexagon rather than by a rhombus.

Focusing on the downlink, the influence of sectorization is not considered in this thesis. Figure 6.2 shows that in downlink at any position within a given sector (bold edges) all six adjacent base stations will interfere with the signal of the central base station. This holds for both aforementioned forms of sectorization. In the uplink direction, however, a reduction of the interfering signals from adjacent sectors can be achieved due to the directivity of the base station antennas.

Two different cell sizes are considered for this work which are of special interest as they represent two typical scenarios. Micro-cells as defined in Tab. 3.2 with a radius of $r = 200$ m represent radio cells in cities and urban areas. Macro-cells are defined by a cell radius of $r = 10$ km. Although macro-cells mainly cover less densely populated rural areas, they might also be deployed in urban areas, e.g., as so-called umbrella cells.

To study the effect of different carrier frequencies f_0 , two typical frequencies are considered. Radio cells representing current 3G networks are assigned a carrier frequency of $f_0 = 2$ GHz, while radio cells with frequencies from the *digital dividend* (790 – 862 MHz, cf. Section 2.3) are assigned a carrier frequency of $f_0 = 0.8$ GHz. In Germany UMTS LTE will also use the 2.6 GHz band, which is not explicitly considered in this thesis. However, it will be shown, that in radio networks with densely positioned base stations (interference limited scenarios), simulation results achieved with $f_0 = 2$ GHz also hold for the 2.6 GHz band. It is assumed, that all base stations, serving BS and adjacent BSs, transmit on the same carrier frequency. This represents the current state of 3G networks with reuse factor one and can be assumed to hold for the near future 4G systems.

Two different frequency bandwidths Δf are considered. A frequency bandwidth of $\Delta f = 5$ MHz represents the configuration of current 3G networks, while $\Delta f = 20$ MHz represents the intended maximum configuration for 4G networks. It has to be noted that a candidate technology for IMT-Advanced is required to operate with a frequency bandwidth of at least $\Delta f = 40$ MHz [56], while LTE-Advanced goes even further by aiming at frequency bandwidths of up to $\Delta f = 100$ MHz, which might even be distributed as smaller frequency blocks over a large range of carrier frequencies, i.e., non-contiguous spectrum might be used. However, for large gaps between these frequency blocks, this *spectrum aggregation* requires high performing RF-front-ends which at this point in time are still subject to research and development.

6.1.2 Signal-to-Interference-and-Noise Ratio

Channel quality, i.e., the signal-to-noise ratio (SNR) at a user's location within a radio cell is determined by the BS transmit power P_{Tx} , path loss L between BS and UE, and the noise power of the receiver. With the assumed network using the same carrier frequency f_0 in all radio cells, the interference power at the user's location has to be taken into account as well, leading to the location specific *signal-to-interference-and-noise ratio (SINR)*. For this work, this *inter-cell interference* is considered to be uncorrelated white Gaussian noise, therefore the interfering power received from the six adjacent base stations at a user's location is added to the receiver noise power. For determining the physical layer performance of a UE at a certain location, the SINR at this location can be used as equivalent SNR in the performance curves presented in Chapters 4 and 5, i.e., for the achieved bits per channel use \mathcal{B} .

The transmission powers of each scenario depend on the considered frequency bandwidth Δf and are chosen in accordance with [15]. Motivated by the assumption of fully loaded cells which is explained below in Section 6.1.3, all base stations are considered to transmit always at maximum transmit power. For a system bandwidth of $\Delta f = 5$ MHz transmit power of all BSs (serving and interfering) is set to $P_{\text{Tx}} = 43$ dBm (≈ 20 W), for $\Delta f = 20$ MHz transmit power is set to $P_{\text{Tx}} = 46$ dBm (≈ 40 W).

A key characteristic of a radio cell is the path loss as defined by (3.8) in Section 3.2 which does not only determine the strength of the data-carrying useful signal at the receiver but also the amount of inter-cell interference received from the adjacent radio cells. Different models have been developed based on measurement campaigns and analytical considerations covering all kinds of cell sizes, topologies, building densities, or user scenarios. As pointed out above, this work considers two different cell sizes (micro- and macro-cell) and two different topology classes (rural and urban environment). However, micro-cells are not common in urban environments, therefore three propagation scenarios are considered: rural macro-cells (RMa), urban macro-cells (UMa) and urban micro-cells (UMi).

The models describing the path loss L for each of the three considered scenarios are taken from literature and described in detail in Appendix B. The urban micro-cell case is covered by the Walfisch-Ikegami-Model of COST 231 (European Co-operation in the Field of Scientific and Technical Research, action 231, [44]) and depicted in Fig. 6.3 for both considered carrier frequencies (solid versus dashed line). For the urban macro-cell case

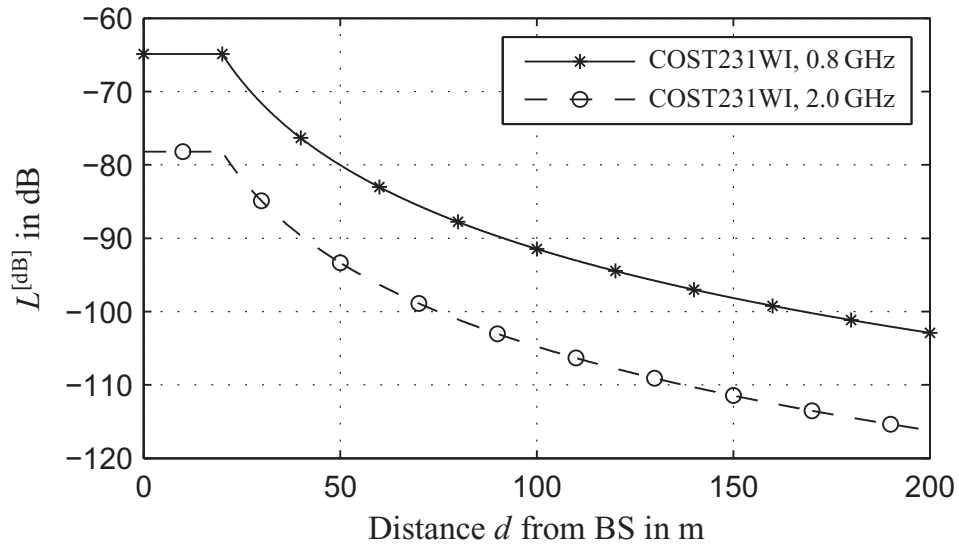


Figure 6.3: Path loss in urban micro-cell propagation scenario (UMi) based on the Walfisch-Ikegami-Model of COST 231 [44] (COST231 WI) for the considered carrier frequencies f_0 .

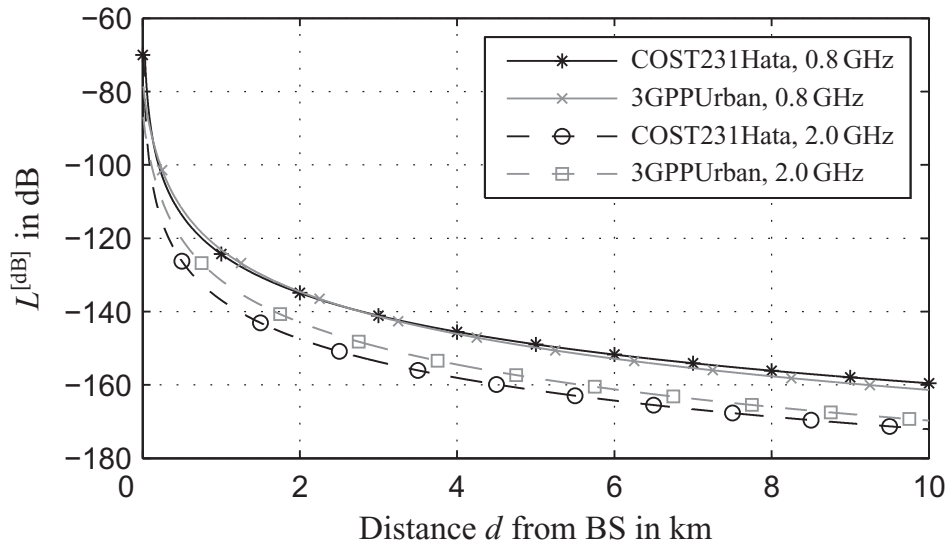


Figure 6.4: Path loss in urban macro-cell propagation scenario (UMa) based on the Hata-Model from COST 231 [44] (COST231Hata, UMa1) and on 3GPP's model from [15] (3GPPUrban, UMa2) for the considered carrier frequencies f_0 .

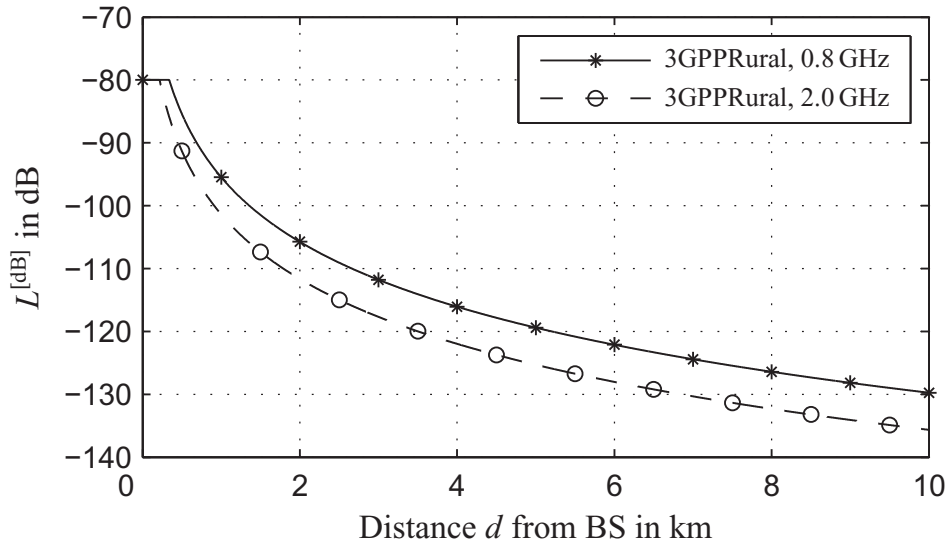


Figure 6.5: Path loss in rural macro-cell propagation scenario (RMa) based on 3GPP's model from [15] (3GPPRural) for the considered carrier frequencies f_0 .

depicted in Fig. 6.4, two models can be compared. The first is based on the Hata-Model from COST 231 [44] (black lines, UMa1), while the second is taken from 3GPP's Technical Report (TR) 36.942 [15] (gray lines, UMa2). Finally, the path loss model for the rural macro-cell propagation scenario depicted in Fig. 6.5 is also based on 3GPP TR 36.942.

As expected, for all depicted cases the lower carrier frequency of $f_0 = 0.8$ GHz exhibits a smaller path loss compared to the higher $f_0 = 2.0$ GHz. The path loss differences between the considered carrier frequencies are

- 13.3 dB with COST231WI (UMi),
- 12.5 dB with COST231Hata (UMa1),
- 8.4 dB with 3GPPUrban (UMa2),
- 5.9 dB with 3GPPRural (RMa).

The path loss difference between the COST231Hata and 3GPPUrban models in the urban macro-cell propagation scenario (UMa1 and UMa2) are < 6.5 dB for $f_0 = 2.0$ GHz and < 2 dB for $f_0 = 0.8$ GHz, at distances $d > 1000$ m from the base station.

These findings confirm that at a given location within the radio cell a higher signal-to-noise ratio can be achieved for $f_0 = 0.8$ MHz than for $f_0 = 2.0$ GHz. In a single cell deployment without interfering adjacent cells, a system transmitting at $f_0 = 0.8$ MHz can therefore be expected to achieve a higher coverage than a system transmitting at $f_0 = 2.0$ GHz. However, so far no statement can be made about the signal-to-interference-and-noise ratio which determines the achievable bits per channel use \mathcal{B} at a certain location within a radio network: As mentioned before, the power received from the interfering adjacent base stations is subject to the same path loss models and has to be regarded as well.

A further effect influencing the strength of a received signal is *log-normal fading*. It describes random additional losses due to shadowing, e.g., behind hills or buildings. However, log-normal fading has been observed to have a negligible effect on system-level simulations when averaging over the area of the radio cell [15]. Therefore, this effect is omitted in system-level simulations.

The thermal noise power at the receiver is determined by the system frequency bandwidth from the noise power spectral density of -174 dBm/Hz which corresponds to a temperature of 288.4 K, i.e., approximately 15°C. This leads to receiver noise powers of $N_{\text{th}} = -107$ dBm and $N_{\text{th}} = -101$ dBm for $\Delta f = 5$ MHz and $\Delta f = 20$ MHz, respectively.

Additionally, certain losses and gains have to be taken into account when calculating the received power at the UE. These include but are not limited to transmit and receive antenna gain, cable and combiner losses, body loss, or fading margins [53]. In accordance with [15] a BS antenna gain of $G_{\text{Tx}} = 15$ dB is considered for all cases which in the following subsumes all aforementioned gains and losses. It will be shown that when calculating the SINR in a loaded cellular network, these omitted gains and losses only marginally affect the system-level simulation results.

Based on the hexagonal cell layout given in Fig. 6.1, the Euclidean distances d_i between BS i at defined locations \mathbf{x}_i and the UE at location \mathbf{x}_{UE} are given by

$$d_i = \|\mathbf{x}_i - \mathbf{x}_{\text{UE}}\|^2, \quad (6.1)$$

where w.l.o.g. $\mathbf{x} \in \mathbb{R}^2$ describes positions in the Cartesian coordinate system with the serving base station $i = 0$ in the origin, i.e., $d_0 = \|\mathbf{x}_{\text{UE}}\|^2$. Hence, the SINR for a cellular radio network according to Fig. 6.1 is calculated as function of the UE location \mathbf{x}_{UE} :

$$\text{SINR}(\mathbf{x}_{\text{UE}}) = \frac{P_{\text{Tx}} G_{\text{Tx}} L(d_0)}{N_{\text{th}} + \alpha \sum_{i=1}^6 P_{\text{Tx}} G_{\text{Tx}} L(d_i)}, \quad (6.2)$$

with $i \in \{1, \dots, 6\}$ denoting the adjacent interfering base stations. The *inter-cell interference factor* α models interference cancellation (IC) algorithms (cf. Section 5.7) and determines the amount of interference taken into account. It takes values $0 \leq \alpha \leq 1$ with $\alpha = 0$ denoting full interference cancellation and $\alpha = 1$ denoting full inter-cell interference. As already mentioned, serving and interfering base stations are transmitting at the same maximum power. Without IC and for low and moderate path losses the system will exhibit interference limitation, i.e., the interference term in the denominator of (6.2) is dominating the thermal noise power. This, however, diminishes the influence of the gain factor G_{Tx} which is considered to be equal for serving and interfering base stations.

Note, that a value of $\alpha = 0$ can also be regarded as the lack of inter-cell interference, occurring, e.g., in single radio cells which are not part of a radio network with area-wide coverage. That is especially the case when single base stations are deployed to enable wireless broadband access in an isolated region like a single village or spread farmsteads in rural areas and transmitting on dedicated carrier frequencies, e.g. from the digital dividend. In this context, the cell radius r and the according cell edges as defined above do not denote the ideal handover regions anymore but indicate an area of intended coverage.

For ease of notation, in the following the distance d defines the UE position according to

$$\mathbf{x}_{\text{UE}} = [d, 0]$$

with $0 \leq d \leq r$ and cell radius r . Distance d therefore describes the complete way from the serving base station to the cell edge for the considered cell radius r . Assuming $\alpha = 1$ (no cancellation of inter-cell interference), the SINR of UEs at distances d from the serving base station according to (6.2) is depicted in Figs. 6.6, 6.7, and 6.8 for UMi, UMa, and RMa propagation scenarios, respectively. A frequency bandwidth of $\Delta f = 20$ MHz is assumed and the transmit power is consequently set to $P_{\text{Tx}} = 46$ dBm.

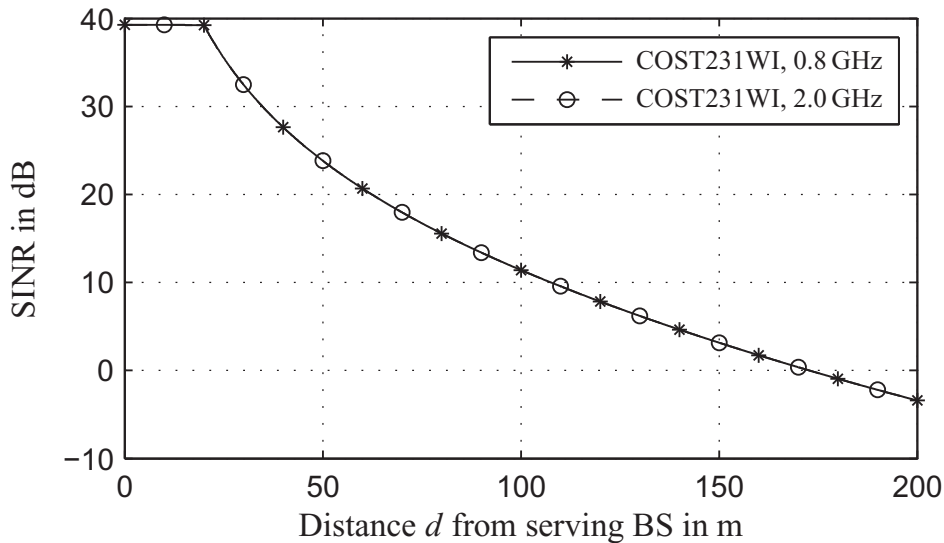


Figure 6.6: SINR in cellular UMi propagation scenario for the considered carrier frequencies f_0 .

All figures exhibit comparable SINR characteristics. In the direct vicinity of the base station a higher SINR is achieved for $f_0 = 2.0$ GHz compared to $f_0 = 0.8$ GHz, see magnification in Fig. 6.7. This is due to different attenuations of the interfering signals for the different carrier frequencies leading to different interference powers at positions close to the serving base station. There, the received useful signal level is considered constant due to the minimum coupling loss, cf. Appendix B.

In the UMi and RMa propagation scenario, SINR differences are hardly noticeable for neither of the considered carrier frequencies (see magnification in Fig. 6.8). Due to moderate path losses with proportional progressions for the considered carrier frequencies in UMi and RMa scenarios (Figs. 6.3 and 6.5), the coverage is interference limited and the resulting capacity is expected to be very similar for $f_0 = 0.8$ GHz and $f_0 = 2.0$ GHz.

The higher path losses in UMa scenarios (cf. Fig. 6.4) result in noise limited coverage, as interfering signals suffer from the high path loss as well. Therefore, a performance gain for $f_0 = 0.8$ GHz is noticeable in Fig. 6.7. In accordance with Fig. 6.4, this gain is higher for the COST231Hata model (black lines, UMa1) compared to the 3GPPUrban model (gray lines,

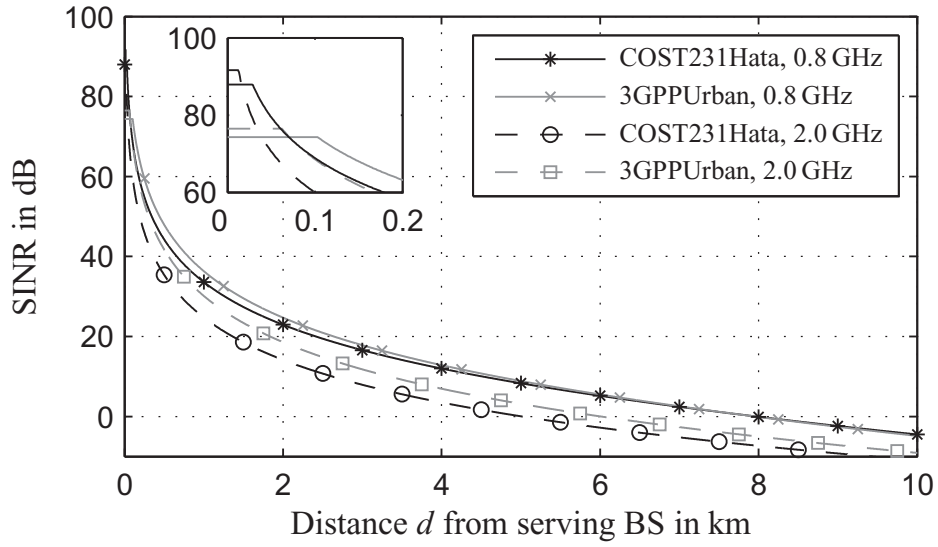


Figure 6.7: SINR in cellular UMA propagation scenario for the considered carrier frequencies f_0 .

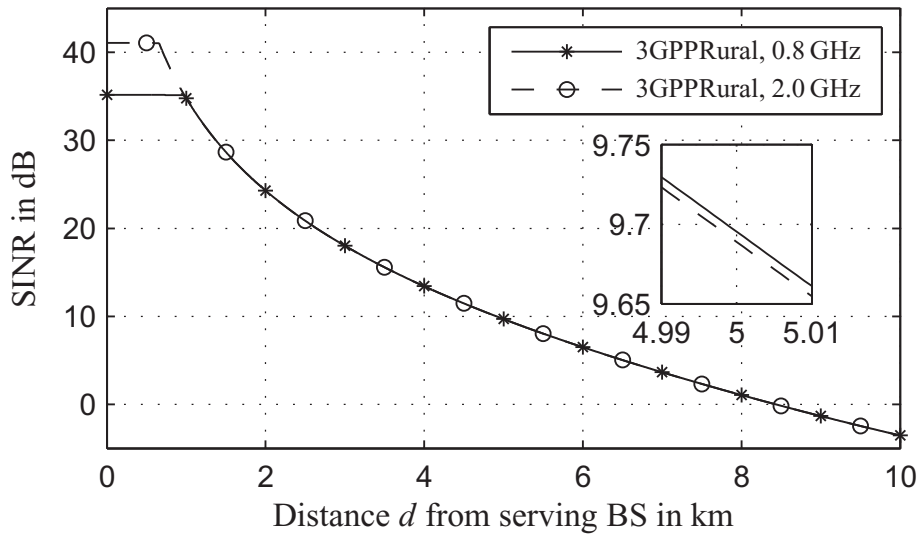


Figure 6.8: SINR in cellular RMA propagation scenario for the considered carrier frequencies f_0 .

UMa2). Accordingly, a performance gain concerning coverage and capacity is expected for $f_0 = 0.8$ GHz in UMa propagation scenarios.

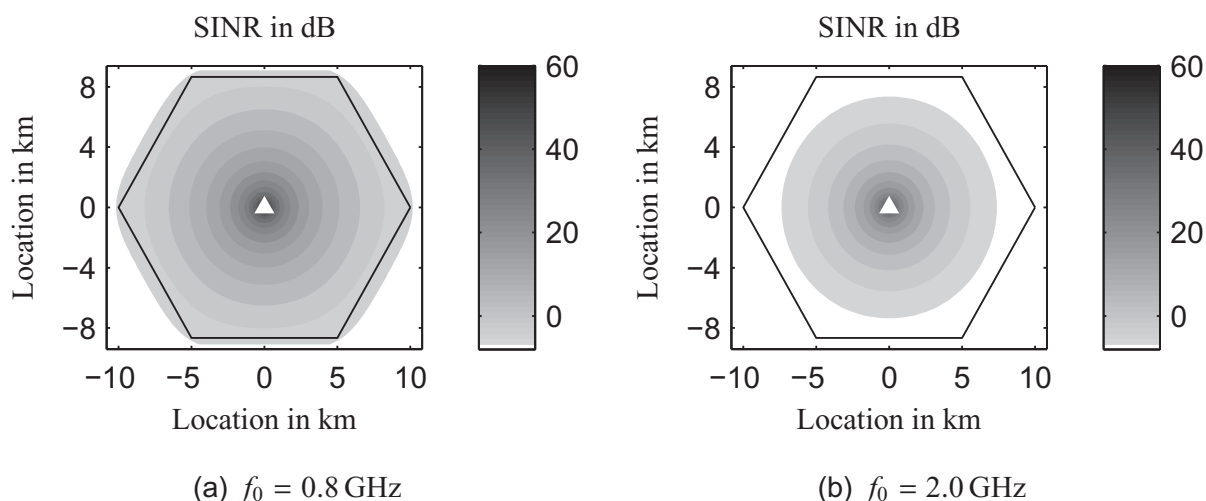


Figure 6.9: Urban macro-cell SINR in a cellular radio network assuming COST231Hata pathloss.

To give an 2-dimensional impression of the SINR distribution within the modeled radio cells, Fig. 6.9 depicts the SINR contour for the UMa1 propagation scenario with frequency bandwidth $\Delta f = 20$ MHz and carrier frequencies $f_0 = 0.8$ GHz and $f_0 = 2.0$ GHz. As predicted by the SINR progressions in Fig. 6.7, a noticeable difference exists for the considered carrier frequencies indicating an advantage of lower carrier frequencies for the considered propagation scenario.

6.1.3 Service Scenarios

The load of a radio cell, i.e., the number of simultaneously active users in combination with the mixture of offered services with different demands on delay, throughput and residual error rates have a deep impact on the performance of the radio network perceived by the user. A scheduling entity assigns the radio resources, i.e., in case of OFDM systems like the considered UMTS LTE the resource blocks (RBs), to the users according to their demand, their instantaneous channel quality (SINR) and the overall load of the system.

A statistical long-term analysis of the radio network behavior would require the modeling of user traffic and their requests for radio resources, e.g., by Poisson processes. Additionally, abstractions of the radio resource management and admission control algorithms had to be included. This work, however, considers the maximum achievable capacity of radio cells, i.e., the capacity in terms of cell and user goodput at a certain point in time, when the maximum possible number of resource elements (REs) is assigned to the UEs within that cell, i.e., a fully loaded cell. Two different service scenarios are considered:

Best Effort In this scenario, a fixed number of users is admitted to the radio cell and the

available REs are equally shared among these users. The choice of allocating REs rather than RBs allows for a finer granularity of the achieved performance. Note that for complexity reasons, RBs are the minimum quantity of radio resources assigned to users of a UMTS LTE radio cell. However, the scheduling of single REs to single users can be interpreted as the scheduling of the same resource block to different users at different time instances. The best effort service scenario is used to illustrate the distribution of individual user goodputs \mathcal{G} within one radio cell.

Fixed Services This scenario describes a situation, where users request the same service which requires a certain service-specific fixed goodput \mathcal{G} . In this scenario, any UE is admitted to the radio cell, if there is a sufficient number of REs left to support the requested service. This will, of course, not only depend on the requested goodput but also on the user's location within the radio cell which determines the user's current SINR. This scenario is used to determine the capacity of mobile radio systems in terms of the number of UEs provided with a certain demanded service.

6.1.4 Summary of System-Level Simulation Parameters

Unless stated otherwise, the parameters summarized in Tab. 6.1 are employed for system-level simulation.

Parameter	Value
Network layout	hexagonal (1 serving, 6 interfering BSs)
Cell radii r	200 m, 10 km (micro-cell, macro-cell)
Network scenarios	UMi, UMa, RMa
Pathloss models L	COST231WI, COST231Hata, 3GPPUrban, 3GPPRural
Carrier frequencies f_0	0.8 GHz, 2.0 GHz
Frequency bandwidths Δf	5 MHz, 20 MHz
Transmit powers P_{Tx}	43 dBm, 46 dBm (depending on Δf)
Thermal noise powers N_{th}	-107 dBm, -101 dBm (depending on Δf)
Additional gains and losses G_{Tx}	15 dB
Inter-cell interference factor α	1, 0.5, 0.2, 0

Table 6.1: System-level simulation parameters for UMa scenarios.

The calculation of the SINR can be summarized in the following steps:

1. The choice of a certain propagation scenario (UMi, UMa1, UMa2, RMa) determines the network topology by setting a cell radius r and a path loss model.
2. The user position \mathbf{x}_{UE} determines the resulting pathloss for useful and interfering signal levels.

3. The choice of the inter-cell interference factor α models the influence of the inter-cell interference, either from the use of interference cancellation (IC) algorithms or due to a single cell deployment without adjacent cells.

6.2 Prediction of Average Cell Goodput $\overline{\mathcal{G}}$

Given the hexagonal network with one central serving base station and a ring of six surrounding interferers, the signal-to-interference-and-noise ratio as given by (6.2) is analytically defined by UE position \mathbf{x}_{UE} and the assumed system-level parameters.

The SNR dependent achievable bits per channel use \mathcal{B} have been determined by simulation of physical layers or bounded by analytical expressions (see Chapters 4 and 5). With the aforementioned assumption of inter-cell interference resembling independent AWGN processes, the location dependent achievable bits per channel use $\mathcal{B}(\mathbf{x})$ are then given by

$$\mathcal{B}(\mathbf{x}) = \mathcal{B}(\text{SINR}(\mathbf{x})). \quad (6.3)$$

From that the average of the achievable bits per channel use $\overline{\mathcal{B}}$ for UEs distributed evenly within the cell area \mathbf{A} can be calculated as expectation

$$\overline{\mathcal{B}} = \mathcal{E}\{\mathcal{B}(\mathbf{x})\} = \frac{1}{\mathbf{A}} \int_{\mathbf{x} \in \mathbf{A}} \mathcal{B}(\mathbf{x}) \, d\mathbf{x}. \quad (6.4)$$

With the number of available resources n_{RE} per symbol duration T_{S} the average cell goodput $\overline{\mathcal{G}}$ can be calculated. For UMTS LTE n_{RE} is given by the frequency bandwidth dependent number of REs per time slot (cf. Tab. 4.1) and the slot duration is $T_{\text{Slot}} = 0.5$ ms. The average cell goodput for the UMTS LTE radio cell is then given by

$$\overline{\mathcal{G}} = \frac{\overline{\mathcal{B}} n_{\text{RE}}}{T_{\text{Slot}}} = \frac{n_{\text{RE}}}{\mathbf{A} T_{\text{Slot}}} \int_{\mathbf{x} \in \mathbf{A}} \mathcal{B}(\mathbf{x}) \, d\mathbf{x}. \quad (6.5)$$

For UMTS LTE and its modifications and alternatives introduced earlier, the achievable bits per channel use \mathcal{B} are obtained from PHY simulations employing different PHY channel models, preventing a closed form solution of (6.5). The upper bounds on \mathcal{B} defined by (5.11) and the approximation $\tilde{\mathcal{B}}$ for UMTS LTE defined by (4.25) are derived from the Shannon limit and contain logarithmic expressions. Therefore $\overline{\mathcal{G}}$ is determined by numerical integration for

- the different system-level propagation scenarios (UMi, UMa1, UMa2, RMa),
- the different inter-cell interference factors α ,
- the achievable bits per channel use \mathcal{B} of UMTS LTE as depicted in Fig. 4.8 for the different PHY channel models (AWGN, TU, Rayleigh, cf. definition of channel models in Sec. 4.1.5),

- and the upper bounds on \mathcal{B} (Shannon, 2×2 MIMO, 4×4 MIMO) as given by (5.11) in Sec. 5.6.

All results are summarized in Annex C, while major observations are described in the following.

6.2.1 HSDPA vs. LTE

As stated in Sections 4.2.2 and 4.3.2, the physical layers of HSDPA and LTE are expected to deliver a comparable performance concerning the achievable bits per channel use \mathcal{B} . The key to the performance gain of LTE over HSDPA lies in the spectral efficiency which is determined by the time bandwidth product of the underlying modulation stages. Assuming a system bandwidth of $\Delta f = 5$ MHz for both systems, LTE generates 4200 modulation symbols per millisecond (including normal CP, cf. Table 4.1), whereas HSDPA generates 3840 modulation symbols per millisecond (3.84 Mchip/s, cf. Sec. 4.2.2). These numbers scale linearly with the system bandwidth Δf . The concept of aggregating multiple 5 MHz carriers in HSDPA is known as Multicarrier-HSDPA [60]. With (6.5) based on the same achievable bits per channel use \mathcal{B} for LTE and HSDPA, the average cell goodput for HSDPA $\overline{\mathcal{G}}^{[\text{HSDPA}]}$ can then be expressed with the help of the average cell goodput for LTE $\overline{\mathcal{G}}^{[\text{LTE}]}$:

$$\overline{\mathcal{G}}^{[\text{HSDPA}]} = \frac{3840}{4200} \overline{\mathcal{G}}^{[\text{LTE}]} \approx 0.914 \overline{\mathcal{G}}^{[\text{LTE}]} . \quad (6.6)$$

In accordance with (4.30) it can be stated that HSDPA in combination with its extensions HSDPA+ (supporting 64QAM mapping) and Multicarrier-HSDPA (supporting carrier aggregation) can achieve approximately 90 % of the average cell goodput of LTE when the same frequency bandwidths Δf are considered.

6.2.2 Influence of the Propagation Scenario

Figure 6.10 depicts the average cell goodput $\overline{\mathcal{G}}$ in Mbit/s based on the physical layer simulation results as given in Fig. 4.8 for the AWGN case. Gray and white bars mark results for carrier frequencies of $f_0 = 0.8$ GHz and $f_0 = 2.0$ GHz, respectively. Depicted are the average cell goodputs for the considered propagation scenarios and system frequency bandwidths Δf . No interference cancellation is employed, i.e., $\alpha = 1$ and AWGN is chosen as PHY channel model.

As expected, in the interference limited scenarios UMi and RMa both carrier frequencies perform equally, while in UMa propagation scenario the lower carrier frequency of $f_0 = 0.8$ GHz achieves significantly higher results. The comparison of the frequency bandwidths (Fig. 6.10(a) vs. Fig. 6.10(b)) reveals the expected quadruplication of the average cell goodput in UMi and RMa propagation scenarios. For the noise limited UMa propagation scenario, however, this gain is observed only partly. With a quadruplication of the frequency bandwidth, the thermal noise power quadruples as well (+6 dB) while the transmit power is only doubled from $P_{\text{Tx}} = 43$ dB to $P_{\text{Tx}} = 46$ dB. This effect is more distinct

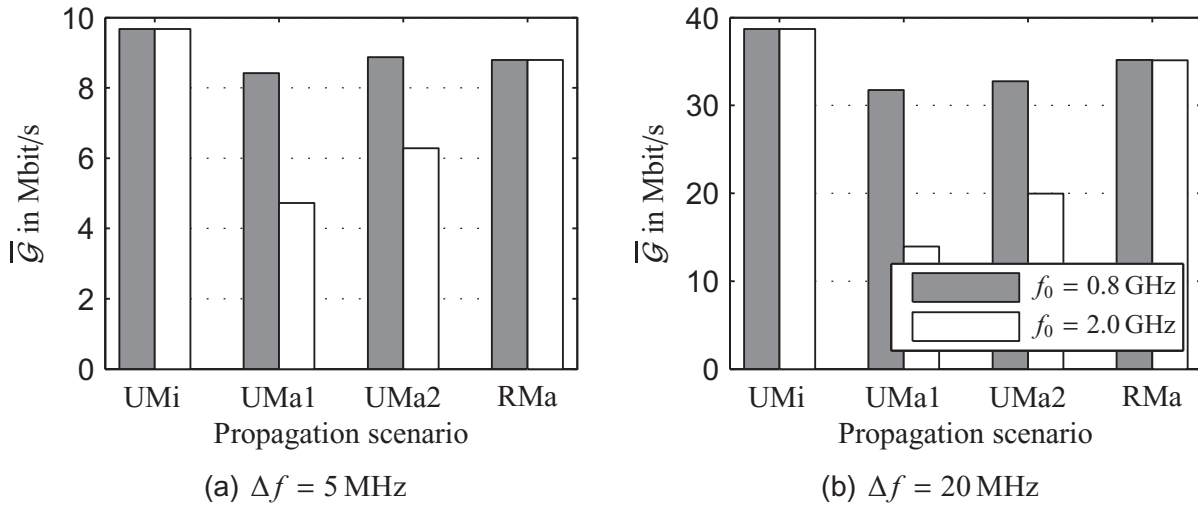


Figure 6.10: $\bar{\mathcal{G}}$ of UMTS LTE for different propagation scenarios, carrier frequencies f_0 , and frequency bandwidths Δf assuming AWGN without interference cancellation ($\alpha = 1$).

for $f_0 = 2.0$ GHz compared to $f_0 = 0.8$ GHz which indicates a larger influence of the inter-cell interference to the SINR for $f_0 = 0.8$ GHz. This again is due to the lower path loss of the lower carrier frequency which does not only account for the transmitted useful signal but also for the interfering signals. The maximum average cell goodput of $\bar{\mathcal{G}} = 38.7$ Mbit/s is observed for $\Delta f = 20$ MHz in a UMi propagation scenario independent of the carrier frequency (cf. Tab. C.1).

6.2.3 PHY Simulation vs. Approximation

Figure 6.11 compares the resulting $\bar{\mathcal{G}}$ obtained from LTE PHY simulations in case of AWGN to the results obtained with the approximation $\tilde{\mathcal{B}}$ for UMTS LTE defined by (4.25). The results are given for both considered system frequency bandwidths and all considered propagation scenarios. No interference cancellation is employed, i.e., $\alpha = 1$, and the carrier frequency is set to $f_0 = 0.8$ GHz.

It is observed that the approximation slightly underestimates the results obtained from the simulated \mathcal{B} . However, this accounts only for several 100 kbit/s of the resulting average cell goodput $\bar{\mathcal{G}}$ which, given the abstract nature of the employed models can be considered negligible. All results are given in Tab. C.2.

6.2.4 Influence of the PHY Channel Model

Figure 6.12 compares the resulting $\bar{\mathcal{G}}$ for the different employed channel models introduced in Section 4.1.5 based on the obtained bits per channel use \mathcal{B} as depicted in Fig. 4.8. The results are given for both considered system frequency bandwidths and carrier frequencies, no interference cancellation is employed, i.e., $\alpha = 1$. Although results are depicted only

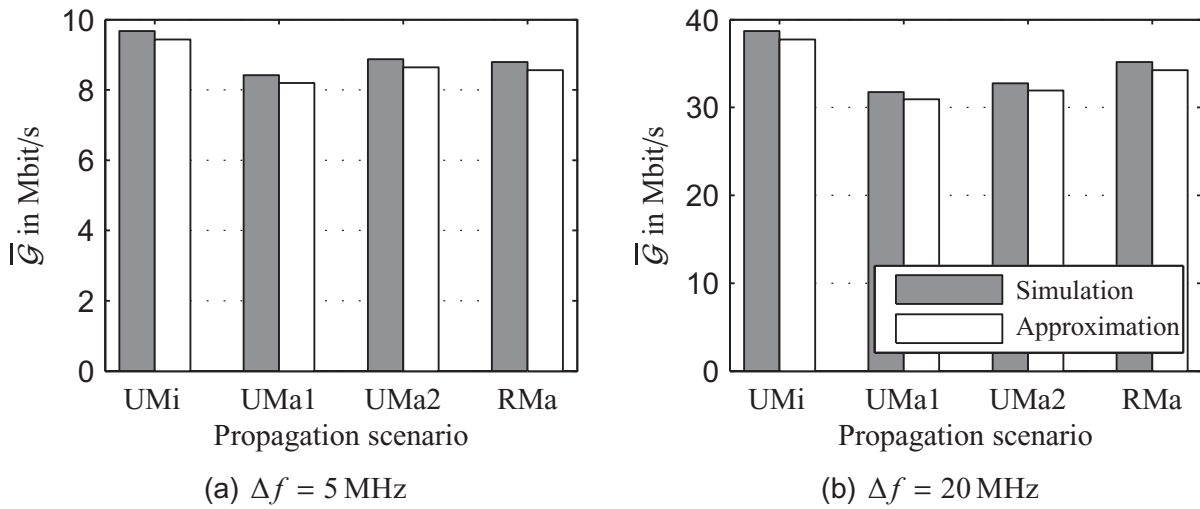


Figure 6.11: $\bar{\mathcal{G}}$ of UMTS LTE and approximation according to (4.25) for different propagation scenarios and frequency bandwidths Δf , carrier frequency $f_0 = 0.8$ GHz, AWGN, no interference cancellation ($\alpha = 1$).

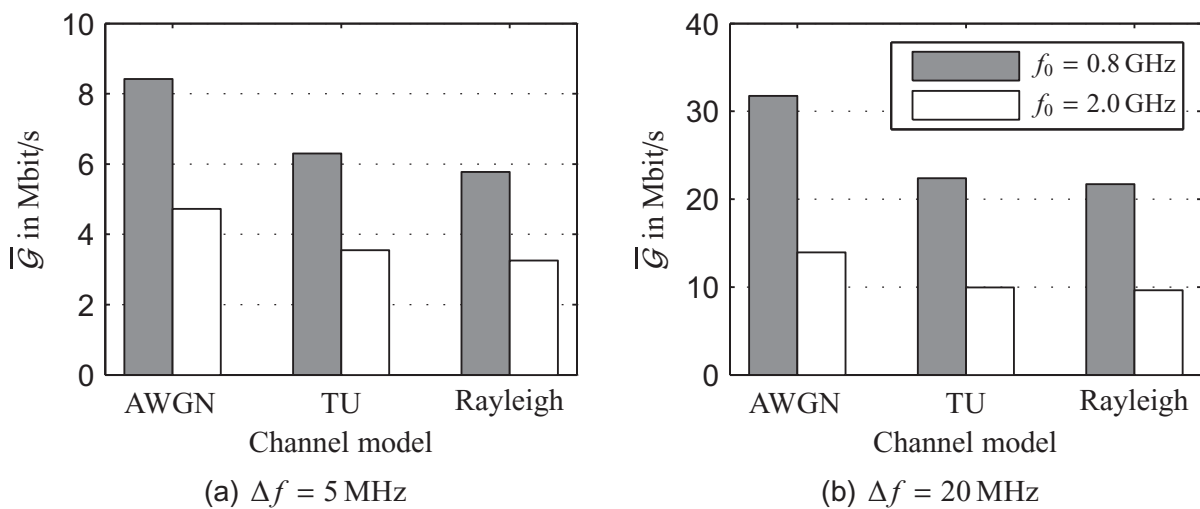


Figure 6.12: $\bar{\mathcal{G}}$ of UMTS LTE in UMa1 propagation scenario for different PHY channel models, carrier frequencies f_0 , and frequency bandwidths Δf , no interference cancellation ($\alpha = 1$).

for the UMa1 propagation scenario, a similar behavior is observed for the other propagation scenarios.

As already indicated by the progressions of \mathcal{B} in Fig. 4.8, the best results are obtained for the AWGN channel while the weakest performance in terms of average cell goodput $\overline{\mathcal{G}}$ is achieved for the frequency flat Rayleigh fading channel. In case of the typical urban (TU) channel model, only slight $\overline{\mathcal{G}}$ gains are observed compared to the frequency flat Rayleigh fading channel. All results for the TU and Rayleigh models are given in Tabs. C.3 and C.4.

6.2.5 Influence of Interference Cancellation

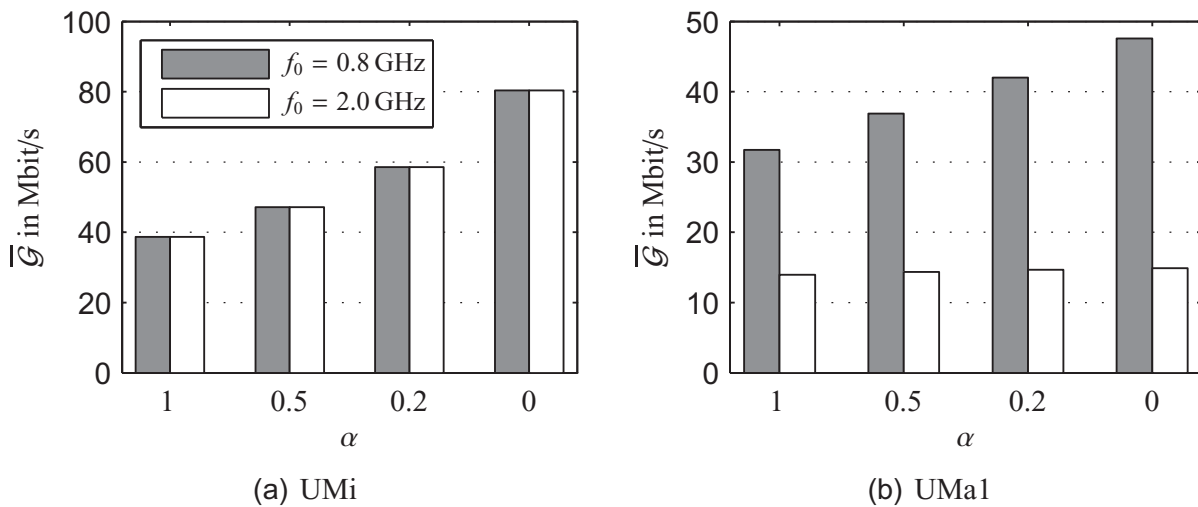


Figure 6.13: $\overline{\mathcal{G}}$ of UMTS LTE for different interference cancellation factors α and carrier frequencies f_0 in interference and noise limited propagation scenarios, AWGN, $\Delta f = 20$ MHz.

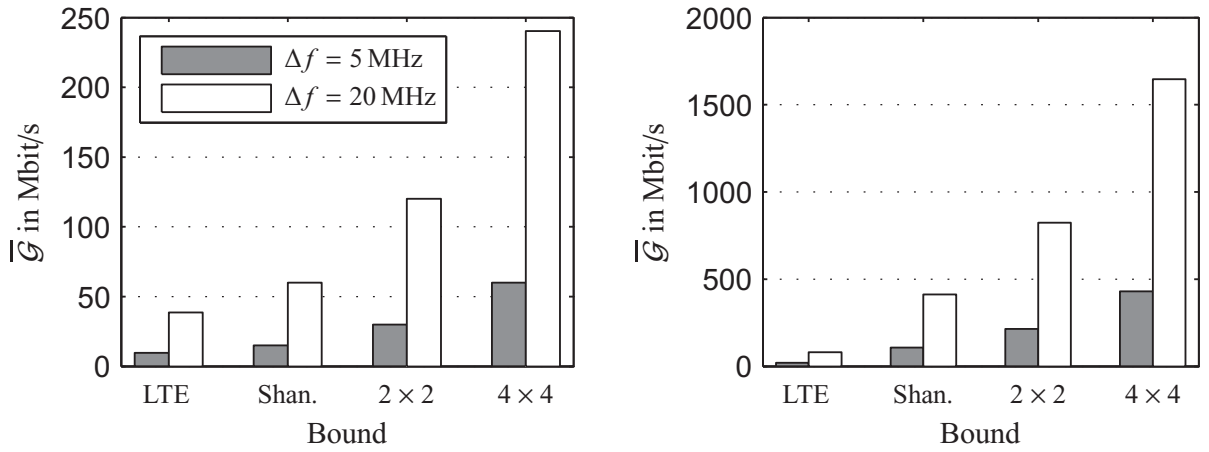
Figure 6.13 depicts the effect of interference cancellation. The resulting $\overline{\mathcal{G}}$ is based on LTE PHY simulations with AWGN for a system frequency bandwidth of $\Delta f = 20$ MHz, both considered carrier frequencies and two propagation scenarios. In Fig. 6.13(a) the average cell goodput for the interference limited UMi propagation scenario is depicted, while Fig. 6.13(b) considers the noise limited UMa1 propagation scenario.

It is observed that with increasing interference cancellation (decreasing α) the performance is significantly improved in the UMi propagation scenario. This improvement is independent of the carrier frequency which is explained by the small cell size and the resulting high SINR at all locations within the cell for all carrier frequencies when interference is canceled out. Compared to the case without IC ($\alpha = 1$), the average cell goodput doubles in the UMi propagation scenario if perfect IC ($\alpha = 0$) is assumed.

For the UMa1 propagation scenario the gains are less significant. Especially for $f_0 = 2.0$ GHz, only marginal $\overline{\mathcal{G}}$ improvements (a few 100 kbit/s) are observed which underlines the noise limitation of this case due to the higher path loss. A gain of approximately 50 % is

achieved by perfect IC for $f_0 = 0.8$ GHz underlining the influence of the interference in UMa propagation scenarios at this carrier frequency. The influence of interference cancellation is given in all tables in Appendix C.

6.2.6 Bounds on $\bar{\mathcal{G}}$



(a) No inter-cell interference cancellation ($\alpha = 1$) (b) Inter-cell interference cancellation ($\alpha = 0$)

Figure 6.14: Bounds on $\bar{\mathcal{G}}$ in UMi propagation scenario for both frequency bandwidths Δf at carrier frequency $f_0 = 0.8$ GHz with and without interference cancellation.

Figure 6.14 depicts the bounds on $\bar{\mathcal{G}}$ based on the bounds on the achievable bits per channel use \mathcal{B} derived in Section 5.6. Both employed frequency bandwidths are considered with a carrier frequency of $f_0 = 0.8$ GHz in a UMi propagation scenario. Figure 6.14(a) assumes no interference cancellation ($\alpha = 1$), while Fig. 6.14(b) assumes perfect interference cancellation ($\alpha = 0$). The different bounds on the abscissa of each plot are denoted

Shan. indicating the bound derived from the Shannon limit, i.e., (5.11) for $A = 1$ Tx and Rx antenna, and

$X \times X$ indicating the bound derived from (5.11) for $A = X \in \{2; 4\}$, i.e., a $X \times X$ MIMO system.

LTE denotes the results from LTE PHY simulations assuming AWGN for comparison.

The results indicate a huge potential to increase the average cell goodput in the depicted propagation scenario by employing MIMO and interference cancellation techniques. The maximum value of $\bar{\mathcal{G}} > 1.6$ Gbit/s is obtained as bound for a 4×4 MIMO system with $f_0 = 0.8$ GHz and $\Delta f = 20$ MHz utilizing full interference cancellation. A major reason for these high values compared to UMTS LTE is the assumption of a Gaussian input distribution with arbitrarily high values of information bits per channel use. With that assumption a high

number of bits per channel use could theoretically be transmitted in ideal conditions (cf. Sec. 5.6). However, this would require sophisticated signal constellation sets and mapping rules μ with large numbers I of bits per complex symbol. Furthermore, the computational complexity of MIMO detection and interference cancellation can at a certain point be expected to exceed the potential gains that can be achieved by these measures.

Coverage, Quality, and Capacity

This chapter presents system-level simulation results based on the findings of Chapters 4 and 5 and the assumptions from Chapter 6. In its first part it summarizes findings on the coverage and capacity that can be expected from UMTS LTE networks. The second part of this chapter highlights the potentials of future mobile broadband access networks and examines the specific influences of modifications and alternative physical layer implementations.

7.1 Coverage and Capacity of UMTS LTE

It has been shown in Section 6.2 that the average cell goodput of a UMTS LTE radio cell is strongly influenced by different cell specific parameters leading to characteristic spatial distributions of the SINR. System-level simulations of a UMTS LTE mobile radio network based on the assumptions of Chapter 6 have been conducted illustrating different aspects such as modulation and coding scheme (MCS) distribution, distribution of the individual user goodput \mathcal{G} and number of users for different combinations of service scenarios and propagation scenarios. As a fully loaded LTE network without interference cancellation (IC) is considered, an interference factor of $\alpha = 1$ (full interference) is considered for all simulations of this section. The findings of Fig. 4.8 provide the PHY basis for all system-level simulations of UMTS LTE networks.

7.1.1 Adaptive Modulation and Coding

A major feature of UMTS LTE is the support of adaptive coding and modulation (ACM): While a MCS allowing for the transmission of a large number of bits per channel use \mathcal{B} is supported only in regions with high SINR, the MCS can be adapted to the SINR if the channel quality degrades, e.g., with increasing distance from the serving base station (BS).

Figure 7.1 shows an example for a possible distribution of signal constellation sets (SCSs) and resulting bits per channel use \mathcal{B} in a UMi propagation scenario with 100 UEs. As expected, high values of \mathcal{B} resulting from SCSs with a high number I of bits per complex symbol, e.g. 64QAM (stars), occur near the BS, while lower valued SCSs, e.g., QPSK (circles), resulting in lower values of \mathcal{B} occur near the cell edges. Determining the SINR at a large number ($> 100,000$) of uniformly distributed locations in the cell area and performing ACM by determining the best achievable \mathcal{B} for all possible MCSs yields the occurrences

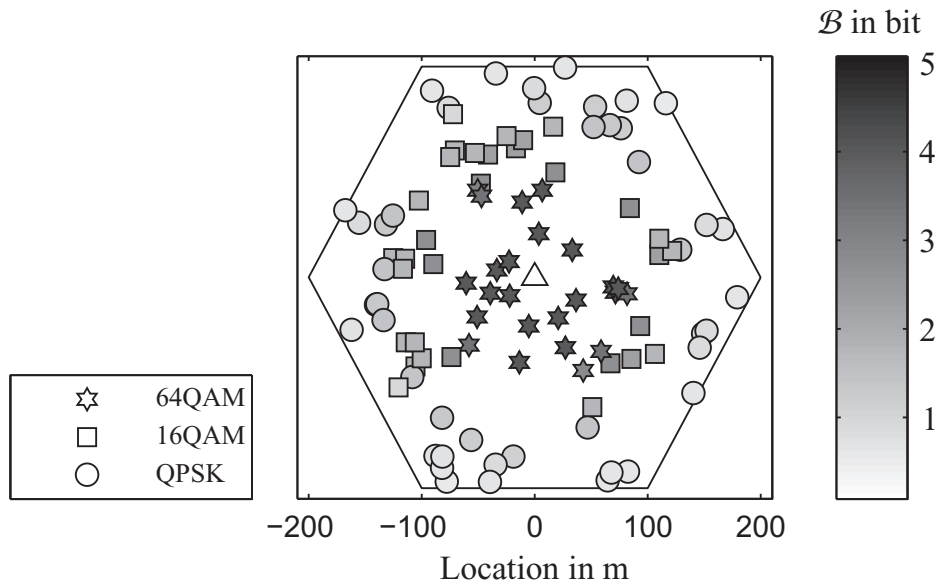


Figure 7.1: Signal constellation set and achievable bit per channel use \mathcal{B} per user in a UMi propagation scenario.

of all MCSs. This MCS distribution varies with the assumed parameters for propagation scenario, channel model, system frequency bandwidth Δf , and carrier frequency f_0 .

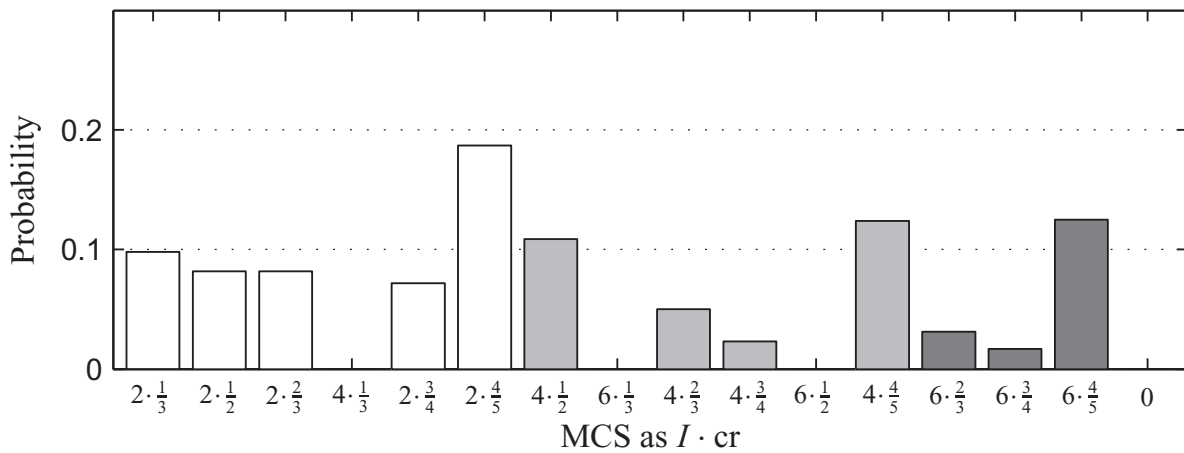


Figure 7.2: MCS distribution for LTE in UMa1 propagation scenario assuming AWGN, $f_0 = 0.8$ GHz, $\Delta f = 5$ MHz, I number of bits per complex mapping symbol, cr code rate.

The MCS distribution for the UMa1 scenario with $f_0 = 2.0$ GHz and $\Delta f = 20$ MHz with AWGN as channel model is shown in Fig. 7.2. The MCS is given on the abscissa by the number I of bits per complex mapping symbol determining the SCS (2: QPSK, 4: 16QAM, 6: 64QAM) and the code rate cr . The product $I \cdot cr$ determines the achievable bits per channel use for the initial transmission (RV0). The rightmost MCS denoted 0 indicates the percentage of UEs which could not be assigned a MCS due to a too low SINR at their

location ($\text{SINR} < -7.5$ dB). It is observed that most of the possible MCSs are assigned with a significant probability, no MCS dominates. The probability for UEs without assigned MCS is zero, which indicates that full coverage is provided by the BS to the cell area.

The depicted distribution has been observed to hardly vary for the different propagation scenarios, carrier frequencies, and frequency bandwidths. A slightly larger impact has been observed for the assumed PHY channel model, which has already been indicated by the findings of Fig. 4.8 and therefore is not depicted separately. Due to the selective nature of the TU and Rayleigh radio channels, SINR losses have been observed in the \mathcal{B} progressions. These results in higher probabilities of the more robust MCSs and consequently lower probabilities of MCS allowing for a higher user goodput.

One interesting aspect in all considered cases is that the two schemes 16QAM with $\text{cr} = 1/3$ coding ($4 \cdot \frac{1}{3}$) and 64QAM with $\text{cr} = 1/3$ coding ($6 \cdot \frac{1}{3}$) never occur at all. These are substituted by the schemes $2 \cdot \frac{2}{3}$ and $4 \cdot \frac{1}{2}$, respectively, which provide the same maximum achievable bits per channel use \mathcal{B} but outperform the non-occurring MCSs in terms of SINR. The MCS $6 \cdot \frac{1}{2}$ only occurs for the typical urban (TU) channel model (not depicted).

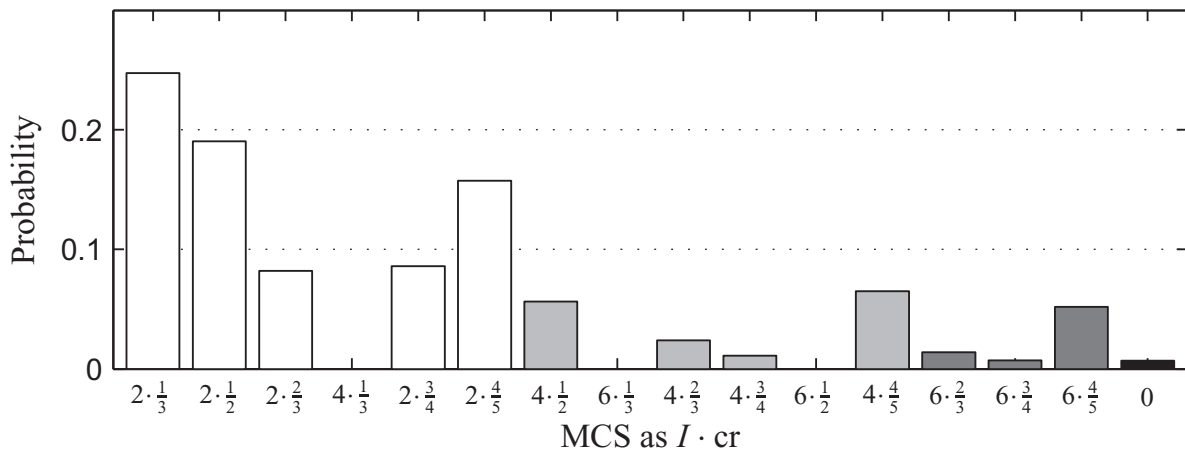


Figure 7.3: MCS distribution for LTE in UMa1 propagation scenario assuming AWGN, $f_0 = 2.0$ GHz, $\Delta f = 5$ MHz, I number of bits per complex mapping symbol, cr code rate.

A significant effect is observed in UMa propagation scenarios, especially for the UMa1 propagation model (COST231Hata), when varying carrier frequency and frequency bandwidth. Comparing Figs. 7.2 and 7.3 it can be recognized, that for the higher carrier frequency $f_0 = 2.0$ GHz more robust schemes occur with higher probability and a small portion ($\approx 1\%$) of the UEs is not assigned any MCS due to too low SINR values. These findings are in line with the findings from Fig. 6.7 indicating SINR values near the cell edge, which do not support any of the considered MCSs (see also Fig. 4.8). As already mentioned in Section 6.1.2, the reason is the high propagation loss predicted by the COST231Hata model in case of $f_0 = 2.0$ GHz.

As depicted in Fig. 7.4, the loss of coverage is even worse when the frequency bandwidth is increased to $\Delta f = 20$ MHz. Approximately 17% of the UEs within the geographic cell

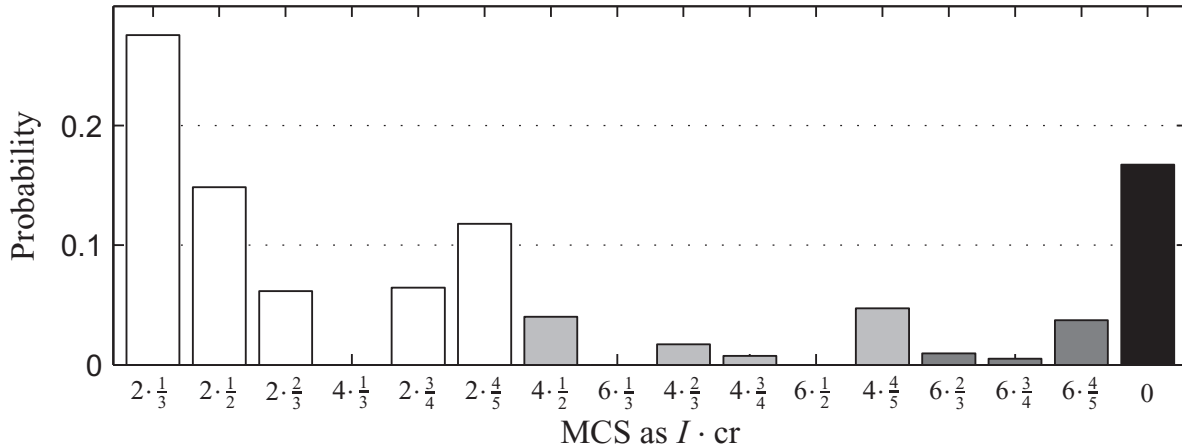


Figure 7.4: MCS distribution for LTE in UMa1 propagation scenario assuming AWGN, $f_0 = 2.0$ GHz, $\Delta f = 20$ MHz, I number of bits per complex mapping symbol, cr code rate.

area cannot be supported by the BS due to their low SINR near the cell edge (cf. Fig. 6.9(b)). This is due to the increased thermal noise power which, as already stated, rises linearly with Δf by a factor of four, while the transmit power is only doubled. This leads to an even lower SINR at the cell edge in this noise limited case.

It has to be noted, that these lacks of coverage have been observed only for both UMa propagation scenarios which are the only noise limited cases. This indicates, that the advantage from lower carrier frequencies like those from the digital dividend are gains in coverage. Due to the better propagation characteristics of the lower carrier frequencies, a larger cell area can be covered by one base station. In a cellular network employing lower carrier frequencies area wide coverage can be achieved with fewer base stations. However, area wide coverage implies that radio cells of such a network are, if fully loaded, interference limited and show MCS distributions similar to those of smaller interference limited cells with higher carrier frequencies.

7.1.2 User Data Rates

The system-level simulation results describing the probability of the occurrences of the different MCSs imply at the same time that a UE with a certain number of resource elements (REs) allotted by the scheduler will experience a certain individual user goodput \mathcal{G} which is determined by its position and the resulting SINR. To illustrate the impact of parameters like carrier frequency f_0 , frequency bandwidth Δf , PHY channel model, or propagation scenario on the individual user goodput, system-level simulations have been conducted in form of Monte-Carlo simulations.

In each of 1000 Monte-Carlo iterations a predefined number of UEs (either 20 or 100) is randomly placed within the cell area of the serving cell. For each UE the individual SINR is calculated and the maximum achievable bits per channel use \mathcal{B} is determined. All available resource elements are then shared equally among all users (Best Effort service scenario)

and the resulting goodput \mathcal{G} of each individual user is recorded. After the final Monte-Carlo iteration, all individual goodputs are evaluated in form of a cumulative distribution function (CDF). The plotted CDF indicates for a certain individual user goodput \mathcal{G} the percentage of UEs which achieve this or a smaller value of \mathcal{G} . From the findings discussed before it can be assumed that the lowest user goodputs will be achieved by the UEs near the cell edge while the upper percentiles are achieved by UEs near the BS. A small slope of the CDF indicates a large variance of user goodputs, while a steep slope indicates less varying goodputs which implies smaller goodput differences between UEs at the cell edge and UEs near the BS. Note that in accordance with the assumptions from Section 6.1.3 the number of UEs present in the radio cell denotes UEs which are requesting radio resources at the same time.

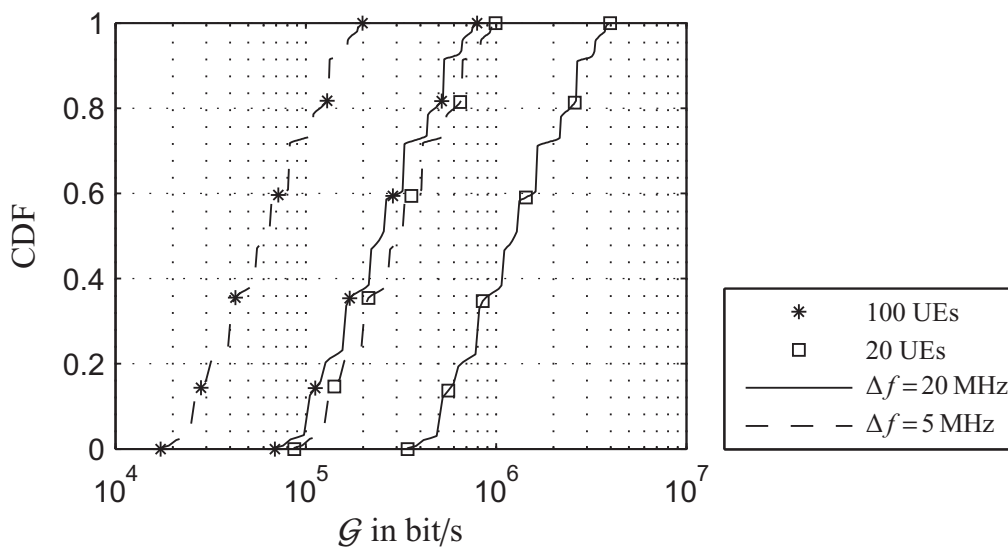


Figure 7.5: Cumulative distribution function of individual user goodput \mathcal{G} for different frequency bandwidths and number of UEs, UMi, AWGN, $f_0 = 2.0$ GHz, Monte-Carlo simulation.

The number of UEs and the available system bandwidth are expected to have a linear effect on the individual user goodputs observed in a radio cell, because these parameters directly scale the number of available REs. This assumption is confirmed by Fig. 7.5 which compares the CDFs of the achieved individual user goodputs for the two considered frequency bandwidths and two different numbers of UEs in a UMi propagation scenario with AWGN at $f_0 = 2.0$ GHz. As expected, all CDFs exhibit the same progression which proves the predicted scaling of resources. For 100 UEs (*) and $\Delta f = 5$ MHz (dashed lines) the weakest 20% (0 – 0.2 on ordinate) of the users, i.e., those at the cell edges, achieve only 20 – 30 kbit/s while the strongest 20% (0.8 – 1 on ordinate) of the users, i.e., those close to the BS achieve 100 – 200 kbit/s. If, on the one hand, only 20 UEs (\square) are present in the cell, these figures quintuple. If, on the other hand, the frequency bandwidth is quadrupled from $\Delta f = 5$ MHz to $\Delta f = 20$ MHz (solid lines), the user goodputs quadruple as well. The maximum goodputs of 2 – 4 Mbit/s are consequently achieved by the best 20% of UEs

near the BS with $\Delta f = 20$ MHz when 20 UEs are present in the cell. It can be concluded from the SINR figures in the UMi propagation scenario, that the carrier frequency does not influence the individual goodputs (cf. Fig. 6.6). This is confirmed by simulation results for $f_0 = 0.8$ GHz (not depicted). One exception of these findings is the UMa propagation scenario, which therefore is discussed later in this section in detail.

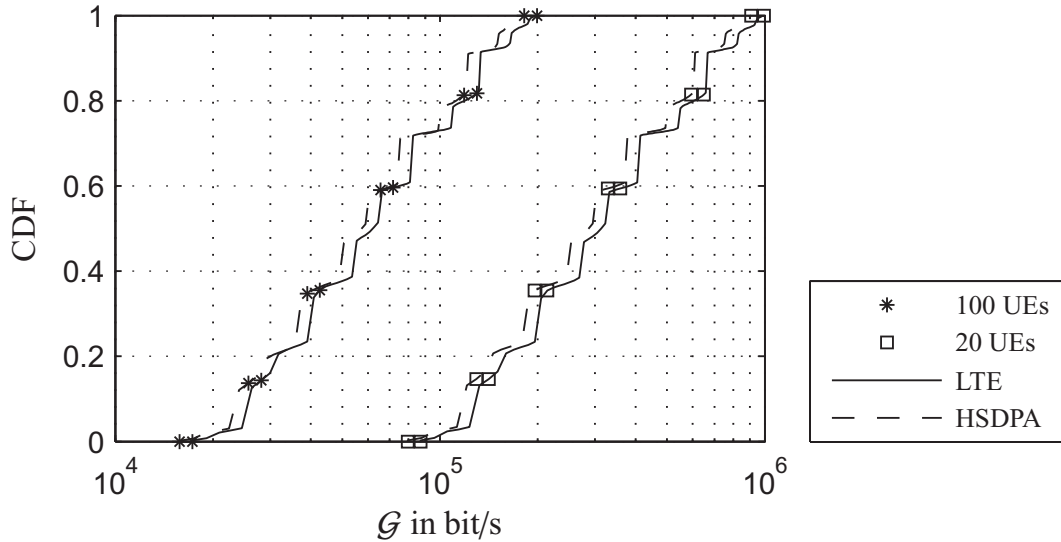


Figure 7.6: Cumulative distribution function of individual user goodput \mathcal{G} for LTE and HSDPA, UMi, AWGN, $f_0 = 2.0$ GHz, $\Delta f = 5$ MHz, Monte-Carlo simulation.

Figure 7.6 compares the achieved individual user goodput of UMTS LTE (solid lines) and UMTS HSDPA (dashed lines) in a UMi propagation scenario for $f_0 = 2.0$ GHz and $\Delta f = 5$ MHz. For a fair comparison to LTE where all REs are assumed to contribute to the user goodput, the HSDPA simulations used here also assume the availability of all resources for user traffic (16 channelization codes). It is observed that both CDFs exhibit the same progressions shifted by a constant offset. This constant offset represents the constant factor of 0.91 between available radio resources in HSDPA and LTE as calculated in Section 6.2.1.

Figure 7.7 compares the results based on PHY simulations (solid lines) to the 3GPP reference approximation from [15] defined by (4.25) (dashed lines). A UMi propagation scenario with AWGN, $f_0 = 2.0$ GHz, and $\Delta f = 5$ MHz is assumed. The figure confirms the validity of the approximation. The characteristic unevenness of the CDF based on PHY simulations resulting from the different MCS which are forming the envelope of \mathcal{B} disappears for the approximation $\tilde{\mathcal{B}}$.

The influence of the different PHY channel models on the individual user goodput is depicted in Fig. 7.8 for 100 UEs in a UMi propagation scenario with $f_0 = 2.0$ GHz and $\Delta f = 5$ MHz. The results confirm the already mentioned findings that the most advantageous AWGN case leads to the highest user goodput near the cell edge while the frequency flat Rayleigh channel is the most disadvantageous concerning the user goodput. As expected from the convergence of the \mathcal{B} progressions for the considered PHY channel models in

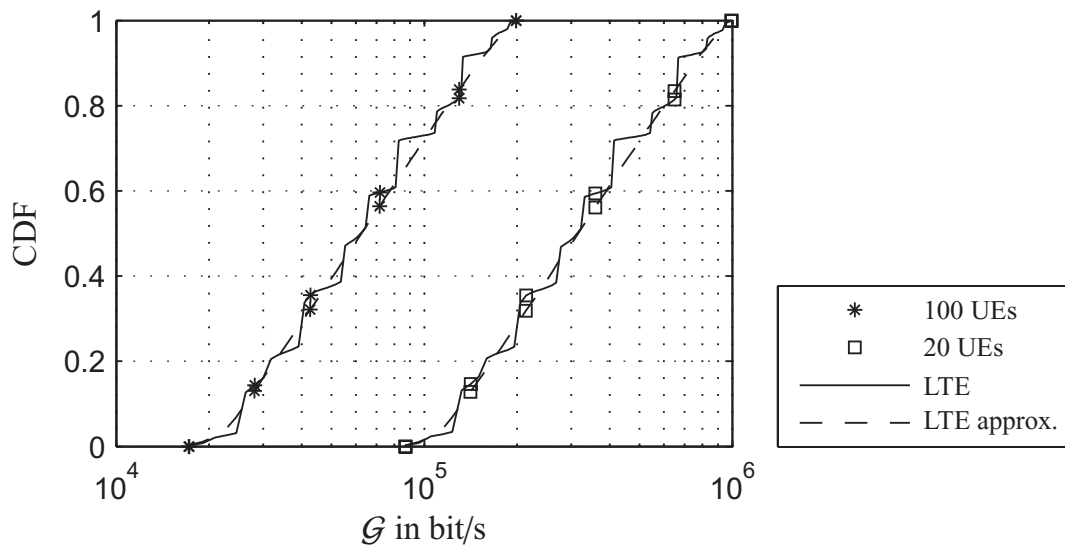


Figure 7.7: Cumulative distribution function of individual user goodput \mathcal{G} for LTE and approximation according to (4.25), UMi, AWGN, $f_0 = 2.0$ GHz, $\Delta f = 5$ MHz, Monte-Carlo simulation.

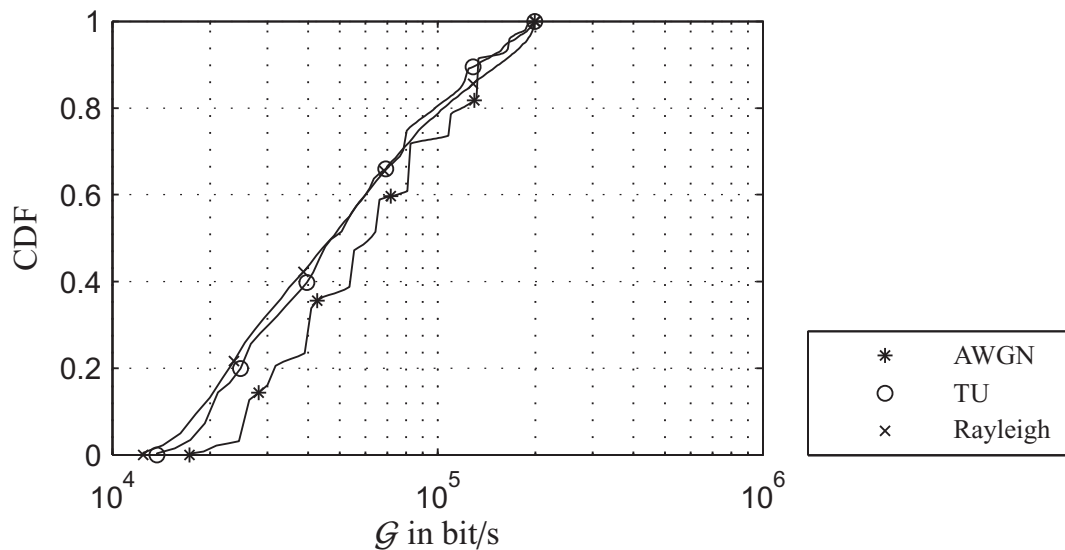


Figure 7.8: Cumulative distribution function of individual user goodput \mathcal{G} for different PHY channel models, UMi, 100 UEs, $f_0 = 2.0$ GHz, $\Delta f = 5$ MHz, Monte-Carlo simulation.

Fig. 4.8, all cases lead to the same maximum goodputs of the strongest UEs near the BS.

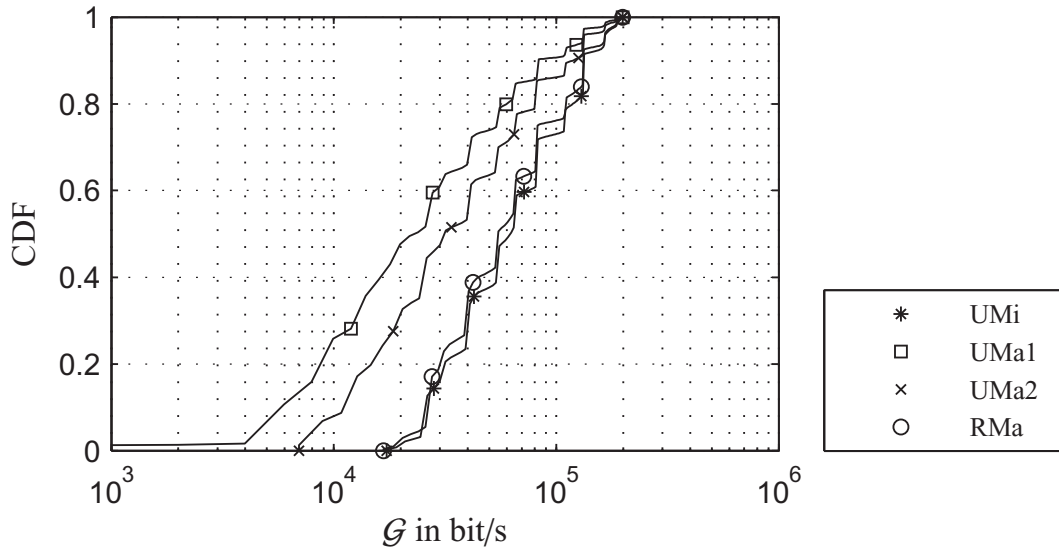


Figure 7.9: Cumulative distribution function of individual user goodput \mathcal{G} for different propagation scenarios, AWGN, 100 UEs, $f_0 = 2.0$ GHz, $\Delta f = 5$ MHz, Monte-Carlo simulation.

Finally, the influence of the propagation scenarios on the achievable individual goodputs is compared in Fig. 7.9 assuming 100 UEs, AWGN, $f_0 = 2.0$ GHz, and $\Delta f = 5$ MHz. The findings in this figure coincide well with those from the SINR progressions in the different scenarios (cf. Figs. 6.6 – 6.8). While the interference limited urban micro-cell (*) and rural macro-cell (o) scenarios exhibit very similar CDFs of the user goodput, the considered path loss models for the urban macro-cells lead to a decreased user goodput near the cell edges. The loss of coverage in case of the COST231Hata model (UMa1, □) is reflected by the almost horizontal progression of the CDF at low data rates, intersecting the ordinate (0 bit/s) at the percentage of UEs without coverage ($\approx 1\%$, cf. Fig. 7.3).

As mentioned before, significant effects of carrier frequency and frequency bandwidth variations occur for the noise limited UMa propagation scenario. Therefore, Fig. 7.10 exemplarily depicts the influence of the considered carrier frequencies and frequency bandwidths on the achievable user goodput assuming path loss according to the COST231Hata model (UMa1), AWGN, and 100 UEs. Again, the results back the conclusions concerning carrier frequency and system bandwidth: The advantageous carrier frequency of $f_0 = 0.8$ GHz (*) yields full coverage of the urban macro-cell. It is also observed that despite the quadrupling of Δf from 5 MHz (dashed lines) to 20 MHz (solid lines) the user goodput at the cell edge is increased by factor smaller four which results from the noise limitation and the aforementioned imbalance of increasing noise and increasing transmit power. The same effect results in the high percentage of unserved UEs in case of $\Delta f = 20$ MHz at $f_0 = 2.0$ GHz (□) already known from Fig. 7.9. The combination of disadvantageous propagation characteristics and high frequency bandwidth which is not compensated by an equal increase of transmit power leads to a significant portion of 17% of unserved UEs.

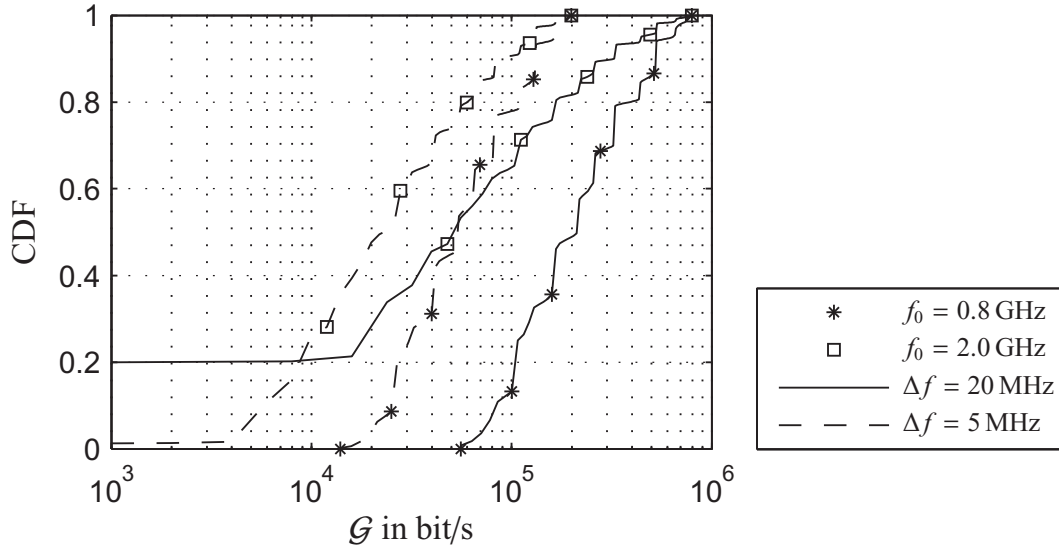


Figure 7.10: Cumulative distribution function of individual user goodput \mathcal{G} for different carrier frequencies and system bandwidths in UMa1 (COST231Hata) propagation scenario, AWGN, 100 UEs, Monte-Carlo simulation.

7.1.3 Capacity with Fixed Services

To determine and compare the capacity in terms of number of served UEs of LTE radio cells for different parameters, system-level Monte-Carlo simulations have been conducted utilizing the fixed services traffic model. For each of 200 iterations a large number of UEs is randomly located within the cell area of the considered radio cell and the channel quality in terms of SINR and the corresponding bits per channel use \mathcal{B} are determined. All UEs are considered to request the same service defined by a certain goodput demand \mathcal{G} . Admission control is executed in a first come first serve manner, i.e., each UE is assigned the number of REs which is required for the chosen service (the requested goodput) with the given \mathcal{B} . If a UE requires more REs than available from the BS, this UE is rejected, i.e., not served at all. As the resource demand of each UE is location dependent, the network is initialized with a large number of UEs at random locations at the beginning of each Monte-Carlo iteration. In that way, the admission control guarantees a maximum usage of REs in each iteration, because the last available REs are assigned to UEs with a high SINR resulting in a low resource demand.

After the final iteration, the average number of users and the resulting sum cell goodput $\check{\mathcal{G}}$ is determined. Due to the depletion of radio resources in the chosen service scenario, generally $\check{\mathcal{G}} \neq \overline{\mathcal{G}}$ holds. Each system-level simulation is repeated for 7 services which require a user goodput \mathcal{G} of 12.2 kbit/s, 64 kbit/s, 256 kbit/s, 348 kbit/s, 1 Mbit/s, 2 Mbit/s, and 6 Mbit/s, respectively, representing a voice service, a video stream service, and typical data streaming services which are provided by current UMTS and DSL connections. The scenarios for the comparison of the influences of different parameters are the same as in the

previous Section 7.1.2 for the user goodput.

Figure 7.11 shows the influence of the frequency bandwidth Δf on the capacity of the considered LTE radio cell assuming a UMi propagation scenario, AWGN, and a carrier frequency of $f_0 = 2.0$ GHz. As expected, the number of served UEs drops with the request for rising user goodput. For lower user goodput, the number of served users approximately quadruples with the quadrupling of the frequency bandwidth from $\Delta f = 5$ MHz (dashed lines) to $\Delta f = 20$ MHz (solid lines). On average, 442 UEs demanding 12.2 kbit/s can be supported with $\Delta f = 5$ MHz while 1767 UEs with the same service can be supported in a $\Delta f = 20$ MHz system, see Fig. 7.11(a). For higher user goodput this linear relation between number of supported UEs and frequency bandwidth does not hold anymore. For the requested goodput of 6 Mbit/s, 2 UEs can be supported on average with $\Delta f = 5$ MHz but only 5 UEs are supported with $\Delta f = 20$ MHz. The sum cell goodput $\check{\mathcal{G}}$ obtained from the multiplication of the number of supported UEs with the demanded goodput (Fig. 7.11(b)) is significantly below the average cell goodput $\bar{\mathcal{G}}$ calculated in Section 6.2. The reason is the disadvantageous admission strategy which assigns the requested amount of REs to all UEs until the depletion of resources, even in case of very low SINRs. Only for the demanded user goodput of 6 Mbit/s and $\Delta f = 5$ MHz it is observed that the obtained cell goodput of $\check{\mathcal{G}} = 12$ Mbit/s significantly exceeds the average cell goodput of $\bar{\mathcal{G}} = 9.7$ Mbit/s (cf. Tab. C.1).

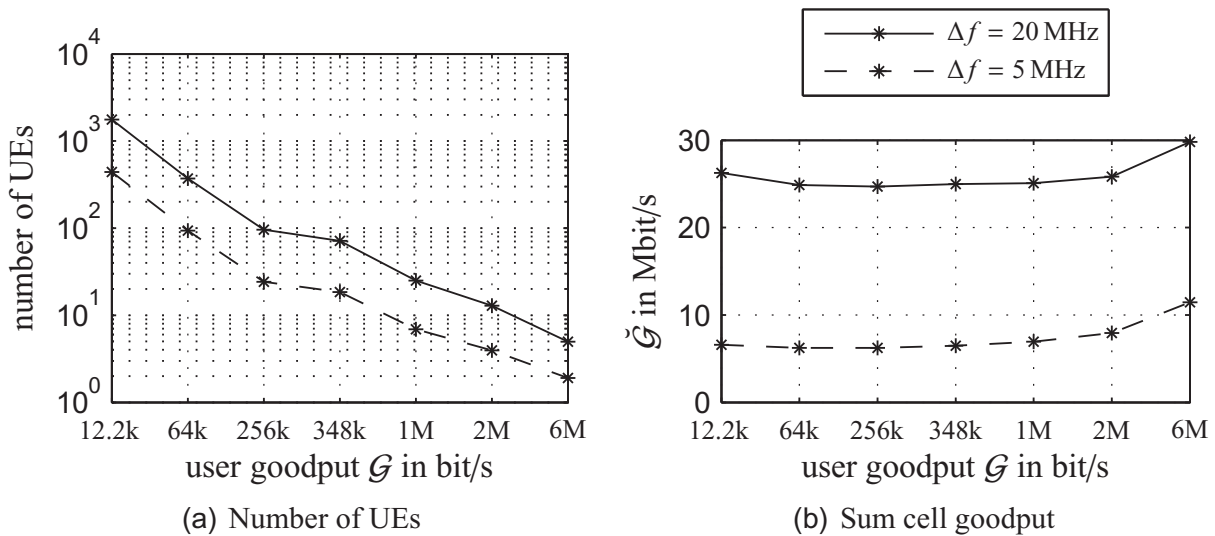


Figure 7.11: Number of UEs and sum cell goodput $\check{\mathcal{G}}$ for different frequency bandwidths, UMi, AWGN, $f_0 = 2.0$ GHz, Monte-Carlo simulation.

The comparison of LTE and HSDPA shown in Fig. 7.12 for a UMi propagation scenario assuming AWGN, $f_0 = 2.0$ GHz, and $\Delta f = 5$ MHz yields only minor advantages of LTE in terms of number of users and cell goodput. These findings are in line with already presented comparisons between LTE and HSDPA concerning goodput distribution for best effort services and average cell goodput $\bar{\mathcal{G}}$.

Figure 7.13 compares the results based on PHY simulations with adaptive coding and

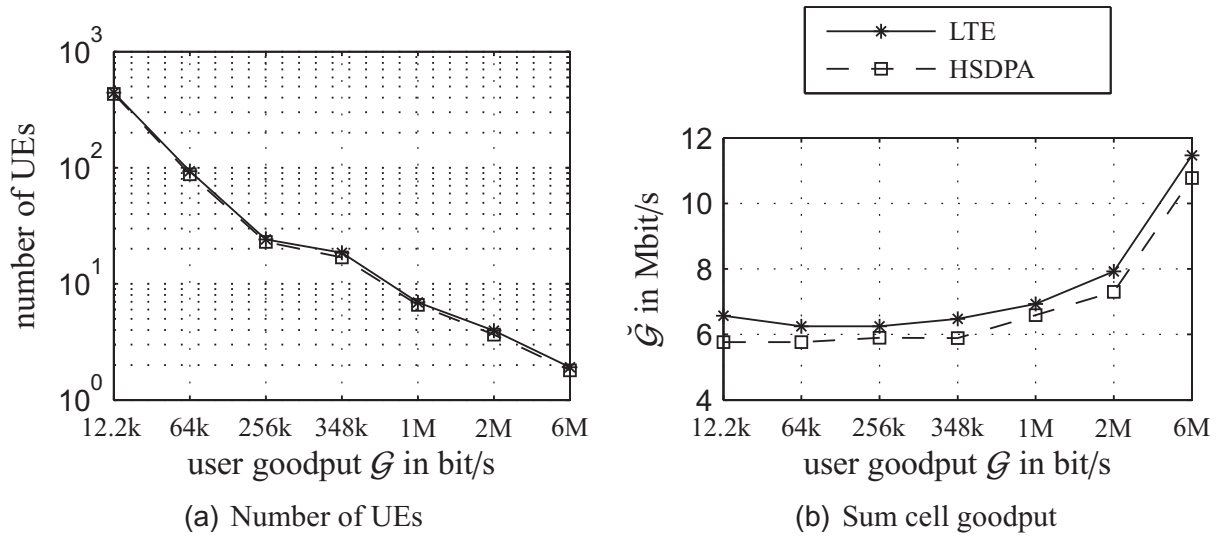


Figure 7.12: Number of UEs and sum cell goodput $\tilde{\mathcal{G}}$ for LTE and HSDPA, UMi, AWGN, $f_0 = 2.0$ GHz, $\Delta f = 5$ MHz, Monte-Carlo simulation.

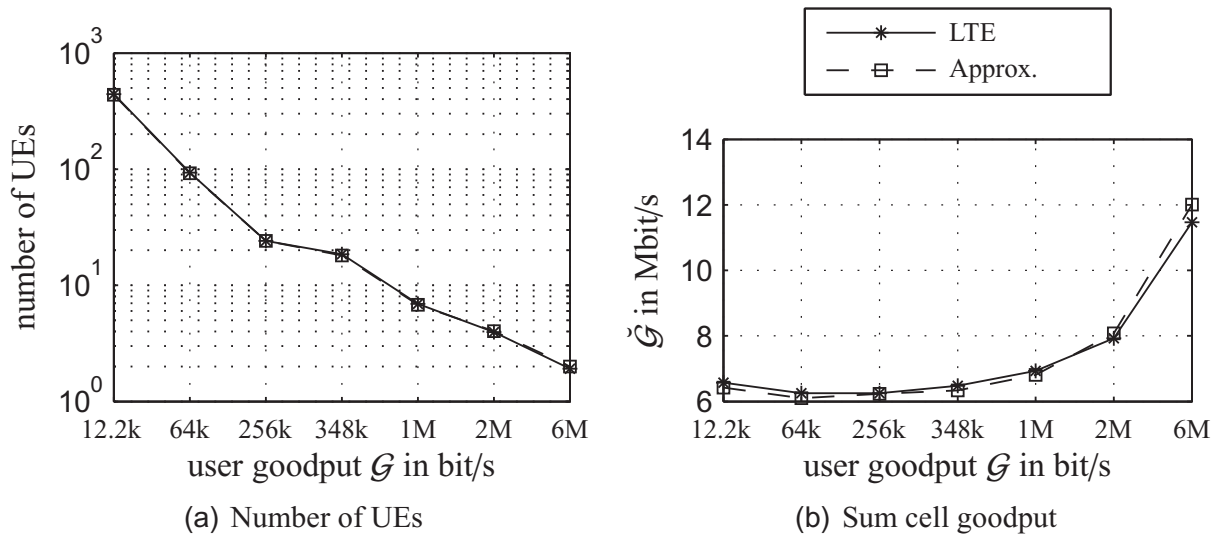


Figure 7.13: Number of UEs and sum cell goodput $\tilde{\mathcal{G}}$ for LTE and approximation according to (4.25), UMi, AWGN, $f_0 = 2.0$ GHz, $\Delta f = 5$ MHz, Monte-Carlo simulation.

modulation (solid lines) to the reference approximation from [15] defined by (4.25) (dashed lines). Again, a UMi propagation scenario with AWGN, $f_0 = 2.0$ GHz, and $\Delta f = 5$ MHz is assumed. The simulation results confirm the validity of the approximation concerning the number of supported UEs and the sum cell goodput $\tilde{\mathcal{G}}$.

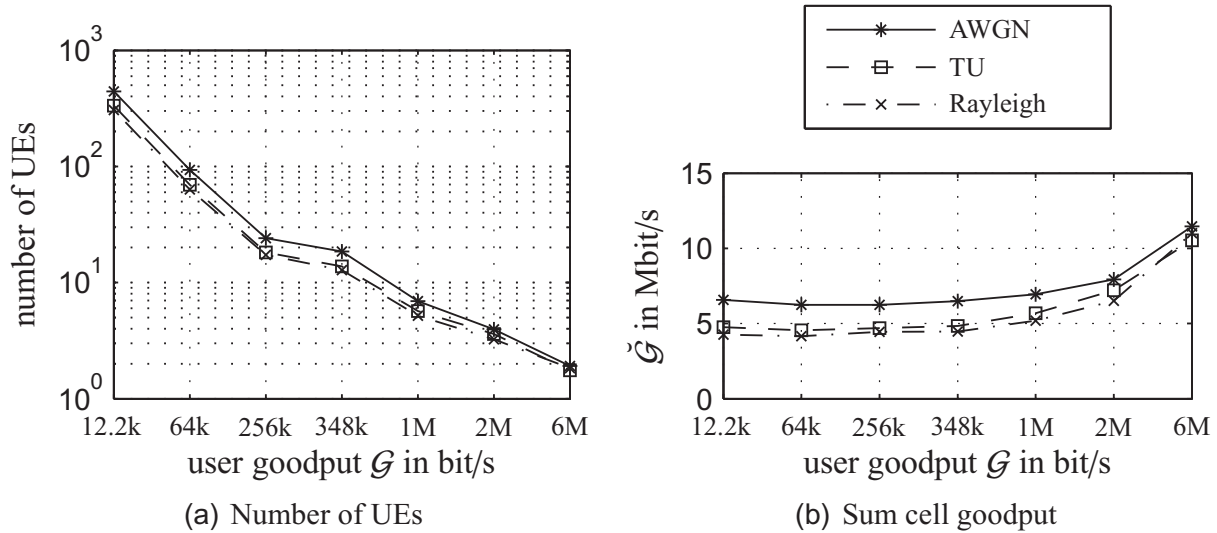


Figure 7.14: Number of UEs and sum cell goodput $\tilde{\mathcal{G}}$ for different PHY channel models, UMi, $f_0 = 2.0$ GHz, $\Delta f = 5$ MHz, Monte-Carlo simulation.

The influence of the different PHY channel models on the number of users is depicted in Fig. 7.14 for a simulation set-up similar to the one used for Fig. 7.8 considering a UMi propagation scenario with $f_0 = 2.0$ GHz and $\Delta f = 5$ MHz. Once again, the results confirm the expectation that the most advantageous AWGN case leads to the highest number of supported UEs and therefore the highest cell goodput while the frequency flat Rayleigh channel is the most disadvantageous concerning number of UEs and cell goodput. The average differences between the numbers of supported UEs reach from approximately 100 UEs in case of the low rate service with 12.2 kbit/s down to single UEs in case of medium to high rate services (256 kbit/s – 2 Mbit/s).

As in case of Fig. 7.9, the influence of the propagation scenarios on the number of supported UEs and the resulting cell goodput is compared in Fig. 7.15 assuming AWGN, $f_0 = 2.0$ GHz, and $\Delta f = 5$ MHz. Again, the findings coincide well with those from earlier comparisons. While the interference limited urban micro-cell (*) and rural macro-cell (o) scenarios exhibit almost the same number of supported UEs and therefore a similar sum cell goodput $\tilde{\mathcal{G}}$, the considered path loss models for the urban macro cells lead to significantly less supported UEs with demand for low and medium goodput (12.2 kbit/s – 348 kbit/s). The difference disappears for services demanding higher goodputs. This is due to the fact that UEs demanding high goodput can be supported only in high SINR regions. UEs at locations with low SINR demand more REs than the BS can support and are therefore rejected. This, of course, holds for all considered cases and can also be interpreted as a loss of coverage for high rate services.

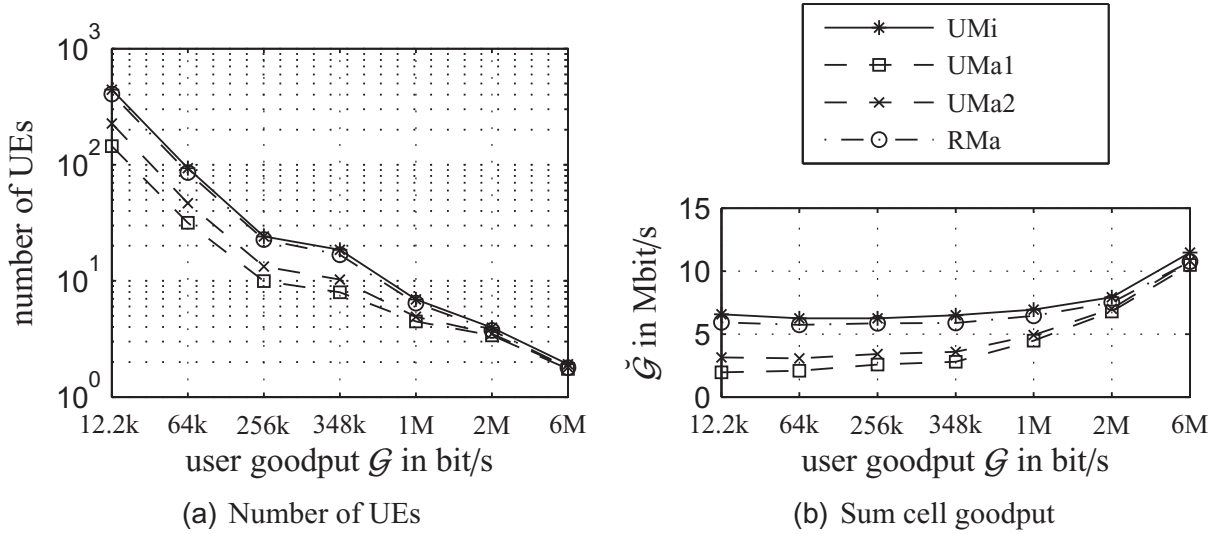


Figure 7.15: Number of UEs and sum cell goodput \tilde{G} for different propagation scenarios, AWGN, $f_0 = 2.0$ GHz, $\Delta f = 5$ MHz, Monte-Carlo simulation.

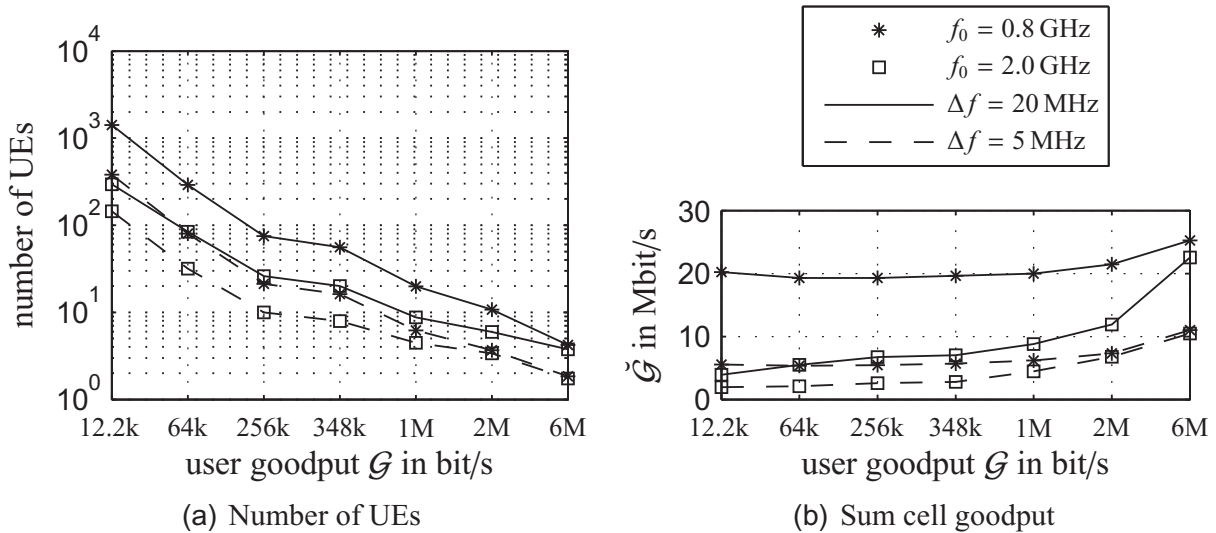


Figure 7.16: Number of UEs and sum cell goodput \tilde{G} for different carrier frequencies and system bandwidths in UMa1 (COST231Hata) propagation scenario assuming AWGN, Monte-Carlo simulation.

The effect of carrier frequency and frequency bandwidth variations is examined once more for the UMa1 propagation scenario in combination with AWGN and the results are given in Fig. 7.16. With the exception of the 6 Mbit/s service, the already drawn conclusions concerning the advantages of the $f_0 = 0.8$ GHz carrier frequency (*) in a noise limited propagation scenario are also reflected by these simulation results: Significantly more UEs are supported for $f_0 = 0.8$ GHz (*) compared to $f_0 = 2.0$ GHz (\square). For the high rate streaming service (6 Mbit/s) this advantage nearly disappears which is again due to the aforementioned loss of coverage for UEs requesting high rate services.

7.2 Beyond UMTS LTE

Having analyzed the system-level performance of the UMTS LTE physical layer in the previous section, this section is concerned with the modifications, alternatives, and bounds introduced in Chapter 5.

7.2.1 Interference Cancellation

The concept on interference cancellation (IC) introduced in Section 5.7 aims at a reduction of the inter-cell interference which, as already shown, is a major limiting factor for goodput performance near the cell edges. For simulating the influence of IC, an inter-cell interference factor α has been introduced in (6.2) for determining the current SINR of a UE at a certain location within the radio cell. This factor α can freely be chosen between 1 (no interference cancellation) and 0 (full interference cancellation). Additionally to these extreme settings, system level simulations have been conducted with $\alpha = 0.5$ and $\alpha = 0.2$ to cover partial cancellation of interference as a trade-off between performance gains and computational and signaling complexity. Recall that the seemingly extreme case of $\alpha = 0$ is more than a purely academic calculation example. This case can also be interpreted as a scenario where an isolated single cell without neighboring interfering cells is assumed, e.g., for broadband wireless access in rural areas using dedicated frequencies.

Figure 7.17 compares the distribution of the user goodput \mathcal{G} of an LTE system assuming a UMi propagation scenario with AWGN and 100 UEs. Frequency bandwidth f_0 and carrier frequency Δf are chosen to resemble a current UMTS set up, i.e., $f_0 = 2.0$ GHz and $\Delta f = 5$ MHz. The inter-cell interference factor α varies between $\alpha = 1$ (*), $\alpha = 0.5$ (\square), $\alpha = 0.2$ (\times), and $\alpha = 0$ (\circ).

It can be seen that, while the maximum user goodput of $\mathcal{G} = 201.6$ kbit/s near the BS is constant, the user goodput at the cell edge increases from below 20 kbit/s to this maximum. The vertical CDF for full interference cancellation (\circ) indicates that the SINR at all locations within the cell suffices to support the highest MCS, i.e., 64QAM ($I = 6$ bit per mapping symbol) with code rate $cr = 4/5$ resulting in $\mathcal{B} = 4.8$ bit per channel use. With 2100 available resource elements per 0.5 s time slot allocated equally among the 100 UEs, each UE would achieve the maximum goodput of $\mathcal{G} = 201.6$ kbit/s depicted in Fig. 7.17.

With noise limitation at the cell edges of urban macro-cell scenarios, especially for high carrier frequencies, it can be concluded, that the effect of interference cancellation will be

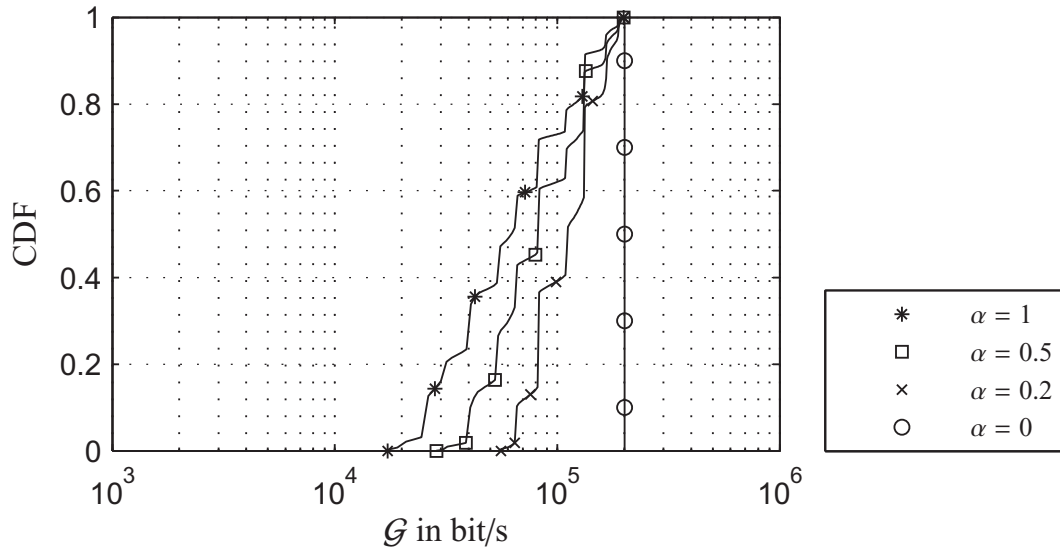


Figure 7.17: Cumulative distribution function of individual user goodput \mathcal{G} for different interference cancellation factors α : UMa1, AWGN, $\Delta f = 5$ MHz, $f_0 = 2.0$ GHz, 100 UEs, Monte-Carlo simulation.

less significant in these scenarios. Figures 7.18 and 7.19 compare the CDFs of the user goodput assuming the UMa1 propagation scenario with AWGN and 100 UEs for $\Delta f = 5$ MHz and $\Delta f = 20$ MHz, respectively. Both carrier frequencies, $f_0 = 0.8$ GHz (*) and $f_0 = 2.0$ GHz (\square) are considered for systems with full interference cancellation (solid lines) and without IC (dashed lines).

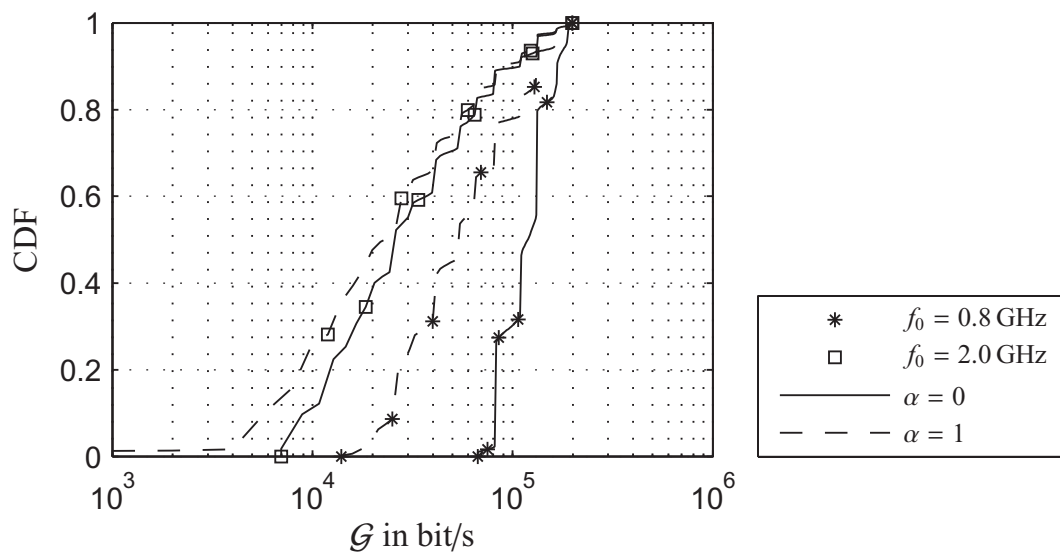


Figure 7.18: Cumulative distribution function of user individual goodput \mathcal{G} for different carrier frequencies and interference cancellation factors α : UMa1, AWGN, $\Delta f = 5$ MHz, 100 UEs, Monte-Carlo simulation.

As expected, the highest improvement of cell edge goodput can be achieved for $f_0 = 0.8$ GHz (*) and $\Delta f = 5$ MHz as with these parameters the inter-cell interference at the cell edges is most influential compared to the other settings. Therefore, interference cancellation raises the cell edge goodput by more than factor five from approximately 13 kbit/s to nearly 70 kbit/s (see Fig.7.18). However, this figure still falls short of the over 200 kbit/s which are achieved near the base station.

For $f_0 = 2.0$ GHz (\square) and $\Delta f = 5$ MHz (Fig. 7.18), full interference cancellation results in an improved coverage. While without IC approximately 1 % of the users within the cell area could not be covered, with full IC a minimum goodput of at least 7 kbit/s is now achieved by all users within the urban macro-cell.

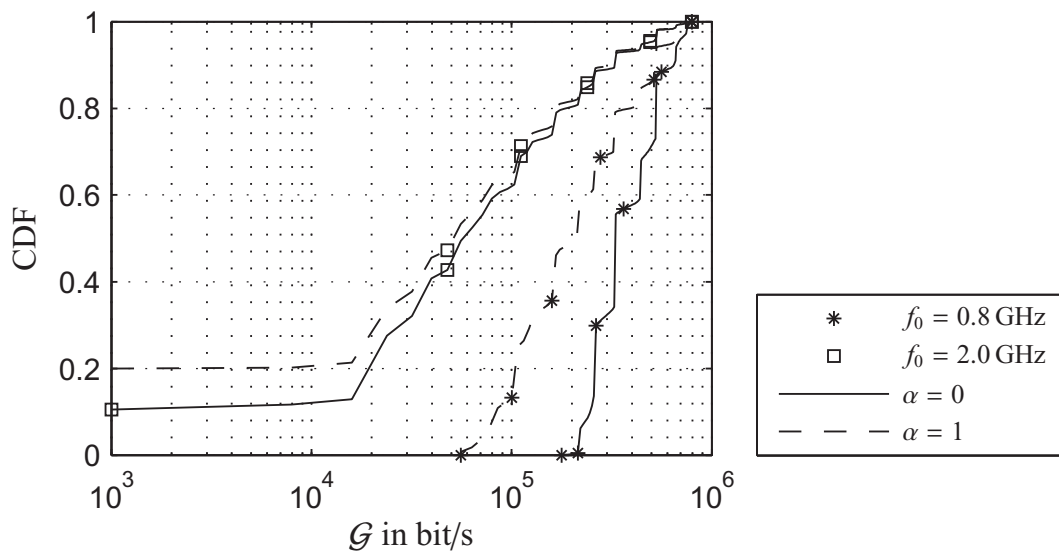


Figure 7.19: Cumulative distribution function of individual user goodput \mathcal{G} for different carrier frequencies and interference cancellation factors α : UMa1, AWGN, $\Delta f = 20$ MHz, 100 UEs, Monte-Carlo simulation.

In case of $\Delta f = 20$ MHz (Fig. 7.19) the same effects can be observed. Due to the increased system bandwidth, the individual user goodput at the cell edges as well as near the base station is increased compared to the case of $\Delta f = 5$ MHz. The maximum goodput achieved near the BS is 806 kbit/s for both considered carrier frequencies. An interesting fact can be observed for $f_0 = 2.0$ GHz (\square). As opposed to the case of $\Delta f = 5$ MHz, where IC could be used to improve the coverage of the radio cell such that all UEs could be provided at least with a minimum goodput, for $\Delta f = 20$ MHz this is not the case. While approximately 20% of the users could not be covered without IC, 10% of the users stay without coverage even with full IC, underlining again the noise limitation of the considered scenario.

The different cell edge user goodputs for $\alpha = 0$ in Figs. 7.18 and 7.19 also illustrate the potential of broadband wireless access concerning coverage and goodput in single cell deployments in areas with adverse topology and path loss characteristics as modeled in the UMa1 scenario. For the less adverse 3GPP Rural path loss model (RMa), performances comparable to those in UMi propagation scenarios have been observed, even for distances

of up to 10 km from the base station.

Similar observations are made when simulating fixed services. Figure 7.20 compares the number of served UEs and the resulting throughput over varying demanded goodput for different interference factors α assuming a UMi propagation scenario with AWGN. The carrier frequency is chosen as $f_0 = 2.0$ GHz and the frequency bandwidth is $\Delta f = 5$ MHz resembling a current UMTS radio cell.

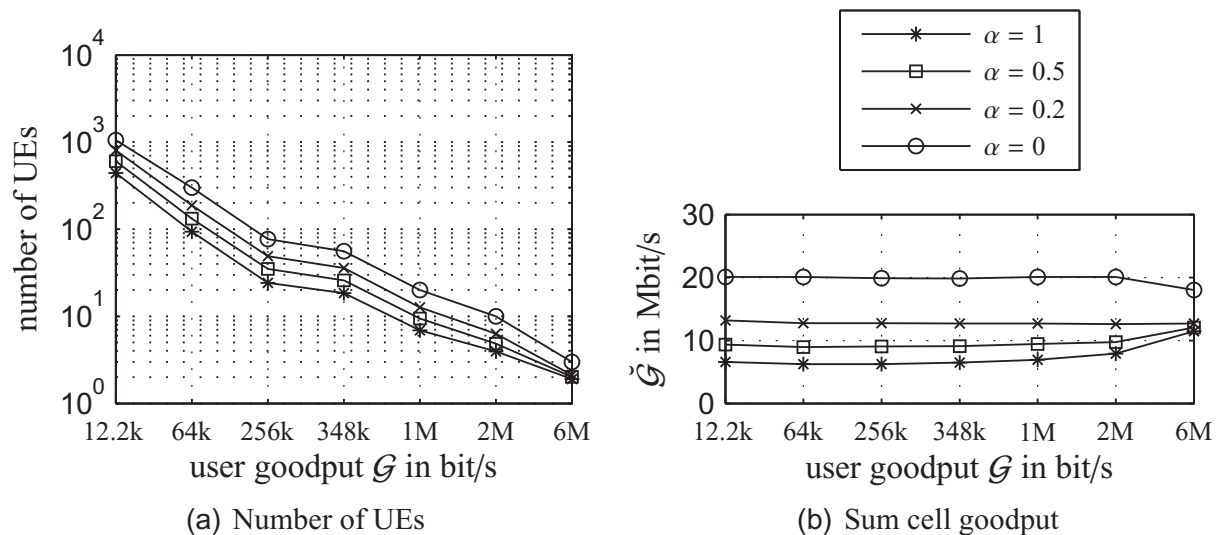


Figure 7.20: Number of UEs and sum cell goodput $\check{\mathcal{G}}$ for different interference factors α in UMi propagation scenario: AWGN, $f_0 = 2.0$ GHz, $\Delta f = 5$ MHz, Monte-Carlo simulation.

For all considered demanded services significant gains can be observed concerning the number of served UEs and the cell goodput. For full interference cancellation (\circ) the maximum achievable cell goodput of $2100 \text{ REs} \cdot 4.8 \text{ bit/RE}/0.5 \text{ ms} = 20.16 \text{ Mbit/s}$ is observed for demanded user goodputs of 12.2 kbit/s up to 2 Mbit/s. With the 6 Mbit/s service the cell goodput drops to 18 Mbit/s supporting 3 UEs. With the modulation and coding schemes limited to 64QAM with rate 4/5 coding, the remaining resource elements are not sufficient to support an additional UE demanding 6 Mbit/s, these REs are not assigned.

Figure 7.21 shows the impact of the different carrier frequencies in combination with IC on number of served UEs and cell goodput for the UMa1 propagation scenario with AWGN and $\Delta f = 20$ MHz. As predicted by Fig. 7.19 a gain in the number of served UEs and cell goodput can also be achieved for the lower carrier frequency of $f_0 = 0.8$ GHz. For the noise limited case with $f_0 = 2.0$ GHz even complete interference cancellation does not yield an observable gain.

7.2.2 Bounds for MIMO Systems

To illustrate the potential of current and future mobile radio systems to provide wireless broadband access, simulations have been conducted using the bounds on the achievable bits

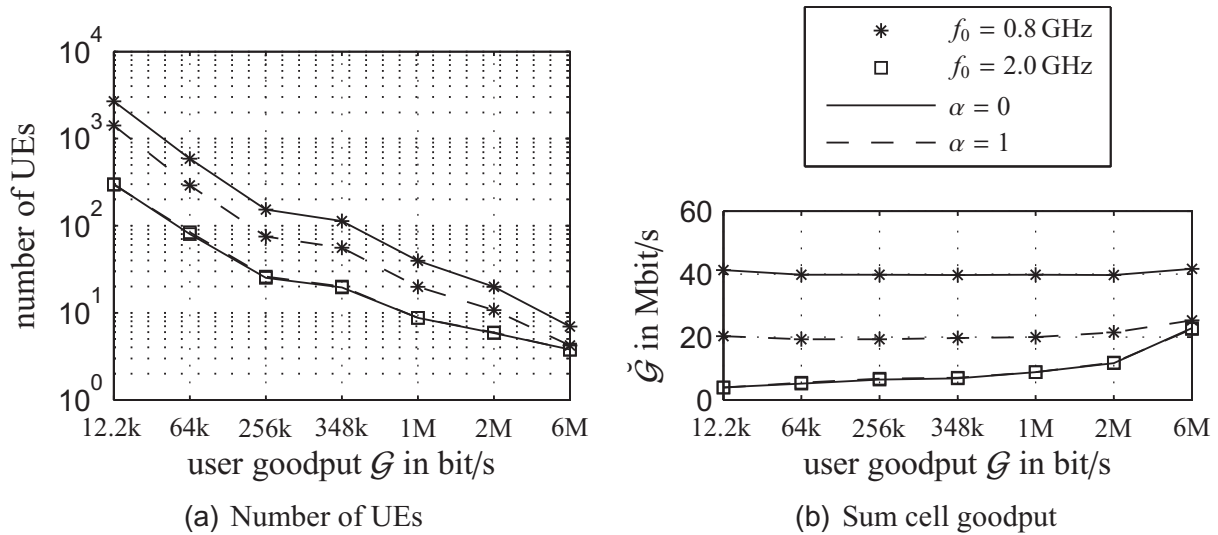


Figure 7.21: Number of UEs and sum cell goodput $\tilde{\mathcal{G}}$ for different carrier frequencies f_0 and interference factors α in UMa1 propagation scenario: AWGN, $\Delta f = 20$ MHz, Monte-Carlo simulation.

per channel use \mathcal{B} given by (5.11) for MIMO systems. Note, that for the single antenna case, i.e., $A = 1$, (5.11) denotes the maximum achievable \mathcal{B} of a transceiver with LTE modulation stage and capacity achieving coding and modulation, i.e., the Shannon limit.

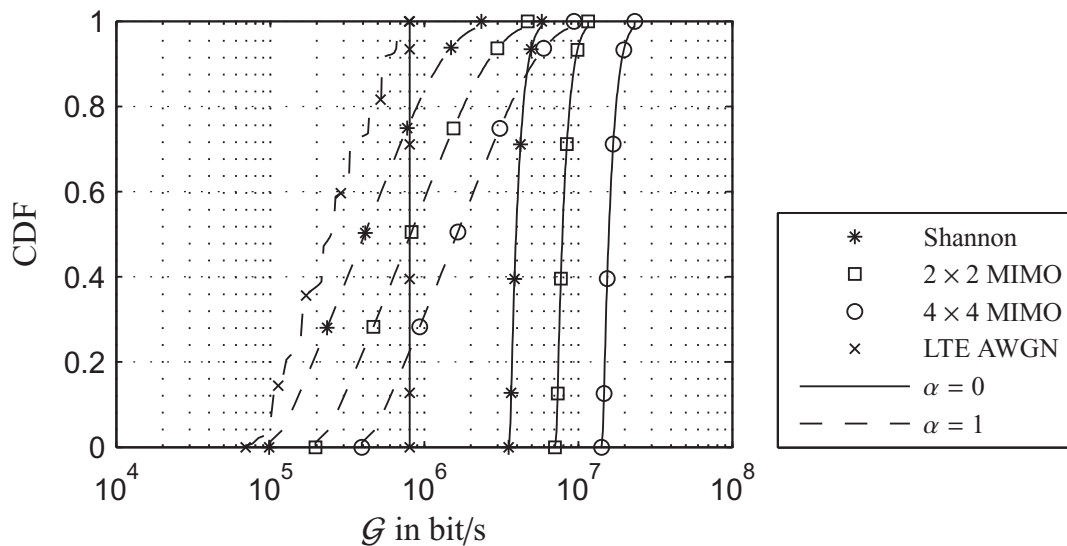


Figure 7.22: Bounds on the cumulative distribution function of individual user goodput \mathcal{G} for different numbers of antennas A and interference cancellation factors α in UMi propagation scenario and comparison to LTE, AWGN, $f_0 = 0.8$ GHz, $\Delta f = 20$ MHz, 100 UEs, Monte-Carlo simulation.

Figure 7.22 compares the bounds on the achievable user goodput distribution for a single

antenna system (Shannon,*), a 2×2 MIMO transceiver (\square), and a 4×4 MIMO transceiver (\circ) to those achievable with UMTS LTE (\times) in a UMi propagation scenario for the best possible configuration with $f_0 = 0.8$ GHz and $\Delta f = 20$ MHz assuming AWGN. The REs are equally shared by the 100 UEs in the radio cell.

A basic observation in Fig. 7.22 is that the single antenna LTE system performs fairly close to the Shannon limit without interference cancellation (dashed lines). The difference in user goodput near the base station originates from the assumed limitation of the MCSs. As expected, the limit on the user goodputs is doubled and quadrupled for 2×2 and 4×4 MIMO. These bounds are pushed toward even higher user goodput when full IC is employed (solid lines). The goodput differences between cell edge users and users near the base station, which is more than factor 10 for UMTS LTE without IC, can theoretically be reduced down to a factor of approximately 2 employing MIMO and IC. In case of 4×4 MIMO with complete IC, the cell edge user goodput is limited to approximately 13 Mbit/s while the user goodput near the base station is limited to 22 Mbit/s assuming 100 UEs in the radio cell.

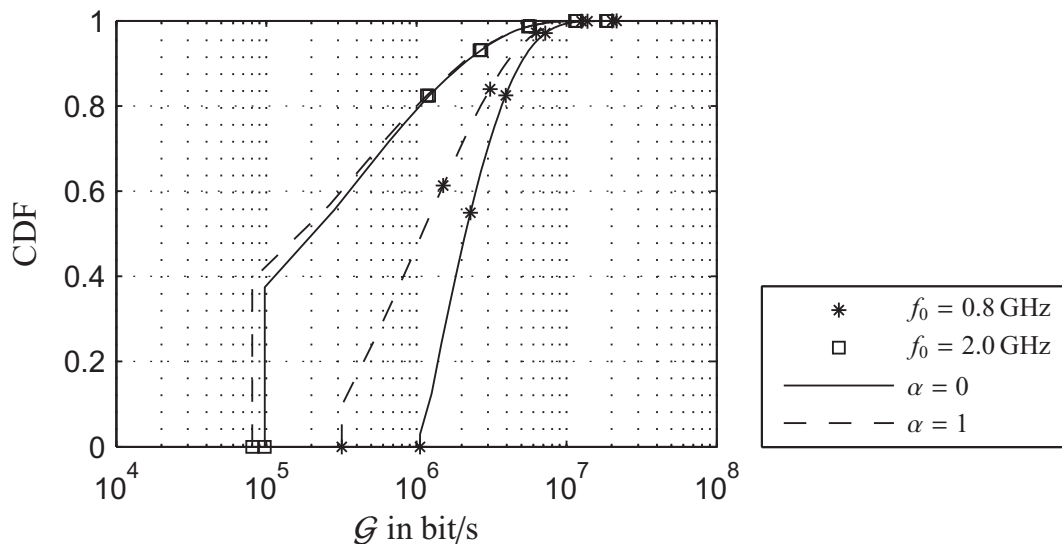


Figure 7.23: Bounds on the cumulative distribution function of individual user goodput \mathcal{G} for different carrier frequencies f_0 and interference cancellation factors α in UMa1 propagation scenario assuming 4×4 MIMO, AWGN, $\Delta f = 20$ MHz, 100 UEs, Monte-Carlo simulation.

Figure 7.23 depicts the impact of different carrier frequencies f_0 on the bounds of the user goodput distribution in the UMa1 propagation scenario for a 4×4 MIMO system with and without IC. The maximum system bandwidth of $\Delta f = 20$ MHz and AWGN are assumed, 100 UEs are equally sharing the REs. It is observed, that for the noise limited case of $f_0 = 2.0$ GHz (\square) the user goodput at the cell edge will not exceed 100 kbit/s, neither with nor without IC. For $f_0 = 0.8$ GHz (*), however, a user goodput of 1 Mbit/s will not be exceeded, even for 4×4 MIMO with IC.

Finally, Fig. 7.24 compares the bounds on the number of served UEs and the corresponding sum cell goodput for fixed services in UMi (solid lines) and UMa1 (dashed lines)

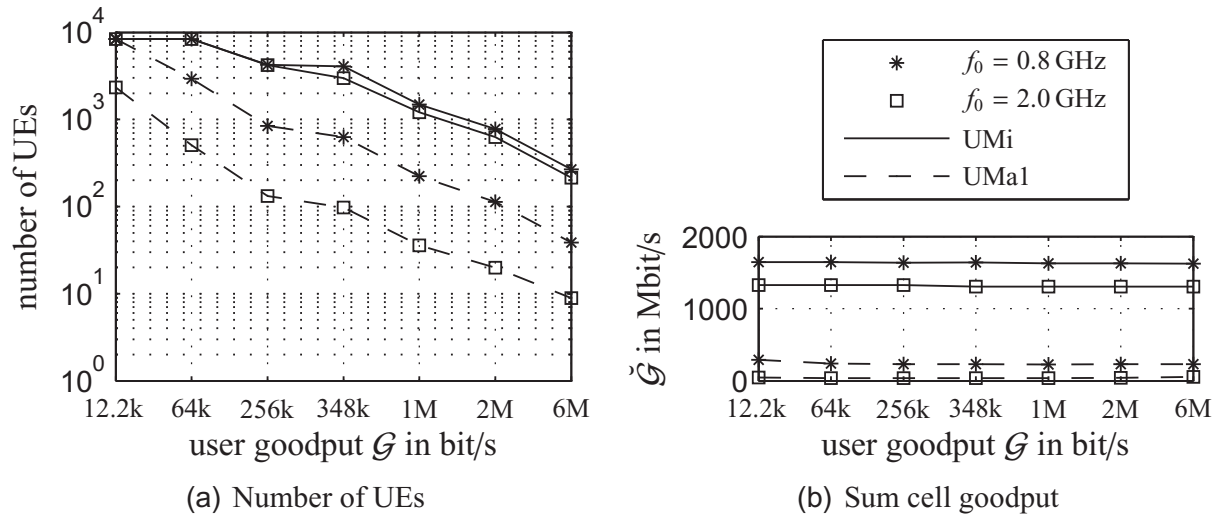


Figure 7.24: Bounds on the number of UEs and the sum cell goodput $\check{\mathcal{G}}$ for 4×4 MIMO with complete IC ($\alpha = 0$) for different carrier frequencies and propagation scenarios, AWGN, $\Delta f = 20$ MHz.

propagation scenarios for a 4×4 MIMO system with complete IC ($\alpha = 0$). Both carrier frequencies are considered. The figures underline the advantages of the lower carrier frequency in the UMa1 propagation scenario concerning the number of served UEs and the cell goodput. The simulation results for the UMi propagation scenario with complete IC show, that a cell goodput of more than 1Gbit/s is theoretically possible with 4×4 MIMO. Considering this UMi radio cell with complete IC to be an isolated single cell with all users distributed within a radius of $r = 200$ m around the base station, the possibility for wireless broadband access using radio techniques is at hand.

7.2.3 Reordered bit mapping for 64QAM

In Section 5.1 the convergence properties of the LTE Turbo decoder have been modified by a simple reordering of the encoded bits \underline{x} before complex mapping to 64QAM symbols. It has been shown, that in that way the achievable bits per channel use \mathcal{B} of 64QAM with rate 1/3 coding could be improved for the non-iterative as well as for the iterative case. This section illustrates the impact of this modification on system level. Therefore, the coding and modulation scheme is fixed to rate 1/3 coding with 64QAM mapping for all simulations. HARQ with up to 3 retransmissions (RV0 – RV3) is considered.

Table 7.1 summarizes the average cell goodput $\overline{\mathcal{G}}$ calculated by numerical integration according to (6.5) assuming the beneficial carrier frequency of $f_0 = 0.8$ GHz and a system frequency bandwidth of $\Delta f = 20$ MHz. Two propagation scenarios are compared, the UMi propagation scenario and the UMa1 propagation scenario. Furthermore, non-iterative decoding and iterative decoding with 10 decoding iterations are considered.

The results for the average cell goodput show that in all considered cases the proposed reordering is somewhat beneficial. For non-iterative decoding the average cell goodput is in-

Prop. Env.	UMi		UMa1	
Decoding	non-iterative	iterative	non-iterative	iterative
LTE	16.1	22.0	12.5	18.1
reordered	17.7	22.2	14.0	18.4

Table 7.1: Average cell goodput $\bar{\mathcal{G}}$ in Mbit/s for standard LTE and reordered bit mapping.

created by approximately 1.5 Mbit/s, which, for the given limitations concerning the MCS, corresponds to a gain of more than 9% for the UMi propagation scenario and even 12% for the UMa1 propagation scenario. For iterative decoding, these gains decrease to 0.2 Mbit/s and 0.3 Mbit/s for the UMi and the UMa1 propagation scenario, respectively. However, despite of the small SNR loss concerning the achievable bit per channel use \mathcal{B} for RV0 observed in Fig. 5.6, the reordering of the encoded bits appears still to be beneficial from this system-level point of view.

To illustrate the impact of the reordered bit mapping on the user goodput distribution within a radio cell, simulations have been conducted with the system-level parameters described above. For each Monte-Carlo iteration 100 UEs are randomly located within the radio cell sharing the available 8400 REs ($\Delta f = 20$ MHz) per time slot equally. Again, only rate 1/3 coding with 64QAM is considered, limiting the maximum available user goodput to $\mathcal{G} = 336$ kbit/s.

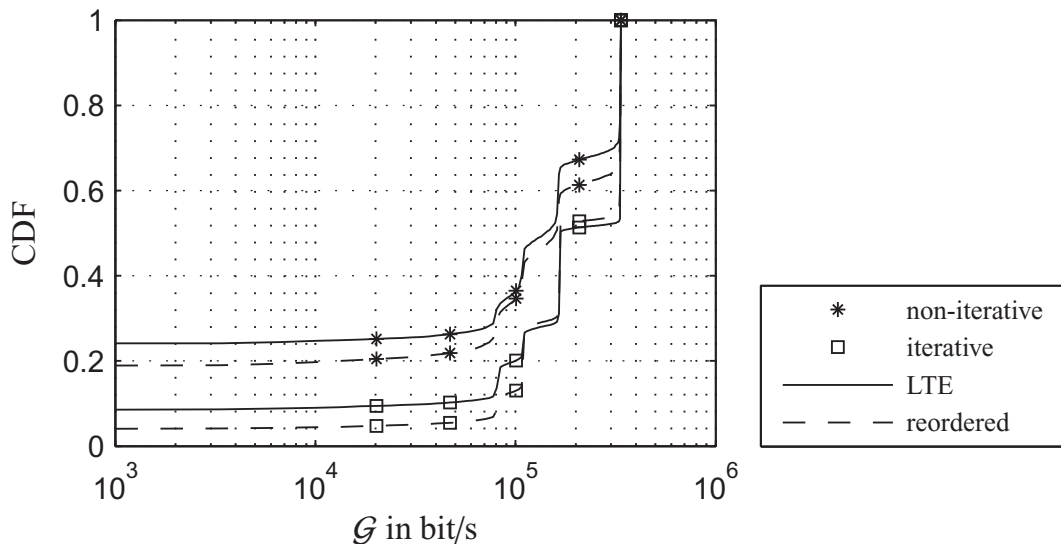


Figure 7.25: Cumulative distribution function of individual user goodput \mathcal{G} for standard LTE and the proposed reordered bit mapping in UMi propagation scenario, AWGN, $f_0 = 0.8$ GHz, $\Delta f = 20$ MHz, 100 UEs, 64QAM, rate 1/3 coding, Monte-Carlo simulation.

Figure 7.25 compares the resulting CDF of user goodput \mathcal{G} for standard LTE (solid line)

and the proposed reordered bit mapping (dashed line) in a UMi propagation scenario. Due to high minimum SINR necessary for successfully decoding the received data with the given MCS, there appear unserved UEs at the cell edges for all considered cases. It is observed that the reordered bit mapping reduces the percentage of unserved UEs by approximately 5% from $\approx 24\%$ to $\approx 19\%$ for non-iterative (*) and from $\approx 10\%$ to $\approx 5\%$ for iterative (\square) decoding, respectively. At the same time, with the reordered bit mapping and non-iterative decoding, the maximum goodput near the base station can be provided to $\approx 35\%$ of the UEs as opposed to LTE where only $\approx 30\%$ of the UEs achieve the maximum goodput. For iterative decoding, only a negligible fraction of additional users are provided with the maximum goodput near the base station with standard LTE compared to the proposed reordering.

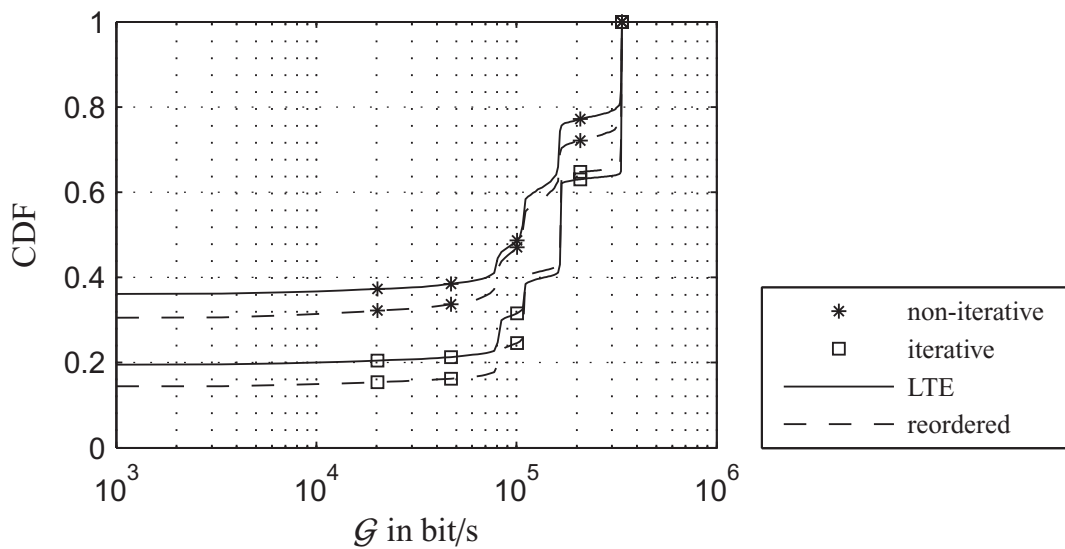


Figure 7.26: Cumulative distribution function of individual user goodput \mathcal{G} for standard LTE and the proposed reordered bit mapping in UMa1 propagation scenario, AWGN, $f_0 = 0.8$ GHz, $\Delta f = 20$ MHz, 100 UEs, 64QAM, rate 1/3 coding, Monte-Carlo simulation.

Similar observations can be made in simulations with the UMa1 propagation scenario as depicted in Fig. 7.26. Here, due to the worse propagation characteristics and the MCS restriction, a higher percentage of UEs is unserved. Again, the proposed reordering leads to a reduction of these unserved UEs of approximately 5%.

7.2.4 BICM-ID with Repetition Coding

Section 5.2 introduced an alternative transceiver scheme based on bit-interleaved coded modulation with iterative decoding (BICM-ID) in combination with repetition coding which allows for a significant reduction of computational complexity. Based on these findings, system-level simulations have been conducted based on the achievable bits per channel use \mathcal{B} as depicted in Figures 5.8 to 5.11. That implies, that modulation and coding schemes are limited to rate 1/3 and rate 1/2 channel coding.

Table 7.2 summarizes the average cell goodput $\bar{\mathcal{G}}$ calculated by numerical integration according to (6.5) again assuming $f_0 = 0.8$ GHz and $\Delta f = 20$ MHz. In accordance with Section 5.2, AWGN and Rayleigh are chosen as PHY channel models and compared in UMi and UMa1 propagation scenarios.

Prop. env.	UMi		UMa1	
PHY channel	AWGN	Rayleigh	AWGN	Rayleigh
LTE	30.4	22.8	25.8	18.9
BICM-ID	28.0	21.8	23.4	17.7

Table 7.2: Average cell goodput $\bar{\mathcal{G}}$ in Mbit/s for standard LTE and the proposed BICM-ID system with repetition coding.

As already indicated by the progressions of the achievable bits per channel use, the average cell goodput $\bar{\mathcal{G}}$ of the proposed BICM-ID system is slightly outperformed by standard UMTS LTE in all considered cases. These losses of 1 – 2 Mbit/s, however, can be considered small in regard of the potential gains in computational complexity.

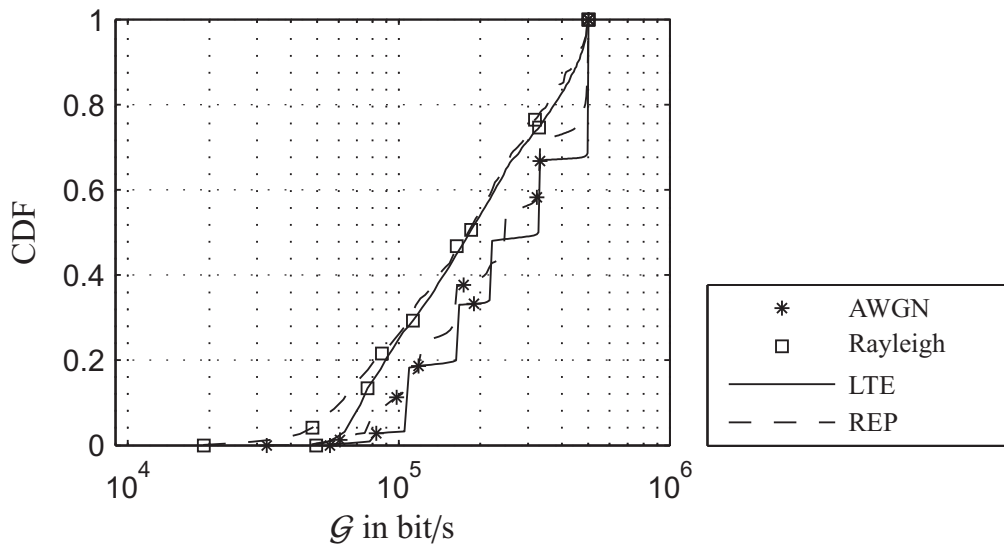


Figure 7.27: Cumulative distribution function of individual user goodput \mathcal{G} for standard LTE and the proposed BICM-ID scheme in UMi propagation scenario, $f_0 = 0.8$ GHz, $\Delta f = 20$ MHz, 100 UEs, Monte-Carlo simulation.

The distribution of the individual user goodput is depicted in Figs. 7.27 and 7.28 for UMi and UMa1 propagation scenario, respectively, assuming 100 UEs per radio cell, a carrier frequency of $f_0 = 0.8$ GHz and a frequency bandwidth of $\Delta f = 20$ MHz. It is observed that for AWGN (*) both CDFs exhibit similar progressions with slight advantages in favor of the standard LTE system. For the Rayleigh fading channel model (\square), both progressions are almost equal for the best 60 % of the users in the radio cell. Users at the cell edge experience

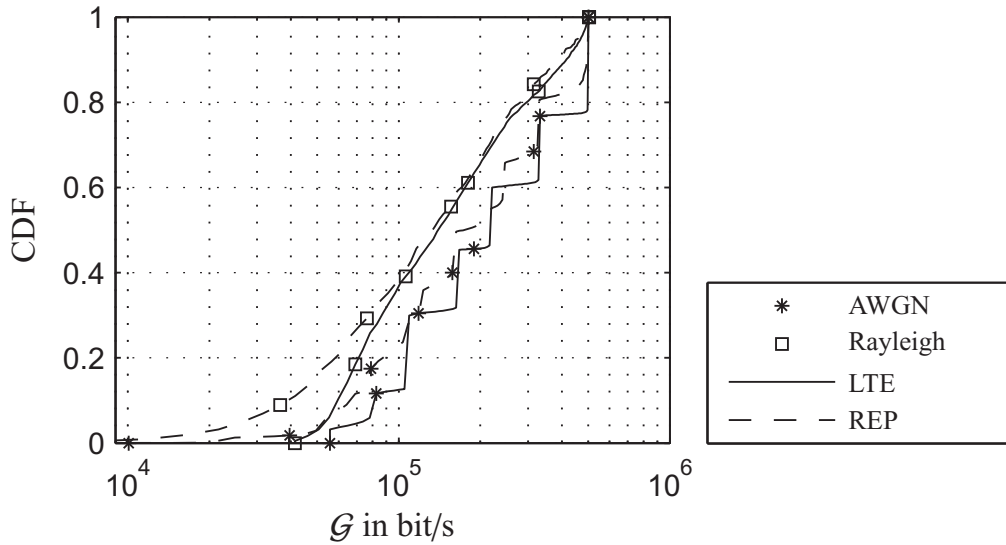


Figure 7.28: Cumulative distribution function of individual user goodput \mathcal{G} for standard LTE and the proposed BICM-ID scheme in UMa1 propagation scenario, $f_0 = 0.8$ GHz, $\Delta f = 20$ MHz, 100 UEs, Monte-Carlo simulation.

a slightly better coverage with standard LTE than with the proposed BICM-ID system, which is completely in line with the findings of Sec. 5.2 (cf. Fig. 5.10 and Fig. 5.11). These losses illustrate the trade-off between capacity and coverage on the one hand and computational complexity on the other hand.

7.2.5 OFDM Turbo DeCodulation

With the Turbo DeCodulation (TDeC) scheme introduced in Section 5.4 being designed to transmit correlated codec parameters it is necessary to define an appropriate service before comparing the system-level performance of UMTS LTE and Turbo DeCodulation. The widely used enhanced full-rate (EFR) codec, for example, encodes speech frames into 36 parameters which, given a frame length of 20 ms, leads to an amount of 1800 codec parameters per second. With an information bit rate of 12.2 kbit/s, 6.7 bit are allocated on average per codec parameter. The more recent adaptive multi-rate (AMR) wide band codec demands an information bit rate of up to 23.85 kbit/s. This bit rate motivates to choose an exemplary service demanding 24 kbit/s. With the configuration of Section 5.5, for each codec parameter 3 bit are used for quantization leading to a service that encodes a data stream into 8000 codec parameters per second.

Based on these assumptions and the PSNR figures given in Section 5.5 for convolutional coded Turbo DeCodulation (CC-TDeC) and block coded Turbo DeCodulation (BC-TDeC), the resulting PSNR for a single user in a mobile radio cell is calculated based on the instantaneous SINR at each given position. Figure 7.29 compares the achieved PSNRs for UMTS LTE, CC-TDeC, and BC-TDeC in a UMa1 propagation scenario assuming a system frequency bandwidth of $\Delta f = 5$ MHz and a carrier frequency of $f_0 = 2.0$ GHz, resembling a

current UMTS deployment. AWGN is assumed as PHY channel model.

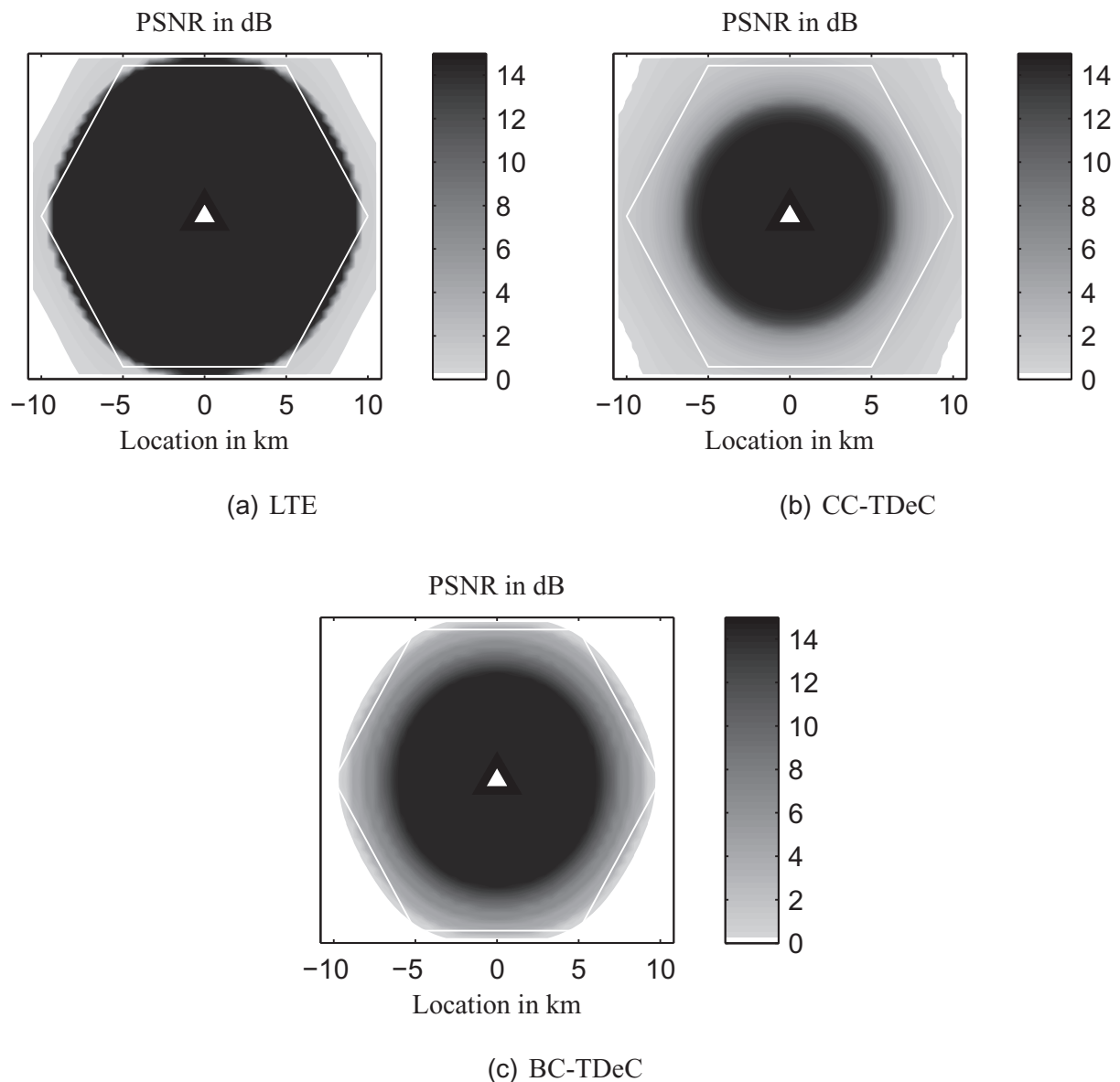


Figure 7.29: PSNR in UMa1 propagation scenario, $f_0 = 2.0$ GHz, $\Delta f = 5$ MHz.

The distribution of the PSNR in the depicted urban macro-cells is in line with the findings of Fig 5.25. UMTS LTE provides a very good coverage with the maximum PSNR of 14.6 dB, see Fig. 7.29(a). The slow degradation characteristic of CC-TDeC is illustrated by the relatively slow fading from high PSNR values near the base station to low values near the cell edge in Fig. 7.29(b). It is also observed that, compared to UMTS LTE, CC-TDeC provides high transmission qualities to a smaller area. Finally, the BC-TDeC system depicted in Fig. 7.29(c) shows a similar slow degradation characteristic compared to CC-TDeC. At the same time, however, the area where transmissions with high quality are possible is increased.

It has been shown, that the considered transmission schemes do not only differ in transmission quality but also exhibit different spectral efficiencies, i.e., different \mathcal{B} performances.

This fact has to be taken into account when judging the performance of the proposed schemes. Therefore, simulations have been conducted using the fixed service traffic model with the 24 kbit/s service defined above and based on the average bits per channel use \mathcal{B} depicted in Section 5.5. UMi and UMa1 propagation scenarios are assumed along with AWGN and the typical UMTS setting with $f_0 = 2.0$ GHz and $\Delta f = 5$ MHz. Table 7.3 summarizes the simulation results.

Prop. Env.	UMi		UMa1	
System	$\check{\mathcal{G}}$ in Mbit/s	No. UEs	$\check{\mathcal{G}}$ in Mbit/s	No. UEs
LTE	5.0	197.4	1.9	76.0
CC-TDeC	5.5	229.3	3.7	153.4
BC-TDeC	5.5	229.7	2.8	116.8

Table 7.3: Sum cell goodput $\check{\mathcal{G}}$ in Mbit/s and average number of served UEs for standard LTE with SQ, convolutional coded Turbo DeCodulation, and block coded Turbo DeCodulation.

It is observed that in case of UMi, UMTS LTE provides the demanded service to 13 % fewer users than CC-TDeC and BC-TDeC which serve 230 UEs. The reason for the good capacity performance of CC-TDeC and BC-TDeC is its higher spectral efficiency near the cell edges. It has to be kept in mind, however, that the cell edge users in the both TDeC radio cells will experience less quality, especially with CC-TDeC.

For the UMa1 case, a similar behavior is observed. The superiority in terms of served users and cell goodput of both TDeC systems comes, as seen in Fig. 7.29(b) for this propagation scenario, at the cost of a lower transmission qualities in the cell edge areas. Surprisingly, in the UMa1 propagation scenario twice the number of users can be provided with the demanded service using CC-TDeC rather than LTE. In case of BC-TDeC this factor is 1.5. The obvious reason for that is the higher spectral efficiency of CC-TDeC and BC-TDeC in the low SINR regime, which takes a larger portion of the radio cell area in UMa1 propagation scenario compared to UMi. Lower transmission quality for the additionally served users is the price to pay for this gain in capacity.

The combined results of coverage, capacity and quality performance confirm the potential of flexible resource allocation which is enabled by the proposed OFDM Turbo DeCodulation schemes.

Summary

Two important factors fuel the fast evolution of mobile broadband access technologies: The ever-increasing demand for high data rates due to the availability and acceptance of mobile devices and applications and the demand for affordable broadband access in under served areas where radio technologies are regarded as a substitute to fixed line technologies. The current release 8 of the UMTS LTE standard promises high data rates provided by a flat all-IP system architecture. This thesis describes the physical layer of UMTS LTE and analyzes its performance in terms of the achievable bits per channel use \mathcal{B} for different channel models.

Assuming the same physical layer performance for UMTS LTE and UMTS HSDPA+ implied by similar channel coding and complex mapping, both systems mainly differ in their modulation stages. It is concluded that with the transition from CDMA used in HSDPA+ to OFDM used in LTE, a gain in spectral efficiency of approximately 10 % is achieved. It is further observed that single antenna LTE operates at 65 % of the Shannon limit considering a capacity achieving physical layer with OFDM modulation equal to that of UMTS LTE.

Based on the \mathcal{B} measure of physical layer performance, system-level simulations have been conducted to illustrate the performance of UMTS LTE in terms of coverage and capacity. It is shown that due to the better propagation characteristics systems operating at frequencies of the digital dividend operating at $f_0 = 0.8$ GHz will achieve a higher coverage, i.e., cover a larger cell area, than those systems operating in the frequency band of current UMTS deployments at $f_0 = 2.0$ GHz. In a cellular network employing carrier frequencies of the digital dividend, area wide coverage can be achieved with fewer base stations. Regardless of their carrier frequency and corresponding size, radio cells of a fully loaded network providing area wide coverage are likely to be interference limited and show similar individual user goodput distributions and similar average cell goodputs.

Independent of the cell size, a bandwidth dependent peak rate can be achieved by users with good channel conditions, i.e., close to the base station. For the considered UMTS LTE single antenna case, a frequency bandwidth of $\Delta f = 5$ MHz and the maximum considered channel code rate $cr = 4/5$, a peak rate of 20.16 Mbit/s can be achieved. This figure scales linearly with the frequency bandwidth, i.e., for $\Delta f = 20$ MHz a peak rate of 80.64 Mbit/s can theoretically be achieved by a single user. Cell edge rates are determined by the minimum considered channel code rate of $cr = 1/3$ and the maximum number of 4 transmissions (3 retransmissions, RV 3) leading to cell edge rates of 0.7 Mbit/s and 2.8 Mbit/s for $\Delta f = 5$ MHz and $\Delta f = 20$ MHz, respectively.

Assuming a radio cell with uniformly distributed users, an average cell goodput $\bar{\mathcal{G}}$ is calculated as sum of all user goodputs. This $\bar{\mathcal{G}}$ depends on the propagation characteristics of the radio cell, the carrier frequency f_0 and the interference situation and varies for $\Delta f = 20$ MHz between $\bar{\mathcal{G}} = 13.9$ Mbit/s for noise limited urban macro-cells and $\bar{\mathcal{G}} = 38.7$ Mbit/s for interference limited urban micro-cells. Again, these figures scale linearly with the frequency bandwidth Δf and lead to average spectral efficiencies of $0.7 \leq \eta \leq 2$ bit/s/Hz.

Some novel modifications of the UMTS LTE physical layer and alternative transceiver concepts are proposed and their influence on coverage, quality and capacity on system-level is analyzed. A simple reordering of the coded bits in combination with 64QAM mapping may improve the average cell goodput $\bar{\mathcal{G}}$ by 10 % in the considered cases. A transceiver using repetition coding and bit doping in the transmitter and a BICM-ID scheme in the receiver significantly reduces the computational complexity while achieving comparable system-level performance. OFDM Turbo DeCodulation enables cross-layer optimization of application and link related transceiver elements resulting in a versatile concept for transmitting correlated source parameters.

Bounds on the potential of mobile broadband access are evaluated based on capacity achieving 2×2 and 4×4 MIMO systems and assuming effective concepts for inter-cell interference cancellation. An upper bound of $\bar{\mathcal{G}} < 1.65$ Gbit/s is obtained for a 4×4 MIMO system with complete interference cancellation utilizing the maximum considered frequency bandwidth of $\Delta f = 20$ MHz and operating at the advantageous carrier frequency of $f_0 = 0.8$ GHz in an urban micro-cell environment.

These results imply that UMTS LTE may be improved significantly in the future by more sophisticated coding and signal processing. The most promising options are MIMO transmission in combination with interference management.

In conclusion it can be stated that mobile broadband access is an option for sparsely populated rural areas if carrier frequencies with advantageous propagation characteristics are available as well as sufficient frequency bandwidth. Emerging technologies like MIMO and intelligent interference management will further improve the performance of future mobile broadband access networks at the price of increasing complexity and energy consumption. However, given the demand for increasing data rates observed for evolving applications and services, mobile broadband access is likely to stay a supplement to wire-line DSL rather than becoming a full substitute. A noticeable difference between high-rate services for fixed line broadband access (e.g. high definition media streams) and lower-rate mobile data services (e.g. media streams fitted for handheld devices) is likely to remain over the next decades.

Typical Urban Channel Model

The typical urban (TU) channel model used for this work is based on the model recommended by 3GPP in [8]. 3GPP suggests a tapped delay line model with 20 paths (taps) defined by their delay and average inverse attenuations $1/\underline{h}^{[\text{att}]}$ as given in Fig. A.1 by the circles. As the given delays are no integer multiples of the modulation symbol duration T_S , oversampled versions have to be derived to adapt the channel model to the employed baseband channel model as given in Fig. 4.2. For the LTE physical layer two system bandwidths $\Delta f = 5$ MHz and $\Delta f = 20$ MHz exist with symbol durations $T_S^{-1} = 512 \cdot 15$ kHz and $T_S^{-1} = 2048 \cdot 15$ kHz, respectively. Furthermore, the attenuations have to be normalized to fulfill (4.3). The subsampled normalized power delay profiles for $\Delta f = 5$ MHz and $\Delta f = 20$ MHz are shown in Fig. A.1 by squares and triangles, respectively, and are summarized in tab. A.1

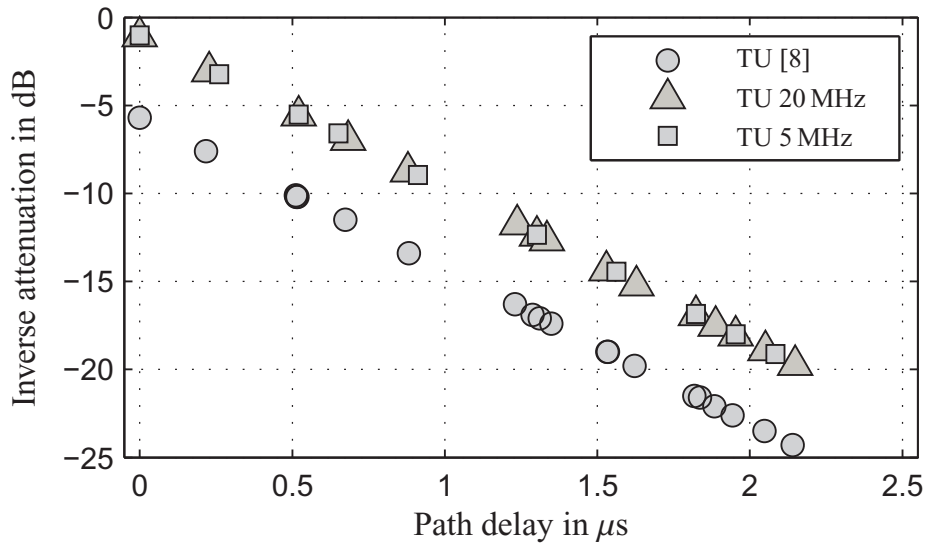


Figure A.1: Power delay profile for the typical urban (TU) channel model in [8] and normalized subsampled derivation.

20 MHz		5 MHz	
FIR tap delay in $T_S = \frac{1}{2048 \cdot 15 \text{ kHz}}$	attenuation in dB	FIR tap delay in $T_S = \frac{1}{512 \cdot 15 \text{ kHz}}$	attenuation in dB
0	1.08	0	1.02
7	3.07	2	3.23
16	5.58	4	5.52
21	6.96	5	6.60
27	8.76	7	8.96
38	11.76	10	12.35
40	12.41	12	14.45
41	12.67	14	16.85
47	14.38	15	18.00
50	15.23	16	19.13
56	16.91		
58	17.52		
60	18.07		
63	18.91		
66	19.75		

Table A.1: Normalized FIR tap delays and attenuations for the typical urban (TU) channel model.

System-Level Simulation Parameters

This chapter summarizes the path loss models used for system-level simulation. Three different system-level scenarios are considered: urban micro-cell (UMi), urban macro-cell (UMa) and rural macro-cell (RMa). All macro-cell path losses are lower bounded by the *minimum coupling loss* MCL between transmitter and receiver. This was adopted for all models from 3GPP's technical report 36.942 [15] and added for better comparability of path loss models from different sources. In accordance with [15] it is set to $MCL = 80$ dB for urban scenarios and to $MCL = 70$ dB for rural scenarios respectively. The effect of the minimum coupling loss is recognizable only in the direct vicinity of the base station and has a negligible effect on practical systems concerning their peak throughput and capacity.

B.1 Urban Micro-Cell Propagation Scenario (UMi)

For micro-cell simulations in urban environment the combination of the models by Walfisch and Ikegami, dubbed COST-Walfisch-Ikegami-Model (COST231WI), from [44] is employed. It distinguishes line-of-sight (LOS) and non-line-of-sight (NLOS) conditions.

The path loss in LOS conditions is calculated as:

$$L^{[\text{dB}]} = 42.6 + 26 \log_{10} \left(\frac{d}{\text{km}} \right) + 20 \log_{10} \left(\frac{f_0}{\text{MHz}} \right), \quad (\text{B.1})$$

In NLOS conditions the path loss is composed of three terms. The first component is the free space loss:

$$L_0^{[\text{dB}]} = 32.4 + 20 \log_{10} \left(\frac{d}{\text{km}} \right) + 20 \log_{10} \left(\frac{f_0}{\text{MHz}} \right).$$

The second term is the roof-top-to-street diffraction and scatter loss $L_{\text{rts}}(w, f_0, h_{\text{Roof}}, h_{\text{Mobile}}, \phi)$ which is a function of street width w , carrier frequency f_0 , building height h_{Roof} , mobile height h_{Mobile} , and road orientation ϕ . The third term is the multiple screen diffraction loss $L_{\text{msd}}(h_{\text{Base}}, h_{\text{Roof}}, d, f_0, b, k)$ which is a function of base station height h_{Base} , building height h_{Roof} , distance d , carrier frequency f_0 , building separation b , and city type factor k . The resulting path loss for NLOS conditions is then given by:

$$L^{[\text{dB}]} = \begin{cases} L_0^{[\text{dB}]} + L_{\text{rts}} + L_{\text{msd}} & \text{for } L_{\text{rts}} + L_{\text{msd}} > 0 \\ L_0^{[\text{dB}]} & \text{for } L_{\text{rts}} + L_{\text{msd}} \leq 0 \end{cases} \quad (\text{B.2})$$

The full definitions of L_{rts} and L_{msd} are given in [44].

The COST231WI model is restricted to the following parameter ranges:

Carrier frequency f_0 :	800	...	2000 MHz
BS height h_{Base} :	4	...	50 m
UE height h_{Mobile} :	1	...	3 m
Distance d :	20	...	500 m

Unless stated otherwise, the NLOS case is considered and the parameters summarized in Tab. B.1 are used throughout this thesis in compliance with [44] for simulation of UMi scenarios.

Parameter	Value
Street width w	10 m
Road orientation ϕ	90°
Building separation b	20 m
Building height h_{Roof}	20 m
BS height h_{Base}	30 m
UE height h_{Mobile}	1.8 m
City type factor k	0.7 (suburban)
Distance d	$\leq \sqrt{7}r$
Cell radius r	200 m

Table B.1: System-level simulation parameters for urban micro-cell propagation scenarios.

B.2 Urban Macro-Cell Propagation Scenario (UMa)

For macro-cell simulations in urban environment, two models are given in [44] that differ in their range of the carrier frequency f_0 . Both are based on Hata's model and are therefore abbreviated COST231Hata in this work.

For $150 \text{ MHz} \leq f_0 \leq 1500 \text{ MHz}$ Hata's model applies:

$$L^{[\text{dB}]} = \max \left\{ \text{MCL}, 69.55 + 26.16 \log_{10} \left(\frac{f_0}{\text{MHz}} \right) - 13.82 \log_{10} \left(\frac{h_{\text{Base}}}{\text{m}} \right) - a(h_{\text{Mobile}}, f_0) + \left(44.9 - 6.55 \log_{10} \left(\frac{h_{\text{Base}}}{\text{m}} \right) \right) \log_{10} \left(\frac{d}{\text{km}} \right) \right\} \quad (\text{B.3})$$

For $1500 \text{ MHz} \leq f_0 \leq 2000 \text{ MHz}$, a modification of (B.3) is used:

$$L^{[\text{dB}]} = \max \left\{ \text{MCL}, 46.3 + 33.9 \log_{10} \left(\frac{f_0}{\text{MHz}} \right) - 13.82 \log_{10} \left(\frac{h_{\text{Base}}}{\text{m}} \right) - a(h_{\text{Mobile}}, f_0) + \left(44.9 - 6.55 \log_{10} \left(\frac{h_{\text{Base}}}{\text{m}} \right) \right) \log_{10} \left(\frac{d}{\text{km}} \right) + C_m \right\} \quad (\text{B.4})$$

In (B.3) and (B.4) f_0 denotes the carrier frequency in MHz, h_{Base} the base station height in meters, and d the distance between user and base station in kilometers. $a(h_{\text{Mobile}}, f_0)$ is a mobile related function depending on carrier frequency f_0 and mobile height h_{Mobile} . C_m is an additional loss reflecting the building characteristics of the considered area. $a(h_{\text{Mobile}}, f_0)$ and C_m are explicitly given in [44].

The COST231Hata model (UMa1) is restricted to the following parameter ranges:

BS height h_{Base} :	30	...	200 m
UE height h_{Mobile} :	1	...	10 m
Distance d :	1	...	20 km

A third model valid for the complete range of considered carrier frequencies $800 \text{ MHz} \leq f_0 \leq 2000 \text{ MHz}$ is adopted from 3GPP's technical report 36.942 [15] and abbreviated 3GPPUrban.

$$L^{[\text{dB}]} = \max \left\{ \text{MCL}, 40 \left(1 - 0.004 \frac{\Delta h}{\text{m}} \right) \log_{10} \left(\frac{d}{\text{km}} \right) - 18 \log_{10} \left(\frac{\Delta h}{\text{m}} \right) + 21 \log_{10} \left(\frac{f_0}{\text{MHz}} \right) + 80 \right\} \quad (\text{B.5})$$

with

$$\Delta h = h_{\text{Base}} - h_{\text{Roof}}$$

According to [15], the 3GPPUrban model (UMa2) is valid only for NLOS and for a range of Δh from 0 to 50 m. It is designed mainly for distance from few hundred meters to kilometers.

Unless stated otherwise, the NLOS case is considered and the parameters summarized in Tab. B.2 are used throughout this thesis for simulation of both UMa propagation scenarios.

Parameter		Value
Minimum coupling loss	MCL	80 dB
BS height	h_{Base}	30 m
UE height	h_{Mobile}	1.8 m
BS above building height	Δh	10 m
Correction factor	C_m	0 dB
Distance	d	$\leq \sqrt{7}r$
Cell radius	r	10 km

Table B.2: System-level simulation parameters for urban macro-cell propagation scenarios.

B.3 Rural Macro-Cell Propagation Scenario (RMa)

The model for rural macro-cell scenarios is again adopted from [15] and consequently abbreviated 3GPPUrban.

$$L^{[\text{dB}]} = \max \left\{ \text{MCL}, 28.61 + 44.49 \log_{10} \left(\frac{f_0}{\text{MHz}} \right) - 4.78 \log_{10} \left(\frac{f_0}{\text{MHz}} \right)^2 - 13.82 \log_{10} \left(\frac{h_{\text{Base}}}{\text{m}} \right) + \left[44.9 - 6.55 \log_{10} \left(\frac{h_{\text{Base}}}{\text{m}} \right) \right] \log_{10} \left(\frac{d}{\text{km}} \right) \right\} \quad (\text{B.6})$$

According to [15], this model is designed mainly for distance from few hundred meters to kilometers.

Unless stated otherwise, the NLOS case is considered and the parameters summarized in Tab. B.3 are used throughout this thesis for simulation of RMa scenarios.

Parameter		Value
Minimum coupling loss	MCL	70 dB
BS height	h_{Base}	40 m
Distance	d	$\leq \sqrt{7}r$
Cell radius	r	10 km

Table B.3: System-level simulation parameters for urban macro-cell propagation scenarios.

System-Level Performance

This chapter summarizes the UMTS LTE system-level performance in terms of average cell goodput $\bar{\mathcal{G}}$ calculated by numerical integration of (6.5) based on the average bits per channel use \mathcal{B} as given in Chapters 4 and 5.

C.1 UMTS LTE with AWGN Channel

Δf	5 MHz				20 MHz			
α	1.0	0.5	0.2	0.0	1.0	0.5	0.2	0.0
Urban Micro-cell (UMi), COST231WI								
$f_0 = 0.8$ GHz	9.7	11.8	14.6	20.1	38.7	47.2	58.6	80.3
$f_0 = 2.0$ GHz	9.7	11.8	14.6	20.1	38.7	47.2	58.6	80.3
Urban Macro-cell (UMa1), COST231Hata								
$f_0 = 0.8$ GHz	8.4	10.0	11.9	14.3	31.7	36.9	42.0	47.6
$f_0 = 2.0$ GHz	4.7	5.0	5.1	5.2	13.9	14.4	14.7	14.9
Urban Macro-cell (UMa2), 3GPPUrban								
$f_0 = 0.8$ GHz	8.9	10.3	11.7	13.3	32.8	36.8	40.4	43.9
$f_0 = 2.0$ GHz	6.3	6.7	7.0	7.2	20.0	20.7	21.3	21.6
Rural Macro-cell (RMa), 3GPPRural								
$f_0 = 0.8$ GHz	8.8	11.0	14.0	20.1	35.2	43.8	55.8	80.3
$f_0 = 2.0$ GHz	8.8	11.0	13.9	20.1	35.2	43.8	55.7	80.3

Table C.1: Average cell goodput $\bar{\mathcal{G}}$ in Mbit/s for \mathcal{B} of UMTS LTE assuming AWGN (cf. Fig. 4.8, AWGN).

C.2 UMTS LTE Approximation

Δf	5 MHz				20 MHz			
α	1.0	0.5	0.2	0.0	1.0	0.5	0.2	0.0
Urban Micro-cell (UMi), COST231WI								
$f_0 = 0.8$ GHz	9.4	11.5	14.3	20.1	37.7	46.0	57.1	80.3
$f_0 = 2.0$ GHz	9.4	11.5	14.3	20.1	37.7	46.0	57.1	80.3
Urban Macro-cell (UMa1), COST231Hata								
$f_0 = 0.8$ GHz	8.2	9.8	11.6	13.9	30.9	36.0	41.0	46.4
$f_0 = 2.0$ GHz	4.6	4.9	5.0	5.1	13.8	14.2	14.5	14.7
Urban Macro-cell (UMa2), 3GPPUrban								
$f_0 = 0.8$ GHz	8.6	10.0	11.4	13.0	31.9	35.9	39.4	42.8
$f_0 = 2.0$ GHz	6.1	6.5	6.8	7.0	19.6	20.4	20.9	21.2
Rural Macro-cell (RMa), 3GPPRural								
$f_0 = 0.8$ GHz	8.6	10.7	13.6	20.1	34.2	42.7	54.4	80.3
$f_0 = 2.0$ GHz	8.6	10.7	13.6	20.1	34.2	42.7	54.3	80.3

Table C.2: Average cell goodput $\bar{\mathcal{G}}$ in Mbit/s for \mathcal{B} of UMTS LTE approximation (4.25) (cf. Fig. 4.8, 3GPP reference).

C.3 UMTS LTE with TU Channel

Δf	5 MHz				20 MHz			
α	1.0	0.5	0.2	0.0	1.0	0.5	0.2	0.0
Urban Micro-cell (UMi), COST231WI								
$f_0 = 0.8$ GHz	7.4	9.1	11.5	20.1	27.9	34.3	43.5	80.3
$f_0 = 2.0$ GHz	7.4	9.1	11.5	20.1	27.9	34.3	43.5	80.3
Urban Macro-cell (UMa1), COST231Hata								
$f_0 = 0.8$ GHz	6.3	7.5	8.9	10.8	22.4	26.0	29.6	33.5
$f_0 = 2.0$ GHz	3.6	3.7	3.8	3.9	10.0	10.3	10.5	10.6
Urban Macro-cell (UMa2), 3GPPUrban								
$f_0 = 0.8$ GHz	6.7	7.8	8.9	10.1	23.4	26.2	28.7	31.1
$f_0 = 2.0$ GHz	4.7	5.0	5.2	5.4	14.3	14.9	15.2	15.5
Rural Macro-cell (RMa), 3GPPRural								
$f_0 = 0.8$ GHz	6.6	8.3	10.7	20.1	24.8	31.2	40.5	80.3
$f_0 = 2.0$ GHz	6.6	8.3	10.7	20.1	24.8	31.1	40.4	80.3

Table C.3: Average cell goodput $\bar{\mathcal{G}}$ in Mbit/s for \mathcal{B} of UMTS LTE assuming the TU channel model (cf. Fig. 4.8, TU 5 MHz, TU 20 MHz).

C.4 UMTS LTE with Rayleigh Channel

Δf	5 MHz				20 MHz			
α	1.0	0.5	0.2	0.0	1.0	0.5	0.2	0.0
Urban Micro-cell (UMi), COST231WI								
$f_0 = 0.8$ GHz	6.8	8.3	10.6	20.1	27.1	33.4	42.5	80.5
$f_0 = 2.0$ GHz	6.8	8.3	10.6	20.1	27.1	33.4	42.5	80.3
Urban Macro-cell (UMa1), COST231Hata								
$f_0 = 0.8$ GHz	5.8	6.9	8.2	10.0	21.7	25.2	28.7	32.6
$f_0 = 2.0$ GHz	3.3	3.4	3.5	3.6	9.7	9.9	10.1	10.3
Urban Macro-cell (UMa2), 3GPPUrban								
$f_0 = 0.8$ GHz	6.2	7.1	8.1	9.3	22.7	25.5	27.9	30.3
$f_0 = 2.0$ GHz	4.3	4.6	4.8	4.9	13.9	14.4	14.7	15.0
Rural Macro-cell (RMa), 3GPPRural								
$f_0 = 0.8$ GHz	6.0	7.6	9.9	20.0	24.1	30.3	39.5	79.8
$f_0 = 2.0$ GHz	6.0	7.6	9.9	19.8	24.1	30.3	39.5	78.3

Table C.4: Average cell goodput $\bar{\mathcal{G}}$ in Mbit/s for \mathcal{B} of UMTS LTE assuming the Rayleigh Channel model (cf. Fig. 4.8, Rayleigh).

C.5 Shannon

Δf	5 MHz				20 MHz			
α	1.0	0.5	0.2	0.0	1.0	0.5	0.2	0.0
Urban Micro-cell (UMi), COST231WI								
$f_0 = 0.8$ GHz	15.0	18.7	24.0	107.4	60.1	74.7	96.0	411.6
$f_0 = 2.0$ GHz	15.0	18.7	24.0	87.5	60.1	74.7	96.0	332.0
Urban Macro-cell (UMa1), COST231Hata								
$f_0 = 0.8$ GHz	12.8	15.4	18.3	22.3	48.1	56.1	64.1	72.8
$f_0 = 2.0$ GHz	7.1	7.4	7.7	7.8	21.6	22.2	22.5	22.8
Urban Macro-cell (UMa2), 3GPPUrban								
$f_0 = 0.8$ GHz	13.8	16.0	18.3	20.9	50.6	56.9	62.6	68.0
$f_0 = 2.0$ GHz	9.6	10.2	10.6	10.9	30.6	31.7	32.4	32.9
Rural Macro-cell (RMa), 3GPPRural								
$f_0 = 0.8$ GHz	13.2	16.8	22.0	65.9	52.9	67.1	88.0	245.6
$f_0 = 2.0$ GHz	13.3	16.8	22.1	57.1	53.1	67.3	88.1	210.6

Table C.5: Average cell goodput $\bar{\mathcal{G}}$ in Mbit/s for bound on \mathcal{B} of a single antenna system with UMTS LTE modulation stage (cf. Fig. 5.28, Shannon).

C.6 2×2 MIMO

Δf	5 MHz				20 MHz			
α	1.0	0.5	0.2	0.0	1.0	0.5	0.2	0.0
Urban Micro-cell (UMi), COST231WI								
$f_0 = 0.8$ GHz	30.1	37.4	48.0	214.8	120.2	149.5	192.1	823.2
$f_0 = 2.0$ GHz	30.1	37.4	48.0	175.0	120.2	149.5	192.1	664.1
Urban Macro-cell (UMa1), COST231Hata								
$f_0 = 0.8$ GHz	25.6	30.8	36.7	44.5	96.1	112.2	128.3	145.6
$f_0 = 2.0$ GHz	14.2	14.9	15.3	15.7	43.2	44.3	45.0	45.5
Urban Macro-cell (UMa2), 3GPPUrban								
$f_0 = 0.8$ GHz	27.6	32.1	36.7	41.9	101.2	113.9	125.3	136.0
$f_0 = 2.0$ GHz	19.2	20.4	21.2	21.8	61.2	63.4	64.8	65.8
Rural Macro-cell (RMa), 3GPPRural								
$f_0 = 0.8$ GHz	26.4	33.5	44.0	131.8	105.7	134.1	176.0	491.2
$f_0 = 2.0$ GHz	26.6	33.7	44.1	114.3	106.3	134.6	176.3	421.2

Table C.6: Average cell goodput $\bar{\mathcal{G}}$ in Mbit/s for bound on \mathcal{B} of a 2×2 MIMO system with UMTS LTE modulation stage (cf. Fig. 5.28, 2×2 MIMO).

C.7 4 × 4 MIMO

Δf	5 MHz				20 MHz			
α	1.0	0.5	0.2	0.0	1.0	0.5	0.2	0.0
Urban Micro-cell (UMi), COST231WI								
$f_0 = 0.8$ GHz	60.1	74.7	96.0	429.5	240.4	298.9	384.2	1646.4
$f_0 = 2.0$ GHz	60.1	74.7	96.0	350.0	240.4	298.9	384.2	1328.1
Urban Macro-cell (UMa1), COST231Hata								
$f_0 = 0.8$ GHz	51.2	61.6	73.3	89.1	192.2	224.5	256.6	291.2
$f_0 = 2.0$ GHz	28.4	29.8	30.7	31.3	86.4	88.6	90.0	91.0
Urban Macro-cell (UMa2), 3GPPUrban								
$f_0 = 0.8$ GHz	55.2	64.2	73.4	83.8	202.4	227.8	250.5	272.0
$f_0 = 2.0$ GHz	38.4	40.7	42.4	43.7	122.4	126.7	129.6	131.6
Rural Macro-cell (RMa), 3GPPRural								
$f_0 = 0.8$ GHz	52.9	67.1	88.0	263.5	211.4	268.2	351.9	982.3
$f_0 = 2.0$ GHz	53.2	67.3	88.2	228.5	212.6	269.2	352.6	842.5

Table C.7: Average cell goodput $\bar{\mathcal{G}}$ in Mbit/s for bound on \mathcal{B} of a 4×4 MIMO system with UMTS LTE modulation stage (cf. Fig. 5.28, 4 × 4 MIMO).

Deutschsprachige Kurzfassung

Es herrscht weithin Einigkeit darüber, dass kaum eine technologische Entwicklung der letzten Dekaden das tägliche Leben so stark und nachhaltig beeinflusst hat wie das Voranschreiten der Informationstechnik. Das Internet bildet heute einen essentiellen Teil moderner Infrastruktur, die nicht nur eine globalisierte und international eng verzahnte Wirtschaft ermöglicht, sondern auch die Lebensweise von Millionen Menschen verändert. Das Aufkommen von hochentwickelten und leistungsfähigen mobilen Endgeräten in Kombinationen mit einfach zu bedienenden Anwendungen verursachen derzeit einen schnell wachsenden Bedarf an mobilen hochratigen Datenzugängen. Einige Vorhersagen gehen davon aus, dass im Jahr 2015 ein Datenvolumen von bis zu $2.0 \cdot 10^{18}$ Byte pro Monat weltweit über Mobilfunknetze angefordert werden wird. Eine Mehrheit von Experten ist nach einer Studie des Münchener Kreises der Meinung, dass zwischen den Jahren 2015 und 2019 mehr Menschen in Deutschland das Internet über mobile Endgeräte benutzen als über drahtgebundene Computer. Gleichzeitig stellen die Mobilfunkbetreiber schon heute fest, dass durch die Dominanz des Datenverkehrs über die Sprachdienste die Umsätze, die mit Mobilfunkdiensten erzielt werden, nicht mehr in der Lage sind, mit dem wachsenden Datenvolumen Schritt zu halten – der Gewinn pro gesendetem Bit verringert sich. Außerdem ist mobiler hochratiger Datenzugang derzeit nur in dicht besiedelten Gebieten möglich, die im Allgemeinen ohnehin über eine gut ausgebaute Kommunikationsinfrastruktur verfügen. Menschen in einigen weniger dicht besiedelten Gebieten sind bezüglich hochratiger Datenzugänge nach wie vor unterversorgt.

Dies alles begründet die Anstrengungen, die derzeit in Forschung und Entwicklung im Bereich des Mobilfunks unternommen werden, um mit künftigen mobilen Zugangstechniken höhere Nutzerdurchsätze erreichen zu können, während gleichzeitig die Komplexität von Netzarchitektur und Algorithmen so gering wie möglich gehalten werden sollen, um so Investitions- und Betriebskosten zu begrenzen. Einen Ansatz zur Versorgung der bisher unterversorgten ländlichen Gebiete in Deutschland stellt die Möglichkeit dar, in naher Zukunft die Frequenzen der digitalen Dividende im Bereich um 800 MHz für den Mobilfunk zu nutzen. Vor diesem Hintergrund zeigt die vorliegende Arbeit auf, welche Technologien zur Verfügung stehen und stellt neue Ansätze vor, mit denen Verbesserungen von Qualität, Kapazität und Abdeckung von Mobilfunknetzen erreicht werden können. Dabei werden schließlich auch Obergrenzen aufgezeigt, die dem Mobilfunk dabei gesetzt sind.

Zunächst wird die Evolution der physikalischen Übertragungsschichten von der zweiten

bis hin zur vierten Generation des Mobilfunks skizziert. Als jene vierte Generation des Mobilfunks wird beispielhaft die Weiterentwicklung des UMTS-Standards (Universal Mobile Telecommunication System) zu UMTS-LTE (Long Term Evolution) eingehend beschrieben und analysiert. Die physikalische Übertragungsschicht von UMTS-LTE erlaubt durch Turbo-Codierung mit Ratenanpassung in Kombination mit dem HARQ-Verfahren (hybrid automatic repeat request) und den komplexen Mapping-Verfahren QPSK (quadrature phase shift keying), 16QAM (quadrature amplitude modulation) und 64QAM eine robuste Übertragung, die sich den Bedingungen des Mobilfunkkanals flexibel anpassen kann. Durch die Verwendung von OFDM (orthogonal frequency division multiplex) auf der Abwärtsstrecke lassen sich Übertragungen auch über frequenzselektive Kanäle mit relativ geringem Aufwand entzerren.

Das UMTS-HSDPA-System (high-speed downlink packet access), das als Mobilfunkstandard der dritten Generation auf dem CDMA-Verfahren (code division multiple access) beruht, verwendet in seiner derzeitigen Version HSDPA+ mit LTE vergleichbare Algorithmen bei Codierung und Modulation. Im dem idealen Fall, dass die Übertragung auf dem Mobilfunkkanal lediglich durch AWGN (additive white Gaussian noise) gestört wird, können also LTE und HSDPA bezüglich der Anzahl \mathcal{B} der pro Kanalzugriff übertragenen Informationsbits als etwa gleichwertig angesehen werden. Lediglich die Ressourcen die in Zeit und Frequenz für einen Kanalzugriff benötigt werden unterscheiden sich. Diese werden durch das Zeit-Bandbreite-Produkt der verschiedenen Modulationsarten charakterisiert. Es wird gezeigt, dass das bei LTE verwendete OFDM-Verfahren gegenüber dem bei HSDPA+ eingesetzten CDMA-Verfahren eine um 10 % höhere spektrale Effizienz aufweist.

Die maximal erreichbare spektrale Effizienz ist durch die Shannon-Grenze gegeben. Diese kann durch den Einsatz von A Sende- und Empfangsantennen in einem MIMO-System (multiple-input multiple-output) maximal um diesen Faktor A erhöht werden. Aus diesen Grenzen der spektralen Effizienz ergeben sich in Kombination mit dem Zeit-Bandbreite-Produkt der in LTE verwendeten OFDM-Modulation Obergrenzen für \mathcal{B} , also für die maximale Anzahl von Bits die pro Kanalzugriff übertragen werden können.

Abbildung D.1 zeigt den Verlauf von \mathcal{B} über der Kanalqualität (SNR, signal-to-noise ratio) für UMTS-LTE und vergleicht diesen mit einer vom 3GPP (Third Generation Partnership Project) vorgeschlagenen Referenzkurve. Dabei stellt die Kurve des LTE-Systems Simulationsergebnisse für die beispielhaft gewählten Code-Raten $cr \in \{1/2, 1/3, 2/3, 3/4, 4/5\}$ dar. Als Obergrenzen für \mathcal{B} sind die sich aus der Shannon-Grenze ergebenden Kurven für Einantennen-Systeme sowie für 2×2 - und 4×4 -MIMO-Systeme gegeben.

Eine neuartige Modifikation des LTE-Systems ist die Umsortierung der codierten Bits bei Übertragung mit 64QAM, die in dieser Arbeit vorgestellt wird. Es wird gezeigt, dass die verschiedenen Bit-Level der 64QAM bei Übertragung über einen gestörten Mobilfunkkanal einen ungleichmäßigen Schutz vor Bitfehlern erfahren. Im vorgestellten System wird diese Eigenschaft der 64QAM genutzt, um durch geschicktes Umsortieren der codierten Bits die Decodier-Eigenschaften des parallel verketteten LTE-Turbo-Decodierers derart zu beeinflussen, dass nach wenigen Turbo-Iterationen ein höheres Maß an Zuverlässigkeit der empfangenen Informationsbits erreicht wird, als beim LTE-System ohne Modifikation. Für die

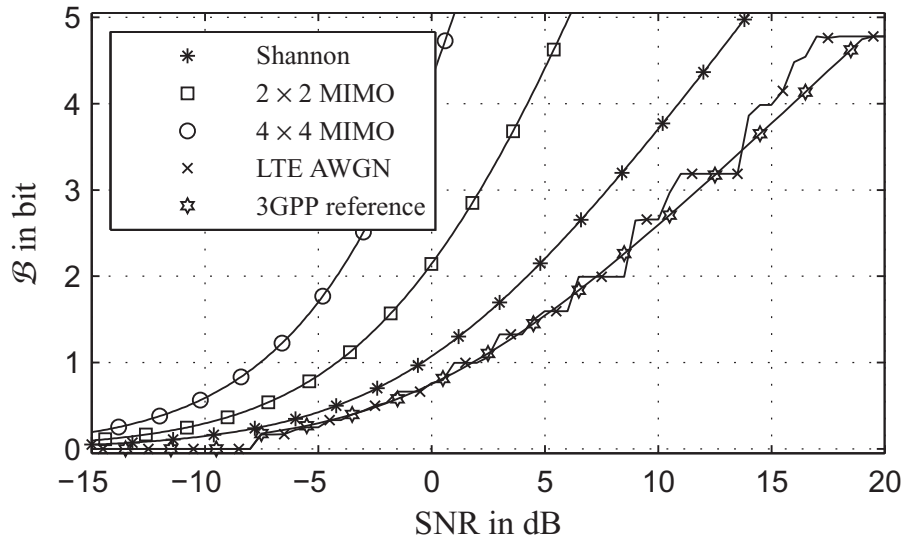


Figure D.1: Übertragene Informationsbit pro Kanalzugriff \mathcal{B} über der Kanalqualität (AWGN-Kanalmodell) gemäß Simulationen der physikalischen Übertragungsschicht von UMTS-LTE, Annäherung nach 3GPP-Standard und Obergrenzen für Ein- und Mehrantennensysteme unter Annahme des Zeit-Bandbreite-Produktes der OFDM-Modulation von UMTS-LTE

betrachteten Beispiele ergeben sich daraus für den nicht-iterativen Empfang SNR-Gewinne von bis zu 1.5 dB. Das Einsparen von Decodier-Iterationen ist hierbei gleichzusetzen mit dem Einsparen von zur Decodierung aufgewendeter Energie.

Eine weitergehende neuartige Abwandlung des UMTS-LTE-Übertragungssystems, die in dieser Arbeit vorgestellt wird, ist das Ersetzen des ursprünglichen Turbo-Codierers durch einen einfachen Wiederholungs-Code und das Zufügen eines rekursiven Rate-1 Faltungs-Codierers mit Einflusslänge 2 vor dem komplexen Mapper als sogenanntes Bit-Doping. Der Empfänger wird hierbei als BICM-ID-System (bit-interleaved coded modulation with iterative decoding) implementiert: Der Addierer zur Decodierung des Wiederholungs-Codes wird mit der Kombination aus Soft-Demapper und MAP-Decoder (maximum a posteriori) des Bit-Dopings iterativ verknüpft. Es wird gezeigt, dass die Leistungsfähigkeit \mathcal{B} dieses Systems vergleichbar ist mit der des ursprünglichen UMTS-LTE-Systems, jedoch erhebliche Einsparungen bezüglich der Rechenkomplexität im Empfänger möglich sind.

Zusätzlich wird eine neue Methode zur Optimierung von OFDM-BICM-ID-Systemen auf Basis von EXIT-Charakteristiken (extrinsic information transfer) des komplexen Demappers für frequenzselektive Kanäle vorgestellt. An einem Beispiel wird gezeigt, dass eine gute Vorhersage der Empfängercharakteristik mit Hilfe der Kenntnis der Übertragungsfunktion des Kanals und einer begrenzten Anzahl gespeicherter EXIT-Charakteristiken möglich ist. Ist diese Information auch am Sender bekannt, kann die Restbitfehlerrate des OFDM-BICM-ID-Systems durch gezielte Beeinflussung der Empfängercharakteristik gesenkt werden, indem verschiedene komplexe Mapping-Verfahren auf den verschiedenen Unterträgern des OFDM-Systems angewendet werden.

Schließlich wird mit der neuartigen Kombination von OFDM mit dem bekannten TDeC-System (Turbo DeCodulation) zu einem OFDM-TDeC-System eine Möglichkeit vorgeschlagen, von den schichtenübergreifenden Optimierungsmöglichkeiten des TDeC-Verfahrens und der hohen spektralen Effizienz der OFDM-Modulation zu profitieren. Der Vorteil des TDeC-Verfahrens besteht in der Ausnutzung vorhandener Restredundanz in den Parametern codierter Multimediasignale (parametrischer Codec) in der Anwendungsschicht und erfordert daher eine iterative Verknüpfung von physikalischer Schicht und Anwendungsschicht im Empfänger. Es werden dabei zwei verschiedene Implementierungen von OFDM-TDeC vorgestellt. Ein Vergleich der Leistungsfähigkeiten beider OFDM-TDeC-Systeme mit dem um ein parametrisches Codierer-Modell erweiterten UMTS-LTE-System erweist sich als nicht eindeutig: Während das UMTS-LTE-System schon bei sehr geringen Kanalqualitäten eine Übertragung der Codec-Parameter mit hoher Qualität gewährleistet, weisen beide OFDM-TDeC-Systeme bei niedrigen Kanalqualitäten auch niedrigere Qualitäten der empfangenen Codec-Parameter jedoch eine höhere spektrale Effizienz bei der Übertragung auf.

Auf Basis der Simulationsergebnisse der physikalischen Schicht wird der erzielbare Nutzerdurchsatz abhängig von der Kanalqualität am jeweiligen Standort des Nutzers bestimmt. Die Kanalqualität in Form eines SINR-Wertes (signal-to-interference-and-noise ratio) für eine bestimmte Position eines Nutzers innerhalb einer Funkzelle wird dabei im Wesentlichen von drei Faktoren beeinflusst, nämlich

- dem Pfadverlust L zwischen Nutzer und Basisstation (BS) und der daraus resultierenden Stärke des Empfangssignals,
- der empfangenen Interferenzleistung aus den benachbarten Funkzellen und
- der Rauschleistung des Empfängers.

Pfadverlust und Interferenz werden sowohl durch die Position des Nutzers innerhalb der Funkzelle als auch durch die Trägerfrequenz f_0 beeinflusst. Es werden exemplarisch zwei Trägerfrequenzen verglichen: Die Frequenz $f_0 = 0.8$ GHz repräsentiert eine Frequenz aus der digitalen Dividende, die Frequenz $f_0 = 2.0$ GHz eine mögliche Trägerfrequenz des in heutigen UMTS-Netzen üblichen 2.1-GHz-Bandes. Der frequenz- und entfernungsabhängige Pfadverlust wird durch verschiedene vorgestellte Modelle beschrieben, deren Einsatz von der betrachteten Zellgröße (Mikrozelle, Makrozelle) und Bebauung (städtisch, ländlich) abhängig ist. Als Ausbreitungsszenarien werden

- UMi (urban micro-cell), innerstädtische Funkzelle mit Radius $r = 200$ m,
- UMa (urban macro-cell), innerstädtische Funkzelle mit Radius $r = 10$ km,
- RMa (rural macro-cell), ländliche Funkzelle mit Radius $r = 10$ km,

definiert, die sich durch das verwendete Pfadverlustmodell unterscheiden.

Die Rauschleistung des Empfängers ist abhängig von der Frequenzbandbreite Δf , die Rauschleistungsdichte beträgt -174 dBm/Hz. Es werden exemplarisch zwei Frequenzbandbreiten $\Delta f = 5$ MHz (heutiges UMTS) und $\Delta f = 20$ MHz (maximale von UMTS-LTE

unterstützte Frequenzbandbreite) angenommen. Für den in alle Richtungen gleichmäßig strahlenden (isotropen) Sender wird je nach verwendeter Frequenzbandbreite eine Sendeleistung von 43 dBm (ca. 20 W) bei $\Delta f = 5$ MHz und 46 dBm (ca. 40 W) bei $\Delta f = 20$ MHz angenommen. Zusätzlich wird ein Antennengewinn von 15 dB berücksichtigt. Ferner wird gezeigt, dass im betrachteten System eine Sektorisierung der Funkzellen keinen Einfluss auf die resultierenden SINR-Werte der Abwärtsstrecke hat.

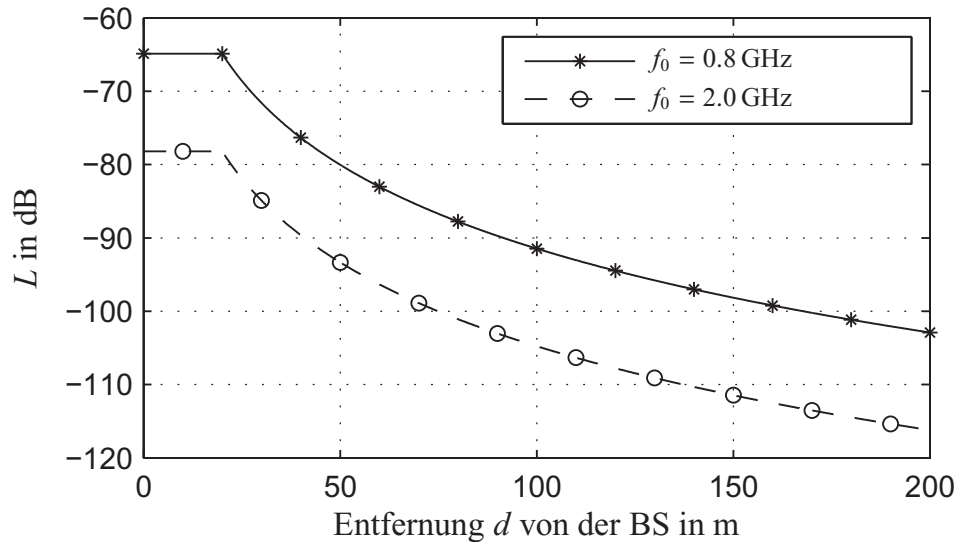


Figure D.2: Pfadverlust für das UMi-Szenario für die betrachteten Trägerfrequenzen.

Abbildung D.2 stellt den ortsabhängigen Pfadverlust L für die beiden betrachteten Trägerfrequenzen beispielhaft für das UMi-Szenario dar. Geht man von einer einzelnen Basisstation aus und lässt Interferenzen benachbarter Funkzellen unberücksichtigt, ist bei konstantem Empfängerrauschen der dargestellte Verlauf des Pfadverlustes äquivalent zum ortsabhängigen SINR. Damit ergibt sich eine Begrenzung der Funkzelle aus der Rauschleistung, das System ist rauschbegrenzt. Der Einfluss der Trägerfrequenz auf die mögliche Flächenabdeckung tritt deutlich zu Tage: der Unterschied des Pfadverlustes beträgt 13.3 dB. Es ist zu beachten, dass dieser Wert sehr stark von den Annahmen des Ausbreitungsmodells abhängt. Im Falle des RMa-Szenarios beträgt der Unterschied 5.9 dB. In jedem Fall kann jedoch festgestellt werden, dass der Einsatz von niedrigen Trägerfrequenzen aus der digitalen Dividende eine um mindestens Faktor 2 effizientere Flächenabdeckung ermöglichen wird.

Im Folgenden wird ein Mobilfunknetz betrachtet, in dem sich Zellgrenzen als ideale Handover-Grenzen ergeben, also an Orten, an denen die Signale zweier benachbarter Basisstationen mit gleicher Leistung empfangen werden. Unter der für die Systemsimulationen getroffenen Annahme, dass zentrale BS und interferierende BS mit derselben Sendeleistung und Trägerfrequenz senden, ist dies an den Punkten gleicher Entfernung von den Basisstationen der Fall. Es wird eine hexagonale zentrale Zelle mit Zellradius r betrachtet, die von einem Ring von sechs interferierenden Basisstationen umgeben ist. Diese Interferenzen werden, wie auch das Empfängerrauschen, als AWGN angenommen. So können der

SNR-Wert wie in Abbildung D.1 gegeben und der ortsabhängige SINR-Wert gleichwertig gegeneinander ausgetauscht werden. Die Leistung der Interferenz ist ortsabhängig und wird wie die Empfangsleistung des Nutzsignals durch das verwendete Pfadverlustmodell, also das Ausbreitungs-Szenario, beschrieben.

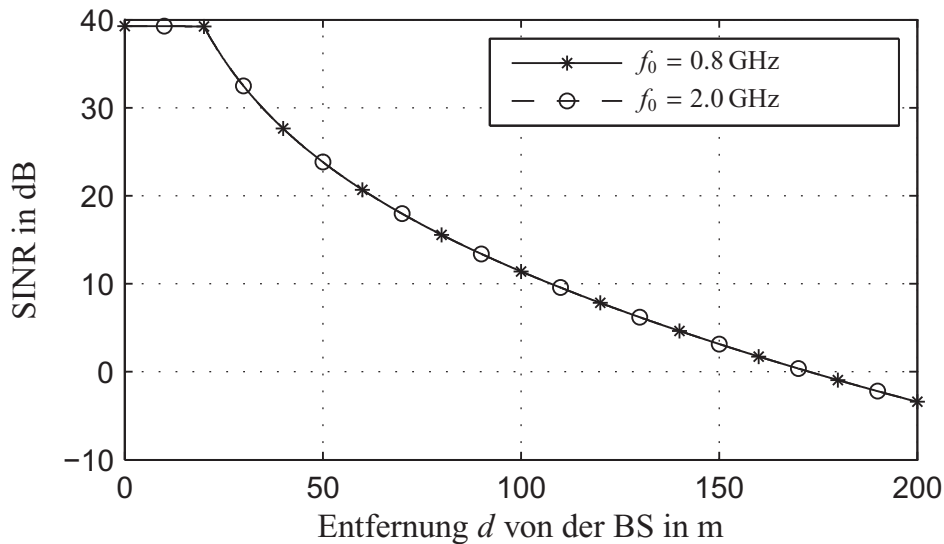


Figure D.3: SINR in einem zellularen UMi-Szenario für die betrachteten Trägerfrequenzen f_0 .

Es ergeben sich ortsabhängige SINR-Werte, wie sie für die beiden betrachteten Trägerfrequenzen in Abbildung D.3 für das UMi-Szenario dargestellt sind. Es wird deutlich, dass sich für beide Trägerfrequenzen ein nahezu gleicher SINR-Wert einstellt, der an der Zellgrenzen bei circa -3 dB liegt. Hier weisen Nutzsignal und jeweils zwei interferierende Signale von benachbarten Funkzellen die gleiche Leistung auf. Die geringe Leistung des Empfängerrauschens spielt bei der Berechnung des SINR-Wertes eine untergeordnete Rolle, die betrachtete Funkzelle ist für beide Trägerfrequenzen interferenzbegrenzt.

Abhängig vom SINR-Wert eines Nutzers innerhalb einer Funkzelle und der Anzahl der ihm zugewiesenen Ressourcen-Elemente (REs, entsprechen den Kanalzugriffen) kann mit Hilfe der in Abbildung D.1 gegebenen \mathcal{B} -Verläufe ein individueller Nutzerdurchsatz \mathcal{G} bestimmt werden. In einer Funkzelle mit einer Frequenzbandbreite von $\Delta f = 20$ MHz stehen beim UMTS-LTE-System 8400 REs pro 0.5-ms-Zeitschlitz zur Verfügung, bei $\Delta f = 5$ MHz ist dies nur noch ein Viertel, also 2100 REs pro 0.5-ms-Zeitschlitz. Der durchschnittliche Gesamtdurchsatz einer Funkzelle $\overline{\mathcal{G}}$ ergibt sich dann als Summe der individuellen Nutzerdurchsätze gemittelt über der Zellfläche. Dieser durchschnittliche Gesamtdurchsatz $\overline{\mathcal{G}}$ ist dabei unabhängig von der Gesamtzahl der Nutzer, skaliert jedoch linear mit den verfügbaren REs, also mit der Frequenzbandbreite Δf .

In Abbildung D.4 sind die erreichten durchschnittlichen Gesamtdurchsätze $\overline{\mathcal{G}}$ für die betrachteten Ausbreitung-Szenarien, Trägerfrequenzen f_0 und Frequenzbandbreiten Δf unter der Annahme von AWGN angegeben. Für $\Delta f = 5$ MHz kann unabhängig von der Trägerfrequenz f_0 im UMi-Szenario ein durchschnittlicher Zelldurchsatz $\overline{\mathcal{G}} = 9.7$ Mbit/s erreicht

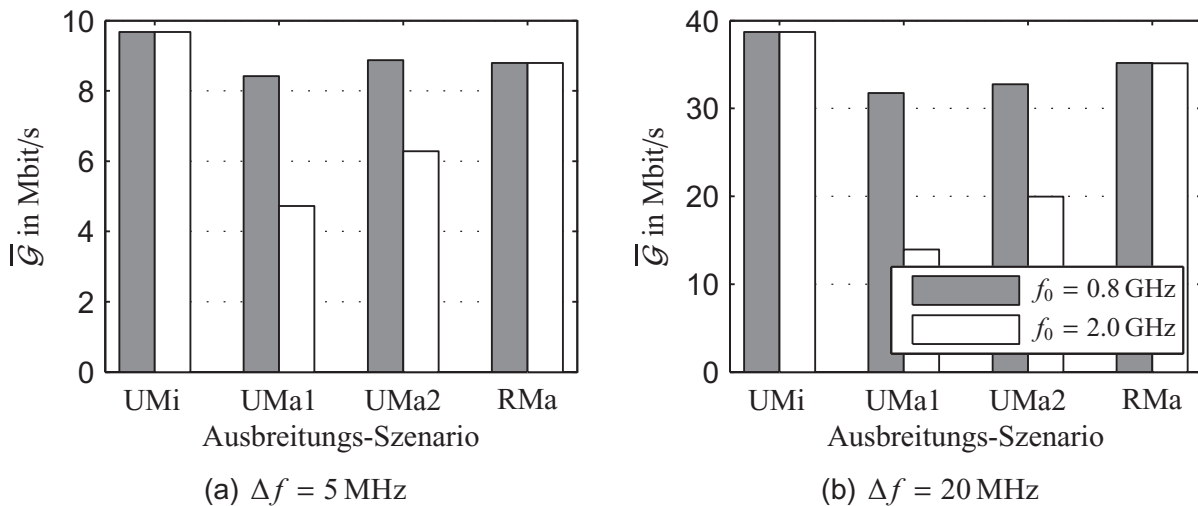


Figure D.4: $\bar{\mathcal{G}}$ für UMTS-LTE für die betrachteten Ausbreitungs-Szenarien, Trägerfrequenzen f_0 und Frequenzbandbreiten Δf unter der Annahme eines AWGN-Kanals.

werden, für das RMa-Szenario ergibt sich $\bar{\mathcal{G}} = 8.8$ Mbit/s. Im Falle der RMa-Szenarien (UMa1 und UMa2 unterscheiden sich durch das verwendete Pfadverlustmodell) wird ein Unterschied für die betrachteten Trägerfrequenzen deutlich: Durch die besseren Ausbreitungseigenschaften der niedrigen Trägerfrequenz $f_0 = 0.8$ MHz ergibt sich weiterhin eine Interferenzbegrenzung der Funkzelle, für $f_0 = 2.0$ ist die Funkzelle dagegen rauschbegrenzt, so dass bereits bei Entfernungen $d < r = 10$ km von der Basisstation der SINR-Wert zu niedrig ist, um einen individuellen Durchsatz $\mathcal{G} > 0$ bit/s zu erzielen (SINR < -7.5 dB, vgl. Abbildung D.1). Deutlich wird in Abbildung D.4, dass in den rein interferenzbegrenzten Fällen (UMi, RMa) der durchschnittliche Zelldurchsatz $\bar{\mathcal{G}}$ linear mit der Frequenzbandbreite Δf skaliert, das heißt, im Falle $\Delta f = 20$ MHz viermal so groß ist wie im Falle $\Delta f = 5$ MHz.

Zur Ermittlung der individuellen Nutzerdurchsätze \mathcal{G} werden zunächst zufällige, innerhalb der Funkzelle räumlich gleichverteilte Positionen für eine festgelegte Anzahl an Nutzern ermittelt. Die von der Frequenzbandbreite abhängige Gesamtzahl der Ressourcenelemente wird durch die Gesamtzahl der Nutzer dividiert und jedem Nutzer wird ein entsprechender Anteil zugewiesen, das heißt, die REs werden gleichmäßig auf alle Nutzer verteilt. Die individuellen Nutzerdurchsätze \mathcal{G} werden mit Hilfe der \mathcal{B} -Verläufe aus Abbildung D.1 ermittelt und gespeichert. Wiederholt man diesen Vorgang mit immer neuen zufälligen Nutzerpositionen (Monte-Carlo-Prinzip) ergibt sich eine statistische Verteilung der Nutzerdurchsätze innerhalb der Funkzelle, die in Form einer kumulativen Verteilungsfunktion wie in Abbildung D.5 dargestellt werden kann. Für 20 und 100 Nutzer und Frequenzbandbreiten von $\Delta f = 5$ MHz und $\Delta f = 20$ MHz sind hier die Verteilungen der individuellen Nutzerdurchsätze \mathcal{G} für UMTS-LTE angegeben. Dabei wird ein UMi-Szenario mit AWGN-Kanalmodell angenommen, es wird über die Ergebnisse von 1000 Monte-Carlo-Iterationen gemittelt.

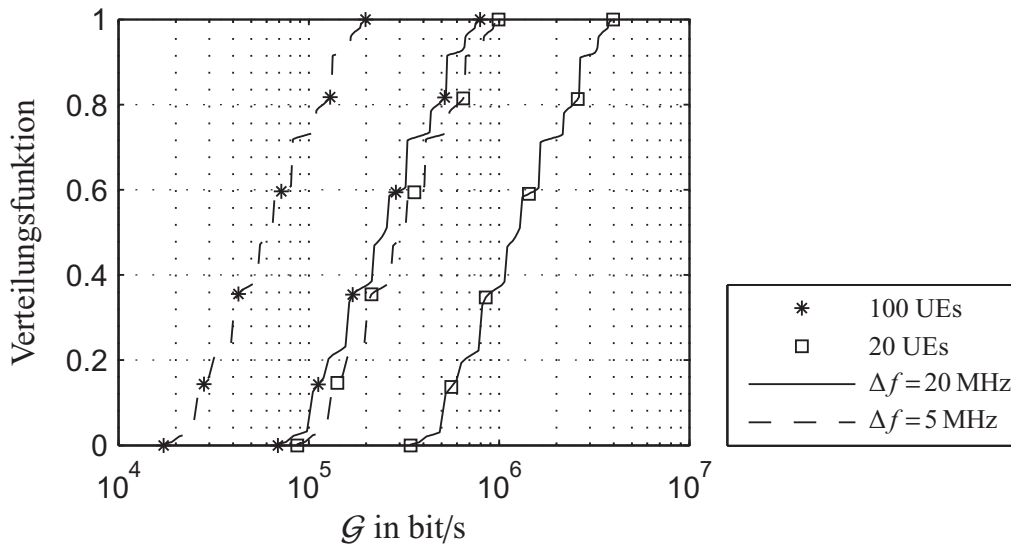


Figure D.5: Verteilungen der individuellen Nutzerdurchsätze \mathcal{G} für UMTS-LTE für die betrachteten Frequenzbandbreiten Δf und verschiedene Nutzerzahlen (user equipments, UEs), UMi, AWGN, $f_0 = 2.0$ GHz, 1000 Monte-Carlo-Iterationen.

Für die 20 % der Nutzer mit den niedrigsten SINR-Werten (nahe dem Zellrand) ergeben sich individuelle Nutzerdurchsätze zwischen $\mathcal{G} = 0.3$ Mbit/s und $\mathcal{G} = 0.6$ Mbit/s bei 20 Nutzern und $\Delta f = 20$ MHz, für die 20 % der Nutzer mit den besten SINR-Werten (nahe der Basisstation) ergeben sich dagegen Nutzerdurchsätze zwischen $\mathcal{G} = 2.3$ Mbit/s und $\mathcal{G} = 4$ Mbit/s. In Abbildung D.5 wird deutlich, dass die Nutzerdurchsätze linear mit der Gesamtzahl der Nutzer sowie mit der zur Verfügung stehenden Frequenzbandbreite skalieren. In allen dargestellten Fällen betragen die individuellen Nutzerdurchsätze am Zellrand nur etwa ein Zehntel der Nutzerdurchsätze nahe der Basisstation.

Die hier präsentierten Zahlenwerte ergeben sich als Berechnungs- und Simulationsergebnisse und basieren auf den beschriebenen Voraussetzungen und Annahmen. Bestätigt werden diese Werte durch Labor- und Feldversuche der LTE/SAE Trial Initiative (LSTI), wobei SAE für Service Architecture Evolution steht. Erklärte Ziele dieser Initiative von 23 Geräteherstellern und 9 Netzbetreibern sind das Vorantreiben der Industrialisierung von LTE-Technologie, das Aufzeigen und die Überprüfung der Leistungsfähigkeit von UMTS-LTE sowie die Förderung eines LTE-Ökosystems. Bei den Feldversuchen kam 2x2-MIMO-Technologie zum Einsatz und bestätigte die maximal erzielbaren Einzelnutzerdurchsätze von bis zu 160 Mbit/s unter Laborbedingungen (ein Nutzer, $cr \approx 1$, 64QAM, keine Interferenz). Extrapolationen, die den Einfluss mehrerer Nutzer in einem interferenzbegrenzten zellularen Mobilfunknetz berücksichtigen, ergaben unter den getroffenen Annahmen ähnliche individuelle Nutzerraten, wie die hier rechnerisch und simulativ ermittelten.

Auch die in Abbildung D.1 angegebenen Obergrenzen für Ein- und Mehrantennen-Systeme werden als Grundlage für Monte-Carlo-Simulationen auf der Systemebene verwendet, um so Obergrenzen für die erzielbaren individuellen Nutzerdurchsätze \mathcal{G} und durchschnitt-

lichen Gesamtdurchsätze $\bar{\mathcal{G}}$ zu ermitteln. Derzeit entwickelt man außerdem verschiedene Konzepte des Interferenz-Managements, die dazu beitragen sollen, den negativen Effekt der Interferenzen aus Nachbarzellen auf den Nutzerdurchsatz zu mindern. Um diesen Effekt auf Systemebene abzubilden, wird ein Faktor α eingeführt, der den Beitrag der Interferenzen zum SINR-Wert eines Nutzers beschreibt. $\alpha = 1$ steht dabei für den vollen Beitrag der Interferenz (keine Kompensation), $\alpha = 0$ für eine vollständige Kompensation. Dieser letzte Fall kann auch als der einer isolierten Einzelzelle interpretiert werden, bei der nur Nutzer in einer durch den Radius r definierten hexagonalen Zellfläche berücksichtigt werden.

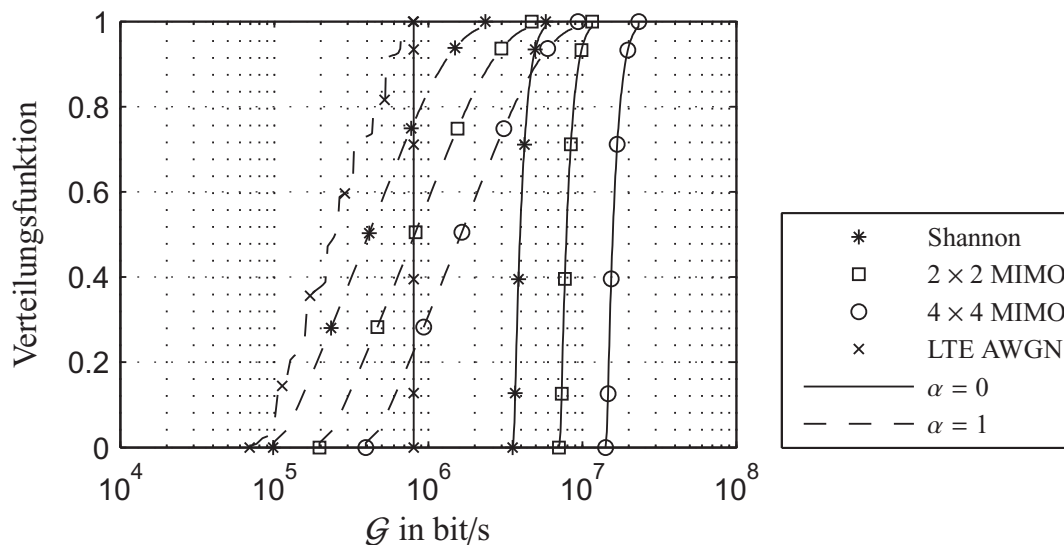


Figure D.6: Obergrenzen der Verteilungsfunktionen der individuellen Nutzerdurchsätze \mathcal{G} für Ein- und Mehrantennensysteme mit und ohne den Einfluss von Interferenz-Kompensation (α) im UMi-Szenario, Vergleich zu UMTS-LTE, $f_0 = 0.8$ GHz, $\Delta f = 20$ MHz, AWGN, 100 UEs, 1000 Monte-Carlo-Iterationen.

Abbildung D.6 zeigt die ermittelten Obergrenzen der Verteilungsfunktionen der individuellen Nutzerdurchsätze für Ein- und Mehrantennensysteme mit und ohne den Einfluss von Interferenz-Management im UMi-Szenario für 100 Benutzer und stellt diese den Ergebnissen gegenüber, die für UMTS-LTE ermittelt wurden. Es ist deutlich zu erkennen, dass das LTE-System insbesondere für schlechte Kanalqualitäten (Zellrand) eine Leistungsfähigkeit zeigt, die der theoretisch maximal möglichen sehr nahe kommt. Die größeren Unterschiede bei höheren Kanalqualitäten (nahe der Basisstation) haben Ihre Ursache in der Limitierung der Code-Raten und des komplexen Mappings. Die Verdoppelungen der Antennenzahl führen wie erwartet zu Verdoppelungen der theoretisch maximal möglichen individuellen Nutzerdurchsätze. Besonders drastisch ist der Effekt der vollständigen Interferenz-Kompensation. Dieser ermöglicht eine Erhöhung der individuellen Nutzerdurchsätze nicht nur in der Nähe der Basisstation sondern auch am Zellrand.

Schließlich betrachtet die Arbeit auch die Effekte, die die vorgestellten Modifikationen und neuen Konzepte der physikalischen Übertragungsschicht mit Blick auf die durch-

schnittlichen Gesamtzelldurchsätze $\bar{\mathcal{G}}$ und die individuellen Nutzerdurchsätze \mathcal{G} erzielen können. So bewirkt die vorgestellte Umsortierung der codierten Bits bei Übertragung mit 64QAM in den betrachteten Beispielen bei nicht-iterativer Decodierung eine Steigerung des durchschnittlichen Gesamtzelldurchsatzes um ca. 1.5 Mbit/s. Die Verwendung des Wiederholungs-Codes mit Bit-Doping im Sender und der BICM-ID-Struktur im Empfänger führt gegenüber UMTS-LTE wie erwartet zu leichten Verlusten beim durchschnittlichen Gesamtzelldurchsatz und den individuellen Nutzerdurchsätze, ermöglicht jedoch ein Übertragungen mit deutlich geringerer Komplexität. Die erwähnte höhere spektrale Effizienz der beiden betrachteten OFDM-TDeC-Systeme führt in den hier betrachteten Beispielen gegenüber dem LTE-System zu einer Steigerung der Anzahl der bedienten Nutzer um 15 bis 100 %. Diese Zunahme der Kapazität geht wie erwartet zu Lasten der Qualität der empfangenen Parameter am Zellrand.

Zusammenfassend wird deutlich, dass heutige physikalische Übertragungsschichten im Falle von Einantennen-Systemen Leistungsfähigkeiten aufweisen, die sehr nahe am theoretischen Maximum liegen. UMTS-LTE kann dabei auch künftig von optimierten Codierverfahren und hochentwickelter Signalverarbeitung profitieren. Die vielversprechendsten Methoden hierbei liegen in Mehrantennentechniken (MIMO) und intelligentem Interferenz-Management.

Abschließend lässt sich feststellen, dass mit Hilfe des Mobilfunks hochratige Datenzugänge auch in dünn besiedelten ländlichen Gebieten realisiert werden können. Voraussetzung dafür ist jedoch das Vorhandensein von Trägerfrequenzen mit vorteilhaften Ausbreitungseigenschaften wie denen der digitalen Dividende in Kombination mit ausreichend großer Frequenzbandbreite. Derzeit entwickelte Konzepte wie MIMO und intelligentes Interferenz-Management werden die Leistungsfähigkeit künftiger Generationen von Mobilfunktechnik zum Preis erhöhter Komplexität weiter verbessern. Betrachtet man jedoch den Bedarf an Nutzerdurchsätzen für die sich derzeit abzeichnenden Anwendungen und Dienste, wird klar, dass mobile Datenzugänge auch künftig eher eine Ergänzung zu drahtgebundenen Techniken bleiben werden, als diese zu ersetzen. Ein deutlicher Unterschied zwischen hochratigen Anwendungen für drahtgebundene Geräte wie hochauflösende Videoprogramme einerseits und mobilen Datendiensten wie auf mobile Endgeräte angepasste Multimedia-Anwendungen andererseits wird auch in den nächsten Dekaden mit großer Wahrscheinlichkeit bestehen bleiben.

Bibliography

- [1] IEEE Standard for Local and Metropolitan Area Networks Part 16: Air Interface for Fixed Broadband Wireless Access Systems. *IEEE Std 802.16-2004 (Revision of IEEE Std 802.16-2001)*, 2004.
- [2] IEEE Standard for Information technology-Telecommunications and information exchange between systems-Local and metropolitan area networks-Specific requirements - Part 11: Wireless LAN Medium Access Control (MAC) and Physical Layer (PHY) Specifications. *IEEE Std 802.11-2007 (Revision of IEEE Std 802.11-1999)*, June 2007.
- [3] IEEE Standard for Local and metropolitan area networks Part 16: Air Interface for Broadband Wireless Access Systems. *IEEE Std 802.16-2009 (Revision of IEEE Std 802.16-2004)*, May 2009.
- [4] 3rd Generation Partnership Project (3GPP); Technical Specification Group GSM/EDGE Radio Access Network. Digital cellular telecommunications system (Phase 2+); Modulation. TS 05.04, Version 8.4.0, Rel. 1999, November 2001.
- [5] 3rd Generation Partnership Project (3GPP); Technical Specification Group GSM/EDGE Radio Access Network. Digital cellular telecommunications system (Phase 2+); Channel coding. TS 05.03, Version 8.9.0, Rel. 1999, January 2005.
- [6] 3rd Generation Partnership Project (3GPP); Technical Specification Group GSM/EDGE Radio Access Network. Radio transmission and reception. TS 05.05, Version 8.20.0, Rel. 1999, November 2005.
- [7] 3rd Generation Partnership Project (3GPP); Technical Specification Group GSM/EDGE Radio Access Network;. Digital cellular telecommunications system (Phase 2+); Multiplexing and multiple access on the radio path. TS 45.002, Version 8.0.0, Rel. 8, February 2009.
- [8] 3rd Generation Partnership Project (3GPP); Technical Specification Group Radio Access Network. Deployment aspects. TR 25.943, Version 8.0.0, Rel. 8, December 2008.
- [9] 3rd Generation Partnership Project (3GPP); Technical Specification Group Radio Access Network. Evolved Terrestrial Radio Access (E-UTRA); Base Station (BS) radio transmission and reception;. TR 36.804, Version 1.2.0, Rel. 8, April 2008.

- [10] 3rd Generation Partnership Project (3GPP); Technical Specification Group Radio Access Network. Evolved Terrestrial Radio Access (E-UTRA); Multiplexing and Channel Coding. TS 36.212, Version 8.2.0, Rel. 8, March 2008.
- [11] 3rd Generation Partnership Project (3GPP); Technical Specification Group Radio Access Network. Evolved Terrestrial Radio Access (E-UTRA); Physical Channels and Modulation. TS 36.211, Version 8.2.0, Rel. 8, March 2008.
- [12] 3rd Generation Partnership Project (3GPP); Technical Specification Group Radio Access Network. Multiplexing and channel coding (FDD). TS 25.212, Version 8.1.0, Rel. 8, March 2008.
- [13] 3rd Generation Partnership Project (3GPP); Technical Specification Group Radio Access Network. Spreading and modulation (FDD). TS 25.213, Version 8.0.0, Rel. 8, March 2008.
- [14] 3rd Generation Partnership Project (3GPP); Technical Specification Group Radio Access Network. Base Station (BS) radio transmission and reception (FDD). TS 25.104, Version 8.7.0, Rel. 8, May 2009.
- [15] 3rd Generation Partnership Project (3GPP); Technical Specification Group Radio Access Network. Evolved Terrestrial Radio Access (E-UTRA); Radio Frequency (RF) system scenarios;. TR 36.942, Version 8.2.0, Rel. 8, May 2009.
- [16] 3rd Generation Partnership Project (3GPP); Technical Specification Group Radio Access Network. UE Radio Access capabilities. TS 25.306, Version 8.7.0, Rel. 8, June 2009.
- [17] 3rd Generation Partnership Project (3GPP); Technical Specification Group Services and System Aspects. Mandatory speech CODEC speech processing functions; AMR speech CODEC; General description. TS 26.071, Version 8.0.0, Rel. 8, December 2008.
- [18] 3rd Generation Partnership Project (3GPP); Technical Specification Group Services and System Aspects. Circuit Switched Fallback in Evolved Packet System; Stage 2. TS 23.228, Version 9.2.0, Rel. 9, December 2009.
- [19] 3rd Generation Partnership Project (3GPP); Technical Specification Group Services and System Aspects. IP Multimedia Subsystem (IMS); Stage 2. TS 23.228, Version 9.2.0, Rel. 9, December 2009.
- [20] F. Adachi, M. Sawahashi, and K. Okawa. Tree-structured generation of orthogonal spreading codes with different lengths for forward link of ds-cdma mobile radio. *Electronics Letters*, 33(1):27–28, Jan 1997.

-
- [21] M. Adrat, P. Vary, and J. Spittka. Iterative Source-Channel Decoder Using Extrinsic Information from Softbit-Source Decoding. In *IEEE International Conference on Acoustics, Speech, and Signal Processing (ICASSP)*, Salt Lake City, USA, May 2001.
- [22] F. Apel-Soetebeer and J. Rentmeister. *Breitbandatlas 2009_01 – Zentrale Ergebnisse, Teil I des Berichts zum Atlas für Breitband-Internet des BMWi*. Bundesministerium für Wirtschaft und Technologie (BMWi), June 2009. in German.
- [23] A. Ashikhmin, G. Kramer, and S. ten Brink. Extrinsic Information Transfer Functions: Model and Erasure Channel Properties. *IEEE Transactions on Information Theory*, November 2004.
- [24] C. Assimakopoulos and F. N. Pavlidou. Unified models for adaptive OFDM systems when QAM or PSK modulation is applied. *European Transactions on Telecommunications*, 18(7):777–790, February 2007.
- [25] C. Ball, T. Hindelang, I. Kambourov, and S. Eder. Spectral Efficiency Assessment and Radio Performance Comparison Between LTE and WiMAX. In *Personal, Indoor and Mobile Radio Communications, 2008. PIMRC 2008. IEEE 19th International Symposium on*, pages 1–6, September 2008.
- [26] C. Berrou, A. Glavieux, and P. Thitimajshima. Near Shannon limit error-correcting coding and decoding: Turbo-codes (1). In *IEEE International Conference on Communications (ICC)*, Geneva, Switzerland, May 1993.
- [27] G. Bertrand. The IP Multimedia Subsystem in Next Generation Networks. May 2007.
- [28] E. Biglieri, R. Calderbank, A. Constantinides, A. Goldsmith, A. Paulraj, and H. V. Poor. *MIMO Wireless Communications*. Cambridge University Press, 2007.
- [29] T. Brüggem. *Unequal Error Protection by Source-Controlled Digital Modulation*. Dissertation, IND, RWTH Aachen, Templergraben 55, 52056 Aachen, 2006.
- [30] F. Büllingen and P. Stamm. Potenziale alternativer Techniken zur bedarfsgerechten Versorgung mit Breitbandzugängen. wik-Consult, Projekt Nr. 22/05, wik-Consult Endbericht für das Bundesministerium für Wirtschaft und Technologie, January 2006. in German.
- [31] G. Caire, G. Taricco, and E. Biglieri. Bit-Interleaved Coded Modulation. *IEEE Transactions on Information Theory*, pages 927–946, May 1998.
- [32] R. W. Chang. Synthesis of Band Limited Orthogonal Signals for Multi-channel Data Transmission. *Bell Systems Technology Journal*, 45:1775–1796, December 1966.
- [33] J. Cheng, A. Nimbalkar, Y. Blankenship, B. Classon, and T. Blankenship. Analysis of Circular Buffer Rate Matching for LTE Turbo Code. In *Proceedings of IEEE Vehicular Technology Conference (VTC-Fall)*, Calgary, Canada, Sept. 2008.

- [34] T. Clevorn. *Turbo Decodulation: Iterative Joint Source-Channel Decoding and Demodulation*. PhD thesis, RWTH Aachen University, 2007.
- [35] T. Clevorn, M. Adrat, and P. Vary. Turbo DeCodulation using Highly Redundant Index Assignments and Multi-Dimensional Mappings. In *Intl. Symposium on Turbo Codes & Related Topics*, Munich, April 2006.
- [36] T. Clevorn, J. Brauers, M. Adrat, and P. Vary. Turbo DeCodulation: Iterative Combined Demodulation and Source-Channel Decoding. *IEEE Communications Letters*, 9(9):820–822, September 2005.
- [37] T. Clevorn, S. Godtmann, and P. Vary. EXIT Chart Analysis of Non-Regular Signal Constellation Sets for BICM-ID. In *International Symposium on Information Theory and its Applications (ISITA)*, October 2004.
- [38] T. Clevorn, S. Godtmann, and P. Vary. PSK versus QAM for Iterative Decoding of Bit-Interleaved Coded Modulation. In *Proceedings of IEEE Global Telecommunications Conference (GLOBECOM)*, December 2004.
- [39] T. Clevorn, L. Schmalen, P. Vary, and M. Adrat. On The Optimum Performance Theoretically Attainable for Scalarly Quantized Correlated Sources. In *Proceedings of International Symposium on Information Theory and its Applications (ISITA)*, Seoul, Korea, October 2006.
- [40] T. M. Cover and J. A. Thomas. *Elements of Information Theory*. J. Wiley & Sons, Chichester, 2 edition, 2006.
- [41] E. Dahlman, S. Parkvall, J. Sköld, and P. Beming. *3G Evolution: HSPA and LTE for Mobile Broadband*. Elsevier, 1st edition, 2007.
- [42] D. Divsalar and F. Pollara. Hybrid Concatenated Codes and Iterative Decoding. TDA Progress Report 42-130, August 1997.
- [43] G. Erber, T. Köhler, C. Lattemann, B. Preissl, and J. Rentmeister. *Rahmenbedingungen für eine Breitbandoffensive in Deutschland*. Deutsches Institut für Wirtschaftsforschung (DIW), Berlin, Germany, January 2004. in German.
- [44] European Co-operation in the Field of Scientific and Technical Research (COST) Action 231. Digital Mobile Radio Towards Future Generation Systems. Final Report, 1996.
- [45] European Telecommunications Standards Institute (ETSI). Radio Broadcasting Systems; Digital Audio Broadcasting (DAB) to mobile, portable and fixed receivers. EN 300 401, V1.4.1, June 2006.

-
- [46] European Telecommunications Standards Institute (ETSI). Digital Video Broadcasting (DVB); Frame structure channel coding and modulation for a second generation digital terrestrial television broadcasting system (DVB-T2). EN 302 755, V1.1.1, September 2009.
- [47] V. Garg. *IS-95 CDMA and CDMA 2000*. Prentice Hall PTR, Upper Saddle River, NJ, USA, 2000.
- [48] S. Godtmann, H. Lüders, G. Ascheid, and P. Vary. A Bit-Mapping Strategy for Joint Iterative Channel Estimation and Turbo-Decoding. In *Proceedings of IEEE Vehicular Technology Conference (VTC-Fall)*, Calgary, Canada, September 2008.
- [49] N. Görtz. On the Iterative Approximation of Optimal Joint Source-Channel Decoding. *IEEE Journal on Selected Areas in Communications*, 19(9):1662–1670, September 2001.
- [50] J. Hagenauer and P. Hoehner. A Viterbi algorithm with soft-decision outputs and its applications. In *Proceedings of IEEE Global Telecommunications Conference (GLOBECOM)*, pages 1680–1686 vol.3, Nov 1989.
- [51] J. Hagenauer, E. Offer, and L. Papke. Iterative Decoding of Binary Block and Convolutional Codes. *IEEE Transactions on Information Theory*, 42(2):429–445, March 1996.
- [52] H. Holma and A. Toskala. *WCDMA for UMTS - Radio Access for Third Generation Mobile Communications*. John Wiley & Sons, Ltd, 3rd edition, 2004.
- [53] H. Holma and A. Toskala. *LTE for UMTS - OFDMA and SC-FDMA Based Radio Access*. John Wiley & Sons, Ltd, 1st edition, 2009.
- [54] International Telecommunication Union (ITU). ISDN user-network interfaces - Interface structures and access capabilities. Recommendation I.412 (11/88), November 1988.
- [55] International Telecommunication Union (ITU). Vocabulary of terms for broadband aspects of ISDN. Recommendation I.113 (06/97), June 1997.
- [56] International Telecommunication Union (ITU). Framework and overall objectives of the future development of IMT-2000 and systems beyond IMT-2000. Recommendation M.1645 (06/03), June 2003.
- [57] International Telecommunication Union (ITU). International telephone connections and circuits; General Recommendations on the transmission quality for an entire international telephone connection; One-way transmission time. ITU-T G.114 (05/03), May 2003.

- [58] International Telecommunication Union (ITU). *digital.life – ITU Internet Report 2006*. December 2006.
- [59] ISO/IEC 7498-1. Information technology – Open System Interconnection – Basic Reference Model: The Basic Model. Second edition, June 1996.
- [60] K. Johansson, J. Bergman, D. Gerstenberger, M. Blomgren, and A. Wallen. Multi-Carrier HSPA Evolution. In *Proceedings of IEEE Vehicular Technology Conference (VTC Spring)*, pages 1–5, April 2009.
- [61] K.-D. Kammeyer. *Nachrichtenübertragung*. Teubner, Wiesbaden, Germany, 3 edition, November 2004.
- [62] X. Li, A. Chindapol, and J. A. Ritcey. Bit-Interleaved Coded Modulation with Iterative Decoding and 8PSK Signalling. *IEEE Transactions on Communications*, 50(8):1250 – 1257, August 2002.
- [63] X. Li and J. A. Ritcey. Bit-Interleaved Coded Modulation with Iterative Decoding. *IEEE Communications Letters*, 1(6):169 – 171, November 1997.
- [64] H. Lüders, B. Eschbach, L. Schmalen, and P. Vary. OFDM Turbo DeCodulation with EXIT Optimized Bit Loading and Signal Constellations. In *IEEE International Conference on Acoustics, Speech, and Signal Processing (ICASSP)*, pages 2589–2592, Taipei, Taiwan, April 2009. IEEE.
- [65] H. Lüders, A. Minwegen, B. Eschbach, and P. Vary. An Improvement of UMTS LTE 64QAM Performance. *to appear in European Transactions on Telecommunications (ETT), Special Issue on MC-CDMA*, (5), 2010.
- [66] H. Lüders, A. Minwegen, and P. Vary. Improving UMTS LTE Performance by UEP in High Order Modulation. In *7th International Workshop on Multi-Carrier Systems & Solutions (MC-SS 2009)*, pages 185 – 194, Herrsching, Germany, May 2009. Springer.
- [67] H. Lüders, A. Minwegen, and P. Vary. Low Complexity Coding and Modulation for UMTS LTE: BICM-ID with Repetition Coding. In *14th International OFDM-Workshop 2009 (InOWo'09)*, Hamburg, Germany, September 2009. TUHH.
- [68] H. Lüders, L. Schmalen, and P. Vary. Approximating EXIT Characteristics of Soft Demodulators in OFDM BICM-ID Systems for Time Variant Frequency Selective Fading Channels. In *Proceedings of International ITG Conference on Source and Channel Coding*, Ulm, Germany, January 2008.
- [69] N. S. Muhammad and J. Speidel. Joint optimization of signal constellation bit labeling for bit-interleaved coded modulation with iterative decoding. *IEEE Communications Letters*, 9(9):775–777, September 2005.

-
- [70] Münchener Kreis. Zukunft und Zukunftsfähigkeit der Informations- und Kommunikationstechnologien und Medien. Internationale Delphi-Studie 2030, November 2009. (in German).
- [71] Ha H. Nguyen and Trung Q. Bui. Bit-Interleaved Coded Modulation with Iterative Decoding in Impulsive Noise. *IEEE Transactions on Power Delivery*, January 2007.
- [72] Organisation for Economic Co-Operation and Development (OECD). *OECD Communications Outlook 2007*. OECD Publishing, ISBN: 978-92-64-00704-8, 2007.
- [73] S. Pfletschinger and F. Sanzi. Error Floor Removal for Bit-Interleaved Coded Modulation with Iterative Detection. *IEEE Transactions on Communications*, 5(11):3174–3181, November 2006.
- [74] J. G. Proakis. *Digital Communications*, chapter 10. McGraw-Hill, New York, 4th edition, 2001.
- [75] P. Robertson, E. Villebrun, and P. Hoeher. A Comparison of Optimal and Sub-Optimal MAP Decoding Algorithms Operating in the Log Domain. In *Proc. IEEE Int. Conf. Commun. (ICC)*, pages 1009–1013, Seattle, USA, 1995.
- [76] F. Schreckenbach. *Iterative Decoding of Bit-Interleaved Coded Modulation*. PhD thesis, Technische Universität München, 2007.
- [77] F. Schreckenbach, N. Görtz, J. Hagenauer, and G. Bauch. Optimization of Symbol Mappings for Bit-Interleaved Coded Modulation with Iterative Decoding. *IEEE Communications Letters*, December 2003.
- [78] E. Seurre, P. Savelli, and P.-J. Pietri. *EDGE for Mobile Internet*. Artech House, Norwood, 2003.
- [79] E. Seurre, P. Savelli, and P.-J. Pietri. *GPRS for Mobile Internet*. Artech House, Norwood, 2003.
- [80] J. Tan and G. L. Stöber. Analysis and Design of Interleaver Mappings for Iteratively Decoded BICM. *International Conference on Communications (ICC)*, 3:1403–1407, April/May 2002.
- [81] E. Telatar. Capacity of Multi-antenna Gaussian Channels. *European Transactions on Telecommunications*, 10:585–595, November 1999.
- [82] S. ten Brink. Designing Iterative Decoding Schemes with the Extrinsic Information Transfer Chart. *AEÜ Int. J. Electron. Commun.*, pages 389 – 398, November 2000.
- [83] S. ten Brink. Convergence Behaviour of Iteratively Decoded Parallel Concatenated Codes. *IEEE Transactions on Communications*, 49:1727 – 1737, October 2001.

- [84] J. Terry and J. Heiskala. *OFDM Wireless LANs: A Theoretical and Practical Guide*. Sams Publishing, 2nd edition, September 2002.
- [85] N. H. Tran and H. H. Nguyen. A Novel Multi-Dimensional Mapping of 8-PSK for BICM-ID. In *IEEE International Conference on Communications (ICC)*, Istanbul, Turkey, June 2006.
- [86] M. Tüchler and J. Hagenauer. EXIT Charts of Irregular Codes. In *Proc. of Conf. on Information Sciences and Systems (CISS)*, Princeton University, March 2002.
- [87] UMTS Forum. Towards Global Mobile Broadband; Standardising the future of mobile communications with LTE (Long Term Evolution). White Paper, February 2008.
- [88] P. Vary and H. Lüders. Mobiler Breitbandzugang in der Fläche durch gemeinsame Nutzung von Infrastruktur? – Technikaspekte und Regulierung –. In Arnold Picot, editor, *10 Jahre wettbewerbsorientierte Regulierung von Netzindustrien in Deutschland*, chapter 9. Verlag C. H. Beck, München, February 2008.
- [89] VoLGA Forum. Voice over LTE via Generic Access; Requirements Specification; Phase1. VoLGA - Requirements V1.3.1, June 2009.
- [90] S. Weinstein and P. Ebert. Data Transmission by Frequency-Division Multiplexing Using the Discrete Fourier Transform. *IEEE Transactions on Communications*, 19(5):628–634, October 1971.
- [91] Marc Werner. *Maßnahmen zur Qualitäts- und Kapazitätssteigerung in UMTS-Mobilfunknetzen*. Dissertation, IND, RWTH Aachen, Templergraben 55, 52056 Aachen, March 2006.
- [92] T.-W. Yu, C.-Y. Wang, C.-H. Wang, and W.-H. Sheen. EXIT-Chart Based Labeling Design for Bit-interleaved Coded Modulation with Iterative Decoding. In *Information Theory, 2007. ISIT 2007. IEEE International Symposium on*, pages 56–60, Nice, June 2007.

Curriculum Vitae

Helge Erik Lüders

geboren am 30. November 1977

in Bernau bei Berlin

09.1984 – 12.1989	Werner-Seelenbinder-Oberschule, Groß Schönebeck
01.1990 – 06.1997	städtisches Gymnasium Velbert-Langenberg
Juni 1997	Abitur
07.1997 – 04.1998	5. Kp St/FmBtl 820, Düsseldorf: Wehrdienst als Fernmelder
06.1998 – 07.1998	Helmut Mauell GmbH, Velbert Neviges: mechanisches Grundpraktikum
10.1998 – 05.2004	RWTH Aachen: Studium der Elektro- und Informationstechnik, Vertiefung: Informations- und Kommunikationstechnik
10.2000 – 02.2003	Lehrstuhl für Mathematik I, RWTH Aachen: studentische Hilfskraft
10.2003 – 03.2004	
05.2003 – 07.2003	Australian Telecommunications Cooperative Research Centre, Perth, Australien: Fachpraktikum
Mai 2004	Diplom
07.2004 – 02.2010	Institut für Nachrichtengeräte und Datenverarbeitung, RWTH Aachen: wissenschaftlicher Mitarbeiter
seit März 2010	E-Plus Mobilfunk GmbH & Co. KG, Düsseldorf: strategischer Funknetzplaner

Köln, im Juli 2010